

# The Middle-to-late Eocene Greenhouse Climate

Simulated using the CESM 1.0.5

Michiel Baatsen

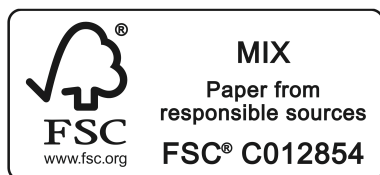
December 2018

Copyright © 2018 by Michiel Baatsen

Institute for Marine and Atmospheric research Utrecht (IMAU)  
Faculty of Science, Department of Physics, Utrecht University.  
Princetonplein 5, 3584 CC Utrecht, The Netherlands.

Cover: Impression of the Antarctic continent prior to (front) and after (back) the Eocene-Oligocene transition, based on present-day Antarctic bedrock topography and ice thickness (Bedmap2, Fretwell et al. 2013), the first being blended with a late Eocene geography reconstruction (Wilson et al., 2012).

ISBN 978-90-393-7087-2  
Printed by Gildeprint





# The Middle-to-late Eocene Greenhouse Climate

Simulated using the CESM 1.0.5

## Het Broeikas Klimaat tijdens het Midden tot Laat Eoceen

Gesimuleerd met het CESM 1.0.5

(met een samenvatting in het Nederlands)

### Proefschrift

ter verkrijging van de graad van doctor aan de Universiteit Utrecht op  
gezag van de rector magnificus, prof. dr. H.R.B.M. Kummeling, inge-  
volge het besluit van het college voor promoties in het openbaar te  
verdedigen op 13 februari 2019 des middags te 2.30 uur

door

**Michiel Liliane Johan Baatsen**

geboren op 15 juli 1990

te Brasschaat, België

Promotor: Prof. dr. ir. H.A. Dijkstra  
Copromotor: Dr. A.S. von der Heydt

This thesis was accomplished with financial support from the Dutch Ministry of Education, Culture and Science as a part of the Gravitation programme 'Reading the past to project the future', through the Netherlands Earth System Science Centre (NESSC) and organised by the Netherlands Organisation for Scientific Research (NWO).

---

# Contents

---

	Page
<b>Front Matter</b>	
<b>Figures and Tables</b>	<b>v</b>
List of Figures . . . . .	vii
List of Tables . . . . .	viii
<b>Frequently used Acronyms</b>	<b>ix</b>
<b>Summary</b>	<b>xi</b>
<b>Samenvatting</b>	<b>xiii</b>
<b>Acknowledgments</b>	<b>xv</b>
 <b>Main Matter</b>	
<b>1 Introduction</b>	<b>1</b>
1.1 The Cenozoic Climate . . . . .	3
1.2 Palaeoclimate Modelling and Palaeogeography . . . . .	5
1.3 The middle-to-late Eocene and EOT . . . . .	7
1.4 Research Questions and Outline. . . . .	9
1.4.1 Specific Scientific Questions	
1.4.2 Outline of the Thesis	
 <b>2 Eocene and Cenozoic Geography Reconstruction</b>	<b>13</b>
2.1 Palaeoclimate Modelling and Palaeogeography . . . . .	15
2.2 Plate-tectonic Reconstruction. . . . .	17
2.3 Generic Adjustments. . . . .	21
2.4 Specific Adjustments for the Middle-to-late Eocene . . . . .	23
2.5 Final Modifications and Smoothing . . . . .	26
2.6 Summary and Additional Reconstructions . . . . .	28

<b>3</b>	<b>Model Set-up and Experimental Design</b>	<b>31</b>
3.1	The Community Earth System Model (CESM) . . . . .	33
3.2	Experiments using Standalone POP Simulations . . . . .	35
3.2.1	Model Grid and Geography	
3.2.2	Atmospheric Forcing	
3.2.3	Experimental Design	
3.3	Experiments using Coupled CESM Simulations . . . . .	39
3.3.1	Pre-Industrial Reference	
3.3.2	Middle-to-late Eocene Configuration	
3.3.3	Overview of CESM Experiments	
<b>4</b>	<b>Multiple Equilibria in the Ocean Circulation State</b>	<b>45</b>
4.1	Introduction. . . . .	47
4.2	Model Spin-up . . . . .	48
4.3	Results. . . . .	51
4.3.1	Geometry-dependent Flow Patterns	
4.3.2	Multiple Equilibria within the PaleoMag Geography	
4.4	Summary and Discussion . . . . .	61
<b>5</b>	<b>CESM Simulations of the Eocene Climate</b>	<b>63</b>
5.1	Simulations and Spin-up . . . . .	65
5.2	Results: Middle-to-late Eocene Equilibrium Climate . . . . .	69
5.2.1	Ocean	
5.2.2	Atmosphere	
5.2.3	Climate Sensitivity	
5.3	Summary and Conclusions . . . . .	92
<b>6</b>	<b>Antarctic Summer Monsoons and Eocene Ice</b>	<b>95</b>
6.1	The Eocene Antarctic Climate . . . . .	97
6.2	Warm and Wet Antarctic Summers. . . . .	99
6.3	An Antarctic Summer Monsoon . . . . .	102
6.4	Eocene Ice on Antarctica . . . . .	105
6.5	Summary: Antarctic Ice and Warmth, a Paradox? . . . . .	108
<b>7</b>	<b>CESM Simulations using a 30Ma Geography</b>	<b>109</b>
7.1	Model Geography Difference . . . . .	111
7.2	Spin-up and Simulations . . . . .	113
7.3	Equilibrium Climate for 30Ma 2× PIC . . . . .	117
7.3.1	Ocean Circulation	
7.3.2	Atmosphere	

7.4 Climatic Changes between 38Ma and 30Ma 2× PIC . . . . .	121
7.4.1 Ocean	
7.4.2 Atmosphere	
7.5 Multiple Equilibria in the 30Ma Ocean Circulation . . . . .	127
7.6 30Ma 1× PIC Simulation and Climate Sensitivity . . . . .	131
7.6.1 Transports and Meridional Overturning Strength	
7.6.2 Climate Sensitivity	
7.7 Summary and Conclusions . . . . .	135
 <b>8 Overview of CESM Simulations – Antarctic Glaciation</b>	<b>137</b>
8.1 Temperature and Circulation . . . . .	139
8.1.1 Ocean	
8.1.2 Atmosphere	
8.2 Southeast Asian Monsoons in the Eocene . . . . .	147
8.3 Antarctic Glaciation at the EOT . . . . .	150
8.3.1 Pre-industrial versus Eocene Antarctica	
8.3.2 Antarctic Ice Growth and Equilibrium Level	
8.4 Summary and Conclusions . . . . .	159
 <b>9 Summary and Outlook</b>	<b>161</b>
9.1 Summary . . . . .	163
9.2 Outlook . . . . .	168
 <b>Back Matter</b>	
<b>Appendices:</b>	<b>169</b>
<b>A Pre-industrial Reference Climatology</b>	<b>169</b>
<b>B 38Ma 2× PIC Climatology</b>	<b>173</b>
<b>C Additional Model-Proxy Comparisons</b>	<b>177</b>
C.1 Sea Surface Temperature Proxies . . . . .	177
C.2 Terrestrial Temperature Proxies . . . . .	179
C.3 2× PIC Model-Proxy Temperature Comparison . . . . .	182
C.4 4× PIC Model-Model Comparison . . . . .	183
 <b>Bibliography</b>	<b>185</b>
<b>List of Publications</b>	<b>199</b>
<b>Curriculum Vitae</b>	<b>201</b>



---

# Figures and Tables

---

## List of Figures

### 1 Introduction

1.1	GSA Geologic Time Scale . . . . .	3
1.2	Cenozoic benthic $\delta^{18}\text{O}$ stack . . . . .	4
1.3	Early Eocene proxies versus models . . . . .	5
1.4	EOT at ODP site 1218 . . . . .	7

### 2 Eocene and Cenozoic Geography Reconstruction

2.1	Geography reconstruction flowchart . . . . .	16
2.2	Plate-tectonics in GPlates . . . . .	17
2.3	38Ma Boundary masks . . . . .	18
2.4	38Ma geography reconstruction: first step . . . . .	20
2.5	Reconstruction after generic adjustments . . . . .	21
2.6	Masks for specific adjustments . . . . .	23
2.7	Specific adjustments . . . . .	24
2.8	Final 38Ma geography reconstruction . . . . .	26
2.9	30Ma geography reconstruction . . . . .	29
2.10	Comparison with previous reconstructions . . . . .	30

### 3 Model Set-up and Experimental Design

3.1	Pre-industrial model grid . . . . .	34
3.2	38Ma PaleoMag model bathymetry grid . . . . .	35
3.3	Ocean-only forcing fields . . . . .	36
3.4	Model bathymetry grids (PaleoMag - Hot Spot) . . . . .	38
3.5	38Ma CESM geography . . . . .	40
3.6	38Ma CESM vegetation . . . . .	41
3.7	38Ma versus 30Ma model grid . . . . .	43

### 4 Multiple Equilibria in the Ocean Circulation State

4.1	Curvilinear model bathymetry . . . . .	48
4.2	POP Spin-up . . . . .	49
4.3	POP transport and MOC time series . . . . .	51

4.4	POP general circulation . . . . .	52
4.5	POP transports . . . . .	54
4.6	POP MSF and MHF . . . . .	55
4.7	Northern versus southern sinking . . . . .	57
4.8	Wind curl and BSF comparison . . . . .	58
4.9	Geography versus overturning change . . . . .	59
4.10	Estimated $\delta^{18}\text{O}$ response . . . . .	60

## 5 CESM Simulations of the Eocene Climate

5.1	38Ma CESM spin-up . . . . .	66
5.2	38Ma CESM ideal age tracers . . . . .	67
5.3	38Ma CESM Gregory plot . . . . .	68
5.4	38Ma 4× PIC ocean . . . . .	69
5.5	38Ma CESM MSF and MHF . . . . .	71
5.6	38Ma transport and MOC time series . . . . .	73
5.7	38Ma 4× PIC SST proxy comparison . . . . .	74
5.8	38Ma 4× PIC ocean seasons . . . . .	76
5.9	Model-model ocean comparison . . . . .	77
5.10	38Ma 4× PIC atmosphere . . . . .	80
5.11	38Ma 4× PIC air temperature zonal mean . . . . .	81
5.12	38Ma 4× PIC land proxy comparison . . . . .	82
5.13	38Ma 4× PIC atmosphere seasons . . . . .	85
5.14	38Ma 4× PIC atmosphere zonal mean . . . . .	86
5.15	38Ma CESM climate sensitivity . . . . .	88

## 6 Antarctic Summer Monsoons and Eocene Ice

6.1	Pre-industrial - 38Ma Antarctic model geography . . . . .	97
6.2	38Ma 4× PIC - pre-industrial Antarctic climate . . . . .	99
6.3	Summer atmosphere zonal mean . . . . .	100
6.4	Antarctic regional climatology . . . . .	102
6.5	Antarctic temperature and flow patterns . . . . .	104
6.6	Antarctic Eocene ice . . . . .	105
6.7	Antarctic winter climate . . . . .	107

## 7 CESM Simulations using a 30Ma Geography

7.1	30Ma versus 38Ma model geography . . . . .	111
7.2	30Ma CESM spin-up . . . . .	114
7.3	30Ma CESM transport and MOC time series . . . . .	115
7.4	30Ma CESM ideal age tracers . . . . .	116
7.5	30Ma 2× PIC ocean . . . . .	117
7.6	30Ma 2× PIC ocean season . . . . .	119
7.7	30Ma 2× PIC atmosphere . . . . .	120
7.8	30Ma - 38Ma 2× PIC ocean . . . . .	121
7.9	30Ma - 38Ma 2× PIC ocean season . . . . .	122
7.10	30Ma - 38Ma 2× PIC atmosphere . . . . .	124
7.11	30Ma - 38Ma 2× PIC atmosphere season . . . . .	125



7.12 30Ma - 38Ma 2× PIC atmosphere arctic winter . . . . .	126
7.13 30Ma 2× PIC Adjusted - 30Ma 2× ocean . . . . .	127
7.14 30Ma CESM MSF and MHF . . . . .	129
7.15 30Ma 2× PIC Adjusted - 30Ma 2× ocean season . . . . .	130
7.16 30Ma climate sensitivity . . . . .	132
7.17 30Ma adjusted climate sensitivity . . . . .	133
7.18 30Ma Antarctic regional climatology . . . . .	134

## **8 Overview of CESM Simulations – Antarctic Glaciation**

8.1 All CESM cases zonal mean SST . . . . .	139
8.2 All CESM cases MSF and MHF . . . . .	141
8.3 CESM Eocene DWF source regions . . . . .	142
8.4 All CESM cases zonal mean air temperature . . . . .	145
8.5 Eocene Asia precipitation . . . . .	147
8.6 Eocene Asia temperature and circulation . . . . .	149
8.7 30Ma 1× PIC case and pre-industrial Antarctica . . . . .	150
8.8 All CESM cases Antarctica regional climate . . . . .	152
8.9 CESM Eocene Antarctic surface mass balance . . . . .	154
8.10 38Ma 2× PIC Antarctic surface mass balance . . . . .	155
8.11 Eocene CESM Antarctic equilibrium level . . . . .	156
8.12 38Ma 2× PIC ice sheet model simulation . . . . .	158

## **9 Summary and Outlook**

9.1 Middle-to-late Eocene model proxy comparison . . . . .	165
--	-----

### **A Pre-industrial Reference Climatology**

A.1 Pre-industrial ocean . . . . .	169
A.2 Pre-industrial ocean season . . . . .	170
A.3 Pre-industrial atmosphere . . . . .	170
A.4 Pre-industrial atmosphere season . . . . .	171
A.5 Pre-industrial atmosphere zonal mean . . . . .	172
A.6 pre-industrial Asian monsoon . . . . .	172

### **B 38Ma 2× PIC Climatology**

B.1 38Ma 2× PIC ocean . . . . .	173
B.2 38Ma 2× PIC ocean season . . . . .	174
B.3 38Ma 2× PIC atmosphere . . . . .	174
B.4 38Ma 2× PIC atmosphere season . . . . .	175

### **C Additional Model-Proxy Comparisons**

C.1 38Ma 2× PIC SST proxy comparison . . . . .	182
C.2 38Ma 2× PIC land proxy comparison . . . . .	182
C.3 Eocene model-model SST comparison . . . . .	183
C.4 Eocene model-model land comparison . . . . .	183

## List of Tables

### 4 Multiple Equilibria in the Ocean Circulation State

4.1 POP cases and drifts . . . . .	50
------------------------------------	----

### 5 CESM Simulations of the Eocene Climate

5.1 38Ma CESM simulations . . . . .	65
5.2 38Ma CESM drifts . . . . .	66
5.3 38Ma CESM temperature . . . . .	89
5.4 38Ma CESM ECS and geography effect . . . . .	91

### 6 Antarctic Summer Monsoons and Eocene Ice

6.1 Antarctic regional climatology . . . . .	103
--	-----

### 7 CESM Simulations using a 30Ma Geography

7.1 30Ma CESM cases and drifts . . . . .	113
--	-----

### 8 Overview of CESM Simulations – Antarctic Glaciation

8.1 All CESM cases oceanic temperature . . . . .	140
8.2 All CESM cases air temperature . . . . .	146

### C Additional Model-Proxy Comparisons

C.1 42–38 Ma SST proxies . . . . .	177
C.1 Continued . . . . .	178
C.2 Overview of 38–34 Ma SST proxies . . . . .	178
C.3 Late middle Eocene terrestrial temperature proxies . . . . .	179
C.3 Continued . . . . .	180
C.4 Late Eocene terrestrial temperature proxies . . . . .	180
C.4 Continued . . . . .	181

---

# List of Frequently used Acronyms

---

Colour code: Model – Atmosphere – Ocean – Palaeo – Other

ACC	Antarctic Circumpolar Current
AIS	Antarctic Ice Sheet
BAM	Bulk Aerosol Model
BSF	Barotropic stream function
CAM	Community Atmosphere Model
CCD	Carbonate compensation depth
CCSM	Community Climate System Model
CESM	Community Earth System Model
CMT	Coldest month mean temperature
DJF	December-January-February
DP	Drake Passage
DWF	Deep water formation
EAC	East Australia Current
ECS	Equilibrium climate sensitivity
EECO	Early Eocene Climatic Optimum
EL	Equilibrium level
EOT	Eocene-Oligocene transition
ESS	Equilibrium system sensitivity
GCM	General circulation model
HS	Hot Spot reference frame
IRD	Ice rafted debris
ISM	Ice-sheet model
ITCZ	Inter-tropical convergence zone
JJA	June-July-August
LHF	Latent heat flux
Ma	Mega annum (i.e. 1 million years)

**Colour code:** Model – Atmosphere – Ocean – Palaeo – Other

<b>MAT</b>	Mean annual near surface air temperature
<b>MECO</b>	Middle Eocene Climatic Optimum
<b>MHF</b>	Meridional heat flux
<b>MLD</b>	Mixed layer depth
<b>MOC</b>	Meridional overturning circulation
<b>MSF</b>	Meridional stream function
<b>MSLP</b>	Mean sea level pressure
<b>NH(S)</b>	Northern Hemisphere (sinking)
<b>ODP</b>	Ocean Drilling Program
<b>PD</b>	Present-day
<b>PDD</b>	Positive degree days
<b>PETM</b>	Palaeocene-Eocene Thermal Maximum
<b>PI</b>	Pre-industrial
<b>PIC</b>	Pre-industrial carbon (i.e. 280ppm CO <sub>2</sub> – 671ppb CH <sub>4</sub> )
<b>PM</b>	PaleoMag reference frame
<b>POP</b>	Parallel Ocean Program
<b>PrOM</b>	Priabonian Oxygen isotope Maximum
<b>psu</b>	Practical salinity unit (i.e. ppt or g/kg)
<b>PW</b>	Petawatt (i.e. 10 <sup>15</sup> W)
<b>RH</b>	Relative humidity
<b>RF</b>	Radiative forcing
<b>SFWF</b>	Surface fresh water flux
<b>SH(S)</b>	Southern Hemisphere (sinking)
<b>SMB</b>	Surface mass balance
<b>SSH</b>	Sea surface height
<b>SSS</b>	Sea surface salinity
<b>SST</b>	Sea surface temperature
<b>Sv</b>	Sverdrup (i.e. 10 <sup>6</sup> m <sup>3</sup> /s)
<b>TG</b>	Tasmanian Gateway
<b>TOA</b>	Top of the atmosphere
<b>TOM</b>	Top of model
<b>WMT</b>	Warmest month mean temperature
<b>ZM</b>	Zhang & McFarlane (1995) deep moist convection scheme

---

# English Summary

---

What happens to the earth's climate after you double or even quadruple the concentration of greenhouse gases in the atmosphere? This question has occupied climate scientists for many decades and is becoming awfully relevant as the anthropogenic impact on the climate system gets larger. The most logical approach towards finding the answer is to try and simulate the climate using a model, alter the boundary conditions and assess the induced changes. A major limitation is the lack of validation, when those models are pushed far out of their comfort zone for which they are calibrated. Fortunately, the earth system has already performed a large number of experiments with both colder and warmer climates than the one seen today (which for the sake of self preservation, we should better not repeat in practice).

In order to find a relevant analogue to an extreme future scenario, one needs to go far back in time to the point where there were no continental-scale ice sheets yet. While the present Antarctic Ice Sheet is thought to have originated at the Eocene-Oligocene transition (EOT, ~34 million years ago), the preceding Eocene epoch held some of the warmest conditions known in the climatic record. Not only the earth was warm in general, but the differences between low and high latitude regions were much smaller than they are today. Such an equable climate provided near-tropical conditions to middle or even high latitudes and has proven notoriously difficult to reproduce in conventional models.

Here, the focus will be on the middle-to-late Eocene which is seen as a mostly gradual transition between the extremely warm early Eocene and the glaciation of Antarctica at the EOT. This relatively under-sampled period is crucial to understand, as it covers the variability within a warm greenhouse climate but also a shift towards a colder icehouse state. The study of the middle-to-late Eocene climate will be threefold, consisting of:

1. a reconstruction of the most likely climatic state, using general circulation models and a compilation of the latest available proxy records;
2. sensitivity studies of how the climate responds to different types of external forcing, within the range of variability seen within the considered period;
3. an assessment of the changes needed before a large-scale ice sheet is able to grow over the Antarctic continent.

First, a new adequate reconstruction of the middle-to-late Eocene global geography is needed as it is currently lacking. Furthermore, the plate-tectonic models that serve as a basis for this reconstruction also have their uncertainties of which the impacts need to be explored. Therefore, a set of global geography reconstructions is made for different time intervals and using two possible plate-tectonic reference frames. Then, a number of global climate model simulations is carried out using the Community Earth System Model (CESM) as well as its standalone ocean component (POP). These experiments eventually lead to the following main findings;

1) Using the new geography reconstruction and realistically high levels of atmospheric greenhouse gases, the middle-to-late Eocene climate can be successfully reproduced in the model. Warm tropical conditions and regional variability seem to agree well with the available climatic proxy record. High latitude regions see mostly mild and ice-free conditions even under modest radiative forcing, indicative of a much more equable climate than the one seen today. Importantly, high latitude warmth in the model is not sustained by increased meridional heat fluxes but rather by a locally altered radiative balance.

2) Multiple stable states of the ocean circulation are consistently found within different model configurations. A shift between preferred states can complicate the response to changes in both geography and radiative forcing. These are the first such simulations to find multiple equilibria within a full-complexity climate model for the middle-to-late Eocene (or any other period, considering the coupled version of the model).

3) The sensitivity of the simulated climate to altered levels (within the likely range) of atmospheric greenhouse gases nicely covers the variability seen throughout the middle-to-late Eocene period. Polar amplification of the temperature response is a universal property of the climate system, while the processes behind it are dependent on its background state. Changes in geography only induce a minor global response, but associated reorganisations of the circulation pattern can lead to much larger and possibly non-trivial regional impacts.

4) Sufficient model resolution and the new geography reconstruction reveal a fascinating Antarctic climate when the continent is still mostly ice-free. Substantial summertime warming leads to a reversal of the conventional temperature gradient and the associated jet stream. A much less restricted flow of heat and moisture towards the continent leads to the formation of a sub-tropical like summer monsoon, which helps to sustain an abundance of vegetation. Meanwhile, large amounts of precipitation on higher terrain near the coast allow the formation of local ice caps that can explain indications of Eocene ice.

The simulated warm and equable climate of the middle-to-late Eocene is thus vastly different from the one seen today. Even under similar levels of atmospheric greenhouse gases, the system is considerably warmer as a result of the different geography and land surface properties (mainly vegetation and ice). Surprisingly warm and wet conditions are seen on Antarctica, featuring extreme seasonality and a particular resilience to external forcing. This challenges the conventional image of a spontaneous Antarctic glaciation at the EOT within a gradually cooling global climate.

---

# Samenvatting in het Nederlands

---

Wat gebeurt er met het klimaat op aarde wanneer we de concentratie broeikasgassen in de atmosfeer verdubbelen of zelfs verviervoudigen? Deze vraag houdt klimaatwetenschappers al decennialang bezig en wordt steeds prangender naarmate de menselijke invloed op het klimaat toeneemt. Een voor de hand liggende manier om hierop een antwoord te vinden is door gebruik van modellen, waarin gekeken wordt naar veranderingen in het gesimuleerde klimaat onder aangepaste randvoorwaarden. Een belangrijke beperking hierbij is het gebrek aan referenties, wanneer de modellen ver buiten hun betrouwbare bereik opereren waarvoor ze goed gekalibreerd zijn. Gelukkig heeft de aarde zelf al een groot aantal historische experimenten uitgevoerd, waarin het klimaat zowel kouder als warmer is geweest dan dat van vandaag (die we met de focus op zelfbehoud beter niet in de praktijk herhalen). Om een goed precedent te vinden voor een mogelijk dramatisch toekomstscenario, moet ver in de tijd worden teruggekeken tot aan het punt waarop er nog geen continentale ijskappen aanwezig waren. De huidige Antarctische ijskap is waarschijnlijk ontstaan rond de Eoceen-Oligoceen transitie (EOT, ~34 miljoen jaar geleden), die voorafgegaan werd door het bijzonder warme Eoceen. Het klimaat was aan het begin van deze periode niet alleen ongekend warm, maar werd in vergelijking met nu ook gekenmerkt door sterk verminderde contrasten tussen gebieden op lage en hoge breedtes. In zulk een gelijkmatig klimaat heersten nagenoeg tropische condities op gematigde of zelfs hoge breedtegraden, dewelke haast onmogelijk goed te reconstrueren zijn met klimaatmodellen.

Hier zal vooral worden gekeken naar het Midden tot Laat Eoceen, dat grotendeels bepaald wordt door een gestage afkoeling van het Vroeg Eoceen naar de glaciatie van Antarctica bij de EOT. Deze relatief onbekende periode is cruciaal, omdat ze een beeld kan geven van de variabiliteit binnen een warm broeikas klimaat maar ook de overgang naar koudere condities. De studie van het klimaat tijdens het Midden tot Laat Eoceen wordt vervolgens opgebouwd uit drie delen:

1. een reconstructie van de klimatologische condities met gebruik van een klimaatmodel en een compilatie van de nieuwste historische (proxy) gegevens;
2. gevoeligheidsstudies van hoe dit klimaat reageert op verschillende externe veranderingen die zich voordeden binnen de beoogde periode;
3. een beoordeling van de aanpassingen die nodig zijn voordat een grootschalige ijsgroei op het Antarctische continent mogelijk wordt.

In eerste instantie is er een nieuwe reconstructie nodig van de globale geografie tijdens het Midden tot Laat Eoceen. Daarnaast hebben de plaat-tectonische modellen die aan de basis liggen van zulke reconstructies ook de nodige onzekerheden, welke in acht moeten worden genomen. Om die redenen wordt er een nieuwe reeks geografische reconstructies gemaakt, gebruik makende van twee mogelijke tectonische referentiekaders en voor variërende tijdsspanne. Deze dienen als basis voor meerdere simulaties, waarbij het Community Earth System Model (CESM) wordt gebruikt alsook de individuele oceaancomponent (POP). Uit de verschillende experimenten komen de volgende belangrijkste resultaten;

- 1) Met de nieuwe geografische reconstructies kan het Midden tot Laat Eoceen klimaat succesvol worden gesimuleerd. Intense tropische warmte, maar ook regionale contrasten stemmen goed overeen met de beschikbare klimatologische indicators. Op hoge breedtegraden heersen zelfs onder beperkte atmosferische forcering voornamelijk zachte en ijsvrije condities, kenmerkend voor een meer gelijkmatig klimaat. Een belangrijk aspect hiervan is dat de relatieve warmte op hogere breedte niet in stand wordt gehouden door versterkte transporten, maar met name door veranderingen in de lokale stralingsbalans.
- 2) In de verschillende modelconfiguraties worden consistent meerdere mogelijke toestanden gevonden voor de oceaancirculatie. Een overgang tussen zulke toestanden in het systeem kan een versterkte respons teweegbrengen op bepaalde externe veranderingen. Dit zijn de eerste simulaties met complexe klimaatmodellen waarbij meerdere stabiele evenwichten worden gevonden voor het Midden tot Laat Eoceen (of eender welke andere periode in het volledig gekoppelde model).
- 3) De temperaturen in het gesimuleerde klimaat bij verschillende mogelijke atmosferische samenstellingen omvatten de verwachte variabiliteit binnen het Midden tot Laat Eoceen. Een versterkte gevoeligheid van de poolgebieden lijkt universeel, maar wordt veroorzaakt door andere processen naargelang de klimatologische achtergrond. Ondanks hun beperkte globale invloed, kunnen geografische verschuivingen een soms onverwacht grote lokale impact teweegbrengen via een reorganisatie van het circulatiepatroon.
- 4) Dankzij voldoende hoge modelresolutie onthullen de simulaties fascinerende eigenschappen van een ijsvrij Antarctisch klimaat. Een forse opwarming in de zomermaanden doet de conventionele temperatuurgradiënten omkeren samen met de daaraan gelinkte straalstroom. Extra warmte en vocht kunnen zo het continent opstomen en een subtropische zomerwoestijn laten ontstaan, die de aanwezige rijke vegetatie in stand houdt. Lokale ijskappen tijdens het Eoceen kunnen ook verklaard worden door grote hoeveelheden neerslag in nabij de kust gelegen hooglanden.

Het warme en gelijkmatige klimaat zoals gesimuleerd voor het Midden tot Laat Eoceen verschilt dus sterk met dat van vandaag. Zelfs onder gelijkaardige atmosferische condities is het op aarde merkbaar warmer door de verschillende geografie en landbedekking (voornamelijk vegetatie en ijs). Opvallend op Antarctica zijn de (sterk seizoensgebonden) erg warme en natte omstandigheden, die bijzonder hardnekkig blijken onder externe veranderingen. Dit betwist het gebruikelijke beeld van een geleidelijke afkoeling die leidt tot Antarctische glaciatie bij de EOT.



---

# Acknowledgments

---

Some would argue that the acknowledgements section is a waste of time and effort, both to the reader and writer, and is therefore only rarely read. Yet, it is paramount to realise that a project like this one is never a single person's effort and could not have been completed successfully without the help of a number of people who are mentioned here. Therefore, I will try my best to keep this part entertaining and rewarding to those who do take the time to go through it.

First and foremost I should thank Anna and Henk for being my promoters who guided me through the entire process. Frankly, I have to admit not knowing either of them well before I started the project and was a bit hesitant after being invited to an interview. Any doubts quickly melted away as I immediately felt their enthusiasm and dedication to the subject: palaeoclimate. It was a bit daunting at first: an entirely new subject to someone who was mostly looking at storms and cyclones.

Luckily, Anna did a great job at introducing me in the matter as well as getting me acquainted with an international community of researchers. The summer school in Urbino was particularly helpful at getting to know both teachers and fellow PhD students, many of which I still meet regularly at conferences or other meetings. Through time, I have grown to appreciate and admire the fascinating palaeoclimate; how it forces us to challenge our understanding about the system and how it can hold surprises that you had never imagined.

Henk is a great promotor and a bit of a wizard, firstly because of the observation that he often passes by in a 'whizz'. Most importantly, Henk knows something about pretty much everything and knows someone pretty much everywhere. Therefore, he will always have the right tools ready for you when you are in need and gets work done at a rate that makes you wonder if there is actually some magic involved. Together with Anna he has formed a perfect team, helping me to keep my focus (which at times I definitely needed) and supporting me whenever I got stuck or frustrated for things not going the way I intended. This team eventually got me to the point where I am writing this very last piece of my thesis, at the end of my *quest* through Middle Eocene Earth.

Despite going on many adventures (read: meetings) you end up spending most of the time in your own office with several fellow PhD students. From the start, I've had the pleasure to sit together with Fiona and Erik who were wonderful colleagues and made working feel like being at home. All of us having the same promotor, we quickly became 'team Henk' which after some time was adjusted to the 'fellowship of Henk' when René joined us. Regardless of having to make a long commute from Groningen, Erik still came to Utrecht regularly and gave us the impression that weekends started on Thursday and did not end until Tuesday. I should definitely thank René for all the lovely coffee breaks (411 or 50?) and lunch 'potjes' (if this is gibberish to you do not despair, it simply means that you are normal). Like Henk, René is one of those persons who can manage a dozen projects at a time (polynia!) and get through an inconceivable amount of work in limited time. He even used some of his free time to help me get through the painstaking process of typesetting the thesis and get rid of the seemingly everlasting typos (As you know, for every  $n$  corrections made you are bound to find  $n/2$  new ones pushing the number of iterations needed towards perfection to infinity).

Together we have had a great time in our room 6.68, which to most is considered a cave as it is often rather dark (at least, so we have been told). While technically being part of the ocean group, there is a nice atmosphere (bad joke...) both socially and professionally as part of IMAU. In particular, I would like to thank Claudia for organising many work meetings and agreeing with me on the fact that 'onweer' (free translation: 'non-weather') is a hopelessly poor term to define thunderstorms. Countless other colleagues have helped me out on all sorts of matters; Marcel to keep the hardware going and batteries replenished, Heiko for kindly running ice-sheet models in a ridiculously warm climate, André to oxygenate the air in the jungle room, Melchior who organised the regular 'cooo... loquium', Lisa for getting us to play badminton, the management team (Yvonne, Floor, Clara and Sandra) for helping out whenever you messed up your administration or entered an expense claim missing a comma and many others still. Last but not least I owe a pledge of gratitude to Michael for building up and managing the model simulations, at times working day and night to get things done.

Outside IMAU, I was lucky to be part of NESSC which was a great platform for me to get in touch with people from different fields. At the start of the project, I worked together with Douwe van Hinsbergen who taught me all about plate-tectonic models, made me aware of the fact that the pole can wander and he had an immense part in creating the geography reconstructions that were a crucial part of the project. Furthermore, I should thank Appy Sluijs and Peter Bijl for teaching me the language of palaeo and helping me to make sense of data gathered from 35 million year old mud. On several trips to different meetings, I was lucky to get in touch with people from various research groups such as Bette Otto-Bliesner, Matt Huber, Christine Shields, Dan Lunt, Alan Haywood, Caroline Lear, Helen Coxall, Rob DeConto, Jim Zachos, Howie Scher, David Evans, Ed Gasson, Jean-Baptiste Ladant, Alan Kennedy, David Hutchinson and many others. Thank you for making me feel appreciated and learning me so much about the climate system.

Although not being that far from home, moving to Utrecht changed many things in my life and allowed me to study the things that truly fascinated me. For supporting me and helping me make that choice, I want to thank my family and friends. In particular I also greatly appreciate the help and dedication from Maxime, who transformed my ‘quick and dirty’ design into an actual thesis cover. After all, a thesis is not really appealing to read if it is not at least looking a bit fancy.

In and around Utrecht I met many fellow weather enthusiasts (of whom some were even as crazy as me) both inside and outside the university. Here I should also thank Rein for being a great supervisor at KNMI and staying in touch throughout the PhD course. Also I want to thank Aarnout for having me as his teaching assistant for Dynamical Meteorology, never blaming me for my consistently too long weather discussions and helping me understand the atmosphere when it was doing things I could not grasp. Furthermore, Aarnout was the person who convinced me I was ‘going to be OK’ doing the Master in Utrecht helping me greatly to make the switch. Finally, Utrecht also brought another amazing person into my life who joined me and supported me throughout the course of my PhD project. Annelies, thank you for giving me a home I want to return to after work every day because you know I would stay and sleep there otherwise. At last, I want to thank the persistent reader who made it to the end of this section. If you made it down to this point, all that follows will simply be some further light reading.

“I would rather spend one lifetime with you,  
than face all the ages of this world alone.”

**J.R.R. Tolkien**

# Introduction

---

One of the biggest challenges currently faced by humanity is anthropogenic climate change. As a result of greenhouse gas emissions and changes in land use, the earth's climate is warming at an accelerating pace. Both the observed and predicted mass losses at most of the polar ice sheets are of major concern due to feedbacks related to ice melt and sea level rise. In contrast to the present so-called icehouse state, earth's climate has seen much warmer intervals referred to as greenhouse states. Under such warm conditions, without the presence of any significant ice and altered feedback mechanisms that dictate the response to an external forcing, the climate system behaves quite differently. If current warming trends continue for much longer, polar ice sheets could disappear and the climate may end up in a greenhouse state. As comparable transitions have occurred in the geological past, it is crucial to understand how they take place and to what extent the resulting climate behaves differently to that of today.

This study focusses on the climate of the middle-to-late Eocene (~42–34 million years ago), leading up to one of the major climatic transitions in the known record: the Eocene-Oligocene transition (EOT). Throughout the Eocene, polar regions were mainly ice free and most of the land surface was covered with either tropical or sub-tropical vegetation. The EOT is believed to concur with the formation of a continental ice sheet on Antarctica marking the transition from a greenhouse into an icehouse state. In order to better understand this particular transition, it is crucial to have an accurate reconstruction of the climate leading to the event. This is achieved with new geographical boundary conditions and higher resolution climate model simulations presented here. The results of those simulations allow a better understanding of the late Eocene climate and the changes leading up to the EOT.

This introduction will first give a brief overview of Cenozoic (last 65 million years) climate change within both greenhouse and icehouse states. Next, the current state in palaeoclimate modelling is presented along with the importance of reconstructing global geography. Finally, the focus will be on the Eocene climate and the challenges faced trying to explain both Eocene warmth and the glaciation of Antarctica.

The main questions addressed in this thesis will be centred around the climatic state that was in place prior to the EOT and how it may have determined the timing of Antarctic glaciation;

**1)** The importance of different boundary conditions compared to today and how higher model resolution can help to improve the agreement with the available proxy record. Changes in model boundary conditions prove to be crucial in explaining Eocene warmth and low meridional temperature gradients. Furthermore, model resolution needs to be adequate in order to benefit from a more detailed geography reconstruction, while it can also help in resolving regional processes to help explain proxy estimates.

**2)** The existence of multiple equilibria in the climatic state and how they enhance the sensitivity to different possible geography reconstructions for the middle-to-late Eocene. Multiple equilibria are found in different model set-ups and may explain the occurrence of (or susceptibility to) rapid transitions in the middle-to-late Eocene climate.

**3)** How well the new model results succeed at reconstructing the warm and wet Antarctic regional climate during the Eocene. The simulated Antarctic conditions can reconcile proxy indications of regionally mild conditions with Eocene ice, but have important implications to the climatic changes needed to grow a continental ice sheet.

“You step into the Road, and if you don’t keep your feet,  
there is no knowing where you might be swept off to.”

J.R.R. Tolkien

## 1.1 The Cenozoic Climate

The Cenozoic Era covers the time interval between the late Cretaceous mass extinction involving the Dinosaurs (K-Pg or K-T Boundary) ~66 million years (Ma) ago and the present (Figure 1.1). Of this period there is a substantial amount of proxy data, mainly from ocean sediments, to get a general image of the climatic state that was in place. One of the most used proxies is benthic  $\delta^{18}\text{O}$ , indicative of both deep ocean temperature and global land ice volume. A stack of  $\delta^{18}\text{O}$  values from all of the available marine sequences, compiled by Cramer et al. (2009) is shown in Figure 1.2. The Cenozoic Era is divided into a number of shorter Epochs:

- **Palaeocene:** 66Ma–56Ma;
- **Eocene:** 56Ma–34Ma;
- **Oligocene:** 34Ma–23Ma;
- **Miocene:** 23Ma–5.3Ma;
- **Pliocene:** 5.3Ma–2.6Ma;
- **Pleistocene:** 2.6Ma–12ka;
- **Holocene:** 12ka–Present.

The above time intervals are in accordance with those in the Geological Society of America (GSA) Time Scale shown in Figure 1.1, adopted from Walker et al. (2013).

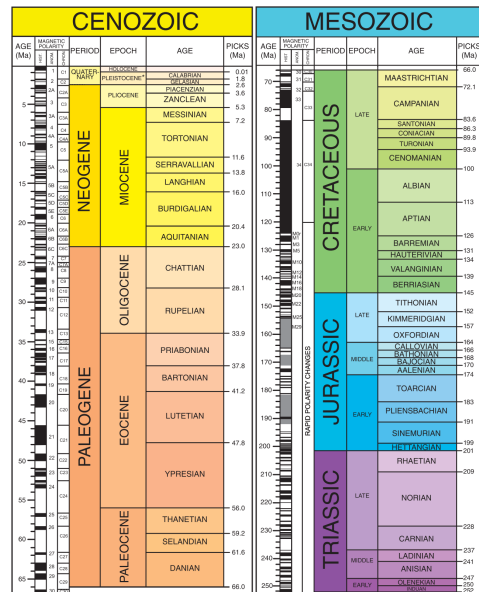
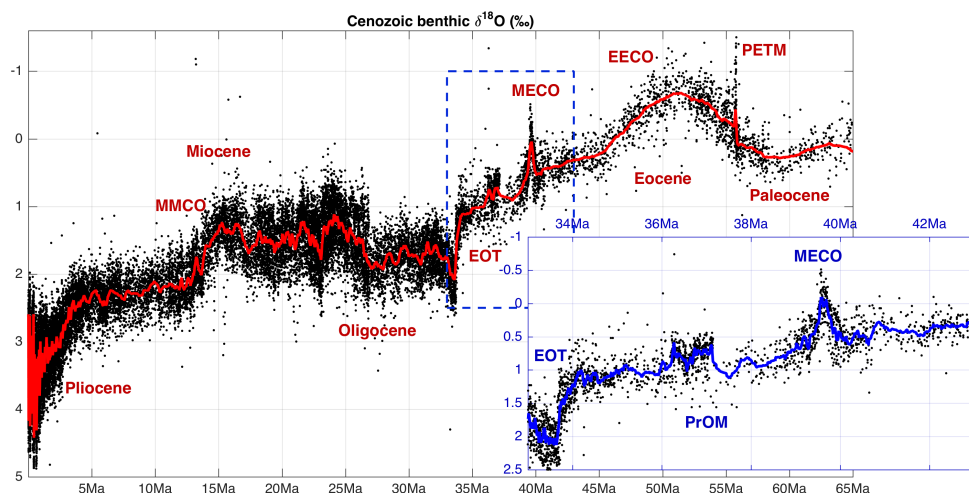


Figure 1.1: GSA Geologic Time Scale.

Following the warm Cretaceous period, the climate of the Palaeocene Epoch is generally warm and ice free (indicated by low  $\delta^{18}\text{O}$  in Figure 1.2; Zachos et al. 2001, 2008): a typical example of a greenhouse climate. A late Palaeocene warming led to one of the most extreme warming events known: the Palaeocene-Eocene Thermal Maximum (PETM). This interval was initiated by a relatively short (~10ka) warming and saw tropical-like conditions all the way into polar regions. The most striking feature of this climate is the very low equator to pole temperature gradient, making it what is known as an equable climate (Greenwood & Wing, 1995; Huber & Caballero, 2011). A series of less extreme, but similar warming events or hyperthermals occurred in the early Eocene and culminated into the Early Eocene Climatic Optimum (EECO) which is also characterised by having an equable climate.

Throughout the remainder of the Eocene, a gradual cooling and increase of the meridional temperature gradient was mainly driven by decreases in the concentration of atmospheric greenhouse gases (Anagnostou et al., 2016; Beerling et al., 2011; Bijl et al., 2010).

At the Eocene-Oligocene transition (EOT), the climate is believed to have had cooled down to the point where Antarctica glaciated (Coxall et al., 2005; DeConto & Pollard, 2003; Zachos et al., 2001). From this point in time to the present, the  $\delta^{18}\text{O}$  proxy is a mixed signal of temperature and ice volume: lower  $\delta^{18}\text{O}$  indicating warmer/less ice and higher indicating colder/more ice (hence why the y-axis is reversed in Figure 1.2). The Antarctic Ice Sheet is an important source of variability in the Oligocene and Miocene climate, at a time when large fluctuations in temperature and ice volume occurred. During the late Oligocene and Middle Miocene Climatic Optimum (MMCO), many regions were similarly warm as they were in the late Eocene, but Antarctica remained largely glaciated. The formation and intensification of an Antarctic Circumpolar Current (ACC) during the Oligocene and Miocene in the Southern Ocean isolated the Antarctic continent and further increased the meridional temperature gradient in the Southern Hemisphere. In contrast, Northern Hemisphere ice sheets did not exist until the late Pliocene when the Greenland Ice Sheet first formed. The Pleistocene was then governed by large swings in global mean temperature associated with the growth and decay of expansive ice sheets dictated by orbital variability, known as glacial cycles.



**Figure 1.2:** Cenozoic compilation (Cramer et al., 2009) of benthic (deep ocean)  $\delta^{18}\text{O}$  values (black dots) and a 50-point running mean (red line). The inset shows the same data for the middle-to-late Eocene (blue dashed line) with a 10-point smoothing average in blue. MMCO: Middle Miocene Climatic Optimum, EOT: Eocene-Oligocene transition, PrOM: Priabonian Oxygen isotope Maximum, MECO: Middle Eocene Climatic Optimum, EECO: Early Eocene Climatic Optimum, PETM: Palaeocene-Eocene Thermal Maximum, see text for further details.



## 1.2 Palaeoclimate Modelling and Palaeogeography

Predicting the future development of earth's climate is mainly done using coupled atmosphere-ocean general circulation models (AOGCM's). Such models are mainly tested and validated using pre-industrial to present-day conditions and therefore quickly reach unknown territory when representing a much warmer future climate. The best analogues to climates very different to that of today are found in the palaeo record for both warmer and colder states. By trying to reconstruct such climatic intervals and comparing the results to proxy estimates, much can be learned about both the climate system and the models themselves. Instead of using state of the art AOGCM's, slightly older and lower complexity model versions are often used in a palaeo framework as a result of their computational cost. In order to accurately represent a completely different climatic state, a long equilibration is needed by spinning up the model simulation several thousands of years. The acquired equilibrium state is then analysed and compared to proxy estimates to assess how well the model results agree with what is known about the climate of the considered period.

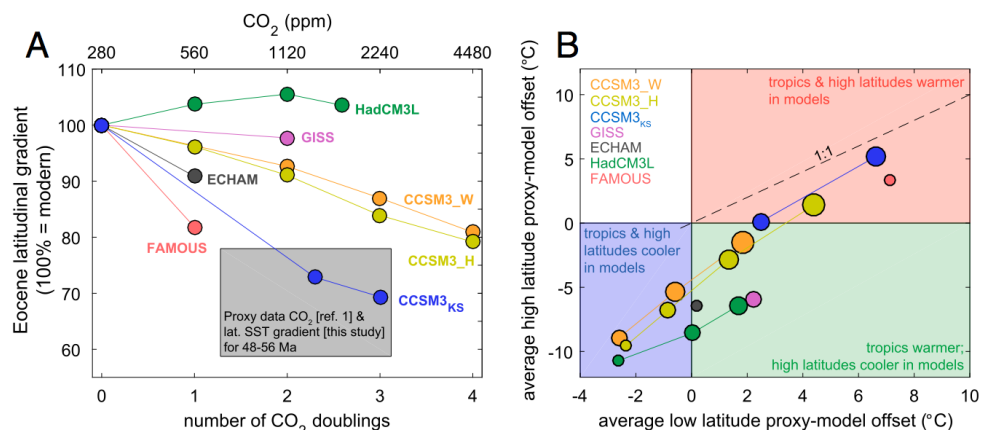


**Figure 1.3:** Compilation of early Eocene sea surface temperature proxy range (grey box) and model results (markers), adopted from Evans et al. (2018). A comparison of meridional gradients is made in A, while a cross plot between high and low latitude temperature offsets (model versus proxy) is shown in B.

One of the most challenging intervals to palaeoclimate modellers is the Eocene and especially early Eocene equable climate (Huber & Caballero, 2011; Lunt et al., 2012, 2017; Sagoo et al., 2013). An overview of the current best estimate in both low and high latitude temperature estimates from both proxies and models is given in Figure 1.3, adopted from Evans et al. (2018). In general, the Eocene greenhouse climate has proven challenging to simulate adequately with climate models (Huber & Sloan, 2001; Huber & Caballero, 2011). Previous model simulations needed very high radiative forcing in order to reproduce high-latitude warmth but at the expense of equatorial temperatures being significantly higher than indicated by proxy data (Huber & Caballero, 2011; Lunt et al., 2012).

In more recent studies, consensus between models and proxy data is growing as firstly equatorial temperature estimates have risen (Evans et al., 2018; Inglis et al., 2015; Pearson et al., 2007). Meanwhile, estimates of high-latitude temperatures are possibly biased towards warm season conditions (Bijl et al., 2009; Schouten et al., 2013; Sluijs et al., 2006). Finally, global climate models are continuously being improved by including more processes (e.g. cloud properties; Abbot et al. 2009; Kiehl & Shields 2013 or enhanced mixing; Huber et al. 2004; Thomas et al. 2014) and using a higher spatial resolution with better resolved palaeogeographies (Hutchinson et al., 2018; Lunt et al., 2016).

Simulating deep time palaeoclimate is challenging, since most of the applied boundary conditions are still poorly constrained. Between geography reconstructions, differences in e.g. lat/lon coordinates, heights, coastlines and basin depths are often considerable. Next to the atmospheric composition, solar insolation and land surface properties, the global geography can be of great importance (Barron & Washington, 1984). The breakup and collision of continents likely drove major climatic transitions in the past. For example, the India-Eurasia collision caused a large-scale uplift that resulted in regional climatic changes but also affected the global circulation and hydrological cycle (Caves et al., 2014; Dupont-Nivet et al., 2007, 2008; Ramstein et al., 1997). Furthermore, the opening of ocean gateways such as the Tasmanian Gateway (TG) impacted ocean circulation and thus the redistribution of heat, resulting in both changed surface and deep ocean temperatures (Bijl et al., 2013; Sijp et al., 2014). Many of these themes are the subject of ongoing studies that lead to a continuous acquisition of new data, either of palaeo-altimetry/bathymetry or from tectonic reconstructions.

The implementation of different geographies into climate models is not without issues; the increasing but limited model resolution obscures certain potentially critical features (such as narrow ridges, mountain ranges and straits). Additionally, plate-tectonic reconstructions have their own uncertainties and are continuously being expanded and improved. This causes large discrepancies between model simulations because different studies use reconstructions of varying age and approach. A simple but striking example is given by Gasson et al. (2014), who used the output of several coupled global atmosphere-ocean models to force an ice sheet model simulating the Antarctic glaciation during the Eocene-Oligocene transition (~34Ma). Their main conclusion states that it is nearly impossible to determine the CO<sub>2</sub> threshold for the inception of ice sheets since the models use such different Antarctic topographies. Geographical reconstructions used in palaeoclimate modelling are often based on older reconstructions (such as Markwick, 1998; Sewall et al., 2000) that are adjusted for a specific case. These reconstructions may thus be based partially on information that is outdated and are usually only made for a unique set of time frames, which greatly limits their application in other studies. Since small-scale topographic features can be crucial in the climate system, they always need to be considered and may require additional manual changes. Finally, developments in coding and computer hardware allow for model simulations with a significantly higher resolution that in turn require more detailed boundary conditions.

## 1.3 The middle-to-late Eocene and EOT

The Eocene-Oligocene transition (EOT; Figure 1.4) is one of the most dramatic climatic transitions of the Cenozoic and thought to be associated with the formation of a continental-scale ice sheet on Antarctica (Coxall et al., 2005; Lear et al., 2008; Zachos et al., 1994). A possible cause for the inception of ice is a long-term decline of greenhouse gas concentrations through the middle Eocene, eventually crossing a threshold for glaciation (DeConto & Pollard, 2003; DeConto et al., 2008; Gasson et al., 2014). Following the early Eocene (~50Ma), a general cooling levelled off to a plateau in the middle Eocene (43–42 Ma, see inset of Figure 1.2) and eventually reversed into a warming until ~40Ma (Bijl et al., 2009; Zachos et al., 2001, 2008). At the Middle Eocene Climatic Optimum (MECO; Bohaty & Zachos 2003; Sluijs et al. 2013), conditions returned to values close to those seen in the early Eocene (Bijl et al., 2010, 2013; Cramer et al., 2009; Zachos et al., 2008) and quickly cooled down again into the late Eocene (~38Ma). This was followed by a cooling event at ~37.3Ma characterised by the Priabonian Oxygen isotope Maximum (PrOM, Scher et al. 2014). Significant swings in global temperature thus occurred prior to the EOT. Yet, conditions only allowed the growth of a continental-scale Antarctic ice sheet after 34Ma, although indications of significant ice volume in the late Eocene have been found (Carter et al., 2017; Passchier et al., 2017; Scher et al., 2014).

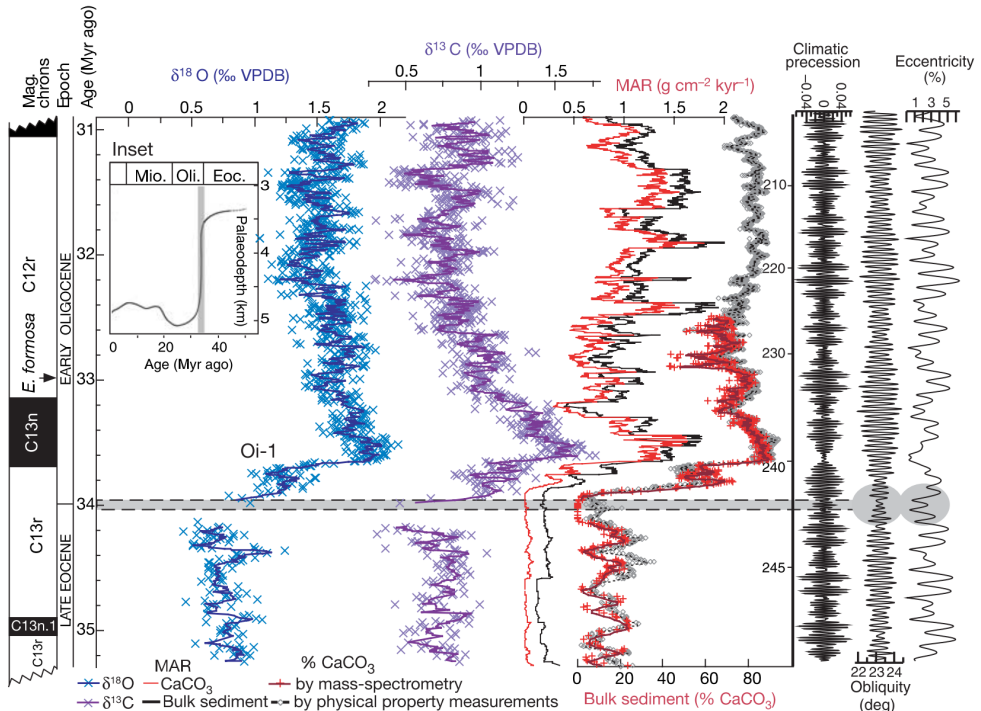


**Figure 1.4:** High resolution record showing the Eocene-Oligocene transition at ODP site 1218 (Central Pacific Ocean), adopted from Coxall et al. 2005.

A crucial aspect of the EOT is the suggestion of two smaller steps rather than one, seen in Figure 1.4 (from Coxall et al. 2005). Earlier studies suggested that this is inherent to the processes behind Antarctic glaciation (buttressing feedback; DeConto & Pollard 2003), but the first step may also be related to circulation changes prior to the main glaciation (Coxall et al., 2005; Scher et al., 2011). A dissolution event (data gap and absence of  $\text{CaCO}_3$  at 34Ma) at the onset of the first step also suggests some reorganisation of deep water masses, possibly resulting from a switch in circulation regimes. It remains a question to what extent continental geometry (e.g. opening of Southern Ocean Gateways) next to gradual shifts in both the atmospheric and oceanic circulation, was a driver to regional as well as global climate change during the Eocene (Bijl et al., 2013; Bosboom et al., 2014a; Sijp et al., 2014, 2016). Both the timing and effects of Southern Ocean Gateways opening during the Eocene and Oligocene remain uncertain and are not necessarily related to the EOT (Lagabrielle et al., 2009; Stickley et al., 2004).

Prior to the EOT, not only the exceptionally warm early Eocene (Bijl et al., 2009; Greenwood & Wing, 1995; Huber & Caballero, 2011), but also the later part of the Eocene were characterised by a low equator-to-pole temperature gradient (Bijl et al., 2009; Douglas et al., 2014; Evans et al., 2018; Hollis et al., 2012). Despite significant model improvements, it remains unclear whether a simulated climate can match the one reconstructed from proxies. Most of the recent modelling studies focussed on reconstructing either early Eocene extreme (Herold et al., 2014; Huber & Caballero, 2011; Lunt et al., 2012) or the latest Eocene – early Oligocene (Hill et al., 2013; Kennedy et al., 2015; Ladant et al., 2014) conditions. Proxies and especially model results are both relatively scarce for the middle-to-late Eocene considered here (i.e. Bartonian and Priabonian  $\sim 41.2$ – $33.9$  Ma; Cramwinckel et al. 2018; Evans et al. 2018). An overview of many palaeoclimate modelling studies involving the Eocene is given by Gasson et al. (2014), where the atmospheric fields are used as drivers for an ice sheet model to study the Eocene-Oligocene transition (EOT,  $\sim 34$ Ma). In these studies, either early Eocene boundary conditions were applied (Goldner et al., 2013; Huber & Caballero, 2011; Lunt et al., 2010a; Winguth et al., 2010) or global climate models of reduced complexity were used (DeConto et al., 2008; Heinemann et al., 2009; Sagoo et al., 2013). Finally, a comprehensive model study of four time slices covering the Eocene (including Bartonian/Priabonian) is presented in Inglis et al. (2015) and Lunt et al. (2016) using a lower resolution version of the HadCM3 model, albeit with a relatively short spin-up time.

Despite many previous studies concerning the Eocene climate, several aspects remain unclear. While much effort was spent on the early Eocene and EOT, coverage of the middle and late Eocene is mostly poor by both the proxy record and modelling results. The respective roles of greenhouse gases, orbital cycles, internal feedbacks (e.g. land coverage and biological activity) and especially changes in the global geography are still under debate. Limited model resolution and simplified reconstructed Antarctic topographies lead to poorly represented regional climatologies that are unable to match proxy estimates. Both the resolution and model geography need to be improved before it is possible to reconstruct the Eocene climate and more accurately determine the conditions leading to Antarctic glaciation at the EOT.

## 1.4 Research Questions and Outline

In order to better understand the climatic changes that took place before the EOT, more adequate simulations of the global climate system during the middle-to-late Eocene are needed. This period is interesting for climate modelling as, within the same geographical boundary conditions, it exhibits both early Eocene-like warmth (MECO) as well as conditions cool enough for possible (limited) precursor glaciations of Antarctica (PrOM). As a part of this thesis, newly reconstructed 38Ma geographic boundary conditions are made at a higher spatial resolution than previous ones (e.g. Sewall et al. 2000), representative of the Bartonian (41.2–37.8 Ma) and Priabonian (37.8–33.9 Ma) ages. Previously used geography reconstructions (Herold et al., 2014; Lunt et al., 2017) were more representative for the early Eocene. To cover the mean, but also both warmer and colder interval during the middle-to-late Eocene, simulations using 1×, 2× and 4× pre-industrial levels of greenhouse gas (CO<sub>2</sub>, CH<sub>4</sub>) concentrations are considered. The corresponding CO<sub>2</sub> values (280, 560 and 1120ppm, respectively) cover most of the range in proxy estimates for the Bartonian and Priabonian (~300–1500 ppm; Anagnostou et al. 2016; Beerling & Royer 2011 and latest estimates from <http://www.p-co2.org>) and allow for an analysis of equilibrium climate sensitivity. Both CO<sub>2</sub> and CH<sub>4</sub> are increased with the same factor, in order to represent middle-to-late Eocene estimates (Beerling et al., 2009; Beerling et al., 2011; Herold et al., 2014).

### 1.4.1 Specific Scientific Questions

This thesis focuses on simulating the middle-to-late Eocene climate using a set of both uncoupled and coupled climate models. The main motivation to study this interval lies in the remaining uncertainty in the mechanism causing Antarctic Glaciation at the EOT and the scarcity of both model and proxy data over much of the preceding period. The importance of global geography changes is also debated, yet poorly captured by earlier reconstructions or coarse resolution in climate models. The existence of multiple climatic states under the same forcing conditions (e.g. greenhouse/icehouse, oceanic circulation) poses interesting ways of explaining some of the variability seen in the Cenozoic record. Additionally, the seemingly contradictory presence of ice and sub-tropical conditions on Antarctica poses a challenge to most climate models and explaining these conditions is crucial in order to understand the greenhouse-icehouse transition.

The issues stated above motivate the three central research questions of this thesis:

1. **Can we simulate the middle-to-late Eocene climate using new geographical boundary conditions within a higher resolution climate model to improve the agreement with the proxy record?**

*The main goal is to get a better match between model results and the proxy record; this will require new model simulations but also an updated compilation of (marine and terrestrial) temperature proxies for the middle-to-late Eocene.*

This first question will be the focus of **Chapters 2 through 5**, treating the geography reconstruction itself, model boundary conditions and middle-to-late Eocene climate simulations in both an ocean-only and coupled model framework.

2. **Do changes in global geography affect the simulated late Eocene climate, which different equilibrium states exist and what are their consequences for the EOT?**

*The continental geometry during the Eocene was significantly different to that of today, but also gradually changing through time (especially the depth and width of Southern Ocean gateways). We will investigate whether these changes are enough to contribute to climatic changes leading up to the EOT. Furthermore, the presence of multiple equilibria in the circulation pattern may introduce large responses to a subtle geographical difference.*

The effect of late Eocene geography variations is treated in **Chapter 7**, together with the possibility of multiple states in the oceanic circulation. The latter are also examined using ocean-only simulations in **Chapter 4**.

3. **Can we reproduce the warm and wet Eocene conditions on Antarctica suggested by proxies and how do they affect continental glaciation?**

*The aim of the model simulations here is not only to study the global middle-to-late Eocene climate, but also more regionally the conditions over Antarctica. An important question is how on one hand proxy records indicate the presence of frost-weary vegetation, but on the other hand also suggest ice during the Eocene. If a warm and wet climate can be simulated over Antarctica, then what changes are needed in order to allow a continental-scale ice sheet to grow?*

After the discussion on the simulated middle-to-late Eocene climate in general in **Chapter 5**, the Antarctic climate is studied in more detail using the same model results in **Chapter 6**. Together with an overview of the different model simulations, the possibility of Antarctic Glaciation at the EOT is explored in **Chapter 8**

### 1.4.2 Outline of the Thesis

A new method to create geographical boundary conditions for Cenozoic palaeoclimate modelling studies and in particular the middle-to-late Eocene is presented in Chapter 2. Different rotational frameworks for the plate-tectonic reconstructions are explored to develop two possible 38Ma reconstructions and a 30Ma one that will be used as model boundary conditions.

How the different model simulations are set up for a number of ocean-only and coupled cases using different boundary conditions and external forcing (where needed) is explained in Chapter 3.

This is followed by a discussion of the sensitivity of the ocean circulation to different geography reconstructions and the existence of multiple equilibria in Chapter 4.

Then, results of the pair of 38Ma coupled model simulations to reconstruct the middle-to-late Eocene climate are considered in Chapter 5. This central part includes a discussion of the general climatic state, a comparison to proxy temperature estimates and an assessment of climate sensitivity.

A more regional approach to the Antarctic climate prior to large scale glaciation is made in Chapter 6, featuring what resembles a sub-tropical summer monsoon and the potential for regional ice caps.

The discussion on the importance of late Eocene geography changes and the existence of multiple equilibria is continued in Chapter 7, but within the framework of a coupled model set-up.

Finally, a more general overview of the different model simulations, a comparison of forcing mechanisms and a discussion regarding the implications for the EOT are given in Chapter 8. The overview also includes some general statistics and analyses of the range of climatic states covered by the set of CESM simulations, revisiting the discussion on equilibrium climate sensitivity from Chapter 5 and assessing the importance of geography changes.

The thesis is concluded in Chapter 9, where the main research questions are reconsidered and an outlook to potential future research is given.





# Eocene and Cenozoic Geography Reconstruction

---

**Abstract** Studies on palaeoclimate and palaeoceanography using numerical model simulations may be considerably dependent on the implemented geography reconstruction. Because building the palaeogeographic datasets for these models is often a time-consuming and elaborate exercise, palaeoclimate models frequently use reconstructions in which the latest state-of-the-art of plate-tectonic reconstructions, palaeotopography and -bathymetry, or vegetation estimates have not yet been incorporated.

In this chapter, a new method is presented to efficiently generate a global geography reconstruction for the middle-to-late Eocene. The generalised procedure is also reusable to create reconstructions for other time slices within the Cenozoic, suitable for palaeoclimate modelling. A plate-tectonic model is used to make global masks containing the distribution of land, continental shelves, shallow basins and deep ocean. The use of depth-age relationships for oceanic crust together with adjusted present-day topography gives a first estimate of the global geography at a chosen time frame. This estimate subsequently needs manual editing of areas where existing geological data indicates that the altimetry has changed significantly over time. Certain generic changes (e.g. lowering mountain ranges) can be made relatively easily by defining a set of dynamic masks, while other features may require a more specific treatment. Since the discussion regarding many of these regions is still ongoing, it is crucial to make it easy for changes to be incorporated without having to redo the entire procedure.

Using the method presented here, a complete reconstruction can be made that suffices as a boundary condition for numerical models with a limited effort. This encourages the interaction between experts in geology and palaeoclimate modelling, keeping reconstructions up to date and improving the consistency between different studies. Moreover, it facilitates model inter-comparison studies and sensitivity tests regarding certain geographical features as newly generated boundary conditions can more easily be incorporated in different model simulations. The general workflow is presented covering a middle-to-late Eocene geography reconstruction (38Ma), next to an alternative 38Ma and a 30Ma one. The procedure makes use of a MATLAB script which is provided online in the supplementary material of Baatsen et al. (2016), together with a complete set of source files.

The geography reconstructions derived here are a key component of the different model experiments carried out in the scope of this thesis, which will be introduced in Chapter 3. Two possible 38Ma configurations are then considered for the uncoupled model simulations in Chapter 4, to test the sensitivity of the ocean circulation to uncertainties in the assumed global geography during the middle-to-late Eocene. Additionally, coupled model simulations using geography reconstructions for 38Ma and 30Ma will be discussed in Chapters 5 and 7, respectively. These model experiments are designed to assess the influence of gradual geography changes on the late Eocene climate.

**Acknowledgement** The author would like to thank dr. Douwe van Hinsbergen in particular for making his plate-tectonic reconstruction available and helping set up the basis for the geography reconstruction. Also the help and advice of dr. Appy Sluijs, dr. Peter K. Bijl, dr. Nadine McQuarrie, dr. Alexis Licht, dr. Guillaume Dupont-Nivet, dr. Christopher R. Scotese, dr. Dietmar Müller, dr. Matthew Huber and dr. Robert M. DeConto in building and adjusting the reconstruction should be acknowledged and is greatly appreciated.

This chapter is partially based on the following publication:

Baatsen, M. L. J., D. J. J. van Hinsbergen, A. S. von der Heydt, H. A. Dijkstra, A. Sluijs, H. A. Abels, et al. (2016), “Reconstructing geographical boundary conditions for palaeoclimate modelling during the Cenozoic”, *Climate of the Past*, vol. 12, no. 8, 1635-1644.

“Not all those who wander are lost.”

J.R.R. Tolkien

## 2.1 Palaeoclimate Modelling and Palaeogeography

As the interest grows in assessing how the climate may change under increasing anthropogenic forcing, the field of climate modelling is steadily growing and improving. The models being used are mainly tested by making hindcasts of the present-day and pre-industrial climate. Anthropogenic forcing may lead to future climate states that are beyond the range for which models can be validated with observations. Reconstructing the palaeoclimate can help to increase the confidence in predictions by simulating episodes in Earth’s history with climatic conditions that were drastically different to those seen today.

While the number of measurements is generally much more limited than for the present-day, a considerable amount of proxies is available to constrain the conditions of several such periods, like the Palaeocene-Eocene Thermal Maximum, Eocene-Oligocene transition or Eemian interglacial period. The equable climate problem (Huber & Caballero, 2011; Lunt et al., 2012; Sagoo et al., 2013) is one good example showing that models still lack some essential dynamics to explain how the meridional atmospheric and sea surface (Bijl et al., 2009) temperature gradient can become so low in a warm greenhouse climate. It is therefore essential to try and simulate the past climate with a similar amount of detail as is done for the present to better understand the climate system when it is forced far beyond its present state.

The need for improved model boundary conditions calls for a new approach (Figure 2.1), where the latest geological reconstructions can be directly incorporated. Together with improving constraints on palaeo-altimetry (e.g. Dupont-Nivet et al. 2008), a plate-tectonic reconstruction is eventually translated into a gridded topography and bathymetry map. A method is presented here that allows for the derivation of global geography reconstructions, based on the most recent geological insights with relative ease. Since there is a relative scarcity in middle-to-late Eocene reconstructions, the composition of a 38Ma geography will be worked out step by step to serve as an example of the general workflow. The set of files (and downloads) required to reproduce this procedure for 38Ma, as well as other time frames, is provided online in the supplementary material of Baatsen et al. (2016) along with a *Readme* text file for guidelines. Although somewhat similar workflows have been presented in the past (Herold et al., 2008; Markwick & Valdes, 2004), the innovative aspects here are in the approach of directly incorporating a plate-tectonic reconstruction. This grants the user the freedom of choosing a different plate-tectonic model framework and the ability to consider multiple time frames within the same workflow.

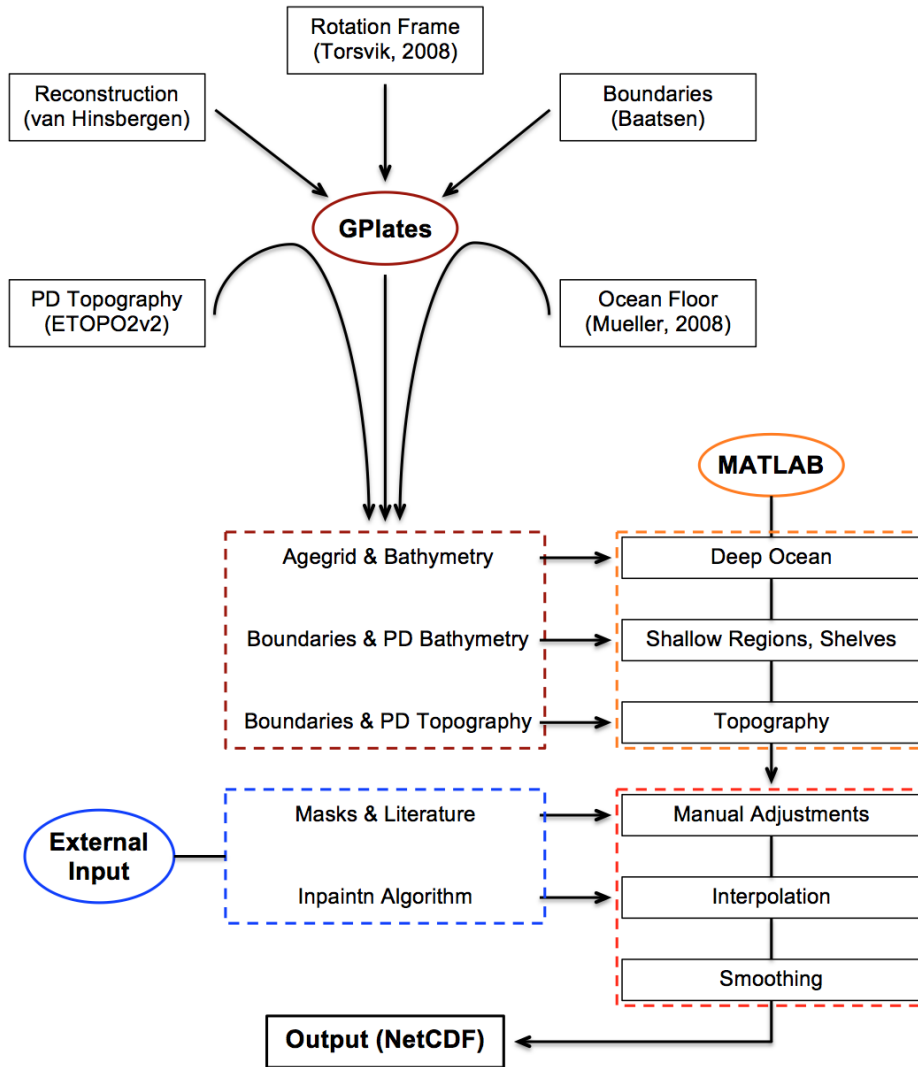


**Figure 2.1:** Flowchart of the procedure; a general plate-tectonic reconstruction is made within GPlates (Boyden et al., 2011), using a set of reconstructed plate trajectories (Hinsbergen et al., 2015; Seton et al., 2012), a reference rotational frame (Torsvik et al., 2008) and a set of boundary masks delimiting present-day coastlines, continental shelf breaks, shallow ocean regions and some regions that need manual adjustments (Figures 2.3 and 2.6 below). In addition to the reconstruction, present-day (PD) topography and bathymetry base files are manipulated using the same rotational frame and adjusted to the configuration at the aimed time frame. The resulting output files as well as some specific external input are then fed into a MATLAB script, which builds up a global geography dataset through several consecutive steps and stores it as a NetCDF file.

## 2.2 Plate-tectonic Reconstruction

The backbone of the new method is a plate-tectonic model (Figure 2.2) that provides a first-order, 200Ma to present-day reconstruction of palaeogeography (Seton et al., 2012). This model is provided in the freely available plate reconstruction software GPlates ([www.gplates.org](http://www.gplates.org), Boyden et al. 2011), which is widely used in tectonic research. The reconstruction of Seton et al. (2012) serves as a basis, and can be updated when new reconstructions become available.

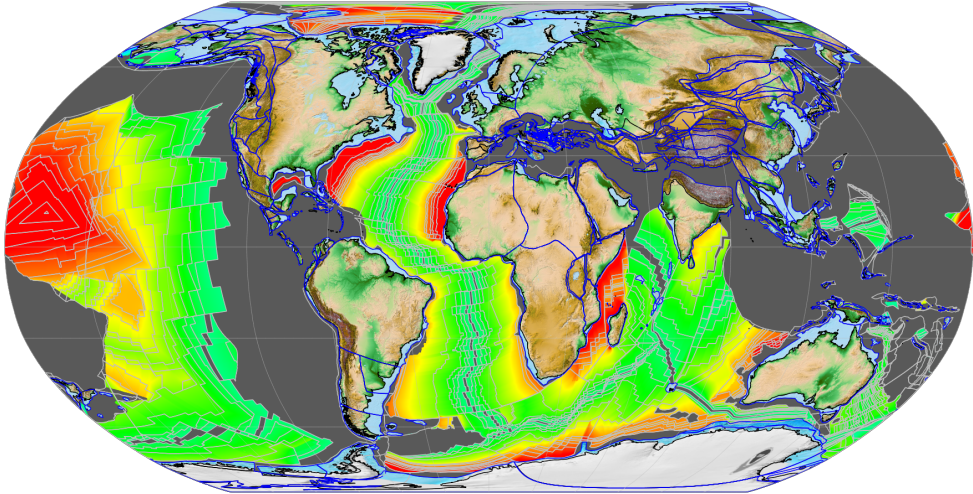


**Figure 2.2:** Example of a plate-tectonic reconstruction from Hinsbergen et al. (2015) at 38Ma using GPlates (Boyden et al., 2011). Blue lines show continental plate and grey lines oceanic plate boundaries. Present-day topography is projected onto the continents and the age is shown for oceanic crust (PD; green: ~50Ma, yellow: ~100Ma and red: ~150Ma). Dark grey regions indicate data gaps, mostly caused by subduction that has occurred since the considered time frame.

Because the main aim here is to provide boundary conditions suitable for palaeoclimate models, the reconstruction is placed in a palaeomagnetic reference frame (Hinsbergen et al., 2015; Torsvik et al., 2012). A different reference frame can be used by simply changing the rotation file of the plate-tectonic model, as long as the ocean bathymetry grid is consistent with the latter. Starting from the present-day topography (ETOPO1; <http://www.ngdc.noaa.gov/mgg/global/relief/ETOPO1>), the outlines of land, continental shelves and shallower regions such as intra-oceanic ridges and plateaus are defined. Using the plate-tectonic model, these features are then shifted towards their positions at a chosen time frame (here: 38Ma) and exported as Shapefiles (.shp). The latter are then transformed into numerical grids and stored as a NetCDF file using a simple MATLAB script for easy and unambiguous interpretation by most computational programs. An example showing the gridded masks for the middle-to-late Eocene is shown in Figure 2.3.

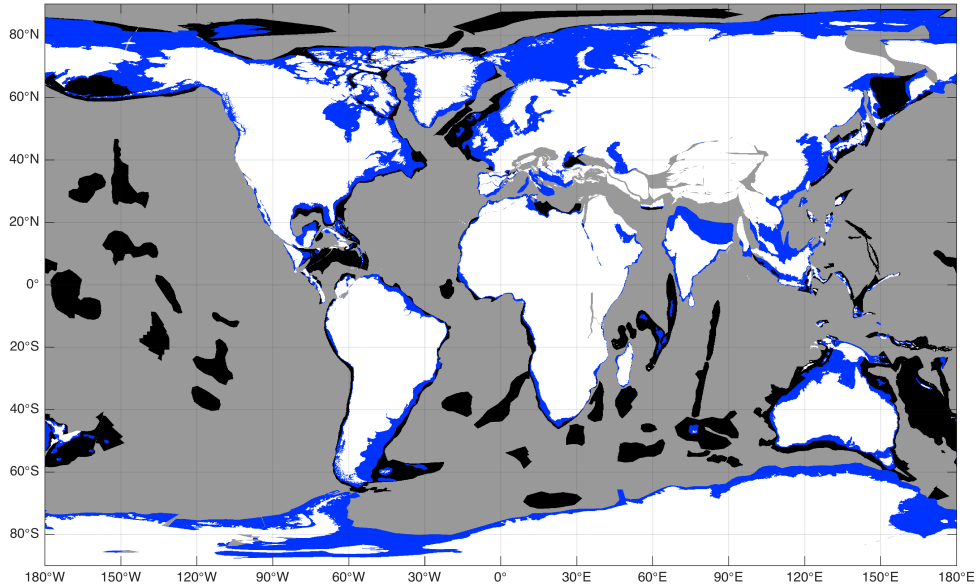


**Figure 2.3:** Earth reconstruction from the plate-tectonic model at 38Ma showing shifted present-day land surface (white), continental shelves (blue) and relatively shallow ocean regions (black). Remaining in grey are then the deep ocean and zones that are yet unidentified in the plate-tectonic reconstruction model.

For its application as a climate model boundary condition, the final geography reconstruction should be stored as a gridded (latitude-longitude) topography and bathymetry dataset of choice. To start with, ocean bathymetry is estimated using the present-day ocean floor age grid provided by Müller et al. (2008a) in combination with the plate-tectonic model. Using the latter, the age grid is shifted into its position at the considered time frame (38Ma here) to be compatible with the rest of the reconstruction. The position and age (corrected for the plate motions that have occurred since then) of oceanic plates in the model is then translated into a bathymetry map using the general depth-age relationship for oceanic crust. Here, an average of the relations given for the main ocean basins (Atlantic, Pacific and Indian Ocean) is used, as treated by Crosby et al. (2006):

$$\begin{cases} Z_{A < 90 \text{ Ma}} = 2620 + 330 \sqrt{A - T_r}, \\ Z_{A > 90 \text{ Ma}} = 5750, \end{cases} \quad (2.1)$$

with  $Z$ : basin depth (m),  $A$ : ocean floor age (Ma) and  $T_r$ : reconstruction time. The method above can only be applied to regions in which the ocean floor is still preserved today, leaving large gaps where oceanic crust has subducted since the reconstruction time (e.g. the western and southeastern Pacific Ocean, see Figure 2.2). An estimated palaeo-age grid was already translated into a rastered geo-referenced ocean depth to basement dataset by Müller et al. (2008a). The latter also provides a reconstructed bathymetry including sediment loading, but this makes it incompatible with other areas where only the age-depth relationship is used.

Furthermore, the thickness of sediment layers is only significant in a few locations where the ocean floor is still very deep (generally below 5000m), resulting usually only in relatively small changes. These are further reduced when the bathymetry grid is translated into depth layer masks that are used in numerical models. The maximum water depth in ocean models rarely extends beyond 5–5.5 km, while the thickness of bottom layers is generally  $>100\text{m}$ . One exception where sediment load is significant is found in the Neotethys Ocean where up to 1500m is added to the ocean basement by Müller et al. (2008a). The same region is treated specifically here, resulting in a similar final depth (i.e. 4.5km). Finally, the age-depth relationship used here (Crosby et al., 2006) is comparable to the one used to reconstruct the Müller et al. (2008a) depth to basement grids (Stein & Stein, 1992) as differences are generally around 50m or less.

The Müller et al. (2008a) grids are provided in a hot spot reference frame (Seton et al., 2012) and thus need to be converted to the palaeomagnetic reference frame used here in the scope of palaeoclimate modelling (Hinsbergen et al., 2015; Moreau et al., 2007). This conversion is carried out by fixing the entire bathymetry grid to the Africa craton which is the central pinning point in both of the reconstruction frameworks. First, the movement of Africa in the past 38Ma is reversed by using an adapted version of the Seton et al. (2012) rotation file. This makes the African continent move back towards its present-day position, starting from where it was at 38Ma instead of doing the opposite normally. The bathymetry map (defined at 38Ma) is then shifted to the configuration it would have at the present-day, disregarding the individual plate movements relative to Africa. Finally, the same is done using the (unaltered) rotation file of the (Torsvik et al., 2012) palaeomagnetic framework, moving the bathymetry grid back to its configuration at 38Ma as if it were made using this plate-tectonic model. After doing so, the adapted Müller et al. (2008a) depth grid fits within the continental margins of the plate-tectonic reconstruction (Figure 2.4).

Differences between the possible rotational frameworks used (PaleoMag/HotSpot) may lead to some discrepancies in the reconstruction. Since oceanic plateaus and ridges are treated separately in the new approach, this does not result in any problems over at least the Cenozoic era. For earlier periods, more specific adjustments may thus be necessary to cope with possible inconsistencies. In addition to the deep ocean, shallow basins and plateaus are adjusted to their present-day depth at the according 38Ma positions, using the same plate movements and of which the resulting boundary masks are shown in Figure 2.3. Finally, all of the defined continental shelves are put to a fixed depth (200m is taken here, values between 50 and 500m are found in literature) as they mark the outer margins of continental crust, that are assumed to be fairly robust over time. It is important to consider here that the shape and depth of continental shelves may be subject to change, depending on the considered time frame (Sømme et al., 2009). Since the middle-to-late Eocene had a greenhouse climate, a flat and relatively shallow shelf is implemented here but this can easily be chosen differently for other periods.

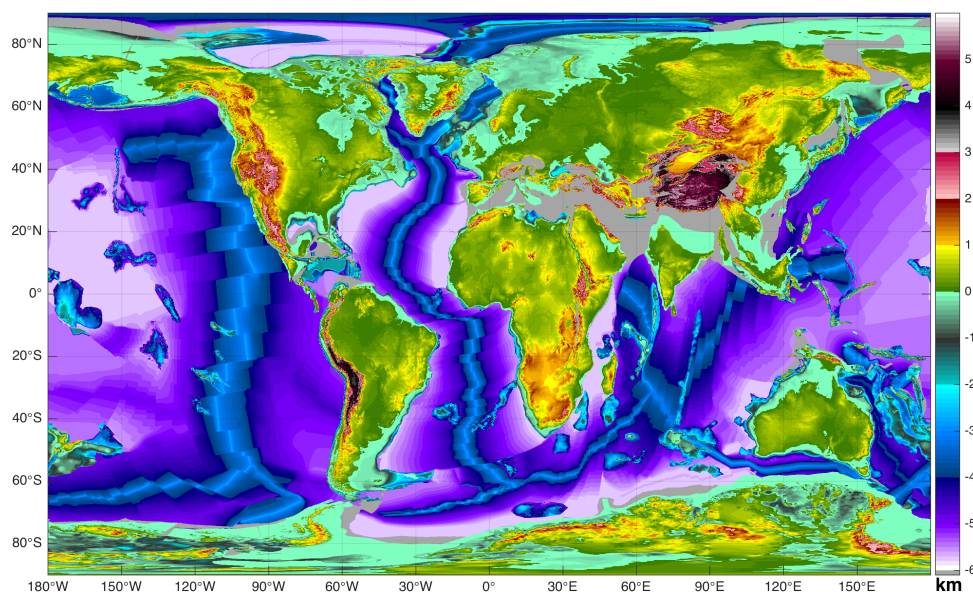


**Figure 2.4:** First stage of the reconstruction: global geography at 38 Ma using the depth-age relationship, the Müller et al. (2008a) reconstruction, shallow basins, continental shelves and the present-day topography. The areas shaded in light grey are gaps which still have to be addressed.

The next, more challenging step is to create a realistic land topography for a chosen time frame. Good estimates of altimetry are only available for a limited number of locations and time intervals, making the reconstruction of palaeotopography a difficult task that requires a lot of manual input. As a result, the global Eocene topography by Markwick (1998) is still used and referred to regularly in palaeoclimate modelling. Our approach here is to first consider the present-day topography (using the ETOPO1 dataset, <http://www.ngdc.noaa.gov/mgg/global/relief/ETOP01>) and adjust it to the 38Ma configuration using the plate-tectonic model and the land mask shown in Figure 2.3. Later on, specific topographical features can be corrected manually, depending on the specific demands of the application and the amount of information that is available. Since the topography is coupled to the plates and shifted within GPlates (using a spherical projections, unlike the figures shown here), there are no issues concerning area preservation or distortion. The resulting first stage of the 38Ma geography reconstruction is given in Figure 2.4.



## 2.3 Generic Adjustments

The geography obtained at this stage (Figure 2.4) is not yet accurate and contains a number of gaps that remain to be filled: mainly collision zones and transition regions between continental and oceanic crusts. Especially the land topography needs to be adjusted so that it better matches palaeo-altimetry estimates for the considered time frame (38Ma).

Although glaciers possibly existed on Antarctica (Carter et al., 2017; Passchier et al., 2017; Scher et al., 2014) and Greenland (Eldrett et al., 2007), the presence of continental-scale ice sheets in the Eocene is unlikely (DeConto et al., 2008). Therefore the effect of isostasy is compensated by raising the present-day bedrock topography one third of the current ice thickness. The changes mainly affect Greenland and Antarctica at first. For the time window chosen here a highly detailed palaeotopography of Antarctica was already derived by Wilson et al. (2012), considering both isostatic rebound and sediment restoration with respect to the present-day topography. The latter, however, assumes the Antarctic continent to be at its present-day location which does not fit into the geography reconstruction made here.

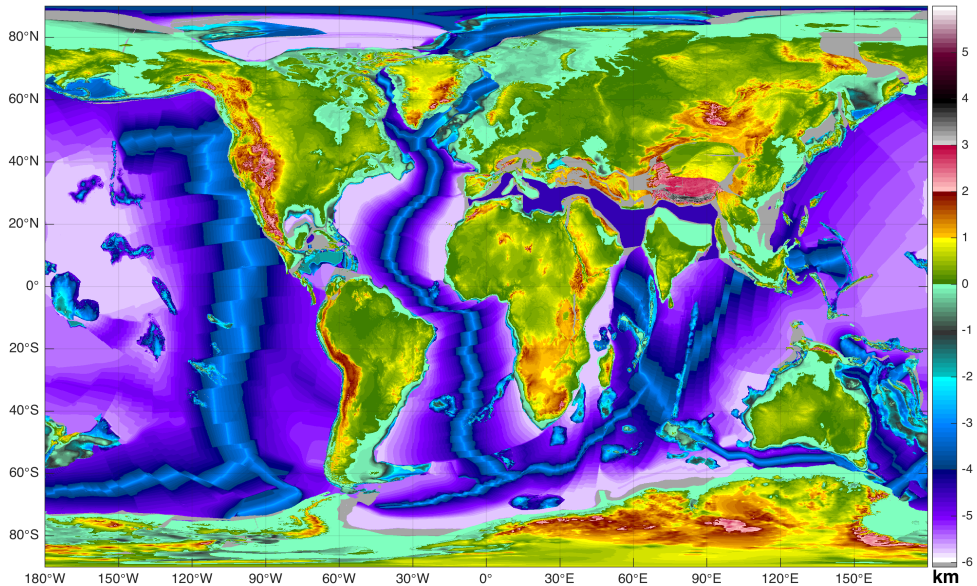


**Figure 2.5:** Second stage of the reconstruction: topography and bathymetry with adjustments to currently glaciated polar regions, a lowering of several mountain ranges and the introduction of oceanic floor where needed. Changes with respect to Figure 2.4 can be noted mainly in Greenland, Antarctica, the Neotethys Ocean, the Andes and the Himalayas.

Similar to how the topography was treated above, the reconstructed Antarctic palaeotopography is fixed to the plate polygons defined in the plate-tectonic model and adjusted towards its 38Ma configuration. In practice, only the area above sea level is incorporated in the reconstruction and combined with the previously determined bathymetry. This is done to minimise possible discrepancies between regions of the ocean floor that may be reconstructed using different methods.

Although the ocean bathymetry now has an estimate at most places, a large gap is still present in the Neotethyan region between Africa, Eurasia, India and Indochina at 38Ma. While in the circum-Pacific area the crust lost to subduction was entirely oceanic, the Neotethys Ocean was characterised by multiple continental collision and subduction episodes (Stampfli & Borel, 2002). The Neotethys Ocean basin is thus introduced manually, based on the incorporation of GPlates reconstructions covering the Mediterranean region by Hinsbergen et al. (2012, 2014), the Arabia-Eurasia collision zone by McQuarrie & Hinsbergen (2013), the Arabia-India plate boundary zone by Gaina et al. (2015) and the India-Asia collision zone by Hinsbergen et al. (2011, 2012). An ocean basin with a depth of 4500m is assumed, a value that is close to the estimate of Müller et al. (2008a), representing the Neotethys Ocean at 38Ma.

Next, The elevation of several mountain ranges is adjusted towards values that are more adequate for the considered time frame. Since most of the current elevated regions underwent a considerable part of their uplift after the late Eocene (such as the Andes, Himalayas and East African Rift) they have to be lowered, while eroded regions may require some uplifting (for instance large river catchments). More specific changes for the example considered here will be discussed in Section 2.4 in more detail, after the result of generic changes shown in Figure 2.5. As this is clearly the most tedious part of the procedure, it will consume a considerable part of the time required to generate a palaeogeography for another time frame. However, time-specific adjustment masks are created as polygons within GPlates and fixed to the plate movements. Consequently, only their extents and effects will need to be adjusted and some masks may need to be removed or added, which facilitates this step significantly. When available, the incorporation of a digital palaeo-elevation model, such as the one presented by Markwick & Valdes (2004) can replace the present-day topography so that no further adjustments are needed.

## 2.4 Specific Adjustments for the Middle-to-late Eocene

The example shown thus far (Figure 2.5) is largely representative for the middle-to-late Eocene (38Ma) geography, but now a number of time-frame specific adjustments are made that have not yet been treated in the previous sections. Several major tectonic events took place prior to and across the Eocene-Oligocene transition that had an impact on the global climate. A brief overview of these events and how their potential impacts are implemented specifically is given below and a map of the masks used to apply the various changes is provided in Figure 2.6. The combined effect of these adjustments is indicated by the highlighted areas in Figure 2.7. Note that the effects of the land mask shown (in white) in Figure 2.6 have not yet been implemented. The latter is used to correct the land boundaries after the final modifications that are discussed in Section 2.5.

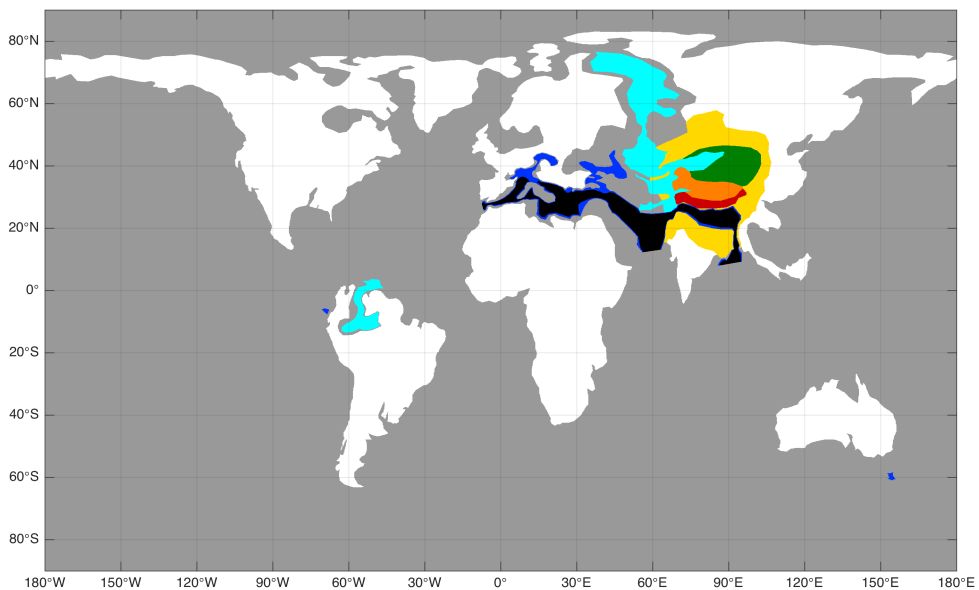


**Figure 2.6:** Masks used for manipulation of the reconstruction; white represents land, cyan shallow water, blue sea and black ocean. In southern Asia, green, yellow, orange and red indicate areas that are lowered manually by different ratios.

The collision between Greater India and Eurasia since the Eocene is causing profound changes to the surrounding geography (Hinsbergen et al., 2012). The Neotethys Ocean narrows due to the combined northward propagation of Africa and India, leaving the Mediterranean Sea and the northern Indian Ocean. Further north, a major intra-continental seaway known as the Paratethys covered much of Europe and a considerable part of western Asia. This was mainly a shallow basin except for the South Caspian and Black Sea regions, as it was mostly underlain by unextended continental crust. The extent of the Paratethys as well as the distribution of the surrounding continents is determined within GPlates, using the plate-tectonic reconstructions mentioned in Section 2.2.

The Neotethyan subduction-collision systems also create a large-scale uplift in southern Asia, resulting primarily in the formation of the Himalaya mountain range and the Tibetan Plateau. To the north and west, the same uplift induces a westward retreat of the relatively shallow Paratethys leaving several isolated basins (Bosboom et al., 2014b; Meulenkamp & Sissingh, 2003). In addition, the formation of a rift between Antarctica and South America causes the opening of the Drake Passage with the introduction of oceanic crust at around 35Ma (Livermore et al., 2005).

A similar process is taking place south of Australia with the formation of the Tasmanian Gateway. While the first opening of the ocean gateway already occurs at around 50Ma, it initially remains shallow (<1000m). Coincident with the transition from a slip-boundary towards north-south spreading between Australia and East Antarctica (Bijl et al., 2013), a profound deepening phase occurs from 35.5Ma onwards. The deepening and widening of the Tasmanian Gateway is further complicated by a northward extension of the Antarctic shelf and an elevated Tasman Rise which both sank over time (Close et al., 2009; Stickley et al., 2004).

Dependent on which absolute plate-tectonic reconstruction frame is used, the opening of the Tasmanian Gateway occurred either to the north or south of 60°S palaeolatitude. This can have important consequences for the direction of a possible initial throughflow (Sijp et al., 2016) and again stresses the importance of using the most accurate geography reconstructions in palaeoclimate modelling. The related northward motion of Australia, combined with the rotation and rifting taking place around Indochina also causes a gradual restriction of the Indonesian Throughflow during the Oligocene (Hall, 2002).

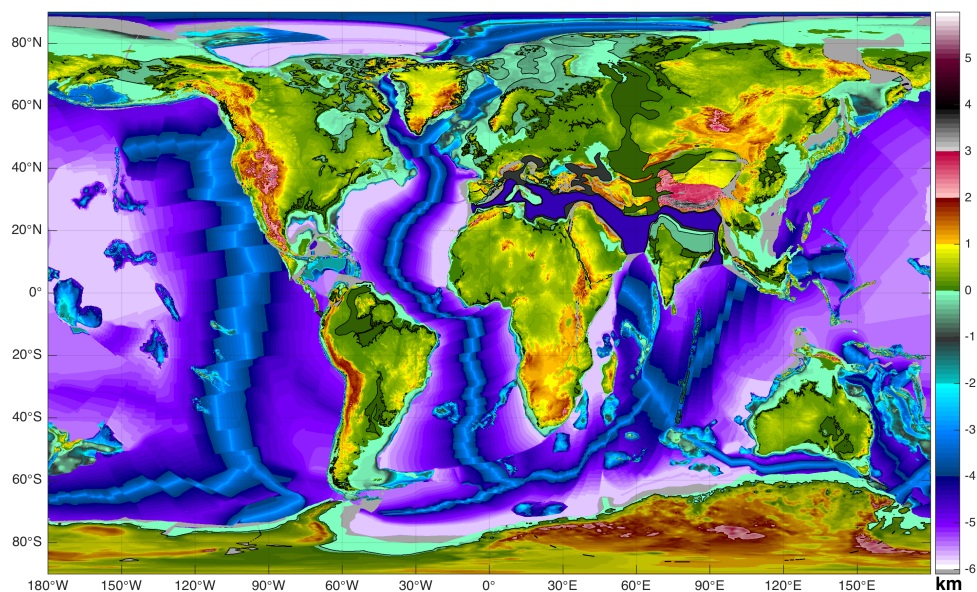


**Figure 2.7:** Reconstructed topography and bathymetry with specific adjustments indicated by shaded areas, these include mainly Antarctica, southern Panama, the Amazon and several other river basins, the Hudson Bay and Great Lakes, Neotethys Ocean and Paratethys Seaway, the Ninety-East Ridge and the Tasman Rise.

As was pointed out before, some smaller geographical features have to be treated individually. Mountain ranges that are believed to have experienced major uplifts since the Eocene are mainly the Andes, Himalayas, Sierra Nevada (USA), East African Rift and Middle East collision zone, which are all lowered significantly with respect to the present-day topography. The southern Tibetan Plateau has been lowered more than the Himalayas since a narrow yet high ridge was already present while the adjacent plateau was still much lower (Hinsbergen et al., 2012). The northern part of the Tibetan Plateau is changed into lowland that surrounds the retreating Paratethys in the Tarim Basin (Bosboom et al., 2014c; Dupont-Nivet et al., 2008; Sobel et al., 2013). Related to the changes in Eurasia mentioned above, the narrow Neotethys is drawn as a deep ocean while the Paratethys consists mainly of shallow seas with the Turgai Strait almost closed (Bosboom et al., 2014b). The latter forms a connection between the Arctic Ocean and the Paratethys and is an important contributor to the water budget in Central Asia.

During the early Eocene, the Arctic Ocean may have been geographically isolated as indicated by episodes of freshening reported by Brinkhuis et al. (2006). No such events have yet been documented for the middle and late Eocene, so here we assume several relatively narrow and shallow channels to be open. The western part of the Amazon basin was still flooded during the middle Eocene according to Hoorn et al. (2010). A kinematic reconstruction of the Caribbean region by Boschman et al. (2014) is adopted to treat the Panama Seaway. This gateway between the tropical Pacific and Atlantic Ocean is still open at 38Ma but only through narrow connections (similar to the Indonesian Throughflow today), as it consists of an intra-oceanic volcanic arc since the late Cretaceous (Boschman et al., 2014). The Ninety-East Ridge (Slotnick et al., 2015) is enhanced (made wider and higher) as it is a pronounced yet narrow feature in the eastern Indian Ocean that would otherwise be obscured by smoothing later on in the procedure. Regarding the areas discussed above, three masks are applied defining ocean (deep oceanic), sea (deep continental) and shallow basins (shallow continental) implying a depth of 4500m, 1000m and 100m, respectively (black, blue and cyan colours in Figure 2.6).

## 2.5 Final Modifications and Smoothing

All major features of the 38Ma geography reconstruction are now present but before it can be used as a numerical grid for a climate model simulation, some additional modifications need to be made. Firstly, to fill in the remaining gaps where the altimetry or bathymetry is still unknown, an interpolation is performed using the *inpaintn* algorithm developed by Garcia (2010) and Wang et al. (2012). An additional land mask was made (shown in white in Figure 2.6) containing regions that should be above sea level to avoid creating artificial basins with this technique. The land mask is based on several available global geography reconstructions such as those made by dr. R. Blakey (<https://www2.nau.edu/rcb7/globaltext2.html>) and the ones from dr. C. R. Scotese (<http://www.scotese.com/earth.htm>), assuming that large alluvial plains were not entirely flooded and glacial basins had not yet formed.

Secondly, during many of the past climatic periods sea level was different from that of today. Global mean sea level is governed by changes in ocean water volume, that are linked to ice sheet volume and steric effects, in combination with varying global ocean basin volume related to the average ocean floor age, shelf depth and continental distribution. In the middle-to-late Eocene, mean sea level was about 100m above that of today (Müller et al., 2008b), so the elevation (and similarly increase the depth) of all data points is decreased by 100m to correct for this. The depths that were implemented before, using the masks shown in Figure 2.6, were initially corrected so they end up being the actual values stated above after changing the global sea level (such that an area assigned to be e.g. 1000m deep does not end up being 1100m instead).

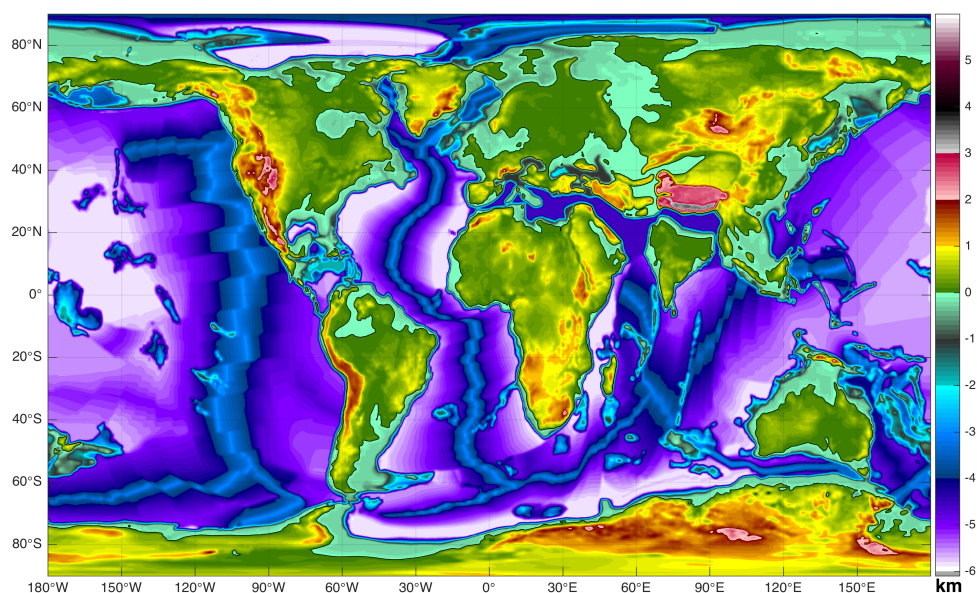


**Figure 2.8:** Final smoothed global topography and bathymetry reconstruction on a  $0.1^\circ$  grid for 38Ma (middle-to-late Eocene).

Again, the land mask (white in Figure 2.6) is used to correct the elevation of certain inundated regions back to sea level where land is believed to be present at the considered time. For instance, river basins such as the Amazon, Rio de la Plata, Congo and Mississippi were just carved out deeper after the sea level dropped. Other depressions such as the North American Great Lakes were only created during glacial periods in the Pleistocene.

Finally, the application of the geography reconstruction will usually be at a lower resolution than the one used until now ( $0.1^\circ$ ) and the high level of detail in the present-day topography can be misleading with respect to how precise palaeotopography is actually known. The last step is then to apply a squared smoothing mask, performing a 2-dimensional running mean with a  $1^\circ$  width for the example, of which the result is shown in Figure 2.8. The mask properties can easily be chosen differently. After smoothing, the global geography data is extrapolated onto the desired output grid (e.g., longitude-latitude) to be stored as a NetCDF file.



## 2.6 Summary and Additional Reconstructions

A new method has been presented to create global geography reconstructions that can be used as boundary conditions in palaeoclimate model simulations. Starting from a plate-tectonic reconstruction, the depth of the ocean floor was estimated and combined with a reconfigured present-day topography. An overview of the different steps making up the procedure was given in Figure 2.1. Reconstructed plate trajectories, a background rotational frame and a set of boundary lines are imported into GPlates to create a customised global plate-tectonic reconstruction for a particular time frame (38Ma here).

Within the same setup, present-day topography and ocean floor data are manipulated and shifted to fit the same geographical configuration as the rest of the output. The latter is then used in a MATLAB script together with some external input (mostly from literature) to create a global gridded altimetry-bathymetry dataset that is stored as a NetCDF file. This results in a highly detailed dataset that needs some time-specific changes, after which it is smoothed and extrapolated onto the desired computational grid for a specific climate model.

Even though a number of manual adjustments were needed, interfacing GPlates with the provided MATLAB script allows for the development of global geography reconstructions with limited effort. The primary focus was to use a plate-tectonic model not originally designed to create numerical grids as output (but it is able to use and manipulate them), that can be altered afterwards without having to run through the entire process again (only some of the masks may need to be reconfigured). Creating a new grid for a different point in time or within a new configuration (e.g. using a different rotation framework) should allow the user to make multiple reconstructions in a few days' time. In case of a time slice experiment, one can also create appropriate boundary conditions for each time frame instead of making some minor adjustments to an average geography, to really try and catch the effect of gradual but global changes.

The amount of manual handling depends on the demands of a specific application and can consequently be very limited. Meanwhile, the procedure does not inhibit additional adjustments to acquire further detail and accuracy. In the 38Ma example treated here, the output grid is defined as having a  $0.1^\circ$  resolution but can easily be extrapolated onto a coarser grid if needed, which may then require some more elaborate smoothing.

An example of another reconstruction created using the same method but slightly altered adjustment masks, is a 30Ma geography presented in Figure 2.9. Most changes with respect to the 38Ma reconstruction are directly related to the plate-tectonic model. Some specific changes have to be reconsidered at the new time frame, such as the height and extent of the Tibetan Plateau and the Outlines of the Paratethys and Neotethys Ocean.



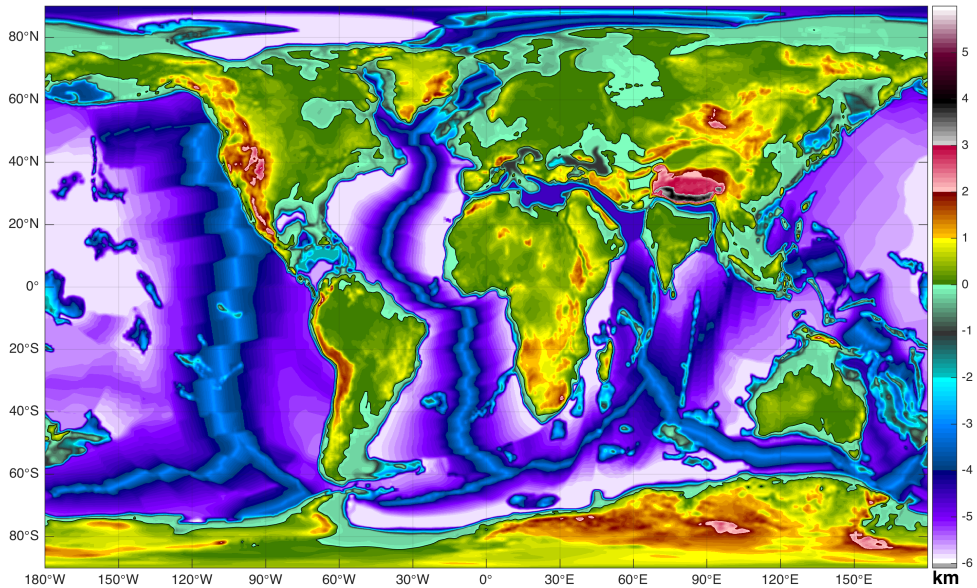


**Figure 2.9:** Global geography reconstruction for 30Ma, created using the same procedure as for the 38Ma one shown in Figure 2.8. Changes compared to 38Ma include the opening of Southern Ocean Gateways, retreat of the Paratethys and the India-Eurasia collision along with related topography changes over the Himalayas and Tibetan Plateau.

As the procedure starts from a plate-tectonic model, most of the features important for climate modelling applications are quite realistic. The width and depth of ocean basins, presence of oceanic ridges and plateaus, position of continents and opening or closing of gateways are all directly incorporated in the final result. The set of boundaries shown in Figure 2.3 are connected to individual plates and can easily be linked to a different plate-tectonic reference framework.

When comparing the result (Figure 2.8) to other recent reconstructions used in palaeoclimate modelling, several differences quickly become evident. For instance, the global geography used in Ladant et al. (2014) is coarser and contains less detail in both land topography and ocean bathymetry. The Southern Ocean gateways are also much wider, which is probably a result of both the large grid spacing used for the climate model and the difference in time frame considered, as this reconstruction is based on an Oligocene geography from Lefebvre et al. (2012).

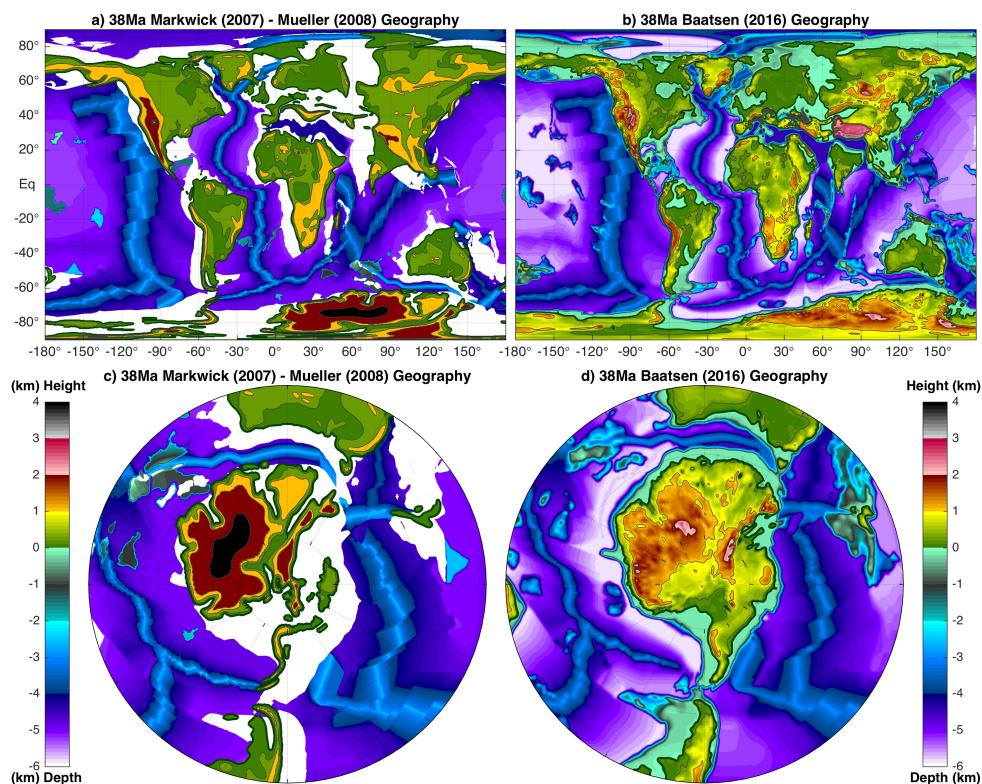


**Figure 2.10:** Comparison of the **a)** Markwick (2007) late Eocene and **b)** new 38Ma geography reconstruction, including **c)** and **d)** Antarctic Stereographic projections. Since there is only a flat bottom ocean available from Markwick (2007), it is replaced by the original (Hot Spot referenced) bathymetry reconstruction from Müller et al. (2008a). There are clearly some discrepancies between land and ocean grids, highlighting the importance of making one integrated global geography reconstruction within the same reference framework.

Herold et al. (2014) have manually added a large amount of detail to both the land surface and ocean floor in their reconstruction. The problem remains that there can be considerable offsets in continental positions as the geography is bound to a specific time frame. Details within the contours of an older reconstruction can still be added but changing the relative positions of various land masses is not straightforward. Most of those reconstructions are based on the ones from Markwick (1998) and Markwick (2007), of which the most recent is compared to the new 38Ma geography in Figure 2.10

In summary, the reconstruction method presented here can provide detailed geographical datasets with relative ease for palaeoclimate model studies and permits users to customise the result to their specific needs. This should facilitate the communication between geologists and climate modellers in their efforts to improve the quality and consistency of future palaeoclimate simulations.

# Model Set-up and Experimental Design

---

**Abstract** The results of a number of experiments carried out for this study, using different configurations and model set-ups will be discussed in the following Chapters 4 through 8. These experiments will include ocean-only as well as fully coupled simulations using the Community Earth System Model (CESM), both using an array of different boundary conditions. In order to introduce the model(s) to be used and the experimental design of the different cases considered, this chapter will list the associated technical details of each simulation. Directly related to the results in Chapter 2, the different geography reconstructions will be one of the main points of interest in setting up model boundary conditions.

First, a general introduction to the CESM is given including its main components, physical schemes and parameterisations. For deep-time (i.e. pre-Pleistocene) cases, palaeoclimate modelling studies require a number of adjustments to reflect changes in the boundary conditions. Not only the atmospheric composition, but also the continental geometry, ocean bathymetry and land surface properties differ from those used for present-day.

Long spin-up simulations are often required that limit the amount of complexity in the model, in order to keep the computational cost feasible. Therefore often slightly older, simpler and/or lower resolution versions of a certain climate model are used in order to speed up the simulations. The respective version and configuration of each of the model components used here are discussed accordingly.

In what follows, the set-up of a series of middle-to-late Eocene ocean-only model simulations is presented, including the required atmospheric forcing and different experiments considered. The results of these ocean-only simulations will be the focus of Chapter 4.

Finally, another set of simulations including both a pre-industrial reference and different middle-to-late Eocene configurations using the coupled version of the CESM is introduced. The results of those experiments will be treated in the remaining Chapters 5 through 8.

**Acknowledgement** The author would like to thank dr. Nicholas Herold for helping a great deal in setting up the CESM simulation, providing his own set of initialisations and parameter settings and assisting with numerous model-related issues. All of the model simulations presented in this thesis were carried out on the Cartesius supercomputer at SURFsara in Amsterdam.

“NO ADMITTANCE EXCEPT ON PARTY BUSINESS.”

J.R.R. Tolkien

## 3.1 The Community Earth System Model (CESM)

The Community Earth System Model (CESM; Hurrell et al. 2013) version 1 is a fully coupled atmosphere-land-ice-ocean general circulation model (GCM) that is being developed at the National Center for Atmospheric Research (NCAR) in Boulder, Colorado. The CESM1 is the successor of the Community Climate System Model (CCSM; Blackmon et al. 2001), which was used to make significant contributions to studies of the past, present and future climate. For use in palaeoclimate modelling, version 1.0.5 of the CESM is a suitable choice motivated by a trade-off between increasing model complexity and computational cost. Apart from using the newer framework, the model as it is implemented here is equivalent to the latest version 4 of the CCSM (Gent et al., 2011) which was released in 2010. The major components of the model and their respective versions used are discussed below;

**Atmosphere:** The atmospheric component of the CESM is the Community Atmosphere Model (CAM), more specifically the seventh generation used in the CCSM4 (CAM4; Neale et al. 2013). A newer version of the CAM (CAM5) is also available within the CESM1, but its computational cost is significantly higher mainly due to improved representations of cloud processes and aerosols. The atmospheric component uses a finite volume grid at a nominal resolution of  $2^\circ$  ( $2.5^\circ \times 1.9^\circ$ ) and 26 vertical levels with a hybrid sigma vertical coordinate extending upward to 2hPa. In this configuration, the CESM1/CAM4 (i.e. CCSM4) has a reported warming response of  $3.13^\circ\text{C}$  to a doubling of  $\text{CO}_2$  starting from pre-industrial conditions (Bitz et al., 2012). This is considerably higher than that of the previous version CCSM3 ( $\sim 2.5^\circ\text{C}$ ), which is regarded as being too low (Kiehl et al., 2006).

**Land:** The physical, chemical and biological processes taking place on land are represented in the Community Land Model (CLM). Both the CESM1 and CCSM4 use the CLM4 (Lawrence et al., 2011; Oleson et al., 2010), in which all anthropogenic influences (such as urban environments and agriculture) are disregarded for palaeoclimate simulations. A static rather than dynamic vegetation model is used here to avoid potentially amplifying erroneous feedbacks, which can become an issue especially in warm greenhouse climates. An example of this effect can be seen in Loptson et al. (2014) where tropical and sub-tropical regions are mostly covered with grassland or desert after running a model with dynamic vegetation. Herold et al. (2014) also use a lower radiative forcing for their land model simulations, to prevent reduced rainforest coverage in a greenhouse climate. The CESM1 also has the capability to include a fully prognostic carbon cycle, but the added computational cost, uncertainties related to deep-time boundary conditions and fixed vegetation types make this option unfeasible in the set-up used here.

**Sea ice:** The CESM1 sea ice component consists of the Los Alamos National Laboratory (LANL) Community Ice Code version 4 (CICE4; Hunke & Lipscomb 2008).

For simplicity, sea ice only forms when the sea surface cools down to  $-1.8^{\circ}\text{C}$ , after which its dynamical behaviour is treated by the model specifically.

**Ocean:** Again similar to CCSM4, the CESM1 uses the the LANL Parallel Ocean Program version 2 (POP2; Smith et al. 2010) for the ocean model component. The standard configuration is applied here, with a nominal  $1^{\circ}$  ( $1.25^{\circ} \times 0.9^{\circ}$ ) horizontal resolution on a curvilinear grid. In the vertical, the POP2 is set up with 60 layers of varying thickness between 10m near the surface and 250m at greater depth. Using a hyperbolic tangent function, the vertical stretching of the grid makes both the upper and lower 20 model layers nearly equidistant. Horizontal viscosity is considered anisotropic (Smith & McWilliams, 2003) and horizontal tracer diffusion follows the parameterisation of Gent & McWilliams (1990). The model further uses the KPP-scheme to determine vertical mixing coefficients (Large et al., 1994). More information and discussion on the ocean model physics and parameterisations can be found in Danabasoglu et al. (2008, 2012).

An example of both the atmosphere and ocean grid as they are used in a pre-industrial reference simulation, is shown in Figure 3.1. Note that there is an additional latitudinal stretching at low latitudes and a cut-off at southern high latitudes in the ocean grid. This is an optimisation specific to the present-day geography and is therefore not implemented for deep-time simulations with a different continental geometry.

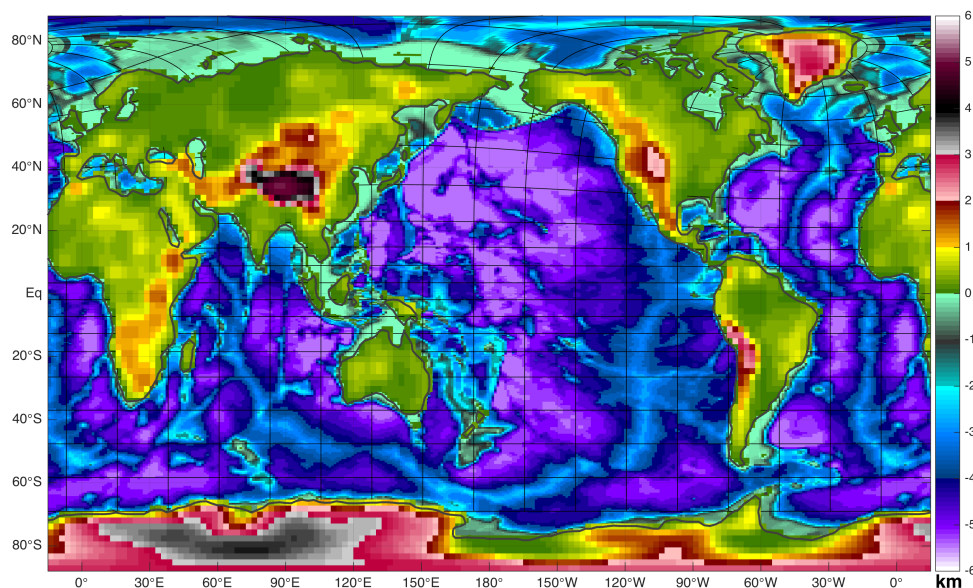


**Figure 3.1:** Atmosphere (topography) and ocean (bathymetry) grid used in the CESM pre-industrial reference simulation. Discrete cells are shown for both grids, having a higher resolution in the ocean. The thick grey line indicates the coastline (i.e. a contour line at 0.5 land fraction) of the atmospheric component while thin lines show the distortion of the curvilinear ocean grid, which has its northern pole over Greenland.

## 3.2 Experiments using Standalone POP Simulations

### 3.2.1 Model Grid and Geography

As in the CESM configuration, the POP standalone model makes use of a nominal  $1^\circ$  horizontal grid resolution and 60 (non-equidistant) vertical layers. For computational efficiency, the existence of singularities in the model grid is omitted by using a curvilinear projection (see Figure 3.2). Rather than using the geographical North Pole, the centre of Greenland is used as the northern pole in the model and the model grid boxes are stretched accordingly. As it is already situated well into the interior of the Antarctic continent, the position of the southern pole in the model is left unchanged.

After the initial interpolation of a  $0.1^\circ$  rectangular bathymetry (Figure 2.8) onto the curvilinear  $\sim 1^\circ$  grid, some manual adjustments are required. Coastlines and continental slopes are checked and smoothed where needed, especially when ripple-like structures are introduced by the interpolation (creating artificial standing waves and checkerboard patterns in the model output). Additionally, all narrow channels are adjusted to be at least 2 grid cells wide (including diagonally) to allow a physically realistic flow of water.

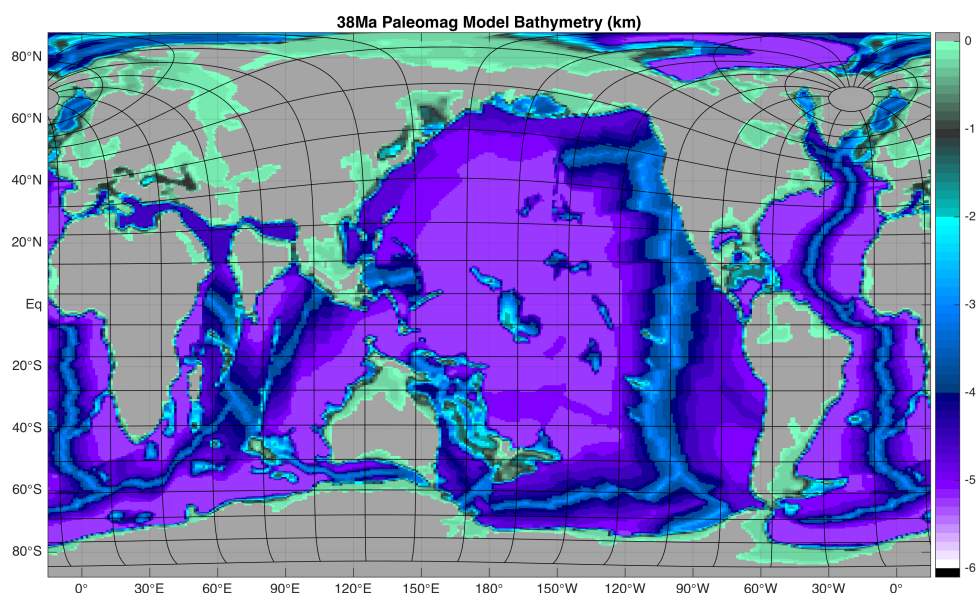


**Figure 3.2:** Model bathymetry grid used for the standalone POP simulations, derived from the 38Ma palaeomagnetic referenced (PaleoMag) reconstruction in Chapter 2 (Figure 2.8). The native curvilinear grid has its northern pole over Greenland and is shown in a rectangular projection here. Black grid lines indicate the distortion introduced by the implementation of a curvilinear model grid, grey regions show land areas not considered in the ocean model.



### 3.2.2 Atmospheric Forcing

Only the ocean is computed explicitly in these standalone POP simulations, so the model needs input from an atmospheric forcing at the surface. The required fields are obtained from a lower resolution (T42;  $\sim 2.5^\circ$ ), fully coupled CCSM3 Eocene simulation under  $4\times$  pre-industrial  $\text{CO}_2$  from Huber & Caballero (2011).

Surface fields of wind stress, freshwater flux, heat flux and sea surface temperature from CCSM3 are adjusted to the new model grid as shown in Figure 3.3. Monthly climatologies (using a 50-year average) are considered, from which original land masses are removed using natural neighbour interpolation. Next, surface forcing fields are adjusted to the new land-ocean mask and interpolated onto the curvilinear grid. Localised extremes in surface fresh water flux from river run-off are removed (to reduce artefacts from altered coastlines; Figure 3.3a) and global fields are bias corrected to conserve the salt budget. Larger scale effects from run-off, precipitation and evaporation are still present in the adjusted forcing as seen in Figure 3.3b.

Similarly, a bias correction is applied to the surface heat fluxes to conserve the global heat budget at the atmosphere-ocean interface. The ocean model is then forced by the adjusted surface fresh water flux, wind stress (shown in Figure 4.8) and heat flux fields, where the latter are combined with restoring conditions to sea surface temperatures.

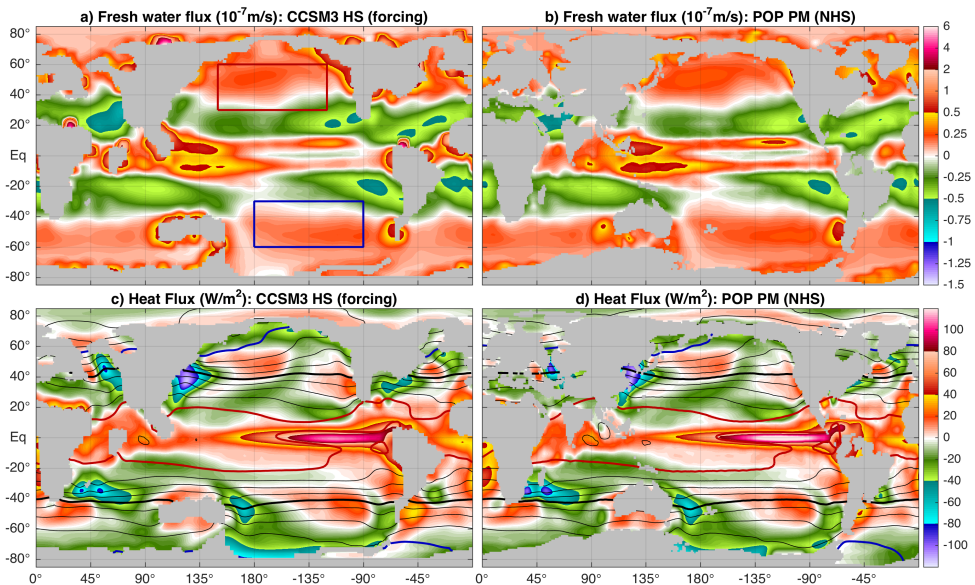


**Figure 3.3:** Surface fresh water flux from **a)** the CCSM3 forcing and **b)** adjusted to the 38Ma model geography (Figure 3.2) as used in the ocean-only simulations ( $10^{-7} \text{ m/s} = 8.64 \text{ mm/day}$ ). Red and blue rectangles denote the areas of changed fresh water fluxes for the adjusted simulation (see Section 3.2.3) over the North and South Pacific, respectively. Surface heat flux (shading) and sea surface temperatures (contours every  $2.5^\circ \text{C}$ ; blue:  $10^\circ \text{C}$ , black:  $20^\circ \text{C}$  and red:  $30^\circ \text{C}$ ), again from the **c)** CCSM3 forcing and **d)** adjusted to the PaleoMag geography.



### 3.2.3 Experimental Design

Two different geography reconstructions for the middle-to-late Eocene (38Ma) were presented in Chapter 2. The differences in ocean circulation between those geographies are assessed by running a set of standalone POP simulations. These experiments, discussed in Chapter 4 include:

1. 38Ma Hot Spot reference geography (HS);
2. 38Ma PaleoMag reference geography (PM);
3. 38Ma PaleoMag with adjusted surface freshwater flux (PM Adjusted).

The first two experiments are designed to look directly at the implications of using a different geography reconstruction as a model boundary condition. The third and last simulation uses the same general configuration as the second one, but has an adjusted surface freshwater flux over selected regions of the North and South Pacific ocean (see Figure 3.3a) to alter the surface density and explore the existence of different circulation regimes within the same geography.

A comparison between both 38Ma reconstructions (Hot Spot and PaleoMag) as used for the ocean model grid in the different experiments, is given in Figure 3.4. Changing from one reference frame to another leads to shifts in the respective geography in the order of 5 degrees at most locations (shading versus black contour lines). Compared to the Hot Spot referenced geography reconstruction, the PaleoMag one mainly sees a southward shift of continents surrounding the Atlantic and a northward shift around the Pacific Ocean. The effect of True Polar Wander is only considered in the PaleoMag reconstruction. It is not just a simple shift in latitude but a transformation around multiple rotational axes, resulting in non straightforward differences in longitude as well between model grids. Of crucial importance to the ocean circulation will be the different latitudes of partly opened Southern Ocean Gateways and the position of Arctic connections in addition to more general shifts in continental boundaries.

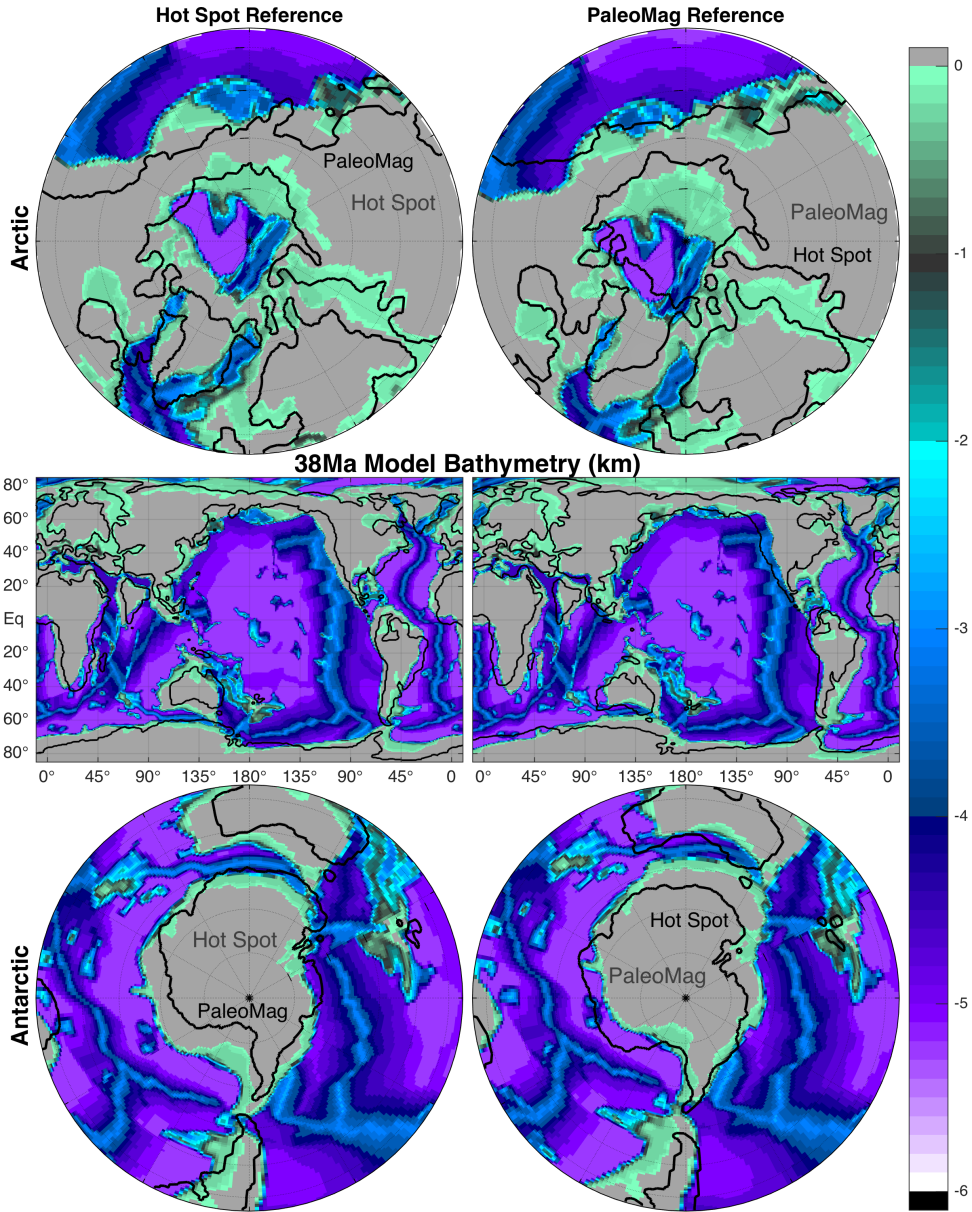


**Figure 3.4:** Model bathymetry grid used in the different standalone POP experiments, with left panels showing Hot Spot and right panels PaleoMag based geography reconstructions. From top to bottom, each grid is shown in a north polar stereographic, global rectangular and south polar stereographic projection. Grey shading indicates the land mask and black contours each time show the coastlines of the opposing model grid, to highlight the differences between both reconstructions.

## 3.3 Experiments using Coupled CESM Simulations

### 3.3.1 Pre-Industrial Reference

For the comparisons of various climatic features between Eocene and pre-industrial conditions within a similar framework, a pre-industrial reference run with the same configuration of the CESM is performed. Since the atmospheric component used here consists of the CAM4 at a nominal  $2^\circ$  horizontal resolution, this reference is similar to the  $2^\circ$  1850 control from Gent et al. (2011). The solar constant in the simulation is  $1361\text{W/m}^2$  and the atmospheric levels of  $\text{CO}_2$  and  $\text{CH}_4$  are 280ppm and 671ppb, respectively. Astronomical orbital parameters are set to their present-day configurations; eccentricity: 0.0167, obliquity:  $23.44^\circ$  and precession placing the aphelion in Northern Hemisphere summer. Both vegetation and atmospheric aerosols are kept fixed at their respective pre-industrial distributions. The corresponding model grid including topography and bathymetry was shown above in Figure 3.1 (Section 3.1).

### 3.3.2 Middle-to-late Eocene Configuration

For deep-time climate simulations there are a number of model parameters and settings that need to be reconsidered, while others are left unchanged with respect to the pre-industrial configuration;

**Resolution:** Both the horizontal and vertical model resolution are kept the same as for the pre-industrial reference.

**Solar constant:** Although this was slightly lower ( $\sim 0.3\%$ ) during the late Eocene, the difference with the present-day is relatively small and therefore not taken into account in these simulations.

**Atmospheric greenhouse gases:** Different cases regarding the radiative forcing of greenhouse gases are considered for the middle-to-late Eocene. The combined reference levels of  $\text{CO}_2$  (280ppm) and  $\text{CH}_4$  (671ppb) are hence forward referred to as Pre-Industrial Carbon (PIC). Various experiments each use one of the following three levels:  $1 \times \text{PIC}$ ,  $2 \times \text{PIC}$  and  $4 \times \text{PIC}$  corresponding to 280, 560, 1120 ppm  $\text{CO}_2$  and 671, 1342 and 2684 ppb  $\text{CH}_4$ , respectively.

**Orbital parameters:** Since the model simulations are designed to reconstruct the climate during longer periods in time (4–8 Ma), there is not a constant set of orbital parameters that is representative for the entire considered time interval. As one of the aims of this thesis is to study the EOT, a set of parameters generally conducive for Antarctic ice growth is chosen: minimum eccentricity (i.e. 0) and present-day obliquity ( $23.44^\circ$ ). Precession is left unchanged as its effect is cancelled in the absence of eccentricity in the Earth's orbit around the sun. The low eccentricity choice is motivated by the conjunction of two such minima occurring around the EOT, as shown by Coxall et al. (2005) and DeConto et al. (2008) (Figure 1.4).

The effect of obliquity can still be important, but it is left at a median value similar to that of today to not just use a single rare combination of orbital parameters. When using an offline ice sheet model, the effect of a different obliquity can still relatively simply be incorporated by adjusting the surface mass balance scheme.

**Geography:** To not only study the middle-to-late Eocene climate but also be able to look at the effect of geography changes, both a 38Ma (Figures 2.8 and 3.5) and 30Ma PaleoMag referenced reconstruction (Figure 2.9; from Chapter 2) are considered in the model boundary conditions. The differences between using a 38Ma and 30Ma geography are highlighted in Figure 3.7, similarly to the comparison between the 38Ma Hot Spot and PaleoMag bathymetries in Section 3.2 (Figure 3.4). From this comparison, it is already clear that despite the 8Ma time interval, the differences between both model grids are more subtle than those corresponding to the Hot Spot and PaleoMag geographies. Although the shifts in continental geometry are subtle, there are several more drastic changes between the 38Ma and 30Ma model grids. These changes include the widening and especially also deepening of both the Tasmanian Gateway and Drake Passage. Furthermore, there are differences in Himalayan and Tibetan uplift, Paratethys Ocean retreat and changes to Arctic Ocean connections.

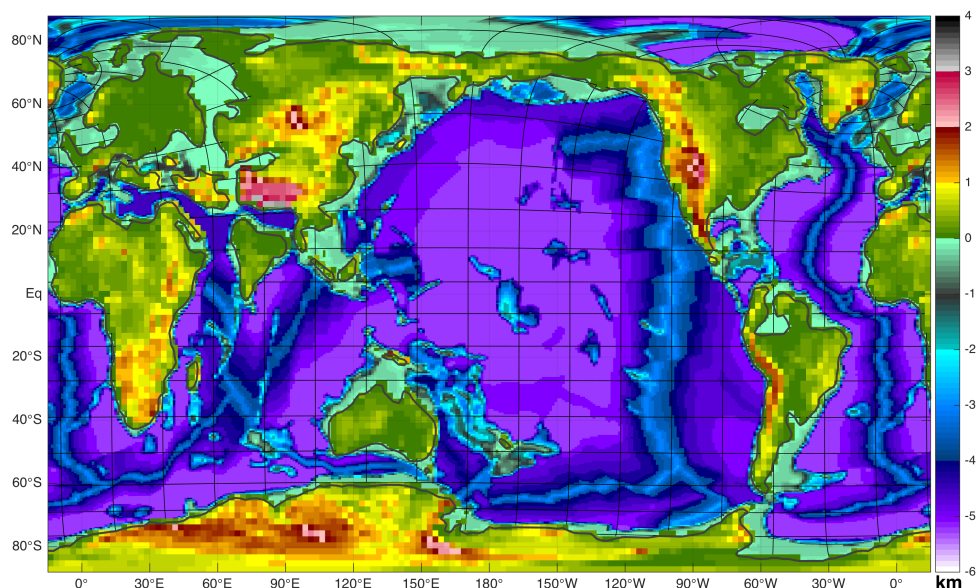


**Figure 3.5:** Similar to Figure 3.1, showing the CESM model geography based on a 38Ma PaleoMag referenced reconstruction from Chapter 2 (Figure 2.8).

**Vegetation:** Not only considering the computational cost, but also the uncertainties in boundary conditions and risk of runaway feedback loops (e.g. dieback of forests and desertification, Herold et al. 2014; Loftson et al. 2014) it is often more appropriate to implement static rather than dynamic vegetation for deep-time palaeoclimate simulations. The middle-to-late Eocene vegetation used here (Figure 3.6) is largely based on the one suggested by Sewall et al. (2000) and mostly consistent with the early Eocene vegetation of Herold et al. (2014). The mostly zonal bands in Sewall et al. (2000) are adjusted to the new geography reconstruction (38Ma PaleMoag in Figure 3.6) and likely marine influences (based on the distance to the coast and expected prevailing winds).

Most of the earth is assumed to be covered by various types of forests and shrubs, with either tropical or sub-tropical vegetation extending well into the middle latitudes. No desert regions are incorporated, but some sub-tropical continental interiors have a savannah-type vegetation. High altitude regions are covered with a separate biome (cool needleleaf deciduous tree) and there is no presence of any land ice. The considered biomes (see Figure 3.6 caption) are then translated into fractions of the corresponding CLM4 plant functional types (PFTs), for which a set of monthly forcing files is finally used in the land model.

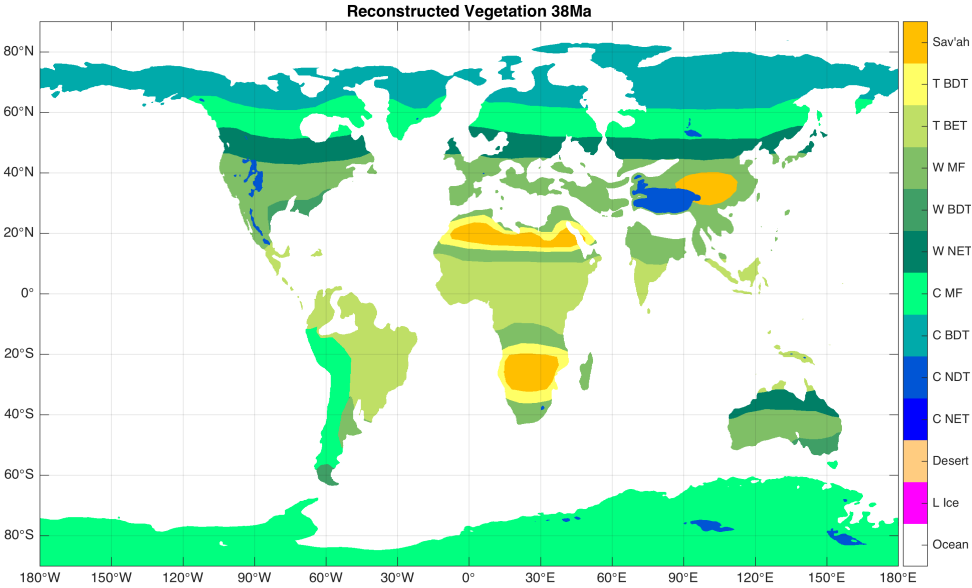


**Figure 3.6:** Middle-to-late Eocene vegetation applied to the 38Ma geography reconstruction (Figure 2.8) to be used in the land model (CLM4). Vegetation types are arranged into the following biomes (top to bottom): savannah, tropical broadleaf deciduous tree, tropical broadleaf evergreen tree, warm mixed forest, warm broadleaf deciduous tree, warm needleleaf evergreen tree, cool mixed forest, cool needleleaf deciduous tree, cool needleleaf evergreen tree, desert and land ice.

**Aerosols:** Despite being an important contribution to the radiative forcing in present and future climate simulations, atmospheric aerosols are tricky to include and therefore often omitted or assumed to be similar to pre-industrial in palaeoclimate model simulations. A big improvement can be made by running a Bulk Aerosol Model (BAM, Heavens et al. 2012) version of the CAM4 to determine a more realistic distribution of aerosols. The sources of naturally formed aerosols (mainly dust, sea salt and organic carbon, excluding volcanic emissions) are adjusted from pre-industrial levels and redistributed based on the new land surface properties. Using these sources the atmospheric component of the model is run for 50 years, at the end of which a monthly climatology of aerosol distributions is derived.

### 3.3.3 Overview of CESM Experiments

In summary, the following series of simulations will be performed using the fully coupled version of the CESM1:

1. Pre-industrial  $1 \times$  PIC reference;
2. 38Ma  $4 \times$  PIC hot middle Eocene;
3. 38Ma  $2 \times$  PIC warm middle-to-late Eocene;
4. 30Ma  $2 \times$  PIC warm late Eocene;
5. 30Ma  $1 \times$  PIC cool late Eocene;
6. 30Ma  $2 \times$  PIC with adjusted surface fresh water flux.

As stated above, the pre-industrial reference simulation mainly serves as a comparison for the other experiments. Instead of taking the results of a pre-existing reference run, the simulation is repeated here using the exact same model configuration (grid, resolution, compiler, machine, etc.) for consistency. General results of the pre-industrial reference simulation can be found in Appendix A.

Two simulations using the 38Ma geography reconstruction are performed and discussed in Chapter 5: a  $2 \times$  PIC middle-to-late Eocene baseline and a  $4 \times$  PIC case to be representative of warmer middle Eocene intervals (e.g. the MECO).

Two more experiments using the 30Ma geography reconstruction are considered in Chapter 7, again including a  $2 \times$  PIC late Eocene simulation. Instead of a PIC doubling, a halving to  $1 \times$  PIC is considered here to cover the full range of possible greenhouse gas levels around the EOT ( $\sim 300$ – $1200$  ppm  $\text{CO}_2$ ; Anagnostou et al. 2016). The 30Ma  $1 \times$  PIC also serves as an additional comparison to the pre-industrial reference, to assess the climatic changes resulting purely from the different geographical boundary conditions (including changes in vegetation and ice cover).

Similar to the standalone POP simulations in Chapter 4 (presented in Section 3.2), a final experiment consists of altering the surface potential density structure of the ocean by modifying the surface fresh water flux in the model. More specifically, a  $-0.5$  Sv (i.e. salt flux) perturbation is applied to the North Pacific north of  $45^\circ\text{N}$  which is compensated by an opposite (integrated)  $+0.5$  Sv flux over the rest of the ocean.



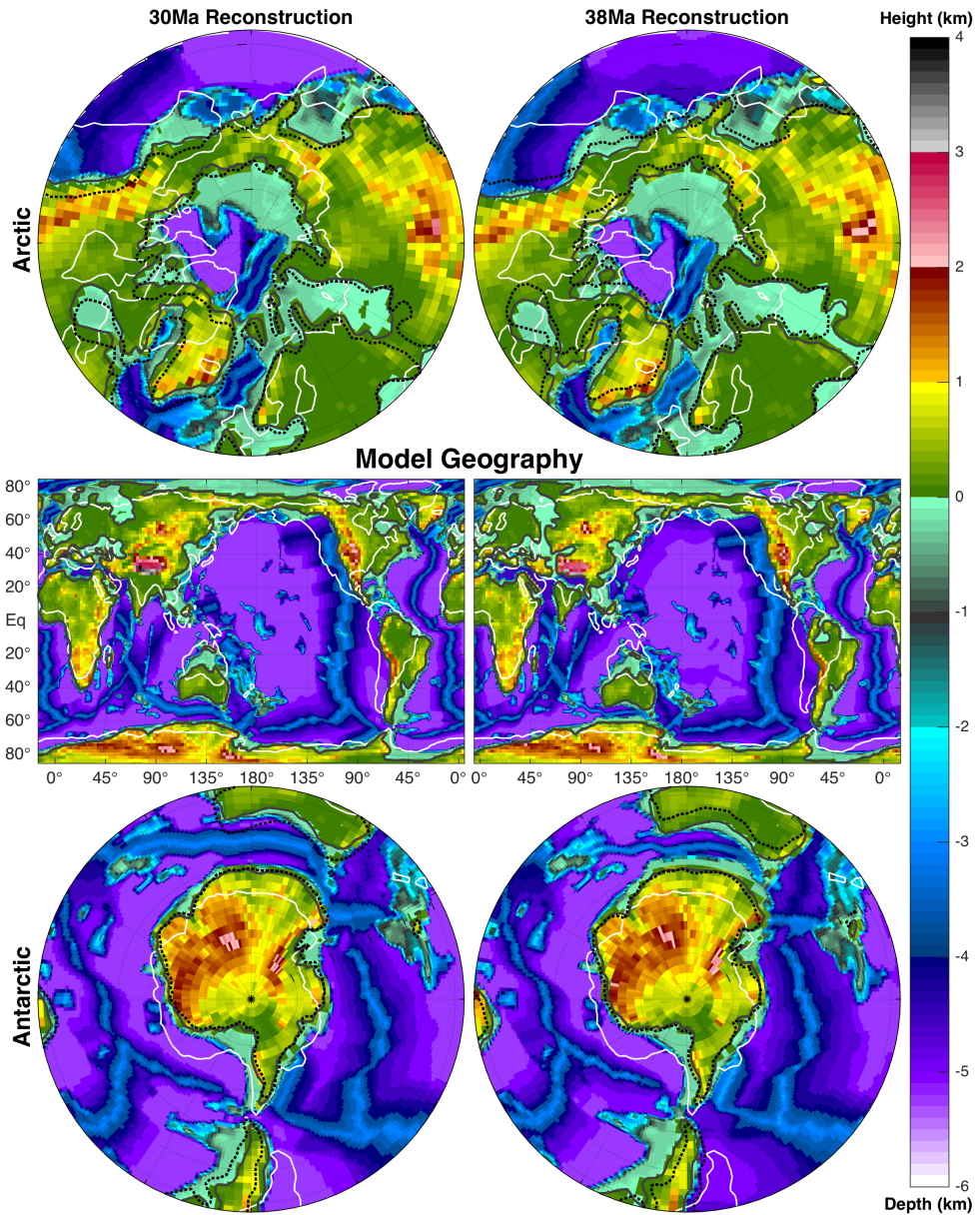


**Figure 3.7:** Similar to Figure 3.4, but showing the topography and bathymetry of both the land and ocean model grid, respectively. Left panels show different projections of the 30Ma geography, while right panels show those of the 38Ma one. Here, coastlines of the opposite reconstruction are again indicated by dark (dotted) contours to highlight the difference with the shaded geography grid (corresponding coastlines in grey). The land-ocean mask of the pre-industrial reference model grid is also shown as a white contour.





# Multiple Equilibria in the Middle-to-late Eocene Ocean Circulation State

---

**Abstract** The Eocene-Oligocene transition (EOT) marks a major step within the Cenozoic climate moving from a greenhouse into an icehouse state, associated with the formation of a continental-scale Antarctic Ice Sheet. The roles of steadily decreasing CO<sub>2</sub> concentrations versus changes in the ocean circulation at the EOT are still debated and the threshold for Antarctic glaciation is obscured by uncertainties in global and regional palaeogeography.

Here, a detailed study of the middle-to-late Eocene ocean circulation is carried out using a standalone ocean general circulation model under two slightly different 38Ma geography reconstructions from Chapter 2. Under the same atmospheric forcing, both geographies give a profoundly different equilibrium ocean circulation state. The underlying reason for this enhanced sensitivity is the presence of multiple equilibria characterised by either North or South Pacific deep water formation. A possible shift from a southern towards a northern overturning circulation would result in significant changes in the global heat distribution. Such changes would consequently make the Southern Hemisphere climate more susceptible for significant cooling and thus possibly ice sheet growth on Antarctica.

Coupled model simulations with the Community Earth System Model (CESM) using the same 38Ma (PaleoMag) geography reconstruction are presented in Chapter 5. A similar study looking into the possibility of multiple equilibria in a coupled model framework is carried out in Chapter 7, using a 30Ma geography reconstruction.

**Acknowledgement** The author would like to thank dr. Matthew Huber for providing the set of fields used for the atmospheric forcing of the ocean-only model and to help interpret the acquired results.

This chapter is based on the following publication:

Baatsen, M. L. J., A. S. von der Heydt, M. A. Kliphuis, J. Viebahn & H. A. Dijkstra (2018a), “Multiple states in the late Eocene ocean circulation”, *Global and Planetary Change*, vol. 163, no. January, 18-28.

“You certainly usually find something, if you look,  
but it is not always quite the something you were after.”

J.R.R. Tolkien

## 4.1 Introduction

The climate during the Cenozoic era (last 65 million years; Ma) has changed dramatically from a warm, mostly ice-free world in the Eocene to the present-day climate with large ice sheets in both polar regions. This long-term transition has not been smooth though: between slow trends of gradual warming or cooling several relatively rapid transitions have occurred, sometimes associated with a change in (quasi-periodic) variability on orbital time scales (Cramer et al., 2009; Zachos et al., 2001).

Often the opening or closing of ocean gateways is used in explanations of the sometimes rather dramatic climatic shifts observed in the proxy record. For example, it has been suggested that the Northern Hemisphere glaciation in the Pliocene resulted from the establishment of the present-day Atlantic Ocean meridional overturning circulation after the closure of the Central American Seaway (Haug & Tiedemann, 1998). Similarly, the closure of the Indian-Atlantic Ocean connection through the Neotethys seaway has been proposed to have had profound impacts on the Miocene climate (Harzhauser et al., 2007).

However, the most widely discussed example of a gateway-related cause for climate change is the establishment of a deep Antarctic Circumpolar Current (ACC) in the late Eocene, due to the opening of the Southern Ocean gateways. The ACC acted to thermally isolate the Antarctic continent such that a large ice sheet could appear at the Eocene-Oligocene boundary (Kennett, 1977).

While all of these hypotheses are being debated for various reasons (e.g. Antarctic glaciation forced by declining CO<sub>2</sub> levels rather than ocean gateways; DeConto & Pollard 2003; Gasson et al. 2014; Ladant et al. 2014), often it is the uncertainty in timing and precise occurrence of the gateway closure/opening that makes a direct causal relationship with a climatic transition problematic.

Uncertainty in palaeobathymetry arises from the complicated structure of plate boundaries and continental fringes meeting each other. Additionally, there are more subtle uncertainties in geographical boundary conditions such as the positioning of plates (and continents) with respect to each other, which is only at the beginning of being quantified (Hinsbergen et al., 2015; Torsvik et al., 2012). Plate-tectonic models rely on a specific frame of reference to determine how the plates are positioned with respect to the Earth’s mantle (Dupont-Nivet et al., 2008). Currently, two such frameworks are used, one referred to as Hot Spot (*HS*; Seton et al. 2012) and the other as PaleoMag (*PM*; Torsvik et al. 2012). Global middle-to-late Eocene reconstructions were made in these two different frames of reference (Chapter 2) for use as boundary conditions for ocean-climate models (Figure 4.1). While the bathymetry of gateway regions is exactly the same in both versions, the rotation of the poles in the PM framework results in continents being shifted or rotated by as much as 5–6 degrees with respect to the HS one.

As more and more time slices of palaeogeography become available and are being used for ocean and climate model studies (Haywood et al., 2011; Herold et al., 2014; Heydt & Dijkstra, 2006; Lunt et al., 2016), it is important to determine how the modelled global ocean circulation is dependent on the chosen boundary conditions. In this chapter, the sensitivity of the ocean circulation to relatively moderate changes in continental geometry is studied using a global ocean-only model for the middle-to-late Eocene. An unexpected sensitivity is found of the global ocean flow to palaeobathymetry that can be explained by the occurrence of multiple equilibria.

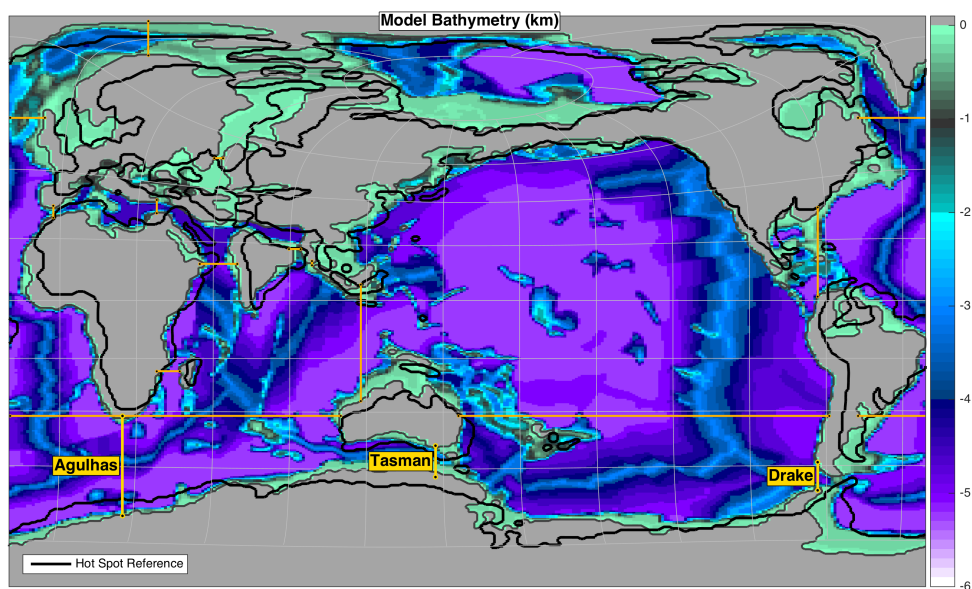


**Figure 4.1:** Global bathymetry grid in curvilinear projection as used by the model; black shading shows the land mask and colours indicate depth. The model grid is based on a PaleoMag (PM) referenced 38Ma reconstruction, while the black contour line indicates the shorelines using a Hot Spot (HS) framework. A rectangular projection grid is added in grey, featuring 30° intervals in longitude and 20° in latitude. Thick yellow lines denote the positions of three Southern Ocean transects with their respective names, which will be used in the text below.

## 4.2 Model Spin-up

Three different POP model simulations are carried out as listed in Section 3.2; the first using a PaleoMag geography (referred to as *PM*), the second using a Hot Spot geography (*HS*). A third and last simulation starts from the PaleoMag configuration but using adjusted surface fresh water fluxes (*PM Adjusted*). The *PM Adjusted* case serves to test the stability of the overturning regime by perturbing the system for a limited amount of time. This is achieved by adding 1 Sv of integrated fresh water flux to the South Pacific and doing the opposite in the North Pacific Ocean (blue and red boxes in Figure 3.3a, respectively).

The oceanic state is initialised for both the PM and HS cases as being motionless and having a horizontally homogeneous temperature distribution, decreasing linearly (as a function of model levels) from 15°C at the upper level down to 9°C at the bottom. Model simulations span 3200 and 2500 years towards an equilibrium state for the PM and HS cases, respectively. In the PM Adjusted case the initial state is that of the PM case at model year 3000, after which the adjusted forcing is applied for 200 years. The model is then run for another 800 years with the unperturbed forcing (i.e. identical to that of the PM case) resulting in a total of 1000 model years.

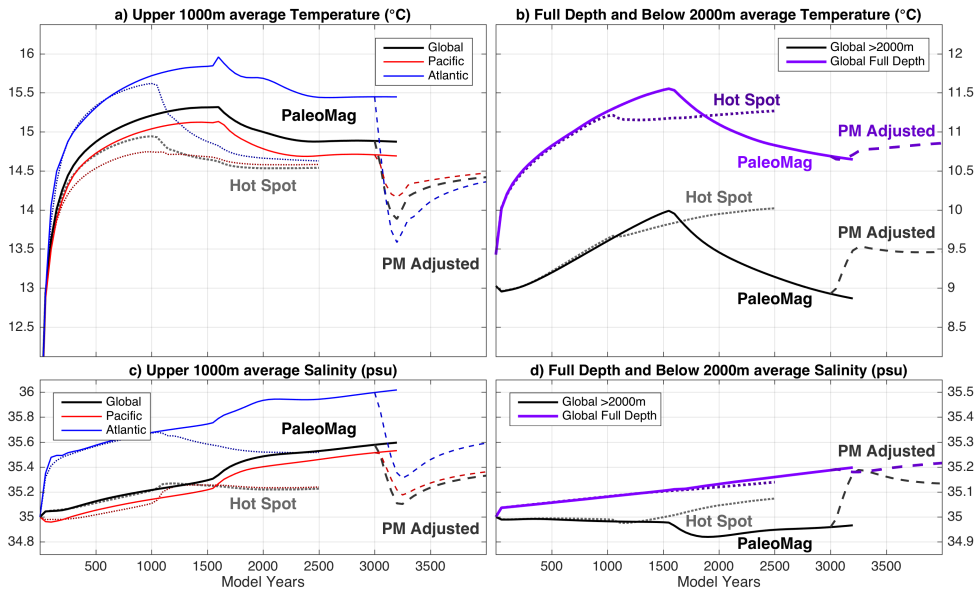


**Figure 4.2:** Time series of average temperature for **a)** upper 1000m and **b)** full depth (purple) and below 2000m (black). Upper 1000m averages are separated in global (black), Pacific-only (red) and Atlantic-only (blue) means, showing the entire spin-up of the PaleoMag (solid), Hot Spot (dotted) and adjusted PaleoMag (PM Adjusted; dashed) simulations. **c)** and **d)** as in **a)** and **b)** but for time series of average salinity.

Trends of (Global, Pacific and Atlantic) volume-weighted average temperature and salinity are shown in Figure 4.2 for the upper 1000m, below 2000m and full depth. Upper 1000m temperatures equilibrate well and show little to no change in the last 500 years of each simulation (250 for PM Adjusted). Deep ocean temperatures take longer to settle, especially in the PM case which thus requires a longer spin-up time. An overview of the drifts in temperature and salinity at the end of all three simulations is given in Table 4.1. Drifts in global mean temperature are generally in the order of 1K per  $10^4$  years over the last 200 model years. Globally averaged salinity continues to show a minor drift of a few psu per  $10^5$  years and is rather steady throughout the spin-up. Some manual adjustments of the model grid result in a small net surface fresh water flux that can explain a 0.1–0.2 psu increase in global mean salinity that is seen throughout the model runs, without being problematic.

Property \ Case	PM	HS	PM Adjusted
<b>Geography</b>	38Ma Paleomag	38Ma Hot Spot	38Ma Paleomag
<b>Spin-up (years)</b>	3200	2500	200+800
<b>Forcing</b>	CCSM3 <sub>PM</sub>	CCSM3 <sub>HS</sub>	CCSM3 <sub>PM,SFWF</sub>
$\Delta T$ (K/year)	$-2.2 \cdot 10^{-4}$	$8.8 \cdot 10^{-5}$	$1.1 \cdot 10^{-4}$
$\Delta S$ (psu/year)	$5.2 \cdot 10^{-5}$	$4.0 \cdot 10^{-5}$	$2.8 \cdot 10^{-5}$
$\Delta T/T$ (1/year)	$-7.7 \cdot 10^{-7}$	$3.1 \cdot 10^{-7}$	$3.8 \cdot 10^{-7}$
$\Delta S/S$ (1/year)	$1.5 \cdot 10^{-6}$	$1.1 \cdot 10^{-6}$	$8.1 \cdot 10^{-7}$

**Table 4.1:** Overview of all three POP spin-up simulations with their boundary conditions, spin-up time and drifts in global mean temperature  $\Delta T$  and salinity  $\Delta S$  over the last 200 model years. Forcing subscripts denote adjustment to geography and *SFWF* indicates changed surface fresh water flux. Normalised drifts  $\Delta T/T$  and  $\Delta S/S$ , with  $T$  temperature in Kelvin and  $S$  salinity in psu, are also shown for each case using the same period.

To monitor the development of the flow in each of the simulations, several indicators are used as described here. Three meridional transects are considered from west to east, referred to as Agulhas, Tasman and Drake (as shown in Figure 4.1) connecting Africa, Australia and South America to Antarctica, respectively. The volume transport (in Sv) through these three transects is displayed in Figure 4.3a for the different cases. The transient behaviour shows the importance of a long model spin-up (beyond 2000 years) as there are still substantial changes around model year 1500 (PM) and 1000 (HS).

The abrupt changes in volume transports can be linked to an invigoration of the meridional overturning circulation (MOC), shown in Figure 4.3b. Time series of global MOC strength are shown for both hemispheres, where black indicates the maximum value of the northern overturning cell while red does so for the (minimum of the) southern cell.

The effects of enhanced overturning are also visible in the globally averaged temperature and salinity in Figure 4.2. Temperatures below 2000m for the PM case are seen to increase initially due to thermal diffusion of surface warmth, after which more efficient ventilation cools down the deep ocean again. A steady warming of oceanic bottom waters acts to reduce thermal stratification in the initial phases of spin-up ( $\sim 1500$  years). At that point the stratification becomes sufficiently small to allow the transition towards a flow regime with significantly stronger meridional overturning cells. This results in a general cooling which is most pronounced in the deep ocean, as the ocean readjusts towards a new balance with the imposed surface restoring fluxes. The same processes cause a slight increase in global mean surface salinity, compensated by a reduction in the deep ocean. A similar transition towards a regime with more vigorous meridional overturning can be seen at around model year 1000 for the HS case, but with less impact on bottom water temperatures.

## 4.3 Results

### 4.3.1 Geometry-dependent Flow Patterns

Despite subtle discrepancies between the Hot Spot and PaleoMag geometries, they result in profoundly different (equilibrium) flow regimes (comparing dotted: HS to solid: PM curves in Figure 4.3). The resulting flow pattern averaged over the last 50 years of simulation for both cases is discussed below. In the PM case, relatively large zonal transports through Southern Ocean transects are associated with a deep Southern Ocean sourced meridional overturning circulation. The opposite is seen for the HS simulations, where Southern Ocean zonal transports and the southern overturning circulation are both relatively weak, while the northern overturning cell is of similar strength to the southern one in the PM case.

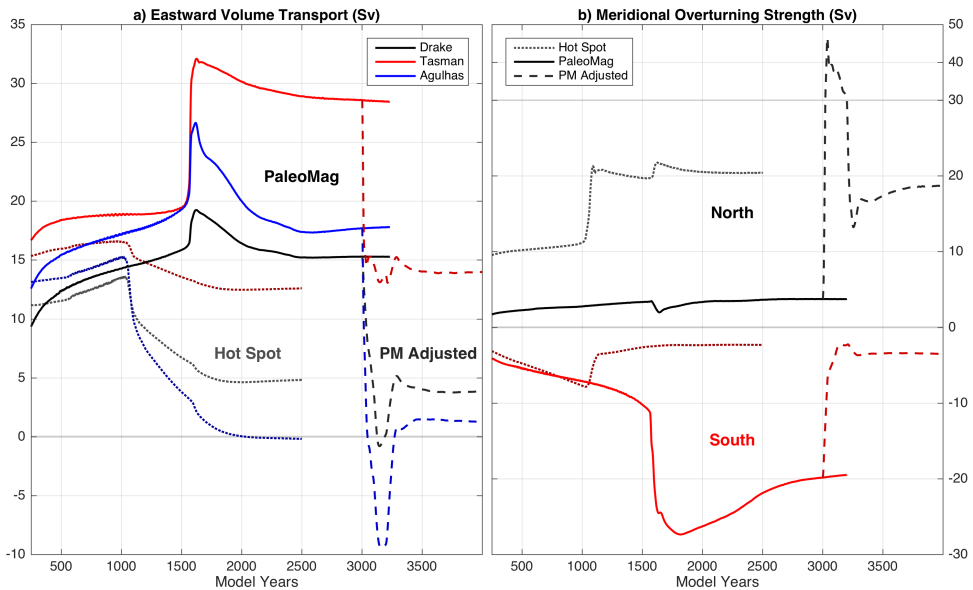


**Figure 4.3:** **a)** Integrated volume transport through the Agulhas transect (blue), Tasmanian Gateway (red) and Drake Passage (black). Yearly averaged values are shown for all three simulations starting at model year 250: PM (solid), HS (dotted) and PM Adjusted (dashed). **b)** As in **a)** for the maximum global meridional overturning strength in the Northern (black) and Southern (red) Hemisphere.

The equilibrium state sea surface temperature (SST), sea surface salinity (SSS), barotropic stream function (BSF) and sea surface height (SSH) for the PM simulation are shown in Figure 4.4a,c. The main feature of the global circulation is an expansive Indo-Pacific sub-tropical gyre system spanning 3/4 of low latitude regions. The associated warm pool with annual mean SSTs reaching up to 34°C, covers most of the Indian Ocean and is accompanied by an extended cold tongue to its east in the equatorial East Pacific. The sub-polar regions are mild at mostly 10–20 °C and reflect a climate with high greenhouse gas concentrations and a reduced equator to pole temperature gradient.

Because of its relatively isolated configuration, the Arctic is significantly colder than the Southern Ocean. However, temperatures hardly drop below freezing and sea ice only occurs sporadically and very locally.

The SSH pattern denotes pronounced gyre circulations across most of the high latitudes (beyond  $45^\circ\text{N/S}$ ) and a strong zonal current at the wind stress maximum around  $45^\circ\text{S}$ . SSH fields further suggest the presence of at least a shallow circum-polar flow in the Southern Hemisphere, despite the Southern Ocean passages being strongly limited in depth and width. As shown in Figure 4.3a, the volume transport through the Drake Passage is only about 15 Sv in the PM case and 5 Sv in the HS one.

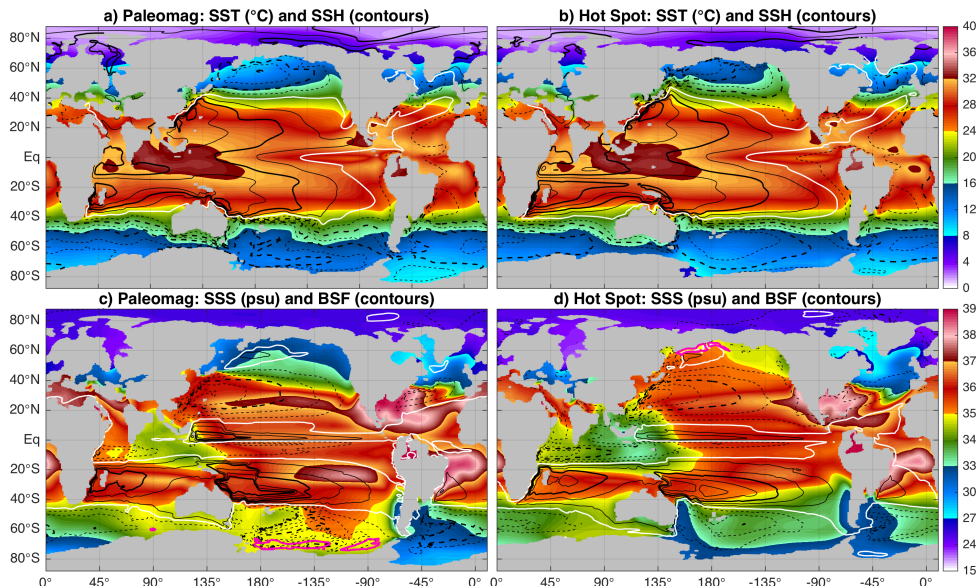


**Figure 4.4:** Annual mean sea surface temperatures (SST; shading) and sea surface height (SSH; contours every 15 cm; solid: positive, dashed: negative, white line at 0) for **a)** the PM and **b)** the HS case. PM Sea surface salinity (SSS; shading) and barotropic stream function (BSF; contours every 10 Sv; solid: positive, dashed: negative, white line at 0) for **c)** PM and **d)** HS, respectively. Thick pink lines highlight deep water formation sites by showing the 500m mixed layer depth contour.

The equilibrium state for the HS case (Figure 4.4b,d) shows warmer and more saline North Pacific high latitude regions compared to the PM case, while the opposite holds for the South Pacific Ocean. Apart from the Tasmanian Gateway, volume transport through the Southern Ocean passages drops to very low values indicative of a circulation dominated by gyres in the Southern Hemisphere. The differences between PM and HS cases thus mostly result from reversed MOC patterns. Where the HS configuration exhibits Northern, the PM geography favours Southern Hemispheric deep water formation. Patterns of mixed layer depth and basin-specific overturning stream functions (not shown) indeed confirm that the deep water formation occurs exclusively in the South Pacific versus North Pacific Ocean for the PM and HS case, respectively.



### 4.3.2 Multiple Equilibria within the PaleoMag Geography

Recalling that both PM and HS simulations use essentially the same atmospheric forcing conditions, the above results suggest a strong dependence of the circulation pattern on model geography. To investigate the occurrence of multiple equilibria regarding the meridional overturning state, an additional simulation is carried out using a density perturbation (PM Adjusted). Starting from the oceanic state of the PM simulation at model year 3000, a negative freshwater flux (-1 Sv) is added to the sub-polar North Pacific. Similarly, a +1 Sv forcing is applied to the sub-polar South Pacific region as shown above in Figure 3.3a. The total flux of 1 Sv is divided over a  $30^\circ \times 90^\circ$  area and results in an anomalous forcing of  $\sim 0.5 \cdot 10^{-7} \text{ m/s}$ , which lies in the same order of magnitude as the unperturbed fresh water fluxes.

To let the circulation adjust to these density perturbations, anomalous freshwater fluxes are applied for 200 model years. Afterwards, the simulation is continued under the original forcing for another 800 years to reach equilibrium again (see dashed lines in Figure 4.2). This makes the third simulation spin-up significantly shorter compared to those of the PM and HS case, but it did not start from a motionless state with a generalised temperature and salt distribution. Model drifts after 1000 years for the PM Adjusted case shown in Table 4.1 are of the same order as those seen in the other simulations. Additionally, the density perturbation drives an enhanced meridional overturning circulation for 200 years which effectively mixes the deep ocean more quickly and speeds up the equilibration.

Indicators of the transient flow are again shown in Figure 4.3, with the dashed curves representing the PM Adjusted case. The applied density perturbation quickly inverts the meridional overturning circulation (Figure 4.3b). After an overshoot (caused by the altered forcing), Southern Ocean gateway transports settle to values similar to those seen in the HS case (with North Pacific deep water formation). In the PM Adjusted equilibrium state, the maximum of the meridional overturning stream function (dashed curves in Figure 4.3b) clearly demonstrates the dominant northern sinking.

The results of the PM Adjusted simulation thus effectively show that different overturning states can be realised in the ocean model using a PaleoMag referenced geography under the same atmospheric forcing. A relatively large flow through the Tasmanian Gateway in the PM case compared to PM Adjusted (and HS) one suggests that this gateway transport is not correlated with a deep circumpolar flow. Other Southern Ocean passages never show such large flows and thus the difference can best be explained by geostrophic adjustment to an enhanced meridional density gradient when the southern overturning cell is active. Deep water formation and the associated salt advection feedback act to increase the density at high latitudes and thus the meridional gradient.

For clarity, the different equilibrium states found within the PaleoMag geography will be referred to as *SHS* (southern hemisphere sinking; PM) and *NHS* (northern hemisphere sinking; PM Adjusted) onwards, reflecting their crucial difference in overturning state.

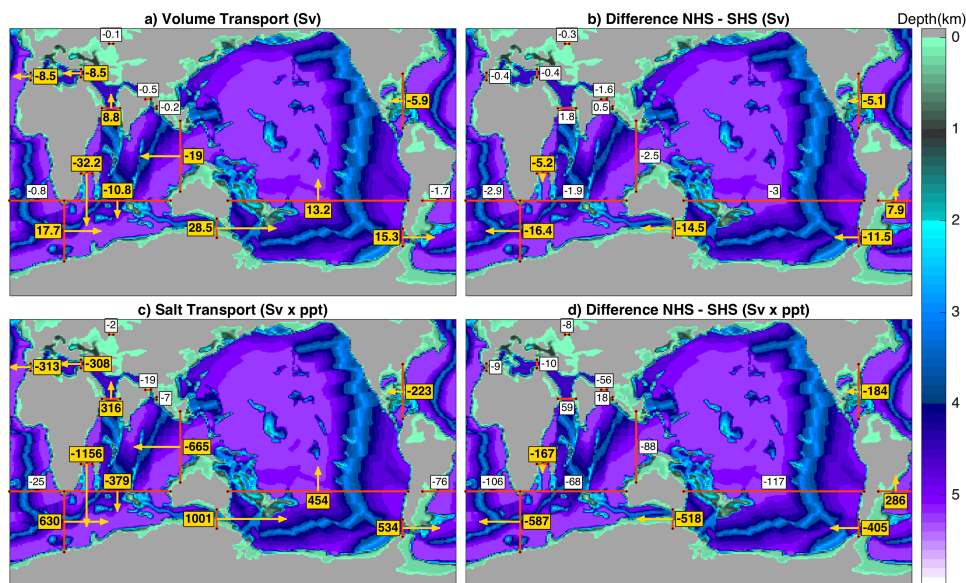


**Figure 4.5:** a) Volume transports for the SHS equilibrium state. b) Difference fields (NHS - SHS state) of the volume transports. c) and d) same as a) and b) but for the total salt flux. Boxes and arrows show the magnitude and direction of the largest and most important fluxes and flux differences, with gold coloured ones highlighting the largest and most important values. Transports are perpendicular to the transects, where positive values denote either northward or eastward flows. Background shading indicates model grid depth and red lines show the transects at which transports are calculated.

A more detailed view on the SHS state and the differences (NHS - SHS) between both states considering total volume and salt transports (shown in Figure 4.5) reveals that transport values in the Southern Ocean are generally small compared to those seen at present-day. For comparison, 150–200 Sv of volume transport is seen through the Southern Ocean gateways in the CESM pre-industrial reference simulation (Appendix A; Figure A.1). This corresponds to an oceanic state dominated by gyre circulations in which flows through gateways are either small, or being compensated for within larger transects. A circumpolar current of 15–20 Sv is present in the Southern Ocean, limited mostly by the Drake Passage (because of its high southerly latitude). The largest transport is seen in the Mozambique channel, characterising the western intensification of the South Indian sub-tropical gyre and the origin of the Agulhas Current. In addition, there seems to be a net 10–15 Sv anticyclonic flow around Australia in response to the the South Pacific meridional density gradient. Finally, a 5–10 Sv global westward current is present in the tropics, allowed by the NeoTethyan passages and those through Central America.

Salt fluxes show a similar picture, closely related to the main currents. What stands out is the large amount of salt transported eastward through the Tasmanian Gateway. A net southward flux in the South Indian Ocean injects additional salt eastward into the South Pacific sub-polar gyre, helping to increase the density and thus the

deep water formation. Since the Tasmanian Gateway is at a higher latitude in the HS reconstruction it is significantly harder to force high salinity water through this gateway, and into the sub-polar South Pacific. As a result, enhanced salt transport seems to be the reason why the PM configuration favours Southern Hemispheric sinking, while the HS one does not. When the overturning circulation is reversed (NHS state), Southern Ocean transports dramatically decrease and a circumpolar current ceases to exist. Westward flow through Central America is now enhanced as a result of a stronger gyre circulation in the North Pacific Ocean.

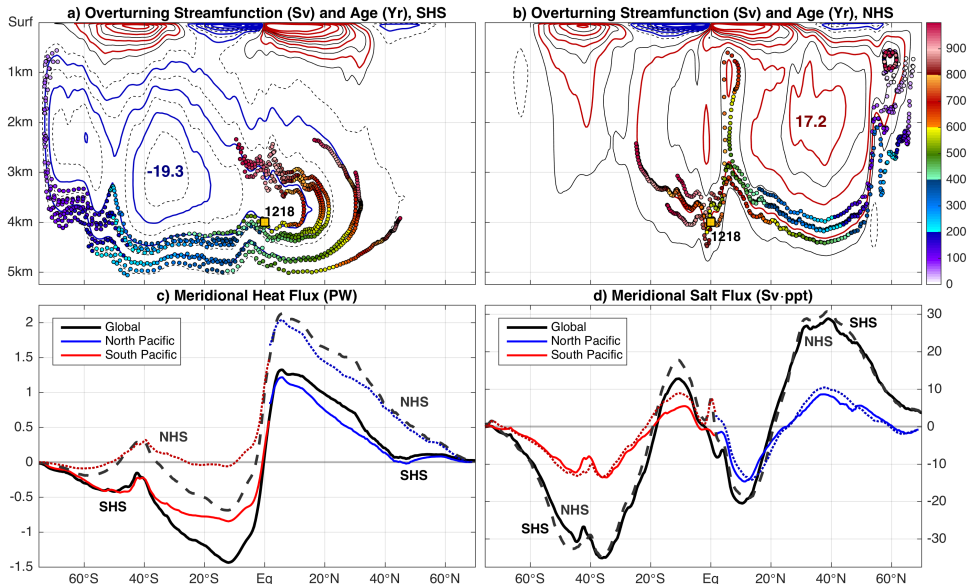


**Figure 4.6:** Global meridional overturning stream function for the a) SHS (PM) and b) NHS (PM Adjusted) state, with contours drawn every 5 Sv (red: positive, blue: negative, thin lines every 2.5 Sv) and numbers indicating maximum values. Coloured dots show different parcel tracks and estimated age (colour axis to the right; in years), and the yellow square denotes the palaeo-location of ODP site 1218. c) Global meridional heat transport in the SHS (solid) and NHS (dashed) state, of which coloured lines show the contribution of the North (blue) and South (red) Pacific Ocean. d) As in c), but for meridional salt transports.

Patterns of the different equilibrium global MOC states (SHS and NHS) are presented in Figure 4.6a-b, clearly showing the different sinking regimes. In addition to the meridional overturning stream function, trajectories are calculated for several parcels starting (for each case) in the areas of deep water formation and assuming that they follow the zonally integrated flow (also in Figure 4.6a-b). This assumption is based on the observation that no deep sinking occurs outside of the Pacific Ocean. While both overturning cells are similar in extent and strength (apart from being mirrored), the NHS one appears to be shallower (related to differences in bathymetry and density between source regions). Weaker flow below 2km depth results in water parcels taking almost twice as long (600–800 years in NHS instead of ~400 years for SHS) to reach the equator at a depth of 4km.

These estimated age tracers are purely indicative, but suggest that bottom water masses in the equatorial Pacific can have very different characteristics besides those determined by their source regions. A change towards an older water mass would cause a significant reduction in the solubility of carbonate and thus a decrease in the carbonate compensation depth (CCD). An example of such a sharp reduction in solubility is observed at ODP site 1218 in the Equatorial Pacific (Figure 1.4; Coxall et al. 2005) as a dissolution event right before the first step of the EOT.

Zonally integrated meridional heat transports (Figure 4.6c) show a picture in agreement with a switch between overturning regimes. The NHS state heat transport looks similar to that of the present-day (pre-industrial reference in Appendix A), where the North Pacific takes over the contribution of the North Atlantic Ocean. A maximum northward heat transport of about 2 PW is seen in the northern subtropical gyre. In the SHS state, an overall amount of 0.5–1 PW is redistributed from the Northern towards the Southern Hemisphere. The overturning cell mostly serves to push oceanic heat beyond 45° latitude, significantly warming the high latitude regions where deep sinking occurs. Looking at the contribution of only the Pacific Ocean (red and blue), both the total heat fluxes and differences between overturning states are dominated by this basin.

Zonally integrated meridional salt transports (Figure 4.6d) show a typical pattern where salt is advected away from evaporative regions in the sub-tropical gyres towards both the tropics and higher latitudes. Changes between SHS and NHS states are minimal here and probably limited by fixed surface fresh water fluxes and the implied meridional response in the ocean model. This is different for the meridional heat transport, where mixed (considering both heat fluxes and SSTs) boundary restoring conditions are used.

Temperature and salinity differences (NHS - SHS) between both states are shown in Figure 4.7 at the surface (a), below 2km depth (b) and for a zonally averaged Pacific cross section (c and d). When switching from the SHS towards the NHS state, a general warming and salinisation of North Pacific surface waters occurs at the expense of cooling and freshening in the South Pacific. These changes are more localised and intense in the north, while they are more evenly distributed across the South Pacific sub-polar gyre. Furthermore, the associated density changes are shallower thus having a limited effect on stratification across southern high latitudes. Additionally, the Atlantic and Indian parts of the Southern Ocean become warmer and more saline in response to a ceased proto-circumpolar current.

Vertical cross sections (Figure 4.7c-d) indicate a general warming of the deep ocean, related to changes in the deep water formation source region. A tongue of colder and fresher water in the NHS state finally suggests the presence of a South Pacific intermediate water mass, similar to the one seen in the present-day South Atlantic Ocean. The largest changes in temperature are seen below the surface as an effect of the mixed restoring conditions, including both heat flux and SST fields. This is in contrast to salinity changes that are maximised at the surface, where only fresh water fluxes are considered. The salt advection feedback, stabilising the overturning regime, is thus facilitated by the model surface boundary conditions applied here.

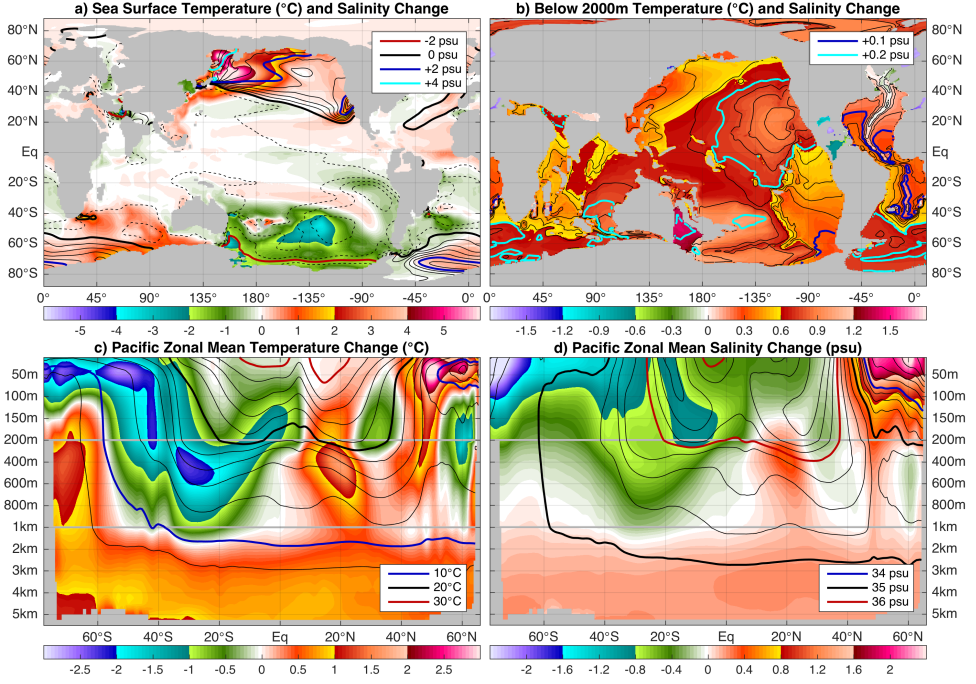


**Figure 4.7:** a) NHS - SHS state sea surface temperature (shading) and salinity change (contours every 0.4 psu). b) Similar to a) for changes below 2000m depth with contours every  $2 \cdot 10^{-2}$  psu. c) Pacific zonal mean temperature change (NHS - SHS) and SHS temperature (contours every 2°C). d) As in c) for salinity change and SHS salinity (contours every 0.25 psu), vertical scaling changes at 200m and 1km depth in c) and d).

A comparison of wind stress curl and barotropic stream function fields of the original CCSM3 simulation (from which the atmospheric forcing was derived) with those of the HS (only NHS) and PM (both SHS and NHS) cases is made in Figure 4.8. POP model results (Figure 4.8b-d) are interpolated onto a  $1^\circ \times 1^\circ$  rectangular grid, and smoothed using a  $3^\circ \times 3^\circ$  mask to be comparable to the CCSM3 fields (Figure 4.8a). Forcing of the wind field is similar in all cases, with only minor shifts and adjustments to the changing continental configuration. As a result, depth averaged flow patterns are also similar and show little change between the HS and PM case when only looking at northern sinking solutions (Figure 4.8 b,d).

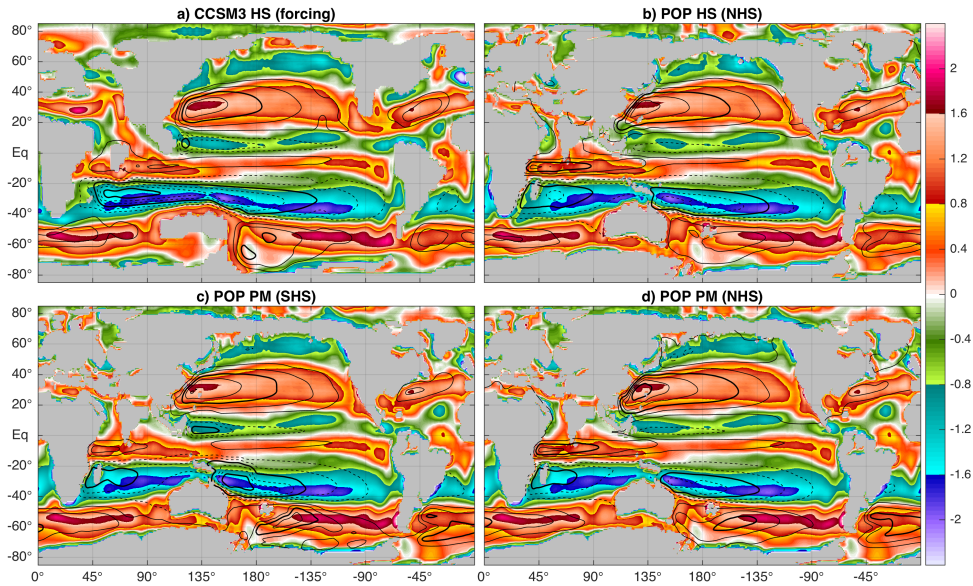


**Figure 4.8:** a) CCSM3 (Eocene forcing) wind stress curl (shading,  $10^{-11}$  Pa/m) and barotropic stream function (contours every 10 Sv, dashed for negative values, thick lines every 30 Sv). b) Similar to a) for the HS case featuring northern sinking (NHS), c) PM SHS and d) PM NHS cases.

More significant changes in gyre strength can be seen in the Indian Ocean, related to the different position of India compared to the one used in the CCSM3 simulation (forcing). Enhanced Southern Ocean zonal flow, stronger South Pacific and weaker North Pacific gyres are present in the SHS state with respect to both NHS cases (HS and PM) and the CCSM3 simulation. Despite featuring a southern sinking state similar to the PM case (Figure 4.8c; SHS), the CCSM3 barotropic stream function resembles that of the HS (Figure 4.8b; NHS) solution more closely. This resemblance is likely due to the combined effect of a better matching model geography (the CCSM3 configuration uses a Hot Spot referenced geography) and the coarser resolution which obscures the effects of bathymetry on the depth-averaged flow (mainly in the South Pacific Ocean).



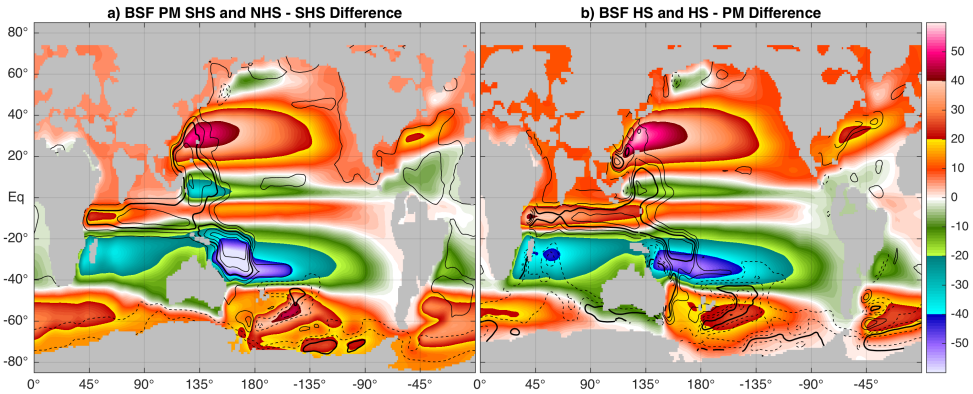


**Figure 4.9:** Barotropic stream function (shading, Sv) and difference (contours every 5Sv, dashed for negative values, thick lines every 15Sv) for **a)** NHS - SHS states and **b)** HS - PM cases. The PM case featuring southern sinking is shown in panel a) while the HS case with northern sinking can be seen in panel b) for reference.

Differences in barotropic stream function between the NHS and SHS states are similar to those between the HS and PM cases (contours in Figure 4.9). Therefore, changes in the flow pattern are dominated by a shift in sinking regime as opposed to the model geography. Some more subtle flow changes related to differences in geography are still present, mainly caused by changes in western boundary currents (e.g. Mozambique Channel and East Australia Current) or the positioning of gateways (e.g. South Atlantic east of the Drake Passage). For this specific case, changes in model geography are thus a significant influence on the preferred overturning state, but otherwise do not change the associated depth-averaged circulation dramatically.

The estimated  $\delta^{18}\text{O}$  signal, based on a simple parameterisation using salinity and temperature (Broecker, 1989), due to a switch from the SHS into the NHS state is shown in Figure 4.10. Changes in the mixed layer reflect straightforward shifts in temperature and salinity in the different overturning states as seen in Figure 4.7. In contrast, a global pattern of decreased  $\delta^{18}\text{O}$  values in the deep ocean is caused by a higher temperature and salinity of the northerly formed deep water mass. This change is seemingly in disagreement with clear increases of benthic oxygen isotope observations across the EOT (Coxall & Wilson, 2011).

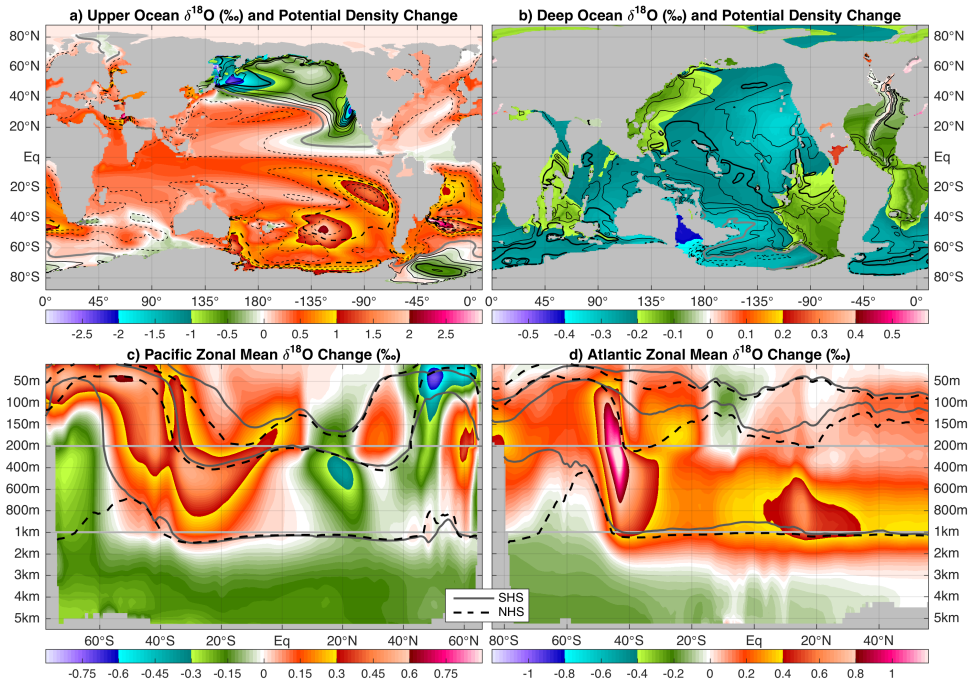


**Figure 4.10:** a) Upper (surface to 200m) and b) deep (below 2km) ocean estimated change in  $\delta^{18}\text{O}$  isotope values for a NHS - SHS state change (contours: change in potential density (surface reference); solid: positive, dashed: negative and grey line at 0; intervals used are a)  $0.25\text{kg/m}^3$  and b)  $10^{-2}\text{kg/m}^3$ , respectively). Zonally averaged c) Pacific and d) Atlantic Ocean cross section of NHS - SHS  $\delta^{18}\text{O}$  change, contours indicate potential density values at 25, 26 and 27  $\text{kg/m}^3$  for the SHS (solid) and NHS (dashed) situation.

However, it is possible that the temperature changes shown by the model are not representative as restoring conditions manipulate the properties of surface waters across the source regions. Even prior to the Eocene-Oligocene transition, a shift from southern towards northern overturning would have resulted in a reorganisation of the circulation pattern. Associated with such a change would be cooling of Antarctica and possibly a response in ice growth, stratification and biological activity. Such an event could thus precondition the climate to ice growth when a certain threshold in radiative forcing is reached, or simply change the threshold itself. Most of the considered changes are taking place across the Pacific Ocean, as its waters are rather weakly stratified across both its northern and southern high latitude regions. The North Atlantic is characterised by weak circulation and ventilation, associated with strong stratification (Figure 4.10d) and low surface salinities (Figure 4.4c-d) resulting from a shallow connection to the relatively fresh Arctic Ocean.



## 4.4 Summary and Discussion

Using a global ocean model with two different palaeobathymetries for the middle-to-late Eocene (38 Ma), the meridional overturning circulation (MOC) is shown to be quite sensitive to details in global geography. In particular, a different choice in reference frame (PaleoMag or Hot Spot) can lead to opposing patterns of the MOC and consequently different sea surface temperature and salinity fields. The underlying reason for this high sensitivity is the existence of two stable equilibria for the 38Ma Eocene configuration under the prescribed forcing, as was demonstrated for the PaleoMag cases (simulations PM and PM Adjusted; SHS and NHS states).

It is often mentioned that multiple equilibria of the meridional overturning circulation (MOC) are an artefact of neglecting the atmospheric feedbacks (and hence would not occur in coupled models), so a discussion is needed here. Indeed, a complete shutdown of the present-day Atlantic MOC has not been found in fully coupled models (Stouffer et al., 2006). However, apart from differences in atmospheric feedbacks between ocean-only and coupled model studies, it is important to distinguish different types of results on multiple equilibria in the relevant modelling literature (mostly for present-day climate studies):

- (i) different statistical equilibria under the same forcing conditions with local differences in deep water formation sites; these equilibria are mostly found only under certain values of parameters (e.g. vertical mixing);
- (ii) different statistical equilibria for the same forcing conditions *and* parameters, showing global changes in observables such as the meridional overturning stream function.

Type (i) multiple equilibria are due to local convective feedbacks, highly sensitive to the surface forcing and basically spurious (Rahmstorf & Willebrand, 1995; Toom et al., 2011). There are very few results with GCMs on type (ii) multiple equilibria (Hawkins et al., 2011) and such equilibria have not definitely been found yet in coupled models (Stouffer et al., 2006).

The reason is not that the multiple equilibria in principle do not exist because of atmospheric feedbacks, but that the computations to systematically find them have not been performed. Moreover, in one present-day climate model (FORTE) the existence of mountain ranges seems to influence surface freshwater flux patterns such that the Atlantic MOC is stabilised (Sinha et al., 2012).

On the other hand, the analysis of the physics of these equilibria points more and more into the direction that such multiple equilibria do exist in the present-day ocean circulation (Liu et al., 2017; Srokosz & Bryden, 2015). For example, an indicator of the MOC induced Atlantic freshwater export is used as an integral measure of the salt-advection feedback in Huisman et al. (2010).

The results presented here show type (ii) equilibria in a global ocean model under 38Ma forcing conditions. This is the first time such multiple equilibria have been found in any global ocean model using a detailed palaeobathymetry for the middle-to-late Eocene. It is indeed in an ocean-only context but this seems a necessary condition for the existence of such equilibria in the modelled climate system. As for the present-day case, these equilibria can still be relevant in the coupled system and may eventually exist in a fully coupled climate model.

The difference in oceanic heat transport between the two equilibria (NHS and SHS states) found here points towards a major redistribution of heat between Northern and Southern Hemisphere and is not unusual in ocean-only model studies (e.g. Viebahn et al., 2016). In coupled models the effect of a MOC switch can be less dramatic in the oceanic heat transport. However, the resulting change in surface temperature is often very similar due to other processes, related to for instance the atmospheric circulation or sea ice feedbacks (England et al., 2017).

The implied  $\delta^{18}\text{O}$  changes, based on a very simplified parameterisation, resulting from a shift from the SHS to the NHS state do not agree with the changes seen at the Eocene-Oligocene transition (EOT). The switch in overturning state could, on the other hand, explain the dissolution event leading up to the EOT at ODP site 1218 (Coxall et al., 2005). Such a switch of the overturning regime would also result in significant changes in heat distribution, a possible cooling of Antarctica and large changes in biological activity. Consequently, the response of the climate system could alter its internal dynamics and sensitivity, for instance through the concept of cascading tipping points proposed by Dekker et al. (2018).

Hence, this mechanism does not directly support the idea that a switch in the ocean circulation from a SHS to a NHS state can explain a first step of the EOT as suggested by Tigchelaar et al. (2011). Nevertheless, such a switch in overturning regime, induced by the changing continental configuration, could have been a precursor event that made the climate more susceptible to Antarctic glaciation.

To conclude, multiple equilibria of the meridional overturning circulation may have existed in the middle-to-late Eocene, but also during other periods throughout the Cenozoic. As a result, long term shifts between different overturning regimes may constitute an important contributor to changes in global climate, biology and variability in the Cenozoic era and require further study.

# CESM Simulations of the Middle-to-late Eocene Climate

---

**Abstract** While the early Eocene has been considered in many modelling studies, detailed simulations of the middle and late Eocene climate are currently scarce. To get a better understanding of both Antarctic glaciation at the Eocene-Oligocene transition ( $\sim 34$ Ma) and late middle Eocene warmth, it is vital to have an adequate reconstruction of the middle-to-late Eocene climate. A set of high resolution coupled climate simulations is represented in this chapter using the Community Earth System Model (CESM) version 1. Two middle-to-late Eocene cases are considered with the same general boundary conditions but a different radiative forcing (described in Chapter 3). Both model simulations use a new detailed 38Ma geography reconstruction presented in Chapter 2, which was also used for the uncoupled simulations in Chapter 4.

Under  $4\times$  pre-industrial concentrations (PIC) of both  $\text{CO}_2$  (i.e. 1120ppm) and  $\text{CH}_4$  ( $\sim 2700$ ppb), equilibrium sea surface temperatures correspond well to the available late middle Eocene (42–38 Ma;  $\sim$ Bartonian) proxies. Being generally cooler, the simulated climate under  $2\times$  PIC forcing is a good analog for that of the late Eocene (38–34 Ma;  $\sim$ Priabonian).

Deep water formation occurs in the South Pacific Ocean, while the North Atlantic is strongly stratified and virtually stagnant. A shallow and weak circumpolar current is present in the Southern Ocean with only minor effects on southward oceanic heat transport within wind-driven gyres. Terrestrial temperature proxies, although limited in coverage, also indicate that the results presented here are realistic.

The reconstructed 38Ma climate has a reduced equator-to-pole temperature gradient and a more symmetric meridional heat distribution compared to the pre-industrial reference. Climate sensitivity is similar ( $\sim 0.7$  °C/Wm<sup>2</sup>) to that of the present-day climate ( $\sim 0.8$  °C/Wm<sup>2</sup>;  $\sim 3$ °C per CO<sub>2</sub> doubling), with significant polar amplification (between  $2\times$  PIC and  $4\times$  PIC) despite very limited sea ice and snow cover. High latitudes are mainly kept warm by albedo and cloud feedbacks in combination with global changes in geography and the absence of polar ice sheets.

The integrated effect of geography, vegetation and ice accounts for a 6–7 °C offset between pre-industrial and 38Ma Eocene boundary conditions. These 38Ma simulations effectively show that a realistic middle-to-late Eocene climate can be reconstructed without the need for greenhouse gas concentrations much higher than proxy estimates (i.e.  $>4\times$  PIC). The general circulation and radiative budget sustain mild high-latitude regions with limited snow and ice cover, without making equatorial regions extremely warm.

After the general model results presented here, Chapter 6 will zoom in on the regional climate of Antarctica within the 38Ma CESM simulations. Similar model experiments using a 30Ma rather than a 38Ma geography reconstruction will then be considered in Chapter 7, followed by an overview of all six CESM simulations (introduced in Chapter 3) given in Chapter 8.

**Acknowledgement** The author would like to thank dr. Appy Sluijs, dr. Peter K. Bijl and Margot J. Cramwinckel for helping to acquire and interpret the considered SST proxies. Also the important contribution of dr. Matthew Huber is acknowledged, providing the basis for both the land temperature proxy and model data comparison for the middle-to-late Eocene.

This chapter is based on the following publication:

Baatsen, M. L. J., A. S. von der Heydt, M. Huber, M. A. Kliphuis, P. K. Bijl, A. Sluijs, et al. (2018b), “Equilibrium state and sensitivity of the simulated middle-to-late Eocene climate”, *Climate of the Past Discussions*, no. April, 1-49.

“Well, I am going back into the open air,  
to see what the wind and sky are doing!”

J.R.R. Tolkien

## 5.1 Simulations and Spin-up

For this study, version 1.0.5 of the CESM (Gent et al., 2011) is used with the 38Ma (PaleoMag) geography reconstruction from Chapter 2. The 38Ma simulations are run with  $2\times$  and  $4\times$  pre-industrial levels (280ppm; 671ppb) of both  $\text{CO}_2$  and  $\text{CH}_4$ , referred to as  $2\times$  and  $4\times$  PIC. Using the estimated radiative forcing from Etminan et al. (2016), these simulations are comparable to  $2.15\times$  ( $\sim 600\text{ppm}$ ) and  $4.69\times$  ( $\sim 1300\text{ppm}$ ) pre-industrial  $\text{CO}_2$ -equivalent for  $2\times$  PIC and  $4\times$  PIC, respectively. For reference, a pre-industrial simulation is performed using the same model version with  $1\times$  PIC and present-day boundary conditions regarding geography and vegetation. A short overview of the main characteristics of each simulation is given in Table 5.1. A more elaborate description of the model specifications and configurations used can be found in Chapter 3.

Property \ Case	Pre-industrial	38Ma $2\times$ PIC	38Ma $4\times$ PIC
Geography	Present-day	38Ma PaleoMag (Chapter 2)	
Vegetation	Present-day	38Ma Eocene; fixed	
Aerosols	Pre-industrial	from 50-year BAM run	
$\text{CO}_2$ (ppm)	280	560	1120
$\text{CH}_4$ (ppb)	671	1342	2684
Spin-up (years)	3000	3000	4000

**Table 5.1:** Overview of characteristics for the different CESM 1.0.5 simulations that were performed (BAM: bulk aerosol model), see Chapter 3 for further details (Section 3.3).

Both 38Ma model simulations start from the same initial conditions as those used for the ocean-only simulations in Chapter 4: a stagnant ocean with a horizontally homogeneous temperature distribution. The initial oceanic temperature distribution decreases linearly (as a function of model levels) with depth, from  $15^\circ\text{C}$  at the surface to  $9^\circ\text{C}$  at the bottom. The pre-industrial reference is initialised using present-day temperature and salinity fields from the PHC2 dataset (Steele et al., 2001).

A long spin-up (see Table 5.1) is performed to allow the deep ocean to equilibrate sufficiently. An overview of absolute ( $\Delta T$ ,  $\Delta S$ ) and normalised ( $\Delta T/T$ ,  $\Delta S/S$ ) temperature and salinity drifts over the last 200 model years of each case is given in Table 5.2. Drifts are generally  $\sim 10^{-4}$  K/year for global mean, volume-weighted average oceanic temperature and comparable to those seen for the simulations in Chapter 4. Similarly for globally averaged salinity, drifts at the end of the spin-up are  $\sim 10^{-6}$  psu/year which is significantly lower than those in the standalone POP due to a better conservation of the total salt budget.

Measure \ Case	Pre-industrial	38Ma 2× PIC	38Ma 4× PIC
$\Delta T$ (K/year)	$-1.2 \cdot 10^{-4}$	$5.7 \cdot 10^{-5}$	$2.6 \cdot 10^{-4}$
$\Delta S$ (psu/year)	$1.9 \cdot 10^{-6}$	$1.7 \cdot 10^{-7}$	$-1.0 \cdot 10^{-6}$
$\Delta T/T$ (1/year)	$-4.3 \cdot 10^{-7}$	$2.0 \cdot 10^{-7}$	$9.1 \cdot 10^{-7}$
$\Delta S/S$ (1/year)	$5.4 \cdot 10^{-8}$	$4.9 \cdot 10^{-9}$	$-3.0 \cdot 10^{-8}$

**Table 5.2:** Overview of drifts in global mean oceanic temperature ( $\Delta T$ ) and salinity ( $\Delta S$ ) over the last 200 model years for all three CESM spin-up simulations. Normalised drifts  $\Delta T/T$  and  $\Delta S/S$ , with  $T$  temperature in Kelvin and  $S$  salinity in psu, are also shown for each case using the same model period.

Time series of the horizontally averaged upper (<1000m), deep (>2000m) and full depth oceanic temperatures are shown for the spin-up of both 38Ma and the pre-industrial cases in Figure 5.1a-b. Starting from present-day initial conditions, the pre-industrial simulation cools down by about 0.5°C globally. The average temperature is also shown for the Pacific and Atlantic basins separately, indicating generally smaller contrasts in the deep ocean compared to the pre-industrial reference.

The (38Ma) 2× PIC simulation appears to equilibrate much faster than the 4× PIC one, probably because the deep ocean equilibrium temperature is close to that of the initial state (i.e. 9°C). With higher greenhouse gas concentrations, the ocean experiences additional heating at the surface, causing it to become more strongly stratified which consequently reduces vertical mixing into the deep ocean.

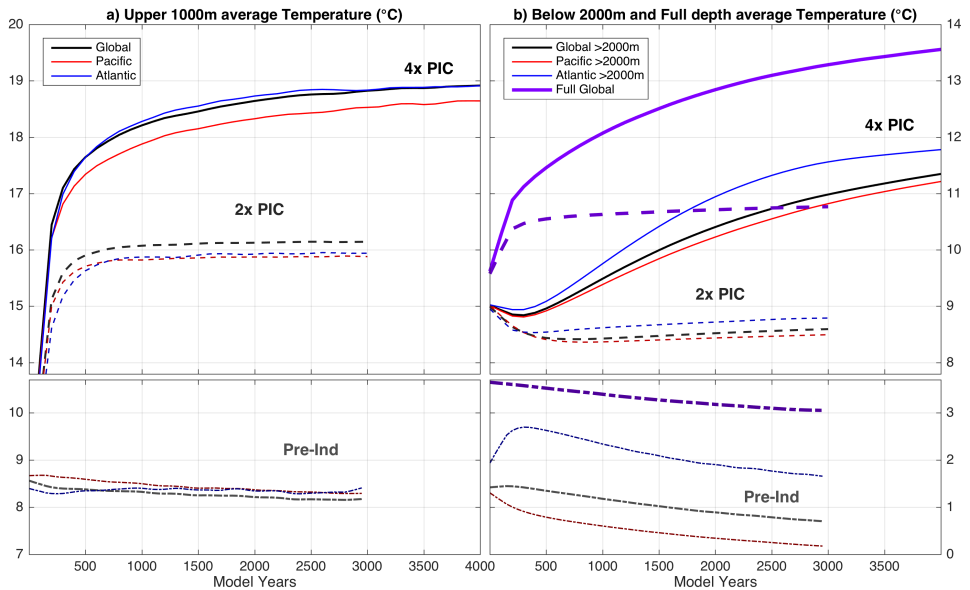


**Figure 5.1:** Time series of a) upper 1000m and b) below 2000m volume-weighted average temperature for pre-industrial (dotted), 38Ma 2× (dashed) and 4× (solid) PIC spin-up simulations. Averages are shown globally (black) and for both the Pacific (red) and Atlantic (blue) ocean basins separately. Full depth global average temperature is also shown for each run using thick purple lines.

Reduced mixing in the  $4\times$  PIC case causes the global mean deep ocean temperature to still increase by about  $0.1^\circ\text{C}$  over the last 500 model years. As expected, changes in the upper 1000m temperatures settle more quickly and are small ( $\sim 0.1^\circ\text{C}$ ) over the last 2000 model years of each simulation.

In addition, global patterns of ideal age tracers (a measure for oceanic ventilation timescales; England 1995; Thiele & Sarmiento 1990) are observed to equilibrate over the last 1000 years of each simulation (Figure 5.2) as well as meridional overturning strength and gateway transports (shown further down in Figure 5.6 of Section 5.2.1). Average values of ideal age still have considerable trends because of further ageing in stagnant deep ocean regions (Figure 5.2a) and upwelling of older water masses into the upper ocean (Figure 5.2b). Such changes will likely continue for many thousands of years, but the associated circulation pattern has equilibrated at the end of each simulation.

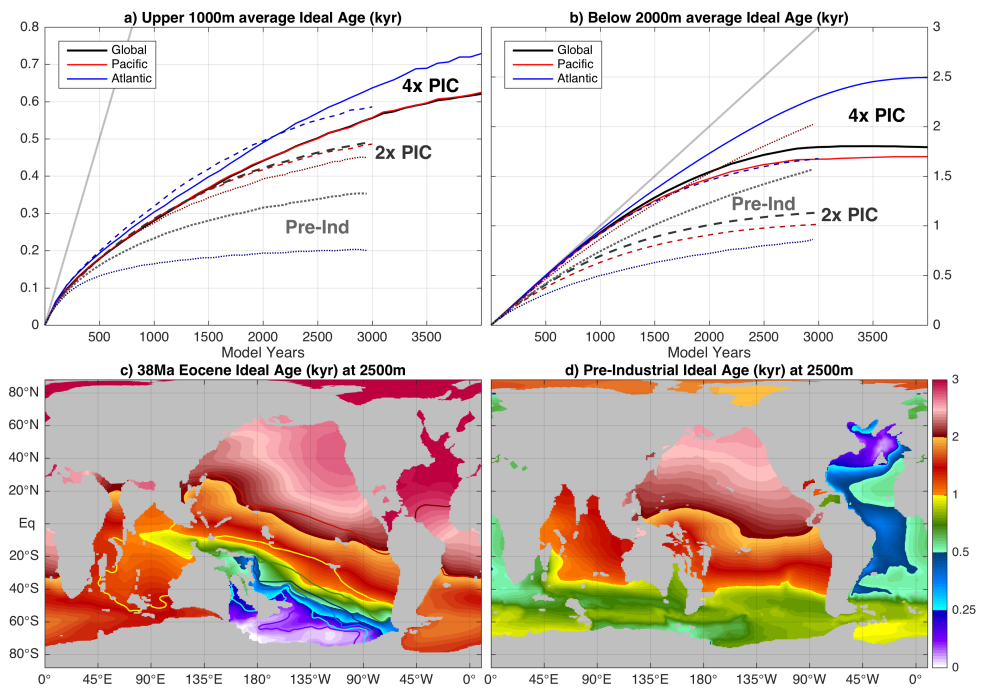


**Figure 5.2:** Time series of **a)** upper 1000m and **b)** below 2000m volume-weighted average ideal age tracers for Pre-Industrial (dotted), 38Ma  $2\times$  (dashed) and  $4\times$  (solid) PIC spin-up simulations. Averages are shown globally (black) and for both the Pacific (red) and Atlantic (blue) ocean basins separately. **c)** 38Ma and **d)** pre-industrial horizontal distributions of ideal age tracers at 2500m depth for the end of each model simulation. Colour shading in **c)** shows the ideal age of  $4\times$  PIC, while contours do so for the  $2\times$  PIC case (coloured contours use the colourmap shown to the right).

Another way to assess the degree to which the modelled climate is equilibrated during the spin-up phase is to consider global mean near surface air temperatures and the top of model flux imbalance (Gregory et al., 2004). An overview of time series (normalised using the spin-up length) and scatter plots of temperature deviation, fluxes and albedo is given in Figure 5.3. As for oceanic temperatures (Figure 5.1), the atmosphere equilibrates much faster in the 2× PIC case compared to the 4× PIC one. In fact, there is hardly any change in temperature while top of model fluxes are balanced after less than 20% (i.e. ~500 years) of the 2× PIC spin-up. Despite some remaining deep ocean warming, the 4× PIC simulation is also close to being in radiative balance when the model is stopped.

Not surprisingly, the top of the atmosphere albedo is lower for the warmer simulation as a result of mostly surface and cloud responses including snow/ice cover and vegetation state. The same processes also explain a positive feedback through a further lowering of the albedo as the climate warms in the 4× PIC case. Despite a large scatter and the model starting from a highly idealised state, a linear fit through the top of model flux imbalance intersects the temperature deviation near the origin for both 38Ma cases. As indicated by the colour coding, deviations in both quantities are mostly small and centred around zero towards the end of the simulations, indicating the latter to be well equilibrated near the surface.

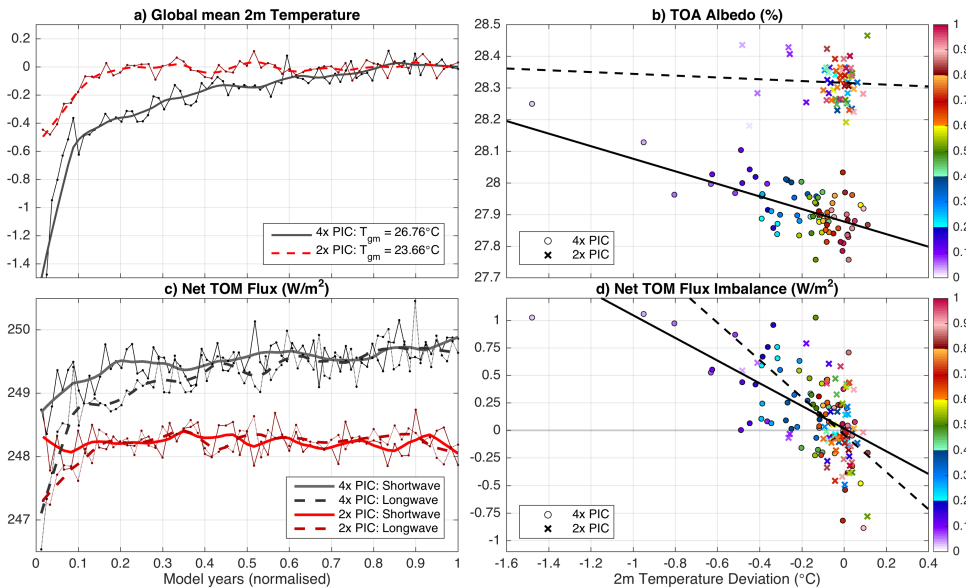


**Figure 5.3:** Overview of the globally integrated radiative balance in the atmosphere for the 38Ma 4× PIC (black) and 2× PIC (red) spin-up simulations; **a)** normalised time series of global mean near surface air temperature deviation (shown at 50-year intervals, thick lines for a 500-year smoothing average), **b)** comparison between the global mean temperature deviation and top of the atmosphere albedo (circles: 4× PIC, crosses: 2× PIC; colours indicating normalised model years and straight lines showing a simple linear fit), **c)** as in a), but for the top of model fluxes, and **d)** as in b), for the net top of model flux imbalance (from the shortwave - longwave fluxes shown in c).



## 5.2 Results: Middle-to-late Eocene Equilibrium Climate

### 5.2.1 Ocean

For each simulation, averages are made using the last 50 model years to represent the corresponding equilibrium climate. The resulting annual mean oceanic state for the 38Ma 4× PIC climatology is visualised by the set of fields shown in Figure 5.4. First of all, sea surface temperatures are quite warm at low latitudes ( $<23.5^\circ\text{N/S}$  average of  $33.9^\circ\text{C}$ , regionally  $>36^\circ\text{C}$ ) but also mild across high latitudes (Figure 5.4a). Mainly the Southern Ocean and especially its Pacific part is characterised by annual mean temperatures of  $10\text{--}20^\circ\text{C}$ , while those of the Arctic Ocean are generally  $6\text{--}10^\circ\text{C}$ . The former Tethyan (now Indo-Pacific) Ocean still acts as one system in the equatorial region, with an expansive warm pool and cold tongue across its western and eastern part, respectively.

Mild temperatures in the sub-polar South Pacific are accompanied by relatively high salinities of around 35psu (Figure 5.4b). Higher salinities are present across low latitude evaporative regions around the world, in contrast to the much fresher Arctic Ocean ( $\sim 20\text{psu}$ ). Low temperatures and salinities in the Arctic Ocean are related to the basin being mostly isolated, apart from the shallow Turgai Strait ( $<100\text{m}$  depth) and connections to the North Atlantic Ocean ( $<1000\text{m}$  depth) where consequently low surface salinities are seen as well.

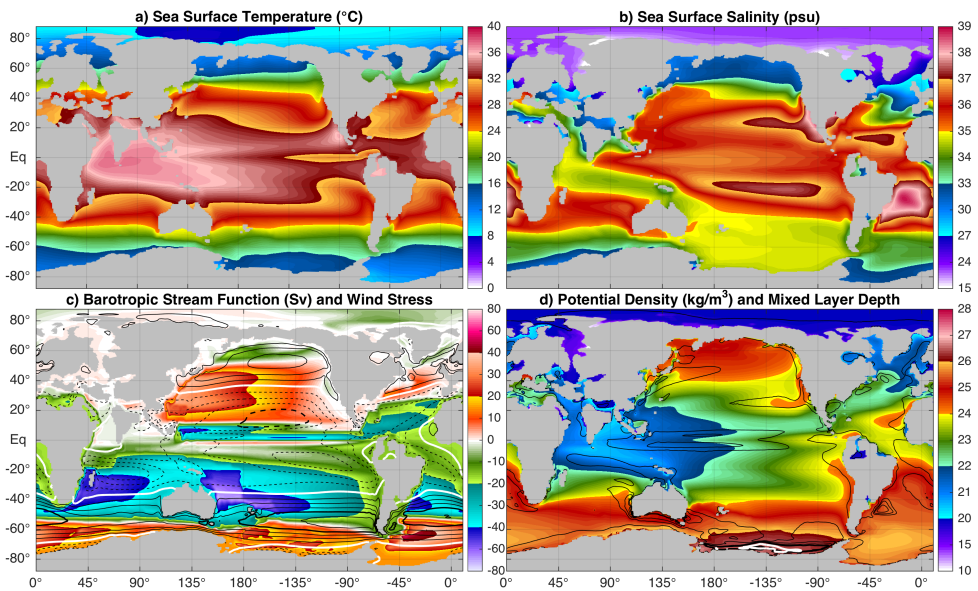


**Figure 5.4:** Annual mean **a)** sea surface temperature and **b)** salinity, **c)** barotropic stream function (positive for clockwise flow) and zonal wind stress (contours every  $2.5 \cdot 10^{-2}\text{Pa}$ , thick lines every  $1 \cdot 10^{-1}\text{Pa}$ ; solid positive and dashed negative values, thick white line at  $0\text{Pa}$ ), and **d)** upper 200m mean potential density and mixed layer depth (contours every 50m down to 250m, thick lines every 250m, thick white line at 500m) for the 38Ma 4× PIC simulation.

These surface temperature and salinity patterns are reflected by upper 200m potential density (Figure 5.4d), with high values throughout the Southern Ocean and much lower densities and thus more stably stratified waters in the North Atlantic and Arctic Oceans. The latter is consistent with proxy indications of a stratified North Atlantic Ocean in the Eocene (Coxall et al., 2018). Deep water formation occurs only in the South Pacific in winter, but low stratification suggests that this may take place virtually anywhere around the Antarctic continental slope. The only location in the Northern Hemisphere where deep water formation could potentially take place consists of the weakly stratified high latitudes of the North Pacific Ocean, but it does not occur in these 38Ma CESM simulations. North Pacific deep water formation is seen in various Eocene simulations (Hutchinson et al., 2018; Thomas et al., 2014) including the ocean-only simulations in Chapter 4, and also suggested by some proxy data (Hague et al., 2012).

Most of the global ocean circulation is dominated by sub-tropical and sub-polar gyres (Figure 5.4c), with the strongest cell in the South Indo-Pacific Ocean. A frontal zone is present in the Southern Ocean, separating cyclonic (sub-tropical) and anticyclonic (sub-polar) gyres. This front coincides with an Antarctic Circumpolar Current (ACC) that is, however, still strongly restricted in its path and depth (200–500 m). Strikingly, the front is located at 55–60 °S, which is 10° poleward of where it is in the pre-industrial reference (Appendix Figure A.1) and the ocean-only results (Figure 4.4; Chapter 4). The region of maximum zonal wind stress coincides with this front, showing that it is truly fixed by the latitudes where winds are the least obstructed by continents.

Due to the more southerly position of Australia in the Eocene, the temperature front separating warm Pacific from colder Antarctic waters also moves further southward. Interestingly, this allows low-latitude derived waters to extend much further southward helping to explain high temperatures in many Southern Ocean regions, especially the Southwest Pacific in summer (Bijl et al., 2009; Douglas et al., 2014). The model response to the 38Ma geography is consistent with the findings of Viebahn et al. (2016), who describe a southward expansion of sub-tropical gyres in response to Drake Passage closure. On the other hand, a strong eastward flow through the Tasmanian Gateway limits the strength and extent of the Antarctic counter current of which the influence is seen at most nearby sites throughout the Eocene (Bijl et al., 2013; Huber et al., 2004; Stickley et al., 2004). The circulation pattern and associated temperature/salinity fields found here generally correspond well with those shown by Hutchinson et al. (2018), who use the GFDL model with the same geographic boundary conditions.

Despite differences in spin-up time, patterns of the equilibrium ocean circulation state are generally similar for the 2× PIC and 4× PIC simulations (38Ma 2× PIC results are shown in Appendix B). The annual mean, global mean sea surface temperature (SST) is 28.4°C in the 4× PIC case versus 25.8°C in the 2× PIC one and 18.4°C in the pre-industrial reference (Appendix A, see also Table 5.3 further down).

Temperature differences of 2.5–3 °C between both 38Ma cases were also seen in the upper and deep ocean in Figure 5.1, resembling the global mean SST change of 2.6°C. Without significant contribution from continental ice sheets, a similar 2–4 °C cooling would be expected between the middle and late Eocene corresponding to a 0.5–1 ‰ shift in benthic  $\delta^{18}\text{O}$  (Cramer et al., 2009; Zachos et al., 2001, 2008). In these 38Ma Eocene simulations, the globally averaged deep-sea temperature (below 2000m) reaches  $\sim 11.5^\circ\text{C}$  in the 4× PIC case (and  $\sim 8.6^\circ\text{C}$  in the 2× PIC case), which is much warmer than for the pre-industrial ocean ( $\sim 0.7^\circ\text{C}$ ). In terms of an oxygen isotope ( $\delta^{18}\text{O}$ ) signal, this would correspond to a  $\sim 2.8\text{‰}$  and  $\sim 2\text{‰}$  difference due to deep sea cooling from the 4× PIC and 2× PIC Eocene climate to pre-industrial conditions, respectively. A more elaborate description of global and regional temperature change patterns associated with climate sensitivity and geography is given in section 5.2.3.

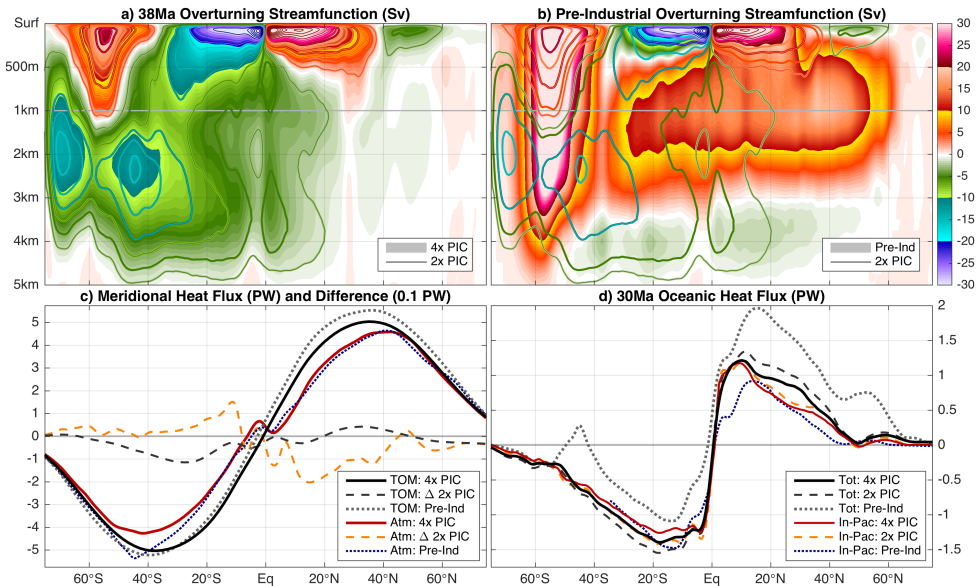


**Figure 5.5:** Global oceanic meridional overturning stream function, averaged over the last 50 model years of the **a)** 38Ma 4× PIC (shading) and 2× PIC (contours) Eocene simulations, and **b)** pre-industrial reference (shading; 38Ma 2× PIC again in contours). Contours are drawn at  $\pm 2.5$  Sv and every 5 Sv onward, using the same colourmap shown at the right side. Top of model (TOM) required total meridional heat flux is shown in **c)** for 4× PIC (solid black) and the pre-industrial reference (dotted grey) with the corresponding atmospheric fluxes in red (4× PIC) and dotted blue (pre-industrial). Differences with respect to 38Ma 4× PIC of both total (dashed dark grey) and atmospheric (dashed orange) heat flux are given for the 2× PIC case, magnified tenfold. **d)** Total integrated meridional heat fluxes in the ocean, globally and Indo-Pacific only, using the same colour coding as in **c)** for TOM and atmosphere, respectively. Note that all horizontal (latitude) scales cover the range [75°S, 75°N] with latitude increasing from left to right, for better comparison with oceanic fields in **a)** and **b)**.

The globally integrated meridional overturning stream function is similar in pattern and extent (Figure 5.5a) for both 38Ma Eocene simulations. Shallow wind driven cells are evident around the equator and a deep overturning cell is present in the Southern Hemisphere, which is slightly stronger in the  $2\times$  PIC case. The effect of upwelling and a shallow positive overturning cell, linked to a proto-ACC, can be seen at around  $55^\circ\text{S}$  in both cases. A similar but much stronger and deeper (northern) overturning cell is seen in the pre-industrial reference, associated with Ekman upwelling near the ACC location. Note that the difference in position of the upwelling cells between Eocene and pre-industrial circulation is smaller than the one seen for the surface polar front in Figure 5.4.

An otherwise predominantly wind-driven gyre circulation is reflected by symmetric oceanic meridional heat fluxes into both hemispheres (Figures 5.5d). This is in contrast to the pre-industrial situation, where approximately a 1PW maximum difference between hemispheres is observed making the Northern Hemisphere relatively warm (Trenberth & Caron, 2001). A major part of the heat flux is generated in the Indo-Pacific Ocean, indicating its dominance within the Eocene circulation. The relative contribution of the Indo-Pacific basin is considerably smaller in the pre-industrial reference, due to the presence of a deep overturning cell in the North Atlantic Ocean.

A subtle but important difference between hemispheres is seen at high latitudes, where about 0.5PW is transported southward at  $45^\circ\text{S}$  while the heat transport is close to zero at  $45^\circ\text{N}$ . This difference can be partly explained by the presence of a deep meridional overturning cell in the South Pacific, pulling warm waters into the southern high latitudes. In addition, land masses obstructing zonal flow at middle/high latitudes (more strongly than at present-day) allow for larger meridional contributions in sub-tropical and sub-polar gyres.

Top of model net shortwave and longwave fluxes are integrated to obtain the required compensating meridional heat flux (Figure 5.5c). Not much difference is seen between both Eocene and the pre-industrial cases, apart from a slight shift towards the Southern Hemisphere at 38Ma. Oceanic heat fluxes are amplified (+0.2PW) in the 38Ma  $2\times$  PIC case compared to  $4\times$  PIC, but the TOM difference is smaller (+0.1PW) inducing an opposite atmospheric response (-0.1PW).

The oceanic heat transport patterns in these 38Ma Eocene simulations generally agree with those seen in previous model studies and the (PaleoMag) SHS state in Chapter 4. In situations with no (or a restricted) ACC, increased southward heat transport is found in the Southern Hemisphere and attributed to both changes in the horizontal gyre circulation (in particular sub-polar gyres; Huber et al. 2004; Huber & Nof 2006; Sijp et al. 2011) and more directly to the meridional overturning circulation (Sijp & England, 2004; Sijp et al., 2009; Toggweiler & Bjornsson, 2000). These differences with respect to the present-day (pre-industrial) ocean circulation have been referred to as the Drake Passage effect (Toggweiler & Bjornsson, 2000), which has been shown to also exist (with different strength) in model simulations resolving meso-scale ocean eddies (Viebahn et al., 2016).

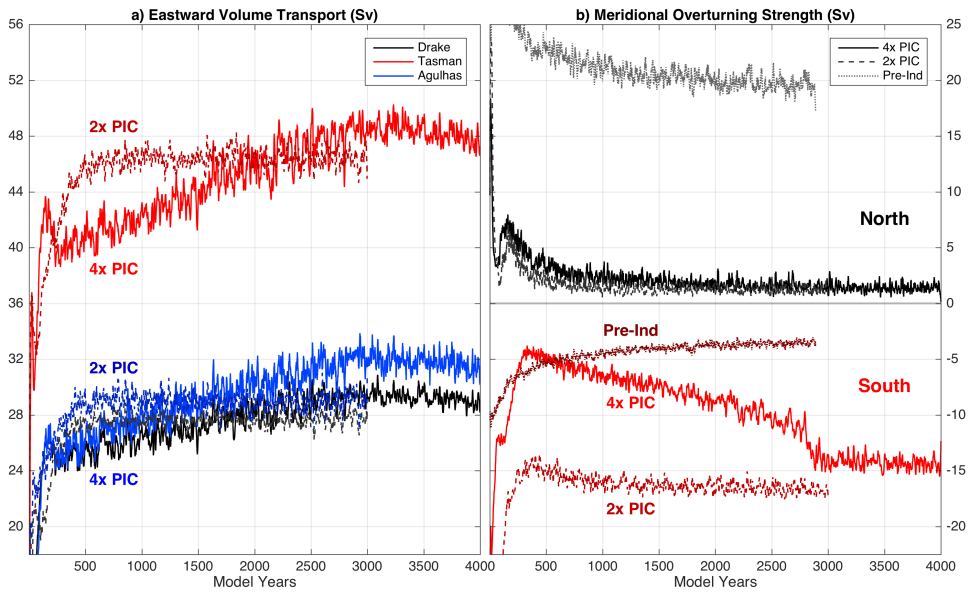


**Figure 5.6:** Time series of **a)** Southern Ocean gateway volume transports and **b)** maximum global meridional overturning stream function for both 2× PIC (dashed), 4× PIC (solid) Eocene and pre-industrial (dotted) spin-up simulations. Transports through three north-south transects in the Southern Ocean are considered: Drake Passage (black, 65°W), Tasmanian Gateway (red, 150°E) and Agulhas (blue, 25°E), with positive values indicating eastward flow.

Subtle differences in spin-up between both 38Ma Eocene simulations are highlighted by time series of gateway transports and global meridional overturning circulation strength (Figure 5.6). Early in the 4× PIC run the southern overturning cell weakens considerably (Figure 5.6b), as the ocean is heated from the surface and becomes stably stratified. Through diffusion, the deep ocean gradually warms up facilitating deep convection in the Southern Ocean. Only after 2700 model years, a deep southern overturning cell develops with a similar strength and extent to the one seen in the 2× PIC run.

Volume transports through the Drake Passage, Tasmanian Gateway and Agulhas transect are shown in Figure 5.6a. Induced by the Southern Ocean (and especially South Pacific) meridional density gradient, zonal transports through the considered transects are connected to the overturning strength. Even after using a 10-year running mean, the smoothed time series still show considerable variability (much more than in the ocean-only cases in Chapter 4; Figure 4.3) involving Rossby waves and multi-decadal scale processes. Additionally, transport strengths are relatively high considering the limited depth and width of both the Drake Passage and Tasmanian Gateway. With 45–50 Sv of volume transport, the flow through the Tasmanian Gateway is almost one third of its present-day equivalent (~180 Sv in the pre-industrial reference). A strong forcing is provided by the meridional density gradient in the South Pacific, pushing water through the Southern Ocean gateways. Continental geometry, being consistent with proxy-based reconstructions (Stickley et al., 2004), does not yet allow the development of a deep ACC at the 38Ma configuration.

As a validation of the model output, sea surface temperatures of the 4× PIC climatology are compared to estimates from 42–38 Ma proxy records (Appendix C: Table C.1, data from Bijl et al. 2009; Cramwinckel et al. 2018; Douglas et al. 2014; Evans et al. 2018; Hines et al. 2017; Kobashi et al. 2004; Liu et al. 2009; Okafor et al. 2009; Pearson et al. 2001, 2007; Tripathi et al. 2003). The model zonal mean, annual mean SST is given by the black line in Figure 5.7 with the (geographical) temperature range at each latitude indicated by the shaded area. A point-by-point comparison with proxy records is made, using the estimated 38Ma positions in accordance with the PaleMag geography from Chapter 2. Proxy-derived values for annual mean temperatures are indicated by blue markers with their calibration uncertainty for different methods (UK<sub>37</sub>, TEX<sub>86</sub><sup>H</sup>, Mg/Ca,  $\Delta_{47}$  and  $\delta^{18}\text{O}$ ). Estimates using UK<sub>37</sub> are disregarded at low latitudes as the calibration saturates at  $\sim 28^\circ\text{C}$  (Conte et al., 2006), those from Mg/Ca use the constraints on sea water chemistry from Evans et al. (2018). Corresponding SST values from the simulated climate are indicated by white and red circles for the annual and summer mean, respectively. Error bars on model temperatures are obtained by taking the variance in a  $4^\circ \times 4^\circ$  box surrounding the reconstructed proxy location, covering the uncertainty associated with the palaeogeographic reconstruction (<http://www.paleolatitude.org>).

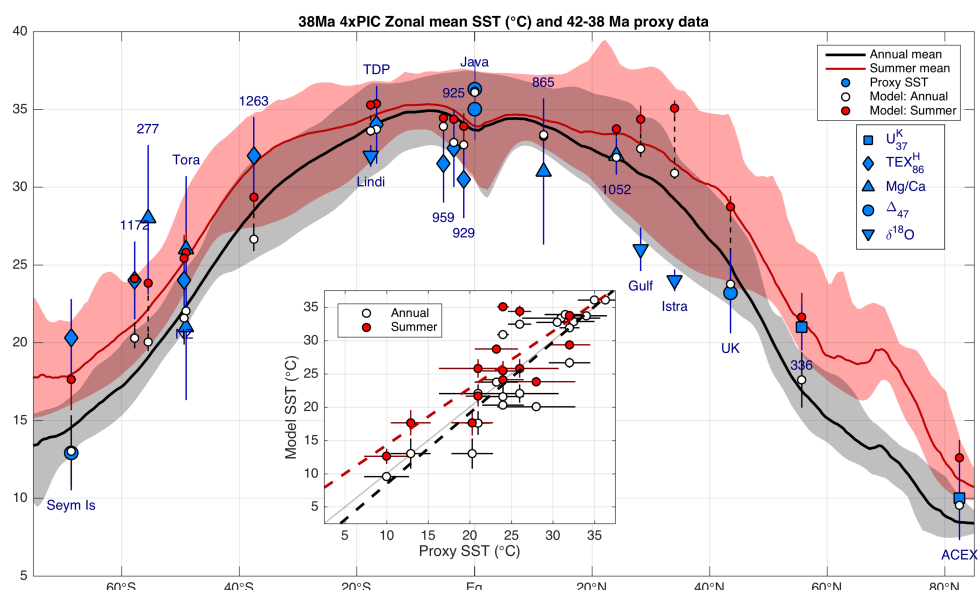


**Figure 5.7:** Zonal mean, annual mean (black) and summer mean (red) sea surface temperature (SST) with shaded regions showing minimum and maximum values for each latitude (4× PIC simulation). Blue markers indicate estimates from 42–38 Ma SST proxies, whereas the white (annual) and red (summer) circles depict model values at the corresponding 38Ma locations. Error bars are obtained using proxy calibration errors and the spatial variation within a  $4^\circ \times 4^\circ$  box surrounding the corresponding location in the model. The inset shows a scatter plot comparing proxy and model SST, with dashed lines indicating a linear fit using annual mean (black) or summer mean (red; only poleward of  $23.5^\circ\text{N/S}$ ) model temperatures.

For low-latitude regions, model results and proxies are in reasonable agreement, with model values mostly in the upper range of SST estimates. Some near-equatorial sites (e.g. Atlantic ODP sites 925, 929 and 959) show cooler temperatures, near 30°C. Model-proxy discrepancies at these sites can be related to the model's limitation in resolving the sharp equatorial upwelling zone with significantly colder waters, or a slight discrepancy in its exact position. The existence of lower near-equatorial temperatures in the model is indicated by the increased spread zonally, down to <30°C.  $\text{TEX}_{86}^H$  estimates from Tanzania show low latitude temperatures of around 34°C and are indicative of waters outside upwelling zones. Additionally, recent clumped isotope measurements from Java suggest 35–36 °C in the West Pacific warm pool, which is in good agreement with 38Ma 4× PIC modelled SSTs.

A mixed agreement is seen at other latitudes, with model results being too warm at northern middle latitudes, too cold in southern middle latitudes and good at high latitudes. The large discrepancy with proxy estimates from the Gulf of Mexico and Neotethys (Mediterranean) stands out. While it seems unlikely that these regions would be colder than they are today, the model possibly also underestimates strong seasonal cooling in shallow coastal waters and other localised effects near the coastline. The complex palaeogeography at both locations is not sufficiently represented even in these relatively high-resolution simulations. SST estimates from other locations at a similar latitude, such as ODP site 1052 on Blake Nose (east of Florida) are much higher bringing the model and proxies into good agreement. A better match is generally found in most middle and high southern latitude regions when summertime temperatures are considered. Since SST proxies are based on past living organisms, it is possible that at higher latitudes these proxies have a bias towards the warm season as their activity and sedimentation are directly or indirectly affected by the available amount of sunlight (Bijl et al., 2009; Hollis et al., 2012; Schouten et al., 2013; Sluijs et al., 2006, 2008). There is, however, a good agreement with annual mean SSTs in the Arctic and considering clumped isotope indicators elsewhere (UK and Seymour Island).

A comparison of 38Ma 2× PIC model SST with 38–34 Ma proxy estimates shows a similar result (Appendix: Table C.2 and Figure C.1). Good agreement between proxy and model results exists in equatorial regions, with again a large spread in proxies and generally a better match with summer temperatures at higher latitudes (except for clumped isotopes). Assuming that temperature proxies represent the annual mean in equatorial waters but are skewed towards the warm season at middle and high latitudes, the model does seem to reconstruct the middle-to-late Eocene (42–34 Ma) temperature distribution quite well.



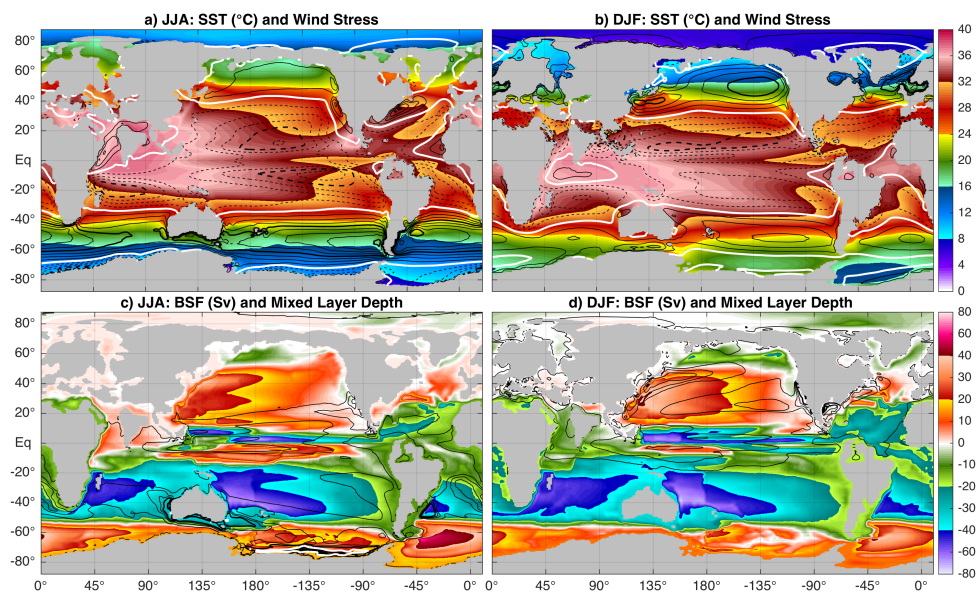


**Figure 5.8:** 4× PIC simulation **a)** June-July-August and **b)** December-January-February averaged sea surface temperature and zonal wind stress (contours every  $2.5 \cdot 10^{-2}$  Pa and thick lines every  $1 \cdot 10^{-1}$  Pa; solid positive and dashed negative, thick white line at 0 Pa). **c)** and **d)** similar to **a)** and **b)**, but for the barotropic stream function and maximum mixed layer depth (contours every 50 m down to 250 m, thick lines every 250 m, thick white line at 500 m).

In addition to the annual mean fields shown in Figure 5.4, winter and summer averaged SST, wind stress, barotropic stream function and mixed layer depth are presented in Figure 5.8. Sea surface salinity and upper 200 m potential density are not considered here as they show little seasonality. Across southern high latitude regions, SST seasonality is strong with winter temperatures of mostly 6–12 °C rising to 16–24 °C in summer. A combination of solar heating and gyre circulations causes the coldest summertime temperatures in the Southern Hemisphere to occur at the centre of sub-polar gyres, rather than near the Antarctic coastline (zonal mean summer SSTs are also seen to increase slightly beyond 65°S in Figure 5.7). Not surprisingly, the South Pacific Ocean holds the warmest high latitude waters as it exhibits additional southward heat transport in the meridional overturning circulation.

Based on the barotropic stream function, warm waters in the Southwest Pacific are carried southward through an East Australia Current (EAC) down to 55°S. This EAC meets the proto-Leewards current from the west, and northward flow in the Ross Gyre further poleward. This is mostly consistent with the picture for the middle Eocene given by Bijl et al. (2009), but shifted southward (with a more confined Ross Gyre) compared to that of Huber et al. (2004).

In contrast, seasonality outside near-equatorial regions is weakest in the Arctic Ocean (related to persistent low cloud cover). Very high summer temperatures stand out in the Mediterranean/Neotethys, caused by heat transport from the Indian Ocean warm pool in combination with strong insolation.



Further north, the shallow Turgai Strait (55°N, 60°E) separates the Arctic from sub-tropical water masses and exhibits high seasonality.

The barotropic stream function and zonal wind stress show similar seasonal cycles (as the gyres are mainly wind-driven), with strong (weak) zonal flow and gyres in winter (summer). This can be directly related to changes in the meridional temperature gradient, which is stronger in winter. Finally, the effect of northward flowing bottom waters (restricted by bathymetry) can be seen in the South Pacific sub-polar gyre. This feature is strongest in winter, which is the time when deep water formation is taking place as indicated by the maximum mixed layer depth.

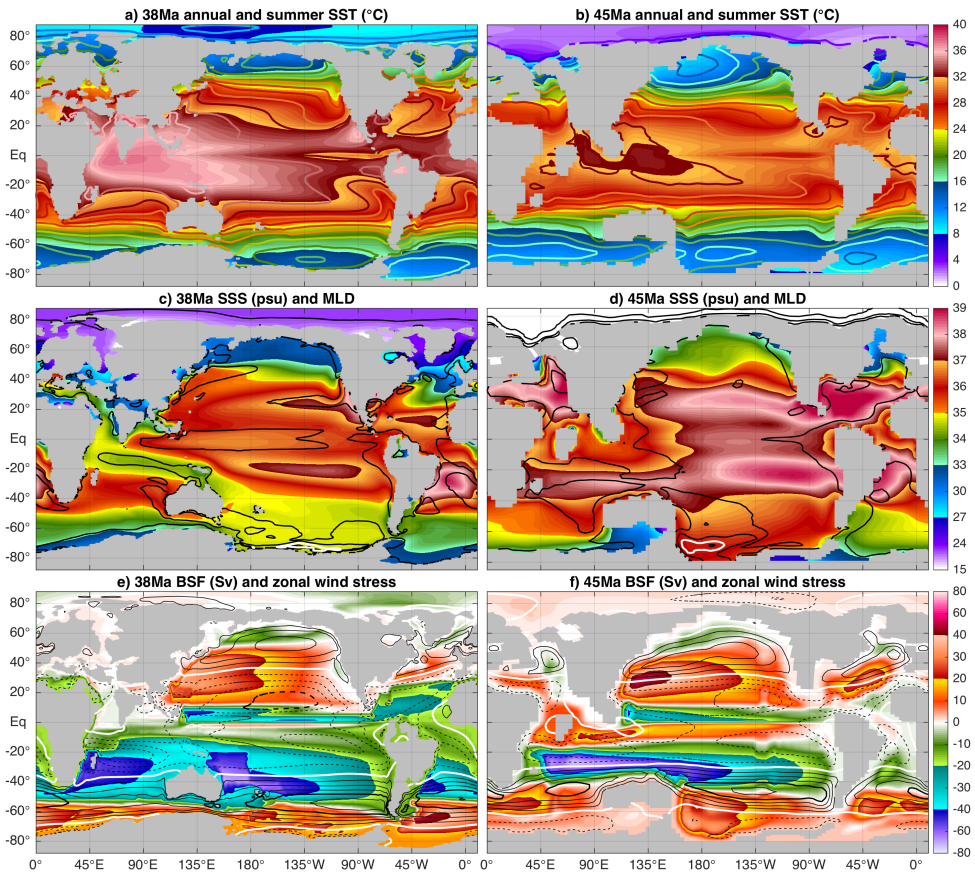


**Figure 5.9:** Annual mean (shading) and summer (contours every 2°C) sea surface temperatures for the **a**) 38Ma 4× PIC simulation presented here and **b**) results from Goldner et al. (2014) (GH14) using a 45Ma geography and 4× pre-industrial CO<sub>2</sub>. A similar comparison is made for **c**) and **d**) sea surface salinity (psu) and mixed layer depth (contours) as well as **e**) and **f**) barotropic stream function (shading) and zonal wind stress (contours). All colour scales and contour intervals use the same conventions as those used in Figures 5.4 and 5.8.

To put the results presented here into perspective, the 38Ma 4× PIC case is compared to previous model simulations from Goldner et al. (2014) (hereafter: GH14) in Figure 5.9. The latter use a 45Ma Hot Spot referenced reconstruction for their geographical boundary conditions and 4× pre-industrial levels of CO<sub>2</sub> (i.e. 1120ppm). The main difference between both studies is the horizontal resolution; ~1° and ~2° in the 38Ma simulations presented here versus ~2.5° and 3.7° in GH14 for the ocean and atmosphere grids, respectively.

While the 38Ma 4× PIC case also has a quadrupling of CH<sub>4</sub> and the 45Ma one does not, the difference in global temperature is much larger than what would be expected based on radiative forcing alone. The grid and resolution used here for the atmospheric component (CAM4) are shown to both increase the sensitivity to a doubling of CO<sub>2</sub> by Bitz et al. (2012). Additionally, using the finite volume instead of a spectral grid greatly influences cloud radiative forcing and causes a warming compared to GH14. Indeed, similar global temperatures are found under comparable radiative forcing by Hutchinson et al. (2018), using a lower resolution but comparable finite difference dynamical core for the atmospheric component. Finally, a warm initialisation of the deep ocean, general circulation changes and aerosol changes may add further to temperatures differences with GH14.

The most prominent differences in geography between the 45Ma and 38Ma simulations are the representation of Antarctica, the Tasmanian Gateway opening and the position of India. Especially the Southern Ocean shows large differences in circulation and the resulting temperatures, mainly related to the different model geographies. The formation of a proto-ACC and southern extent of the East Australia current act to shift the polar front in the South Pacific southward for the 38Ma case, while the opposite happens for 45Ma. These changes can be linked directly to the continental configuration and associated shifts in zonal wind stress (maximum at 55°S versus 45°S in GH14).

The more southerly position of the polar front can explain the thermal heterogeneity in the Southern Ocean; a difference of 6–8 °C is seen between Tasmania and the tip of the Antarctic Peninsula (Seymour Island) in agreement with proxy indications from Douglas et al. (2014). Generally, western boundary currents (e.g. Kuroshio, Agulhas, East Australia Current) and the effects of ocean bathymetry are more pronounced in the 38Ma results. Finally, an issue in the 45Ma results with very low (negative) salinities in the Arctic Ocean, although having seemingly little impact on the general circulation, is mostly resolved (lowest salinities down to ~10psu) in the 38Ma case by having several shallow passages.

A comparison of zonal mean SSTs in the 38Ma  $2\times$  PIC and  $4\times$  PIC cases, 45Ma  $4\times$  CO<sub>2</sub> from GH14 and pre-industrial reference simulation along with proxy estimates is shown in Appendix C (Figure C.3). A comprehensive overview of the CESM cases presented here, model results from Goldner et al. (2014) and Hutchinson et al. (2018) and oceanic temperature proxy records is also given in Figure 9.1 of Chapter 9. Apart from the 38Ma cases being overall warmer, the zonal mean temperature profile seems qualitatively similar for all Eocene simulations. With several indications of near-equatorial temperatures as high as 34–36 °C (Tanzania, Java and Saint Stephens Quarry), only the 38Ma  $4\times$  PIC case is able to match those proxies while still allowing equatorial upwelling zones to be below 30°C. On the other hand, cooler low-latitude proxies of ~30°C are better matched by both the 45Ma  $4\times$  CO<sub>2</sub> and 38Ma  $2\times$  PIC results. Southern Hemisphere high latitude proxies are difficult to match by any model because of their large spread. Still, most of the lower estimates are best matched by the annual mean SST in the 38Ma  $4\times$  PIC case while also meeting the higher estimates when considering summer conditions.

### 5.2.2 Atmosphere

Similarly to oceanic fields above, a climatology for the atmosphere is made from the last 50 years of the 38Ma  $4\times$  PIC simulation of which the annual mean is shown in Figure 5.10. Again, results for the  $2\times$  PIC case (shown in Appendix B) look similar apart from being 3.1°C cooler, globally averaged (23.7°C versus 26.8°C). Near surface air temperatures (at 2m; Figure 5.10a) under  $4\times$  PIC are generally above zero and up to 40°C in the sub-tropics, with annual mean minimum temperatures only below freezing in East Antarctica and Northeast Siberia.

Mean sea level pressure and precipitation patterns (Figure 5.10b) indicate the presence of a typical tropical trough and sub-tropical ridges. The inter-tropical convergence zone (ITCZ) consists of 2 precipitation maxima, extending over the Indo-Pacific basin on both sides of the equator. A pronounced double ITCZ over the Pacific Ocean is also seen in the pre-industrial reference and a known model-related issue (Bellucci et al., 2010; Song & Zhang, 2009). Effects of orographic lift are evident on westward facing coastlines and ridges across middle and high latitudes.

The temperature at 700hPa (Figure 5.10c) highlights warm mid-level air masses in persistent continental high pressure regions in the sub-tropics. Antarctica is substantially warmer than the Arctic at this pressure level because of its elevation and continental climate. Similar to the Tibetan Plateau today, it therefore acts as an elevated heat island (Hoskins & Karoly, 1981; Ye & Wu, 1998). Wind speeds at 200hPa show maxima linked to the positions of both sub-tropical and polar jet streams. Several stationary Rossby Waves are present, but a persistent upper level trough is evident around 90°E, where both jets coincide. Such a pattern can also be seen at present-day but only in the Northern Hemisphere (located at 120°E in the pre-industrial reference; Appendix Figure A.3c), caused by the influence of the Tibetan Plateau.

Finally, the 500hPa geopotential height field (Figure 5.10d) shows a nearly meridionally symmetric pattern, with the sharpest gradient in middle-latitude regions. The 500hPa surface is generally about 200m higher than in the pre-industrial reference, mainly due to warming of the air column. The current  $\sim 200\text{m}$  asymmetry between southern ( $\sim 5\text{km}$ ) and northern ( $\sim 5.2\text{km}$ ) high latitudes (Appendix A Figure A.3d) does not occur in the 38Ma Eocene climate ( $\sim 5.4\text{km}$  for both). The corresponding tropopause height (using the WMO definition of  $2^\circ\text{C}/\text{km}$ ) is at 17–18 km in the tropics and does not fall below 11–12 km at high latitudes, being 1 and 2 km higher than it is in the pre-industrial climate, respectively.

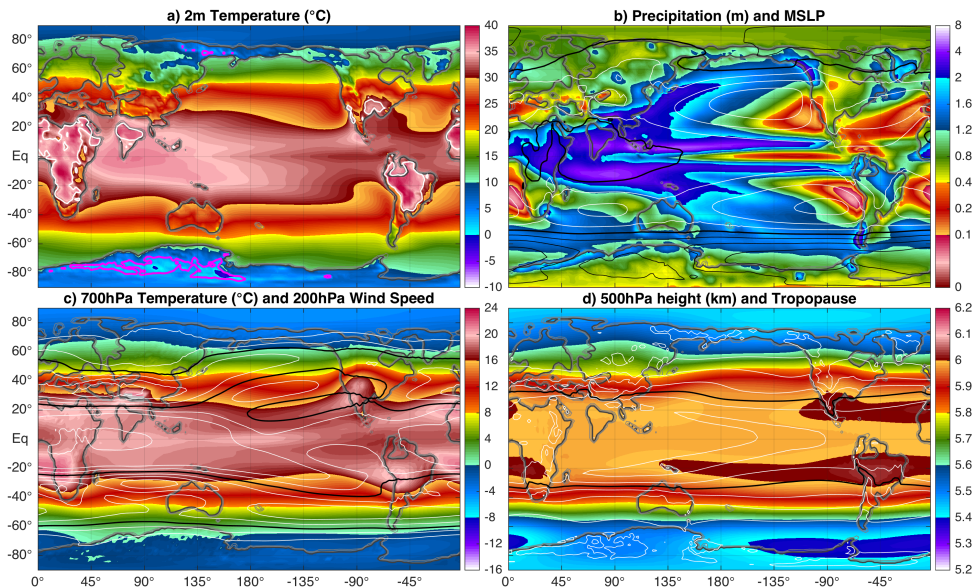


**Figure 5.10:** Annual mean for the  $4\times$  PIC simulation with **a)** near surface (2m) air temperature (coloured) and average min/max temperature (contours; magenta  $T_{min} < 0^\circ\text{C}$  and white  $T_{max} > 40^\circ\text{C}$ ), **b)** precipitation (coloured) and mean sea level pressure (contours every 5hPa, thick black lines every 20hPa,  $\leq 1000\text{hPa}$  in black and  $> 1000\text{hPa}$  in white), **c)** 700hPa temperature (coloured) and 200hPa wind speed (white contours every 5m/s starting at 10m/s, thick black lines every 20m/s), and **d)** 500hPa geopotential height (coloured) and dynamic tropopause height (contours every 1km starting at 12km, thick black line at 16km).

As was done for sea surface temperatures in Section 5.2.1 (Figure 5.7), an overview of zonally averaged 2m air temperatures is given in Figure 5.11. Considering annual mean air temperatures (MAT), a meridionally symmetric pattern with a low equator-pole gradient stands out again. This pattern looks similar for both 38Ma simulations, being about  $3^\circ\text{C}$  cooler in the  $2\times$  PIC case with a slight amplification towards the poles. Regardless of greenhouse gas concentrations, the pre-industrial reference temperatures are in sharp contrast with those seen in the Eocene cases. In addition to being considerably colder (global mean 2m temperature of  $13.7^\circ\text{C}$ ), the pre-industrial climate features a stronger equator to pole temperature gradient with high latitudes up to  $40^\circ\text{C}$  colder than what is seen in the 38Ma  $2\times$  PIC case.

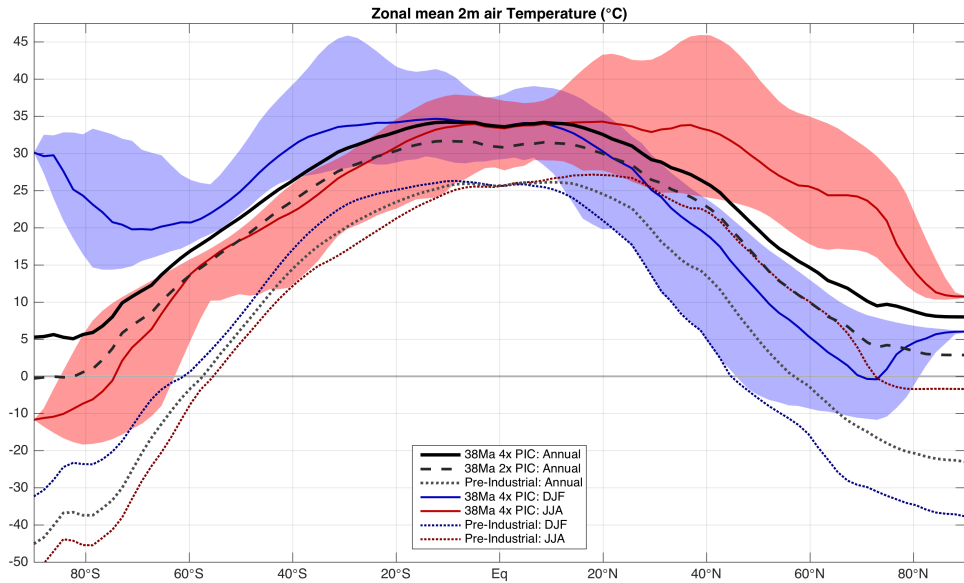


**Figure 5.11:** Annual mean, zonal mean 2m air temperature (black line) for the 38Ma 4× PIC (solid), 2× PIC (dashed) and pre-industrial (dotted) equilibrium climate. Zonal mean temperatures of the 4× PIC climate, averaged for June-July-August and December-January-February are shown in red and blue, respectively. The longitudinal range of seasonal temperatures is indicated by shaded areas for the 4× PIC case, using the same colour coding.

This shows that the absence of ice, changes in continental geometry and land cover have a significant impact on global mean temperature as well as its distribution. Despite changes in the general circulation, total meridional heat fluxes are not substantially different in the Eocene climate compared to the pre-industrial reference (Figure 5.5c). The reduced equator to pole temperature gradient is thus a result of reduced heat loss at high latitudes rather than enhanced heat transport.

Tropical temperatures are closely tied to prevailing water masses and show little variability, both seasonally and zonally. Summer temperatures in the sub-tropics are on average comparable to those in the tropics, but exhibit higher variability. Especially around 40°N and 30°S, land masses are abundant in the Eocene allowing summer temperatures of up to 45°C under 4× PIC. While seasonality is weak at southern middle latitudes it is stronger at northern middle and high latitudes, again caused by differences in land coverage. Remarkably strong seasonality is seen on the Antarctic continent, where average winter (DJF) temperatures drop below -10°C while reaching 30°C in summer (JJA). The continental configuration thus causes the coldest place in winter on the Northern Hemisphere to be at ~70°N (rather than the North Pole), while the warmest place in summer south of ~45°S is on Antarctica. The near meridional symmetry in temperatures is reflected by both oceanic and atmospheric heat fluxes, that were shown in Figure 5.5c-d. This symmetry is only seen in annual mean temperatures, as seasonal variability is influenced by the different land-ocean distributions between hemispheres.

A comparison between late middle Eocene terrestrial proxies (Appendix: Table C.3, data from Boyle et al. 2008; Eldrett et al. 2009; Greenwood & Wing 1995; Greenwood et al. 2004; Gregory-Wodzicki 1997; Hinojosa & Villagrán 2005; Passchier et al. 2013; Prothero 2008; Quan et al. 2012; Retallack et al. 2004; Schouten et al. 2008; Smith et al. 1998; Uhl et al. 2007; Wolfe et al. 1998) and  $4\times$  PIC model air temperatures is made in Figure 5.12. Terrestrial proxies used here consist mainly of (multiple) vegetation-based indicators using pollen, nearest living relative (NLR), leaf physiognomy (LMA, CLAMP, ELPA and LMA; Kowalski & Dilcher 2003; Traiser et al. 2005; Wing & Greenwood 1993; Yang et al. 2011) and MBT-CBT (Peterse et al., 2012). In contrast to Figure 5.11, modelled temperatures are only considered over land when taking the zonal average and pre-industrial values are not shown here. The latitudinal distribution of the available terrestrial proxies is rather limited and covers mostly middle latitude regions.

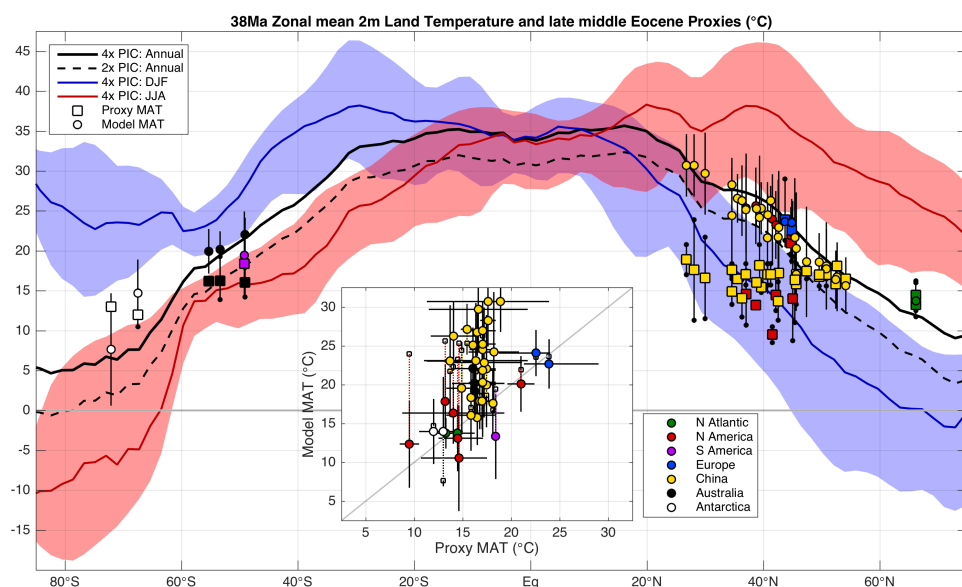


**Figure 5.12:** As in Figure 5.11 for land-only temperatures, proxy estimates (squares) and corresponding model mean annual temperature (circles). Proxy temperatures are colour coded for their region, and error bars (black dots) are indicative of the spread at each site. Similar to model SST in Figure 5.7, error estimates (black lines) show the spacial variation within a  $5^\circ \times 4^\circ$  box surrounding the corresponding location in the model. The inset shows a scatter plot comparing proxy and model air temperatures, where the latter are corrected for differences in model grid and reconstructed topography (uncorrected: small white squares).

A good agreement is seen with proxy data from the North Atlantic (Greenland), South America (Chile), Europe, Australia and the Antarctic margin. While most of the higher latitude ( $>40^\circ\text{N}$ ) proxies agree fairly well with model temperatures over China and North America, there is a large discrepancy at lower latitudes. As mentioned above, continental interiors are seemingly too warm in the model especially in summer. Meanwhile, many of the proxy estimates from China likely underestimate summer temperatures (possibly explaining the apparent lack of a latitudinal

temperature gradient) as there is no present-day equivalent of vegetation that can withstand such high heat stresses. In addition, proxy temperatures are representative of a specific location while the horizontal resolution of the simulated atmosphere is limited ( $\sim 2^\circ$ ). Therefore, the model will underestimate local temperature effects by having a strongly smoothed topography.

Using the  $0.1^\circ$  38Ma geography reconstruction from Chapter 2 (Figure 2.8), model temperatures are corrected for the difference with model topography assuming a free atmospheric lapse rate of  $-6.5\text{K/km}$ . Especially North American sites show a large improvement when correcting for model topography, as shown in the inset of Figure 5.12 (comparing small squares to coloured circles). The discrepancy remains for the lower latitude part of the Chinese sites, where mean annual air temperatures are probably underestimated by proxies as well as overestimated by the model. Comparing  $2\times$  PIC model results to late Eocene proxies shows a similar result (Appendix: Table C.4 and Figure C.2), with again a good agreement in middle latitude regions but larger differences over interior China.

The model results presented here are again compared to those from Goldner et al. (2014) (GH14) and shown in Appendix C (Figure C.4). Similar to the ocean results all of the considered Eocene simulations have a comparable zonal mean temperature distribution, with the 38Ma cases being generally warmer than GH14. High summertime temperatures over low/middle latitude continental regions are more pronounced in the 38Ma  $4\times$  PIC case, but also present for 45Ma  $4\times$   $\text{CO}_2$  from GH14. The large seasonality over Antarctica is enhanced in the 38Ma simulations compared to GH14, with summer temperatures well over  $30^\circ\text{C}$  in the  $4\times$  PIC results (versus  $20^\circ\text{C}$  in GH14). Because of these extreme summertime temperatures on Antarctica and cloud-albedo feedbacks in the Arctic, annual mean (zonal mean) temperatures are globally above  $5^\circ\text{C}$  in our 38Ma  $4\times$  PIC simulation.

Seasonality in the atmosphere is studied in more detail by comparing the months June–August to December–February for the  $4\times$  PIC case as shown in Figure 5.13. The coldest regions in winter are North-East Siberia and Central Antarctica, where average temperatures drop below  $-10^\circ\text{C}$ . Nearby oceanic temperatures keep Antarctic coastal regions mild and at or above freezing in winter. The continental subtropics show the highest summer temperatures on Earth, with maxima on average exceeding  $50^\circ\text{C}$  in many locations. Such temperatures seem unrealistically high and do not agree with the vegetation imposed in the model. This issue is probably related to the use of fixed vegetation types, leading to trees or shrubs losing their foliage in summer and creating a rough surface with very efficient drying and subsequent heating.



Regardless of a reduced equator-to-pole differences compared to the pre-industrial reference, middle latitude regions still exhibit a sharp meridional temperature gradient, especially in winter. This leads to strong zonal flow and orographic lift seen in pressure and precipitation patterns (Figure 5.13c-d). The Indo-Pacific ITCZ is always double, but most intense in summer and connected to monsoonal troughs over land. Heavy rains from summer monsoons are most prominent across South-East Asia, (Northern and Southern) Africa and South America consistent with the Eocene monsoons discussed by Huber & Goldner (2011).

In winter, plumes of precipitation extend poleward and eastward from the western low latitude ocean basins. These are typical storm tracks caused by baroclinic instability in the middle latitudes, which are associated with sharp mid-tropospheric temperature gradients and high upper level winds (through the thermal wind balance, Figure 5.13e-f). Persistent jet streaks around 90°E, linked to stationary Rossby Waves, are most prominent in winter. Smaller stationary waves are seen in summer and linked to sub-tropical ridges where high surface temperatures are mixed upwards to 700hPa under mid-level subsidence. At this level the effect of solar heating at high altitudes (~2km) on East-Antarctica stands out, where temperatures are about 10°C higher than those seen over the Southern Ocean.

A number of interesting features in the atmospheric circulation are considered by looking at the zonal mean zonal wind and temperatures of the 38Ma 4× PIC case for June–August (Figure 5.14a) and December–February (Figure 5.14b). The zonal mean JJA temperature shows a typical pattern consistent with the Northern Hemisphere summer. A steady cooling towards the poles can be seen in the troposphere, but in the stratosphere further cooling only takes place over the winter pole because of summertime solar heating. Persistent cold temperatures are present around the top of the tropical tropopause, at about 70hPa (compared to 90hPa at present-day and in the pre-industrial reference; Figure A.5).

Associated with the meridional temperature gradients in the troposphere are the sub-tropical and polar jet streams. The sub-tropical jet is more pronounced in the zonal mean and both jets are stronger over the winter hemisphere. Thermal wind balance demands an increase of the zonal wind with height as long as temperatures decrease poleward. As a result, the polar jet extends into the stratosphere in the winter hemisphere, while decreasing again above the tropopause in summer. The polar regions are thus surrounded by a cyclonic polar vortex in winter that extends from the surface to the top of the stratosphere.

An extension of the sub-tropical jet towards the equator can be seen, resulting in positive (westerly) zonal winds at the equator and thus superrotation at the tropopause even in the annual mean. This is caused by the momentum transfer of atmospheric Rossby waves (causing the V-shape in the tropical tropopause in Figure 5.10d) and the strong winter cell of the Hadley circulation.



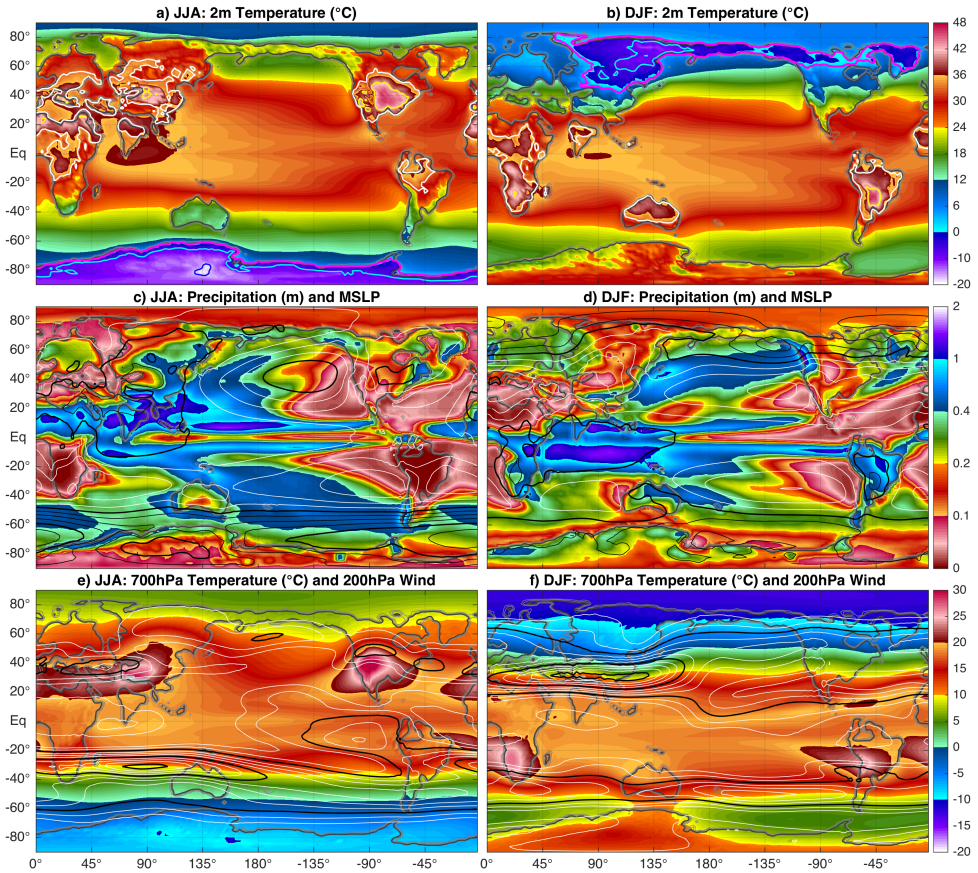


**Figure 5.13:** a) June-July-August and b) December-January-February mean 2m air temperature with contours indicating minimum and maximum values (magenta:  $T_{min} < 0^{\circ}\text{C}$ , cyan:  $T_{min} < -10^{\circ}\text{C}$ , blue:  $T_{min} < -20^{\circ}\text{C}$ , white:  $T_{max} > 40^{\circ}\text{C}$  and yellow:  $T_{max} > 50^{\circ}\text{C}$ ), c) and d) similar for total precipitation and mean sea level pressure, and e) and f) for 700hPa temperature and 200hPa wind speed. Colour scales and contour values are all similar to those used in Figure 5.10.

As shown by Caballero & Huber (2010) superrotation does occur in very warm climate simulations and is therefore no surprise to emerge in the 38Ma  $4\times$  PIC case, where zonal mean equatorial SSTs approach  $35^{\circ}\text{C}$ . Although weaker, zonal mean equatorial westerly winds are still present in the  $2\times$  PIC climate. The highest (zonally averaged) equatorial SSTs in this case are still close to  $33^{\circ}\text{C}$  (Appendix Figure C.1), the threshold found by Caballero & Huber (2010). In the lower tropical troposphere, perennial easterlies (i.e. trade winds) are present with two maxima associated with the double ITCZ of which the strongest component is located on the winter hemisphere (within the stronger Hadley Cell).

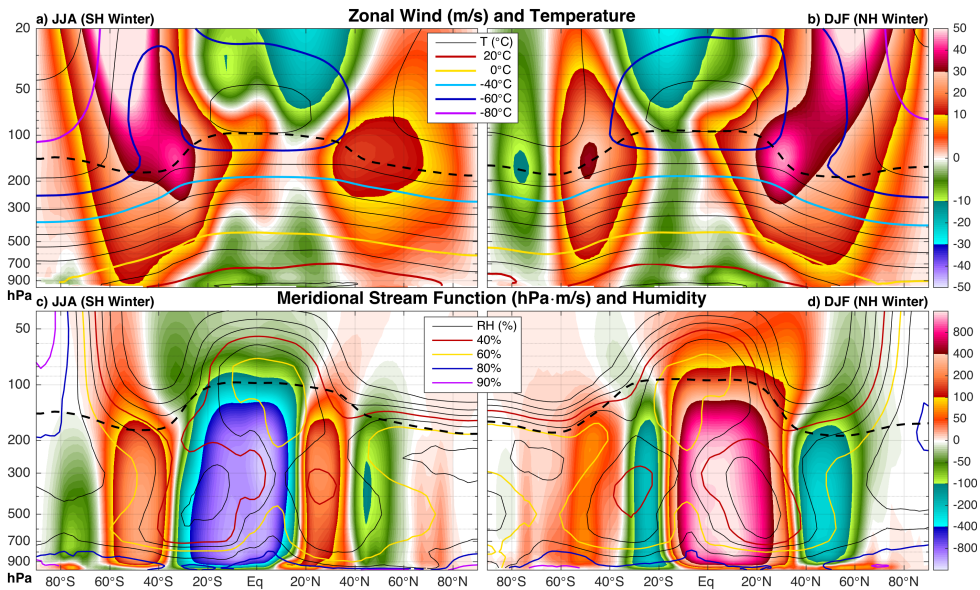


**Figure 5.14:** **a)** Zonal average zonal wind (shading) and temperature (contours every 10°C) for the months June-July-August, **b)** similar to **a)** for December-January-February. **c)** zonally integrated meridional stream function (shading) and relative humidity (contours every 10%) for the months June-July-August, **d)** similar to **b)** for December-January-February. Tropopause height (zonal mean) is indicated by the dashed black line and pressure is used as the vertical coordinate.

A remarkable component of the atmospheric circulation develops in summer over Antarctica. As suggested by temperatures shown in the Figures 5.13e-f and 5.14, the meridional temperature gradient reverses in summer across southern high latitudes. The Antarctic continent thus acts as a (slightly elevated) heat island, reversing the meridional gradients in both pressure and temperature and thus also zonal winds through the thermal wind balance. While the sub-tropical jet remains unaffected (driven by middle latitude gradients), the polar jet becomes anticyclonic in both the troposphere and stratosphere with a maximum near the tropopause. The Antarctic summer climate thus resembles that of the sub-tropics rather than a typical polar summer. This is further supported by the complete absence of a polar cell during Southern Hemisphere summer in the meridional stream function (Figure 5.14d). The strong seasonality and interesting atmospheric circulation over Antarctica will be discussed in more detail in Chapter 6.

### 5.2.3 Climate Sensitivity

By comparing the 38Ma  $4\times$  PIC to the  $2\times$  PIC equilibrium climate state, the according equilibrium climate sensitivity (ECS) can be obtained. To exclude possible effects of decadal-scale variability (see Figure 5.6), 200 years instead of 50 are considered in the climatologies used here. The radiative forcing associated with doublings of  $\text{CO}_2$  and  $\text{CH}_4$  is estimated from the study of Etminan et al. (2016). Doubling of only  $\text{CO}_2$  from the pre-industrial value (280ppm) then corresponds to a radiative forcing of  $\Delta RF^{\text{CO}_2} = 3.8\text{W/m}^2$ . The first doubling of both  $\text{CO}_2$  and  $\text{CH}_4$ , starting from pre-industrial values, results in a combined radiative forcing of  $\Delta RF^{2\times} = 4.23\text{W/m}^2$  and the second doubling gives  $\Delta RF_{2\times}^{4\times} = 4.48\text{W/m}^2$ .

In Figures 5.15a-b the equilibrium temperature difference between the 38Ma  $4\times$  PIC and  $2\times$  PIC simulations is shown, normalised by the associated radiative forcing ( $\Delta RF_{2\times}^{4\times}$ ). Note that both simulations were integrated to equilibrium separately, without ever imposing a strong perturbation from instantaneous greenhouse gas doubling. Even in this virtually ice-free world significant polar amplification can be observed, with the most pronounced warming occurring across high latitude continental regions. As in the present-day climate, the polar amplification is in part due to albedo effects from vegetation, snow cover and (limited) seasonal sea ice. Low latitude regions, on the other hand, warm less as they are more strongly governed by moist processes and tied to SSTs.

Averaging the response (to  $\Delta RF_{2\times}^{4\times}$ ) globally yields an equilibrium climate sensitivity of  $S_{EO} = 0.69^\circ\text{C/Wm}^{-2}$  for these simulations. The Eocene ECS is smaller than the reported  $S_{PI} = 0.82^\circ\text{C/Wm}^{-2}$  for a pre-industrial configuration of CESM1 (i.e. CCSM4), using  $\Delta RF^{\text{CO}_2}$  and  $\Delta T = 3.13^\circ\text{C}$  from Bitz et al. (2012). The difference in ECS suggests that the net effect of the fast feedback processes is less strong in the Eocene climate state than in the present-day climate (Heydt et al., 2014). Note, however, that the present-day ECS is determined from a simulation using a slab ocean model.

The 38Ma Eocene simulations indicate a temperature response to a doubling of  $\text{CO}_2$  and  $\text{CH}_4$  ranging from a  $2^\circ\text{C}$  warming in low latitude regions to as much as  $8^\circ\text{C}$  at high latitudes ( $\sim 0.4\text{--}1.8^\circ\text{C/Wm}^{-2}$  in Figure 5.15a). The zonal variation in the warming signal is highest at middle latitudes because of land-ocean contrasts, while differences in seasonal response are largest in polar regions.

The polar amplification signal within the middle-to-late Eocene climate can be explained by looking into the changes in net fluxes (longwave and shortwave) at the top of model (TOM) as shown in Figure 5.15c-d. Considering only the clear-sky components, a large increase in longwave radiation occurs at high latitudes in correspondence to elevated surface temperatures (Planck feedback) in the  $4\times$  PIC case compared to the  $2\times$  PIC one. A positive lapse rate feedback acts to further enhance high latitude surface warmth. Localised shortwave responses can also be seen (contours in Figure 5.15c) due to decreases in sea ice cover (Arctic Ocean and Ross Sea) and surface albedo changes (snow cover and growth season length). At low latitudes, a general decrease in longwave flux can be explained by tropopause responses and stratospheric cooling, resulting in reduced outgoing radiation.

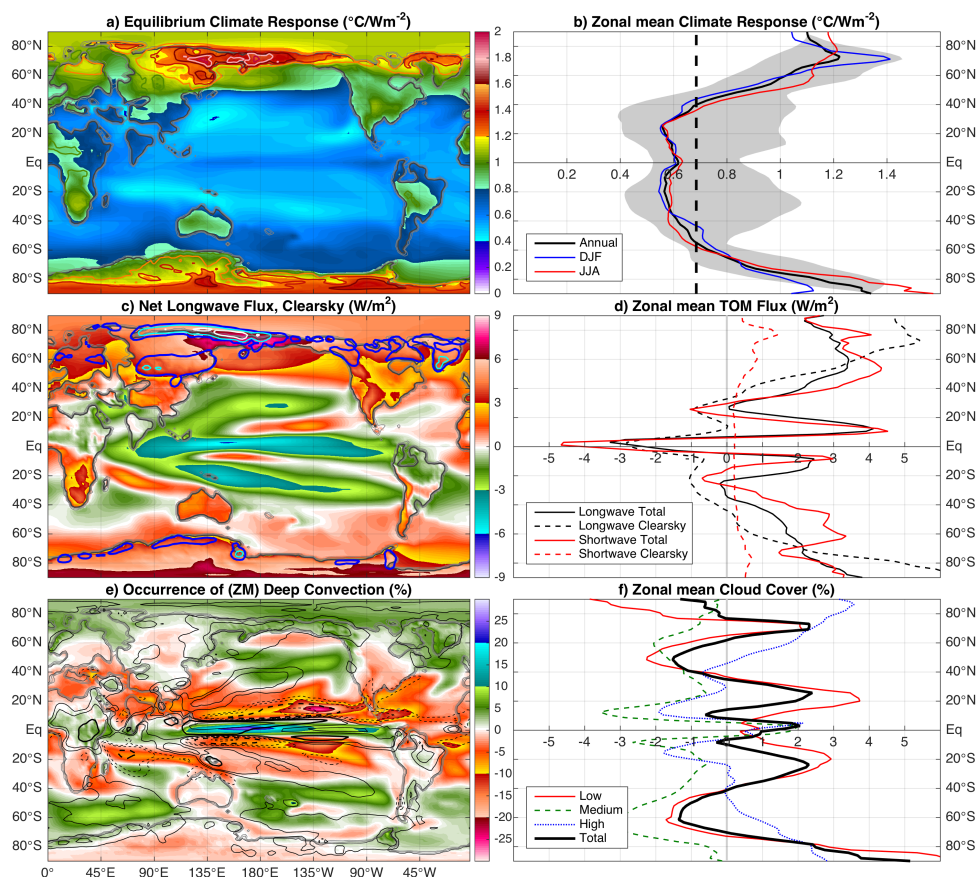


**Figure 5.15:** a) Annual mean temperature response, normalised per  $\text{W}/\text{m}^2$  of the 38Ma 4x PIC compared to the 2x PIC equilibrium climate with contours showing the winter season only (using the same colour scale). b) Zonal mean normalised temperature response; annual (black), December-January-February (blue) and June-July-August (red). The grey shading indicates minimum and maximum values for each latitude of the annual mean. The (area-weighted) global average response (i.e. climate sensitivity) is 0.69  $^{\circ}\text{C}/\text{Wm}^{-2}$  and is indicated by the black dashed line. c) Clear-sky component of the net longwave flux change at the top of model (TOM) for 4x PIC vs. 2x PIC, similar for the clear-sky shortwave flux in contours (blue: 1  $\text{W}/\text{m}^2$ , cyan: 2  $\text{W}/\text{m}^2$  and white: 5  $\text{W}/\text{m}^2$ ). d) Zonal mean TOM flux change for longwave (black) and shortwave (red) fluxes, corresponding clear-sky components are shown using dashed lines. Note that longwave fluxes are defined positive upward while shortwave fluxes are positive downward. e) Change in the occurrence of ZM (Zhang & McFarlane, 1995) parameterised deep moist convection and difference in precipitation (contours at 100, 200, 500 and 1000 mm, dashed for negative changes and thick line indicating 500mm). f) Zonal mean changes in cloud cover (in %) for low (red), medium (green) and high (blue) clouds, the thick black line indicates changes in total coverage.

In addition, strong alternating signals of differences in shortwave and longwave radiation occur with a pronounced minimum at the equator and maxima over the ITCZ locations. This suggests different patterns of deep convection and thus also precipitation, which are both shown in Figures 5.15e-f. Indeed, an increase of convection and precipitation is seen over the equatorial West Pacific, causing increased cloud cover and therefore a decrease in radiative fluxes (i.e. less outgoing longwave radiation and more reflected shortwave radiation, thus less incoming). In contrast, a decrease of deep convection and precipitation in the Pacific and South Indian Ocean ITCZ leads to a decrease in mid- and upper level clouds and thus enhanced shortwave radiation. A net heat loss (shortwave < longwave radiation) at low latitudes versus a gain at middle-high latitudes finally agrees with a reduced meridional heat flux seen in the warmer 4× PIC climate (Figure 5.5).

Stronger warming in the Pacific cold upwelling tongue (Figure 5.15a) suggests a shift towards more El Niño-like conditions in the warmer 38Ma climate. The equatorial westerlies seen in Figure 5.14 may play an important role in the regional climate through a feature resembling the Madden-Julian Oscillation (Zhang, 2005), similar to the one found in Caballero & Huber (2010). A general increase in deep convection and precipitation can be seen in most sub-tropical monsoon regions and the middle-latitudes in the 38Ma Eocene climate. A prominent decrease of low level clouds in the Arctic is also seen, due to the Arctic Ocean warming up and decreasing the strength of a summertime marine inversion. Over Antarctica, on the other hand, a large increase in low-level cloudiness is related to increased moisture helping to keep up winter temperatures at the surface (Figures 5.15e-f).

Measure \ Case	Pre-industrial	38Ma 2× PIC	38Ma 4× PIC
MAT <sub>glob</sub> (°C)	13.71	23.66	26.75
SST <sub>glob</sub> (°C)	18.35	25.83	28.36
SST <sub>eq</sub> (°C)	26.88	31.71	33.91
T <sub>deep</sub> (°C)	0.7	8.6	11.5

**Table 5.3:** Average equilibrium temperatures at the end of each simulation, showing MAT<sub>glob</sub>: global mean near surface air temperature (at 2m reference height), SST<sub>glob</sub>: global mean sea surface temperature, SST<sub>eq</sub>: equatorial (<23.5°N/S) average SST, and T<sub>deep</sub>: global mean deep ocean temperature (below 2000m). These values are calculated using the last 200 years of each simulation.

The Earth System Sensitivity (ESS) for this model set-up can be estimated by comparing either of the 38Ma Eocene simulations to the pre-industrial reference. In the middle-to-late Eocene climate not only greenhouse gases are different, but also the land-sea distribution, orography, vegetation and land ice cover (Lunt et al., 2010b). The global mean air temperature warming from the pre-industrial reference to the Eocene 2× PIC simulation, together with the radiative forcing due to the first CO<sub>2</sub> and CH<sub>4</sub> doubling ( $\Delta RF^{2\times} = 4.23 \text{ Wm}^{-2}$ ) results in  $ESS^{2\times} = 2.36^\circ\text{C/Wm}^{-2}$ . Comparing the Eocene 4× PIC simulation to the pre-industrial reference, on the other hand, gives a lower  $ESS^{4\times} = 1.49^\circ\text{C/Wm}^{-2}$ .



Using the radiative forcing from a CO<sub>2</sub> doubling ( $\Delta RF^{CO_2} = 3.8\text{W/m}^2$ ), the values of ESS determined here correspond to a 5.68–8.97 °C increase per CO<sub>2</sub> doubling. The lower of these values (considering the 4× PIC climate) lies close to the 6°C per CO<sub>2</sub> doubling ESS estimate from geological data (Royer et al., 2012).

Because the radiative forcing of both CO<sub>2</sub> and CH<sub>4</sub> depends nonlinearly on the greenhouse gas concentrations, the radiative forcing due to a quadrupling is not equal to the sum of two doublings (Etminan et al., 2016). As only model equilibrium states are compared that do not result from transient quadrupling of greenhouse gases, a linear combination is assumed here such that:

$$\Delta RF^{4\times} = \Delta RF^{2\times} + \Delta RF_{2\times}^{4\times} = 8.71\text{W/m}^2.$$

When comparing global mean temperature differences between the pre-industrial reference and both Eocene simulations, clearly not all of the warming is a result of higher greenhouse gas concentrations. To separate the effect of palaeogeography from the greenhouse gas driven warming, the 38Ma Eocene equilibrium climate sensitivity  $S_{EO}$  can be calculated using the combined radiative forcing due to greenhouse gas and palaeogeography changes by assuming that:

$$S_{EO} = \frac{\Delta T}{\Delta RF + G}, \quad (5.1)$$

where  $\Delta T$  is the temperature difference between two climatic states,  $\Delta RF$  the radiative forcing change from greenhouse gases and  $G$  the radiative forcing due to the (integral) effect of palaeogeography. Note that the latter also includes changes in the distribution of e.g. land ice and vegetation, as it is an external boundary condition in the model set-up used here. In order to be compatible with estimates of ECS and ESS given above, this formulation gives  $S$  in normalised units of [°C/Wm<sup>-2</sup>], rather than [°C per CO<sub>2</sub> doubling] as used by Royer et al. (2012).

Since both 38Ma Eocene simulations use the same (except CO<sub>2</sub> and CH<sub>4</sub>) boundary conditions, it is reasonable to assume that  $S$  and  $G$  estimated from the comparison with the pre-industrial case should be similar (provided that their nonlinear contribution is small). By comparing the temperatures of both Eocene runs to those of the pre-industrial reference,  $G$  can be then estimated from:

$$G = \frac{\Delta T^{2\times} \cdot \Delta RF^{4\times} - \Delta T^{4\times} \cdot \Delta RF^{2\times}}{\Delta T^{4\times} - \Delta T^{2\times}}, \quad (5.2)$$

where  $\Delta T^{4\times}$  and  $\Delta T^{2\times}$  denote the temperature difference with respect to the pre-industrial climate for the 38Ma 4× PIC and 2× PIC case, respectively. This leads to an estimate of  $G = 10.32\text{W/m}^2$ , and using equation 5.1 with either ( $\Delta T^{4\times}, RF^{4\times}$ ) or ( $\Delta T^{2\times}, RF^{2\times}$ ) leads to  $S = 0.69^\circ\text{C/Wm}^{-2}$  (so  $G \sim 7.12^\circ\text{C}$ ). As expected, the value of  $S_{EO}$  is the same as the one found previously when comparing both Eocene simulations to each other.

Alternatively,  $G$  can be estimated by comparing an altered pre-industrial climate under  $2\times$  PIC forcing, with the results from the modelled 38Ma  $2\times$  PIC case. Using the pre-industrial ECS determined for the model ( $S_{PI} = 0.82^\circ\text{C}/\text{Wm}^{-2}$ ) and radiative forcing of the first doubling of greenhouse gases ( $\Delta RF^{2\times}$ ), a temperature change of  $3.48^\circ\text{C}$  would be expected. As the change in global mean temperature between the pre-industrial reference and  $2\times$  PIC Eocene climate is  $9.97^\circ\text{C}$ , this leaves an additional warming of  $6.47^\circ\text{C}$  owing to integrated global geography changes. In order to convert this warming into an estimate of  $G$ , either the Eocene  $S_{EO}$  or pre-industrial  $S_{PI}$  can be used giving a possible range of  $G = 7.86\text{--}9.30 \text{ W/m}^2$ .

Finally, equatorial ( $<23.5^\circ\text{N/S}$ ) SSTs ( $SST_{eq}$ ; with a  $3/2$  ratio between global and equatorial temperature change to account for polar amplification, as discussed in Royer et al. 2012) or deep sea temperatures ( $T_{deep}$ ) are considered, to be more compatible with ECS estimates from proxy data. An overview of used temperature differences:  $SST_{eq}$  and  $T_{deep}$  in addition to  $MAT_{glob}$  (global mean, annual mean 2m temperature, used above) and the resulting values for  $S_{EO}$  and  $G$  is given in Table 5.4. Not surprisingly, the estimate of  $G$  decreases when using only oceanic temperatures as the direct effect of cooler temperatures over land ice is removed. The results for  $S_{EO}$  show less variation between different methods and are tied to the respective temperature changes between the 38Ma  $2\times$  PIC and  $4\times$  PIC cases, which are more consistent across the methods being used.

While considering global MAT changes will likely overestimate the effect of global geography changes (mainly through lapse-rate effects on ice sheets and mountains), the opposite is true for equatorial SSTs. A possible range of  $G = 5.61\text{--}10.32 \text{ W/m}^2$  is found still, equivalent to  $\sim 1.5\text{--}2.7$   $\text{CO}_2$  doublings with a most likely value around 2 doublings or a  $\sim 6^\circ\text{C}$  warming. This is considerably higher than the estimated  $1.8^\circ\text{C}$  warming related to geography (using HadCM3L) found by Lunt et al. (2012) and the  $\sim 2\text{--}4 \text{ W/m}^2$  (i.e.  $0.6\text{--}1.1$   $\text{CO}_2$  doublings) suggested by Royer et al. (2012). A comparably high warming of  $\sim 5^\circ\text{C}$  from integral geography effects in the Eocene has been proposed by Caballero & Huber (2013) that matches up with the estimates found here. Higher estimates of  $2\text{--}6^\circ\text{C}$  can also be deduced using the different models considered by Lunt et al. (2012).

Method \ Quantity				
	$\Delta T^{4\times} (^\circ\text{C})$	$\Delta T^{2\times} (^\circ\text{C})$	$S_{EO} (^\circ\text{C}/\text{Wm}^{-2})$	$G (\text{W/m}^2)$
<b>MAT<sub>glob</sub></b>	13.0	9.97	0.686	10.32
<b>SST<sub>eq</sub></b>	10.5	7.25	0.736	5.61
<b>T<sub>deep</sub></b>	10.8	7.9	0.647	7.99

**Table 5.4:** Temperature differences comparing the 38Ma  $4\times$  PIC ( $\Delta T^{4\times}$ ) and  $2\times$  PIC ( $\Delta T^{2\times}$ ) Eocene climate to the pre-industrial reference, derived values for equilibrium climate sensitivity ( $S$ ) and forcing from (integral) geography changes ( $G$ ) using equation 5.2. Results are shown using global mean 2m temperature, equatorial SST (with a  $3/2$  ratio, as discussed in Royer et al. 2012) and deep sea temperature (below 2000m).

## 5.3 Summary and Conclusions

Using version 1.0.5 of the Community Earth System Model (CESM), we presented results of simulated 38Ma Eocene climates under both high ( $4\times$  PIC) and moderate ( $2\times$  PIC) concentrations of  $\text{CO}_2$  and  $\text{CH}_4$ , using the most recent palaeogeographic constraints. These are among the first simulations with a fully-coupled and detailed climate model to study the middle-to-late Eocene climate, using a new 38Ma geography reconstruction.

The  $4\times$  PIC case shows a warm climate with a global mean near surface air temperature of about  $27^\circ\text{C}$  (pre-industrial:  $\sim 14^\circ\text{C}$ ) and a low equator to pole temperature gradient. The global heat budget is approximately meridionally symmetric, which is reflected by the zonal mean temperature pattern. Deep water formation occurs in the South Pacific Ocean, while the North Atlantic is stably stratified and stagnant due to the outflow of brackish Arctic waters. A shallow and rather weak precursor of an Antarctic Circumpolar Current is present, mainly driven by seasonally dependent wind stresses. Continental low/middle latitude regions are characterised by high seasonality on both hemispheres and strong summer monsoons. Middle and high latitudes mostly see mild winters, warm summers and pronounced storm tracks. The Arctic is rather cool due to its geographic isolation and the Antarctic continent shows strong seasonality with especially hot summers.

Comparing the 38Ma  $4\times$  PIC simulation to the available 42–38 Ma sea surface and terrestrial temperature proxy records, the simulated climate makes a fairly good match with middle-to-high latitudes without the tropics being too hot. This indicates that the CESM is able to simulate a warm greenhouse climate of the late middle Eocene ( $\sim$ Bartonian) without the need for extremely high ( $>1200\text{ppm}$   $\text{CO}_2$ ) atmospheric carbon. In the  $2\times$  PIC simulation, the patterns of oceanic and atmospheric equilibrium circulation are qualitatively very similar to those of the  $4\times$  PIC one. Based on a similar comparison between model results and 38–34 Ma proxy temperature estimates, the  $2\times$  PIC case presented here is a good analog for the late Eocene climate ( $\sim$ Priabonian).

Previous Eocene simulations (at  $4\times$  pre-industrial  $\text{CO}_2$ ) with a similar model but a different (45Ma) continental geography and lower resolution have resulted in overall similar sea surface temperature distributions (Goldner et al., 2014). However, the 38Ma  $4\times$  PIC case presented here is about  $4\text{--}5^\circ\text{C}$  warmer globally in both SSTs and land temperatures. Higher resolution and a more time-specific geography reconstruction allows for a better representation of regional features, including equatorial upwelling, zonal heterogeneity in the Southern Ocean and Antarctic summer warmth. The increase in temperature is mainly a result of a quadrupling of methane (resulting in a  $4.7\times$  pre-industrial  $\text{CO}_2$  equivalent radiative forcing), different atmospheric grids (finite volume versus spectral), cloud parameterisations and higher spatial resolution in combination with a different geography reconstruction.



Comparing the 38Ma 2× and 4× PIC cases, an equilibrium climate sensitivity of  $S_{EO} = 0.69^{\circ}\text{C}/\text{Wm}^{-2}$  was found, which is slightly lower than the same model's pre-industrial value. The difference in equilibrium climate sensitivity between the Eocene and the present-day reflects a state-dependence of the fast feedback processes, causing the Eocene climate to respond differently to a greenhouse gas doubling than the present-day climate.

When also taking the pre-industrial reference simulation into consideration, a fixed forcing  $G = 10.3\text{W}/\text{m}^2$  from (integral) geography changes was estimated ( $\sim 7.12^{\circ}\text{C}$ , using  $S_{EO}$ ). Previous studies have noted this effect in terms of an offset in global mean temperature between pre-industrial and palaeoclimate simulations (Caballero & Huber, 2013; Lunt et al., 2012). Similar to what was found by Caballero & Huber (2013) the direct effect of ice sheet distribution is limited, leaving a considerable warming due to other geography-related changes. When using oceanic instead of atmospheric temperatures, the influence of topography and land surface changes is indeed reduced mostly by excluding the direct effect of the ice sheets and vegetation changes. Although smaller, the estimate of  $G$  from oceanic temperatures is still larger ( $5.6\text{--}8.0\text{W}/\text{m}^2$ ;  $3.9\text{--}5.5^{\circ}\text{C}$ ) than suggested in most previous studies. This indicates a major contribution to  $G$  from changes in continental geometry and the related circulation patterns, that these simulations are better able to resolve. The discussion on the contribution of  $G$  will be revisited in Chapter 8, where a 1× PIC Eocene simulation is considered as well.

Several peculiar (extreme) phenomena were found in the 38Ma CESM simulations. Extremely high ( $\sim 50^{\circ}\text{C}$ ) summer temperatures occur in the sub-tropics and are probably related to fixed vegetation types. Strong seasonality is also seen on Antarctica, where summer temperatures reach up to  $35^{\circ}\text{C}$  in the 4× PIC case. The absence of an ice sheet, warm waters surrounding the continent and summertime insolation cause the Antarctic continent to become a heat island. Sea ice coverage is very limited and only occurs sporadically during the coldest months for both 38Ma Eocene cases. Even without sea ice or extensive snow cover, significant polar amplification is seen for a doubling of  $\text{CO}_2$  and  $\text{CH}_4$ . With limited surface albedo feedbacks, changes in cloud coverage and radiative forcing are the main drivers behind the further reduction of the meridional temperature gradient.

As the simulated middle-to-late Eocene (38Ma 2× PIC and 4× PIC) climate is in reasonable agreement with estimates from proxy records, the results presented here may be used to try to interpret proxy records in more detail.



# Antarctic Summer Monsoons and Ice during the Eocene

---

**Abstract** Middle and late Eocene climatic conditions seem to have been sufficiently cool to invite dispersed and small glaciations in the Antarctic hinterland. Whereas proxy data are only indicative of coastal climates, Eocene conditions on the Antarctic continent remain largely unknown. The middle-to-late Eocene CESM simulations that were presented in Chapter 5, meanwhile suggest that the Antarctic climate was characterised by extreme seasonal variability and sub-tropical summer conditions. A combination of nearby warm surface waters and strong insolation allowed Antarctica to warm up in summer, reversing the typical meridional temperature gradient. The break-up of an otherwise persistent cyclonic vortex greatly enhanced the transport of heat and moisture onto the continent to help develop a summer monsoon.

As indicated by fossil records, a perennially mild and wet climate existed along the Antarctic coastlines during most of the Eocene (Contreras et al., 2014; Jacques et al., 2014; Pross et al., 2012). Inland regions of Antarctica were characterised by high seasonality, with warm and wet summers alternated by cool and dry winters in agreement with enhanced physical and chemical weathering (Basak & Martin, 2013; Dingle et al., 1998; Dutton et al., 2002). The model results can explain warm and wet conditions suggested by various proxies, but they also permit the formation of small ice caps at higher elevations (Carter et al., 2017; Passchier et al., 2017; Scher et al., 2014). In what appears to be an intermediate greenhouse-icehouse climate, cold winters allowed for the presence of regional ice while summer warmth prevented them from growing into a continental-scale ice sheet.

While the new model results can explain the coexistence of regionally mild climates and ice on the Antarctic continent, they do not allow widespread glaciation within the 38Ma configuration. To what extent late Eocene geography changes, reduced radiative forcing or regime shifts in the meridional overturning circulation could have affected the Antarctic (and global) climate will be assessed in Chapter 7. Finally, the conditions needed for the formation of a continental-scale Antarctic Ice Sheet within the different CESM simulations will be explored in Chapter 8.

**Acknowledgement** The author would like to thank dr. Appy Sluijs, dr. Peter K. Bijl and dr. Aarnout J. van Delden in helping to put the model results into context and discussing the possibilities of Antarctic monsoons and Eocene ice.

This chapter is based on the following publication:

Baatsen, M. L. J., P. K. Bijl, A. S. von der Heydt, A. Sluijs & H. A. Dijkstra (2018c), “Antarctic Summer Monsoons in the Middle-to-late Eocene (in prep.)”, *Nature Geoscience*.

“That’s the only place in all the lands we’ve ever heard of that we don’t want to see any closer; and that’s the one place we’re trying to get to! And that’s just where we can’t get, nohow.”

J.R.R. Tolkien

## 6.1 The Eocene Antarctic Climate

Antarctica’s perennially warm and wet conditions of the early Eocene (Contreras et al., 2014; Pross et al., 2012) underwent a general cooling and amplification of seasonality during the middle and late Eocene (Contreras et al., 2013; Dingle et al., 1998). In between cool and dry winters, Antarctic summers still had high temperatures ( $>20^{\circ}\text{C}$ ) and precipitation (Basak & Martin, 2013; Dutton et al., 2002; Robert & Kennett, 1997). Knowledge of the Antarctic Eocene climate from proxies is mostly limited to coastal regions due to the current presence of the Antarctic Ice Sheet. Previous climate model studies have mainly focused on Early Eocene (Herold et al., 2014; Huber & Caballero, 2011; Huber, 2012; Lunt et al., 2012; Sagoo et al., 2013) or EOT (Gasson et al., 2014; Hill et al., 2013; Kennedy et al., 2015; Ladant et al., 2014) conditions, leaving the majority of the Eocene epoch untouched. Indications of smaller glaciations on Antarctica during the middle-to-late Eocene (Carter et al., 2017; Passchier et al., 2017; Scher et al., 2014) seem difficult to marry with vegetation reconstructions requiring temperate or sub-tropical climates.

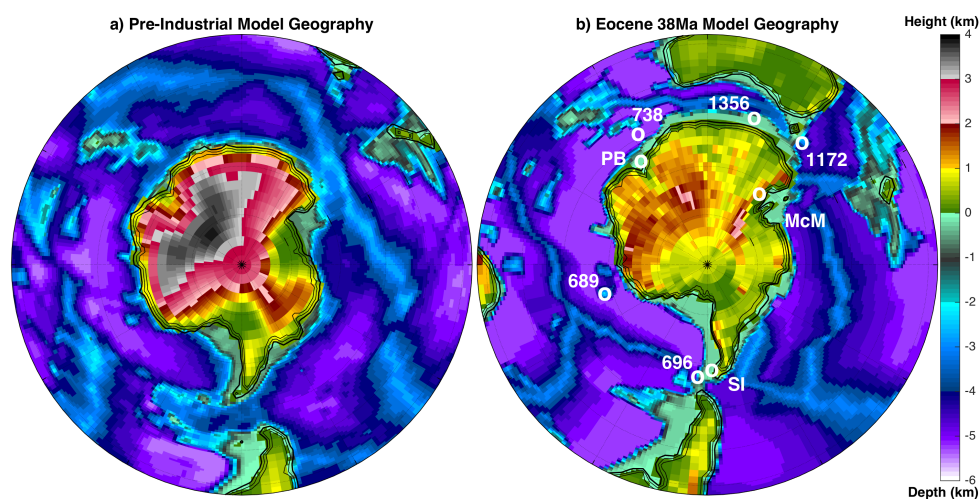


**Figure 6.1:** Comparison of **a)** pre-industrial and **b)** reconstructed 38Ma model bathymetry and topography grid (see also Figures 3.5 and 3.7). White circles show corresponding 38Ma locations of relevant drill sites: Seymour Island (SI), ODP 696, ODP 689, Prydz Bay (PB), ODP 738, U 1356, ODP 1172 and McMurdo Sound (McM).

As shown in Chapter 5 the middle-to-late Eocene (42–34 Ma) climate can be successfully reconstructed using the CESM, in accordance with marine and terrestrial temperature proxies. A recent 38Ma geography reconstruction (Chapter 2; Figures 2.8, 3.7 and 6.1) and sufficient horizontal model resolution allow for a quite detailed and realistic representation of the Antarctic climate prior to continental-scale glaciation. Previous research by Gasson et al. (2014) has shown a strong sensitivity to model (i.e. GCM) geography when considering Antarctic glaciation at the EOT. Large differences between models suggest that it is crucial to resolve the regional circulation patterns over Antarctica to get a realistic late Eocene climate.

A poorly resolved Antarctic topography results in an ice sheet growing mainly from the central highlands (Gamburtsev Range and Transantarctic Mountains) and covering most of East Antarctica before reaching the coast (DeConto & Pollard, 2003; Ladant et al., 2014). In the Antarctic climate simulated by the 38Ma CESM cases, small scale ice caps can be present over near-coastal mountainous regions (mainly Drønning Maud Land and the Antarctic Peninsula) while temperate or even sub-tropical conditions prevail elsewhere on Antarctica (e.g. on Wilkes Land).

## 6.2 Warm and Wet Antarctic Summers

Under the absence of a continental ice sheet (Coxall et al., 2005; Lear et al., 2008; Scher et al., 2011) and with mostly blocked Southern Ocean gateways (Bijl et al., 2013; Sijp et al., 2014, 2016), the Antarctic climate during the Eocene was drastically different from that of today (Figure 6.2). Even in austral summer the pre-industrial reference shows cold and dry conditions on the Antarctic continent, shielded by a belt of cyclonic winds that are associated with a strong pressure and temperature gradient. A minimum in sea level pressure is found near the coast, while the continental interior exhibits high pressure under cold, sinking air.

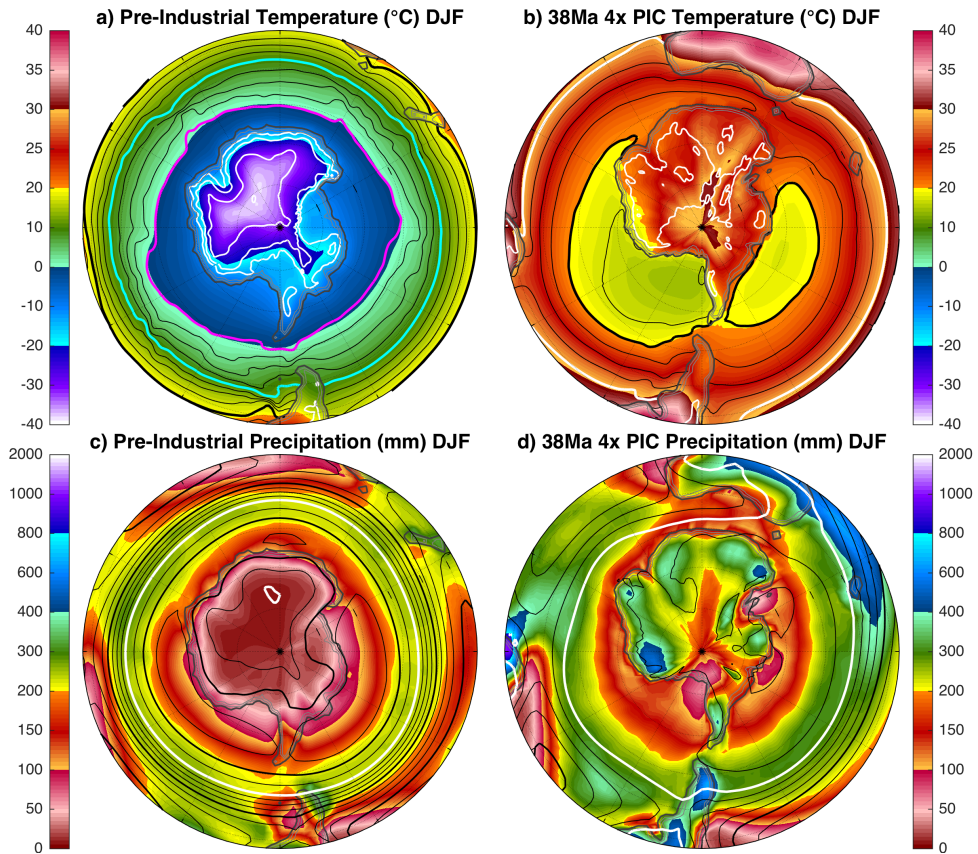


**Figure 6.2:** Southern high latitude summer climate (December–February), with **a)** pre-industrial and **b)** 38Ma 4x PIC near surface air temperature (shading, °C) and SST (contours every 2.5°C; magenta: 0°C, cyan: 10°C, black: 20°C and white: 30°C). **c)** and **d)** as in **a)** and **b)**, but for total summer precipitation (shading, mm) and mean sea level pressure (contours every 2.5hPa >1000hPa, every 5hPa <1000hPa, thick lines every 10hPa and thick white line at 1000hPa).

In contrast, the simulated 38Ma 4× PIC summer climate (without ice sheet) exhibits much weaker meridional gradients and lacks high pressure over the Antarctic continent. Coastal temperatures are a mild 20–25 °C, while the continental interior heats up to over 30°C in low-lying regions. Most of Antarctica receives 100–600 mm of summer (DJF) precipitation, characterised by the influence of local topography and generally decreasing further inland.

In contrast to the Eocene climate, Antarctic pre-industrial summer conditions differ little from those seen during a typical polar winter. The latter is accompanied by a persistent negative poleward temperature gradient in the troposphere and a cyclonic polar jet (positive zonal wind; Figure 6.3a and A.5a-b). The Eocene configuration shows a reversal of the temperature gradient and an anticyclonic polar jet, thus blowing in the opposite direction (Figure 5.14a-b and 6.3b).

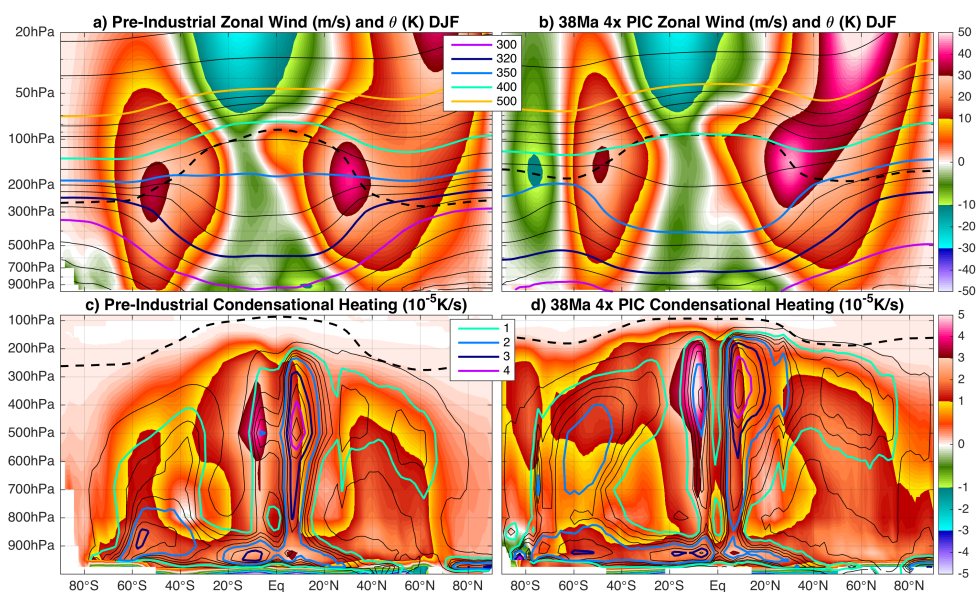


**Figure 6.3:** Southern Hemisphere summer (December–February) average **a)** pre-industrial and **b)** 38Ma 4× PIC zonal mean zonal wind (shading, m/s) and potential temperature (contours every 10K up to 350K, 25K up to 500K and 100K intervals onwards), tropopause height is indicated by the dashed black line. **c)** and **d)** as in **a)** and **b)**, but for condensational heating during SH summer (shading,  $10^{-5}$  K/s) and winter (June–August; contours every  $0.5 \cdot 10^{-5}$  K/s and  $0.25 \cdot 10^{-5}$  K/s in the  $1\text{--}2 \cdot 10^{-5}$  K/s interval).

Potential temperature rather than the actual temperature is shown in Figure 6.3, as it illustrates how southern polar regions are adiabatically connected to low latitude air masses in summer at 38Ma. In the winter hemisphere, polar air is effectively trapped beneath the lowest isotherm ( $\sim 305$  K) isolating it and increasing temperature contrasts. This trapping of polar air is present on both hemispheres for the pre-industrial reference, explaining the winter-like conditions on Antarctica during Southern Hemisphere summer. The meridional connection that can be made in the 38Ma Antarctic climate greatly facilitates southward heat and moisture fluxes in summer.



The profoundly different atmospheric structure and corresponding circulation over southern high latitudes in summer are closely related to the disappearance of a polar cell in the meridional stream function (Figure 5.14d) and the reversal of the polar jet (Figure 6.3b).

Zonal averages of condensational heating (Figure 6.3c-d) can be used as an indicator for the main features governing the hydrological cycle. Latent heat of evaporation is generally absorbed by the atmosphere near the surface, mostly above water. This heat is released again when condensation occurs in rising and thus cooling air. A considerable contribution to such heating takes place in shallow convection, seen as a low level (900–950 hPa) maximum at most latitudes.

A second mechanism to release latent heat is through deep convection, which is most prominent in the tropics and related to the upward branches of the Hadley cells (see Figure 5.14c-d) that are collocated with the ITCZ. A pronounced double structure is present in both the pre-industrial and 38Ma 4× PIC simulation owing to the double ITCZ structure, with its strongest component in the summer hemisphere. The effects of deep convection are also seen at higher latitudes, mainly in summer as a high altitude (~400hPa) maximum in condensational heating. Those maxima indicate the presence of sub-tropical summer monsoons, with a distinct peak located at ~25–30 °N representing the East-Asian Monsoon in both simulations (contours in Figure 6.3c-d).

Finally, the release of latent heat is also an important component of winter storm tracks. In the warm conveyor belt of a middle latitude cyclone, slanted ascent of warm and moist air forces it to cool down resulting in condensation of water vapour. As the slanted ascent starts from low levels and induces a more steady condensation rate, the vertical structure of the resulted heating is different to that of deep convection. Most prominently in winter, a plume of condensational heating is seen at middle latitudes that is connected to the surface and has a maximum in the lower and middle troposphere (~850 and ~600hPa).

Although the general structure and seasonality of condensational heating are similar for the pre-industrial and 38Ma 4× PIC climate, there are several important differences. First of all, the depth of the hydrological cycle is increased in the warmer case and related to a greater tropopause height.

Secondly, the plumes related to winter storm tracks are not only deeper but also more intense in the 38Ma 4× PIC case. This is somewhat surprising, as a decrease in baroclinic activity would be expected with a lower meridional temperature gradient. In contrast, higher moisture content in the atmosphere increases the contribution of latent heating to the deepening of middle latitude cyclones (i.e. the warm sector is kept warm by condensation rather than advection).

Lastly, the intensity of summer monsoons is also increased which is to be expected in a generally warmer climate. Especially over the Southern Hemisphere, condensational heating related to deep convection can be seen all the way to the pole for the 38Ma 4× PIC climate while being completely absent in the pre-industrial reference.

## 6.3 An Antarctic Summer Monsoon

Strong seasonality is seen in all sectors of Antarctica, while increasing further inland (Figures 6.4 and 6.5). A prominent peak in summer precipitation and high temperatures are evident over continental regions in both 38Ma simulations. A secondary peak in precipitation is seen in autumn and can be associated with a rapid decrease in high latitude temperature. The resulting seasonally increased meridional gradient subsequently enhances baroclinic instability.

Coastal regions are generally wet year-round with a broad precipitation maximum in winter, but receiving much higher totals in the Eocene compared to pre-industrial conditions (Table 6.1). This is in agreement with a temperate forest or sub-tropical vegetation (mostly *Nothofagus*) reconstructed for the middle Eocene Wilkes Land East Antarctic Margin (Contreras et al., 2013; Pross et al., 2012). The same regions saw para-tropical forests during the early Eocene. Most of the continent has mild mean annual temperatures of 2–12 °C and 400–1700 mm of precipitation in the 38Ma 4× PIC case. Although still showing strong seasonality, a considerable fraction of coastal regions has a coldest month mean temperature near or above freezing (sustained by nearby ~10°C waters). Meanwhile, a ~40°C temperature difference is seen between the mean coldest and warmest month over central Antarctica.

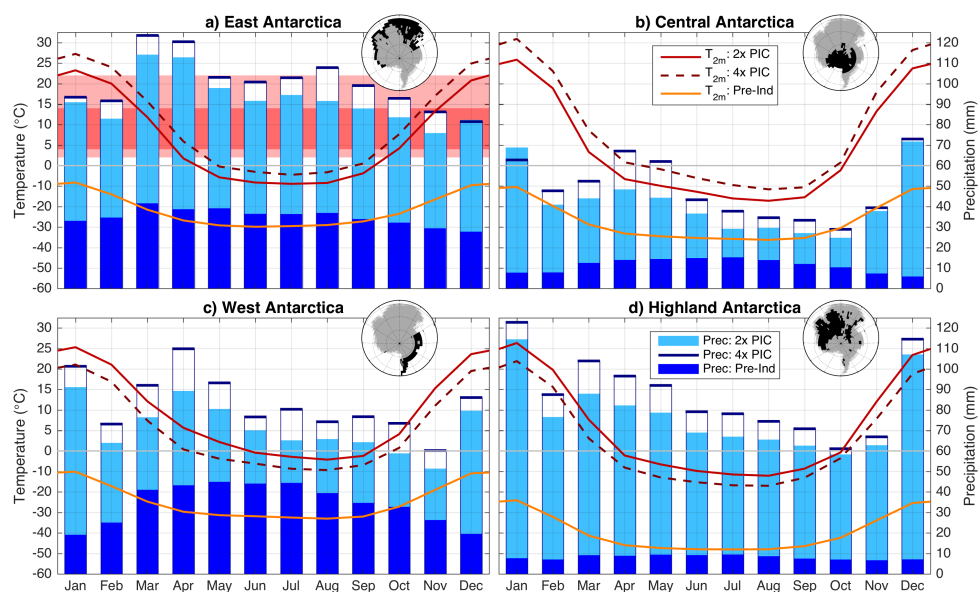


**Figure 6.4:** Monthly climatology for a) East, b) Central, c) West and d) Highland (>1km) Antarctica, showing 2m temperature (lines) and precipitation (blue bars) for 38Ma 4× and 2× PIC cases and the pre-industrial reference. Red bars in a) represent the range of middle Eocene temperature proxies from ODP Site U1356 (Wilkes Land Margin; Passchier et al. 2013; Pross et al. 2012); light: seasonal range, dark: annual mean. The extent of the respective regions in the 38Ma model geography is highlighted by the black shaded region in the upper right corner of each panel.

On average, about half of the annual precipitation falls in summer over the central and elevated Antarctic regions. Some places meet the criteria for a sub-tropical summer monsoon, with at least 300mm of summer (NDJFM) precipitation making up 60% or more of the annual budget. Most places outside of the continental interior don't meet these criteria, because of the short summer wet season (2–3 months) and high winter precipitation (Table 6.1).

Case	Measure	West	East	Central	Highland
38Ma 4×PIC	MAT (°C)	9.2 ± 3.1	9.0 ± 3.2	5.9 ± 1.2	3.3 ± 1.5
	CMT (°C)	-2.1 ± 5.9	-5.3 ± 7.2	-11.8 ± 2.8	-12.4 ± 2.8
	WMT (°C)	24.5 ± 2.6	27.7 ± 4.0	31.2 ± 3.1	26.5 ± 4.0
	MAP (mm)	1159 ± 560	1118 ± 573	573 ± 152	1047 ± 691
	MSP (mm)	468 ± 192	443 ± 184	270 ± 78	494 ± 204
	SPR (%)	42 ± 9	43 ± 11	48 ± 12	52 ± 10
Pre-industrial	MAT (°C)	-23.2 ± 4.4	-22.0 ± 3.2	-27.0 ± 2.3	-39.6 ± 7.9
	CMT (°C)	-31.9 ± 5.0	-30.0 ± 3.8	-36.1 ± 3.8	-47.6 ± 7.8
	WMT (°C)	-9.3 ± 2.6	-8.0 ± 2.0	-10.4 ± 1.4	-23.5 ± 5.9
	MAP (mm)	465 ± 203	407 ± 169	135 ± 54	104 ± 80
	MSP (mm)	154 ± 75	163 ± 70	41 ± 13	40 ± 26
	SPR (%)	33 ± 5	41 ± 6	32 ± 8	43 ± 8

**Table 6.1:** Climate statistics (mean and standard deviation) for West, East, Central and Highland Antarctic regions as defined in Figure 6.4. Shown are annual mean 2m temperature (MAT), coldest month mean (CMT) and warmest month mean temperature (WMT). Concerning precipitation, total annual (MAP) and summer (i.e. NDJFM) precipitation (MSP) are given as well as the ratio of summer to annual (SPR). The latter is determined for each location separately before averaging, and thus not applied to the mean values already shown.

Still, the mechanism behind a sub-tropical like summer monsoon and the related circulation features are all present (Figure 6.5) in the 38Ma 4× PIC Antarctic climate. Cool, sinking air in winter builds up a low level anticyclone within the larger and deeper cyclonic vortex, similar to the one seen year-round over Antarctica in the pre-industrial reference. In summer, rising motion forms a thermal low pressure area over the Antarctic continent featuring onshore cyclonic flow. At mid-upper levels, the same circulation pattern and related advection of heat increase thickness levels to create the ridge responsible for the anticyclonic flow seen in Figure 6.3b.

Moisture transport from lower latitudes and the release of latent heat in deep convection contributes significantly to summer warmth and rainfall, while enhanced storm tracks and orographic lift boost winter precipitation (Figures 6.2d and 6.3d). These model results agree well with fossil records of the middle Eocene, showing a warm and wet temperate climate in coastal regions (Contreras et al., 2013; Pross et al., 2012). Strong seasonality and high summer rainfall suggest the presence of a summer monsoon (Jacques et al., 2014) and are supported by indications of chemical weathering (Basak & Martin, 2013; Scher et al., 2011).

Previous model studies have shown a relatively warm and wet climate on Antarctica during the early Eocene (Huber & Goldner, 2011). Seasonality and annual rainfall are less pronounced in those simulations, probably related to a more limited representation of the Antarctic continent. In this sense, the simulations presented here are the first to show the regional climate of Antarctica in the Eocene with a sufficiently resolved continental geometry. The result is a more extreme, warmer and wetter Antarctic climate that exhibits a summer monsoon as suggested by plant fossil reconstructions (Jacques et al., 2014).

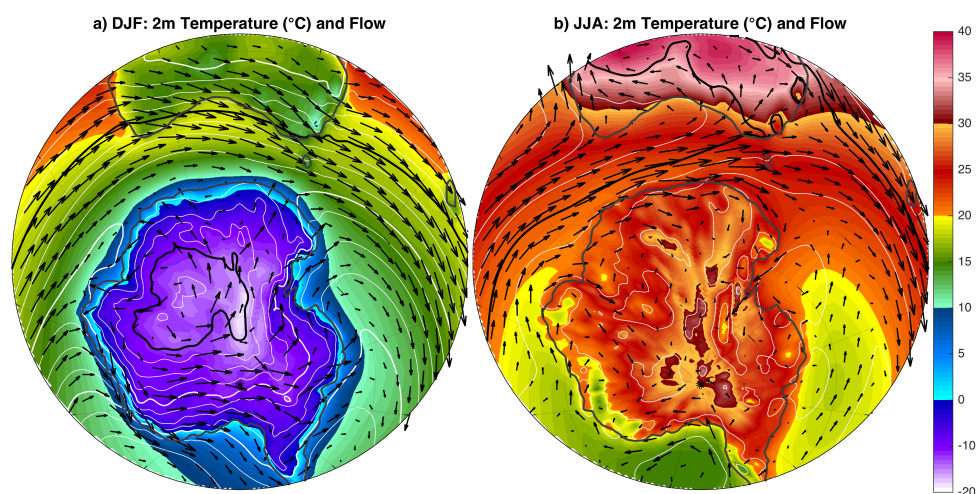


**Figure 6.5:** Oblique polar stereographic view of the Antarctic-Australian region, showing summer (December–February) and winter (June–August) averages of the 38Ma 4× PIC simulation. Colour shading indicates near surface air temperature, contour lines show mean sea level pressure (white line every 2.5hPa, thick black line every 10hPa) and arrows representing near surface (~250m) flow.

## 6.4 Eocene Ice on Antarctica

The possibilities for ice growth on Antarctica are explored by considering the surface mass balance (SMB) in the 38Ma  $2\times$  PIC model results. Using a simple positive degree day (PDD) scheme, the SMB can be estimated by assuming 4mm of melt per PDD and inverted into a potential surface melt (Figure 6.6). For simplicity, the annual mean precipitation is considered here, as this is mostly snow in the highest regions (while low lands are dominated by summer warmth). Using the PDD scheme and total precipitation implies a rather simplified approach, but yields a lower limit to the conditions needed for ice growth. Indeed, the inclusion of additional components (e.g. rain/snow ratio or refreezing) will generally act to reduce the resulting surface mass balance. Model 2m temperatures are adjusted to the original smoothed  $0.1^\circ$  grid of the geography reconstruction (Figure 2.8) using an atmospheric lapse rate of  $-8\text{K/km}$ . The resulting temperature, potential melt, precipitation and topography are shown along a cross section from Drønning Maud Land (A;  $32.5^\circ\text{E}$ ), through the South Pole (SP) towards Wilkes Land (B;  $135^\circ\text{E}$ ). The relatively small difference between model grid and high resolution indicates that the model captures the Antarctic topography quite well.

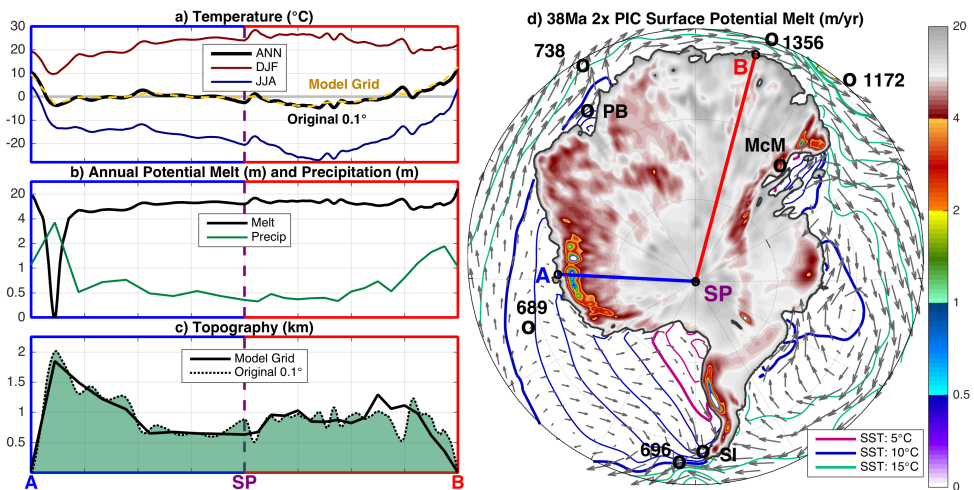


**Figure 6.6:** Antarctic cross sections from Drønning Maud Land (A;  $32.5^\circ\text{E}$ ) through the South Pole (SP), into Wilkes land (B;  $135^\circ\text{E}$ ), showing a) temperature, b) annual potential melt and precipitation, and c) topography for the 38Ma  $2\times$  PIC case. Potential melt is estimated from the yearly sum of positive degree days (PDD) and total precipitation, assuming 4mm of melt per PDD; so ice growth occurs where this reaches 0. An overview of potential melt is given by colour shading in d), along with the transect considered in a-c, annual mean SST (contours) and upper 100m average oceanic flow (arrows). Relevant drilling sites along the Antarctic margin are highlighted and named in black, as illustrated in Figure 6.1.

Even in the cooler 38Ma  $2\times$  PIC case, annual mean temperatures are around or above zero throughout the cross section shown in Figure 6.6, with winter temperatures well above freezing near the coast. Warm summers and limited precipitation result in high ( $>2\text{m/year}$ ) to extreme ( $>10\text{m/year}$ ) potential melt across the continental interior of Antarctica. Apart from some isolated regions (Drønning Maud Land, the Antarctic Peninsula and Transantarctic Mountains), ice sheet growth is highly unlikely even at relatively low radiative forcing. The  $2\times$  PIC forcing (equivalent to  $2.15\times$  PI  $\text{CO}_2$ ) considered here is well below the  $\sim 2.5\text{--}3\times$  PI  $\text{CO}_2$  threshold suggested in previous studies (DeConto & Pollard, 2003; DeConto et al., 2008; Gasson et al., 2014). Surprisingly, the isolated regions that favour ice accumulation lie very close to the coast and do so thanks to a combination of high precipitation (up to 4m annually) and cool temperatures (at  $\sim 2\text{km}$  elevation).

The position of the Antarctic continent is also of importance, as it is shifted away from the South Pole towards the Eastern Hemisphere with respect to today (Chapter 2, Figure 2.8; Hinsbergen et al. 2015). This causes the winter circulation to split into an anticyclone over East Antarctica and a cyclone over both the Weddell Sea and Antarctic Peninsula (Figure 6.7d). The resulting cross-continental flow in between (seen in Figures 6.5 and 6.7) acts to enhance winter precipitation over both Drønning Maud Land and the Antarctic Peninsula in addition to wet autumn/winter storm tracks under prevailing westerlies.

Although less pronounced, a comparable asymmetry in the pressure and circulation patterns is also present in summer (Figure 6.5b). Most of the East Antarctic coastline (Especially Wilkes Land) is dominated by westerlies, suppressing the seasonal cycle and sustaining mild, wet conditions. Those westerly winds at high southern latitude ( $\sim 60^\circ\text{S}$ ) are the main cause of warm surface waters flowing southward and eastward towards Tasmania and New Zealand (discussed in Section 5.2.1).

In contrast, the Antarctic Peninsula and surrounding coastlines are embedded between polar gyre circulations in the Weddell and Ross Sea (seen in Figure 6.6d). Instead of westerly winds, high latitude easterlies thus cause orographic lift and enhanced precipitation over Drønning Maud land, the Antarctic Peninsula and Transantarctic Mountains.

The continental interior is dominated by monsoonal circulation patterns (winter anticyclone, summer cyclone) and the associated extreme seasonality in both temperature and precipitation.

The seasonal circulation patterns thus favour limited ice growth mostly over near-coastal Drønning Maud Land and the Antarctic Peninsula. Surface ocean currents in the Weddell Gyre then allow the transport of (mostly fine;  $\sim 0.1\text{mm}$ ) ice rafted debris (IRD) from marine terminating glaciers at both these locations towards where they are found at ODP Site 696 (Carter et al., 2017) (South Orkney Microcontinent). Meanwhile, mild ( $0\text{--}10^\circ\text{C}$  MAT; Figure 6.6a) and wet ( $1\text{--}2\text{ m}$  MAP; Figure 6.6b) conditions prevail on Wilkes Land explaining fossil records and pollen data (Contreras et al., 2013; Passchier et al., 2013; Pross et al., 2012).

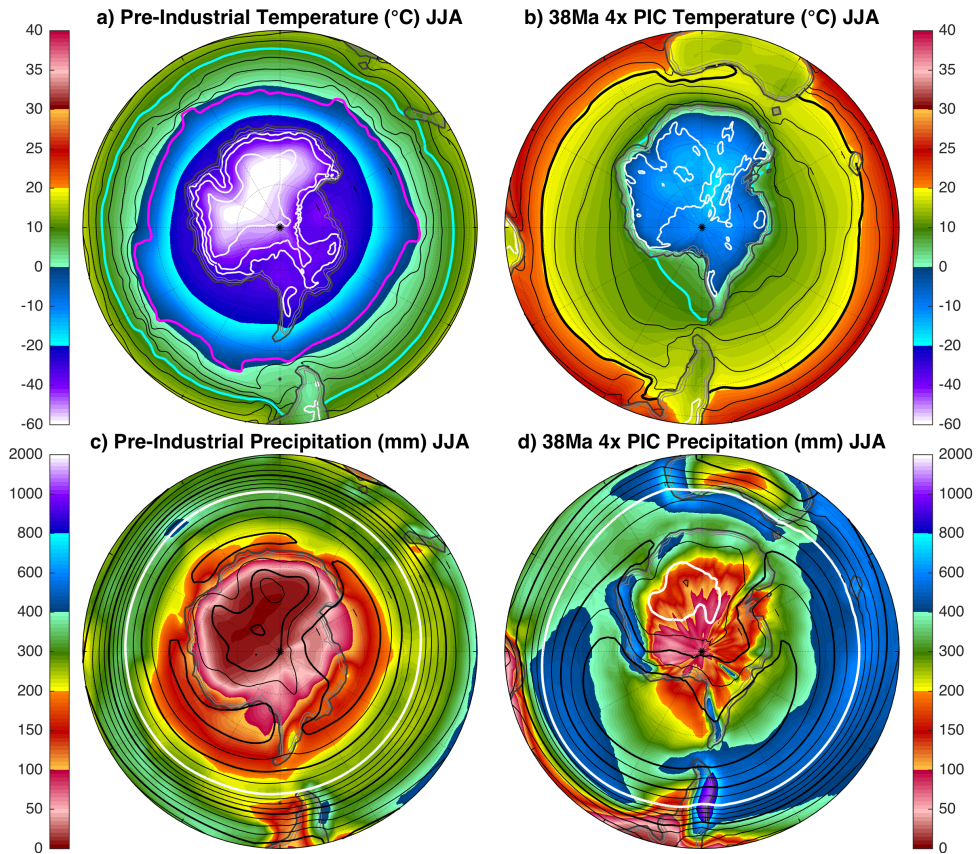


**Figure 6.7:** Southern high latitude winter climate (June–August), with **a)** pre-industrial and **b)** 38Ma  $4\times$  PIC 2m air temperature (shading,  $^{\circ}\text{C}$ ) and SST (contours every  $2.5^{\circ}\text{C}$ ; magenta:  $0^{\circ}\text{C}$ , cyan:  $10^{\circ}\text{C}$ , black:  $20^{\circ}\text{C}$  and white:  $30^{\circ}\text{C}$ ). **c)** and **d)** as in **a** and **b**, but for total summer precipitation (shading, mm) and mean sea level pressure (contours every  $2.5\text{hPa}$   $>1000\text{hPa}$ , every  $5\text{hPa}$   $<1000\text{hPa}$ , thick lines every  $10\text{hPa}$  and thick white line at  $1000\text{hPa}$ ).



## 6.5 Summary: Antarctic Ice and Warmth, a Paradox?

The Antarctic climate of the middle-to-late Eocene was characterised by high seasonality, with notably warm and wet summers (Figure 6.2). Coastal regions experienced mild and wet winters, while further inland winter conditions were cold and dry but far less extreme than those seen today over the ice sheet (Figure 6.4). High latitude warmth was promoted by a much weaker meridional temperature gradient in sea surface temperatures (facilitated without a deep circumpolar current) and the absence of a continental-scale ice sheet. Under 38Ma austral summer conditions, the Antarctic continent heats up and the otherwise dominant cyclonic polar vortex breaks down under a reversed meridional temperature gradient. The release of latent heat in deep convection adds to the warming over Antarctica and enhances a poleward flow of heat and moisture, in a circulation similar to that of a sub-tropical summer monsoon (Figure 6.3).

The conditions seen on Antarctica in these 38Ma CESM simulations fit well with vegetation reconstructions for the middle Eocene. Chemical weathering suggests a climate with warm and wet summers, while physical weathering and various fossil records show the effects of high seasonality further inland. Frost weary vegetation could easily survive in coastal regions even under relatively modest radiative forcing (i.e.  $2 \times \text{PIC}$ ). Mild, ever wet conditions allow for the presence of temperate or sub-tropical rain forests on a significant part of Antarctica, extending beyond the continental fringes.

While warm and wet conditions are seemingly in disagreement with indications of ice on Antarctica during the Eocene (as suggested by IRD; Carter et al. 2017; Passchier et al. 2017; Scher et al. 2014), the model results presented here are able to reconcile both features. Near-coastal regions at a higher elevation see a combination of high precipitation, cool summers and cold winters which permits the growth of glaciers and small ice caps. Especially during cooler intervals of the late Eocene, these ice caps could have grown considerably while the general atmospheric and oceanic circulation kept coastal temperatures mild. Summer warmth in most of the continental interior of Antarctica would still prevent the further growth of localised ice sheets, indicating that considerable regional climatic changes were needed before a continental-scale Antarctic Ice Sheet was able to form.



# CESM Simulations using a 30Ma Geography Reconstruction

---

**Abstract** The formation of an Antarctic Ice Sheet at the Eocene-Oligocene transition (EOT) is often linked to either a decrease in atmospheric CO<sub>2</sub> or the opening of Southern Ocean gateways. Instead of looking at only the influence of several oceanic passages, the effect of global geography changes taking place around the EOT is assessed here. This is done by performing CESM simulations using a 30Ma geography reconstruction (from Chapter 2) in addition to those with a 38Ma one, discussed in Chapters 5 and 6. An additional experiment with a temporary surface fresh water flux perturbation is also considered to explore the possibility of multiple equilibria in the ocean circulation, analogous to those seen in Chapter 4 but in a coupled model set-up here.

Significant differences are found in both the oceanic and atmospheric circulation between the results from model simulations using a 30Ma and 38Ma geography reconstruction. The changes mainly consist of the formation of a deep Antarctic Circumpolar Current (ACC) and shifts in polar fronts along with the associated jet streams. Despite some redistribution of heat fluxes, global temperatures under equal radiative forcing are similar regardless of the (30Ma or 38Ma) geography. Surprisingly, the relatively warm and wet Antarctic monsoonal climate is mostly unaffected by either the onset of a deep ACC or a shift in meridional overturning regime.

An extensive overview of the results from all six different CESM simulations will be given in Chapter 8, along with a discussion on the implications for potential Antarctic glaciation at the EOT.



“The great storm is coming, but the tide has turned.”

J.R.R. Tolkien

## 7.1 Model Geography Difference

The 30Ma PaleoMag geography reconstruction used here was presented at the end of Chapter 2 (Figure 2.9) and a comparison between the corresponding 30Ma model grid and the previously used 38Ma one is shown in Figure 7.1 (see also Chapter 3, Figure 3.7). Apart from the Himalayas and Tibetan Plateau, topography mostly is similar for both time frames so the main geography changes are found at middle/high latitude oceanic gateways.

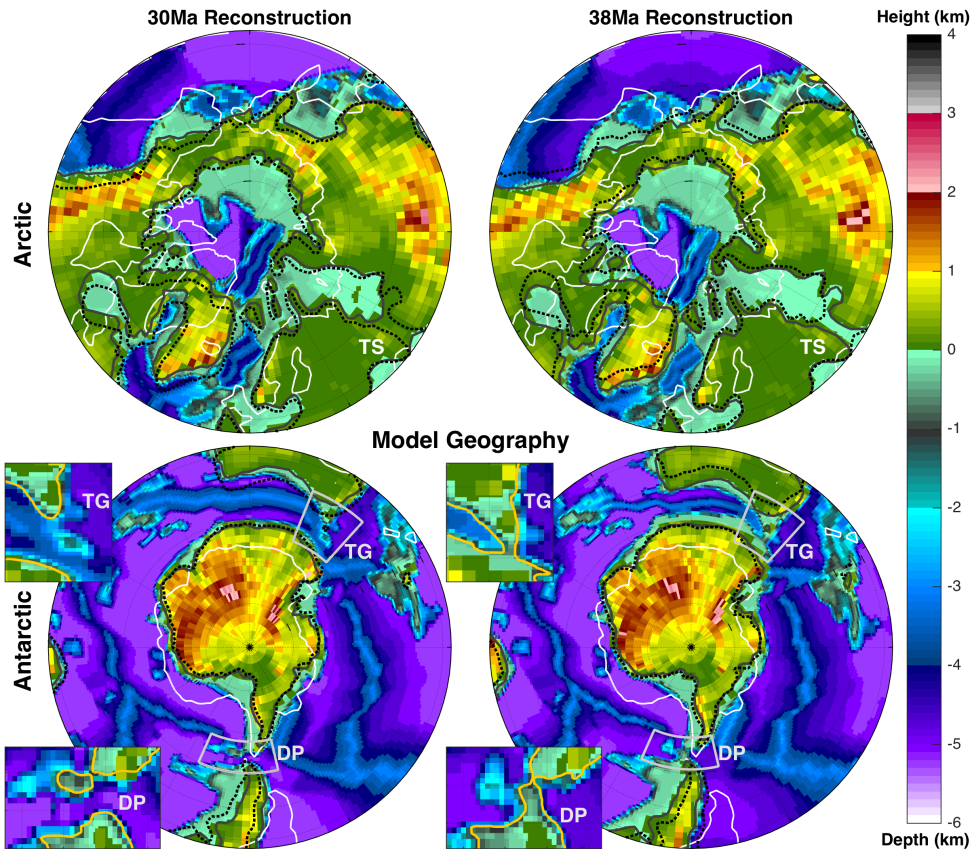


**Figure 7.1:** North (upper panels) and south (lower panels) polar stereographic projections of the 30Ma (left panels) and 38Ma (right panels) geography reconstruction derived model bathymetry and topography grids. Grey lines indicate the corresponding coastlines and white lines the pre-industrial equivalent; TS: Turgai Strait, TG: Tasmanian Gateway and DP: Drake Passage. Similar to Figure 3.7, black dotted lines show the coastlines of the opposing geography for comparison. Insets Of the bottom panels (corresponding to black boxes) show a more detailed geography of the Tasmanian gateway (TG) and Drake Passage (DP).

At 30Ma, the Drake Passage (DP) consists of a relatively narrow yet deep oceanic channel while the Tasmanian Gateway (TG) has overall widened and deepened since 38Ma. In contrast to Australia is moving northward, Antarctica has shifted slightly poleward, but remains displaced towards the Eastern Hemisphere with respect to its present-day position. Oceanic spreading is taking place across the Atlantic, but the most important change in the Northern Hemisphere is the closing of the Turgai Strait (TS; Figure 7.1) formerly connecting the Arctic Ocean to the Paratethys and Neotethys basins.

It is important to note that despite the use of a 30Ma-based geography reconstruction, the simulations considered below are not supposed to represent the early Oligocene. As in the 38Ma cases, a late Eocene vegetation cover is used (adjusted to the 30Ma land mask) and there is no Antarctic Ice Sheet. In fact, we are still looking at the late Eocene climate but simply using a 30Ma-based geography reconstruction to incorporate the purely tectonically driven changes around the EOT.

## 7.2 Spin-up and Simulations

Similar to the 38Ma configuration, a long spin-up is performed for the 30Ma 2× PIC case, starting from the same stagnant initial conditions (i.e. 15°C at the surface, 9°C at the bottom and 35psu everywhere for the ocean). Instead of running parallel from the start, a 1× PIC simulation is branched off from the 30Ma 2× PIC case after 1800 model years. At that point the circulation is mostly equilibrated for 2× PIC, after which the adjustment to reduced radiative forcing should be relatively quick considering the reduced thermal stratification (in contrast to 4× PIC; Figure 5.1). A third simulation (2× PIC Adjusted) is also branched off at the same point from the 30Ma 2× PIC case. This simulation serves to assess whether multiple equilibria regarding the meridional overturning circulation exist in the coupled simulations. An overview of the different 30Ma cases, their spin-up times and trends is given in Table 7.1, the according temperature evolutions during spin up are shown in Figure 7.2 (including the pre-industrial reference).

Property \ Case	30Ma 1× PIC	30Ma 2× PIC	30Ma 2× PIC Adj
CO <sub>2</sub> (ppm)	280	560	560
CH <sub>4</sub> (ppb)	671	1342	1342
Spin-up (years)	1800+3000	3000	1800+1200
$\Delta T$ (K/year)	$-3.2 \cdot 10^{-4}$	$1.9 \cdot 10^{-5}$	$-5.2 \cdot 10^{-4}$
$\Delta S$ (psu/year)	$-1.8 \cdot 10^{-6}$	$-8.3 \cdot 10^{-7}$	$-2.4 \cdot 10^{-6}$
$\Delta T/T$ (1/year)	$-1.2 \cdot 10^{-6}$	$6.5 \cdot 10^{-8}$	$-1.8 \cdot 10^{-6}$
$\Delta S/S$ (1/year)	$-5.2 \cdot 10^{-8}$	$-2.4 \cdot 10^{-8}$	$-6.9 \cdot 10^{-8}$

**Table 7.1:** Overview of characteristics for all the CESM 1.0.5 simulations that were performed using a 30Ma geography and late Eocene vegetation. Temperature and salinity trends are determined using the last 200 model years of each simulation, normalised values are divided by the temperature in K and salinity in psu averaged over the same time interval.

Following up on the results of Chapter 4, the possibility of a northern sinking state is explored within a coupled model framework in the 30Ma 2× PIC Adjusted case. This is done by applying a -0.5 Sv perturbation to the surface fresh water flux over the North Pacific Ocean northward of 45°N (equivalent to a ~2.3mm/day net evaporation). An opposing +0.5 Sv fresh water flux is also distributed over the rest of the ocean (excluding the Arctic; ~0.1mm/day) to conserve the global salinity budget. The adjusted forcing is maintained for 200 model years, after which the simulation is continued without further external perturbations.

Considering the similar boundary conditions and radiative forcing, it is not surprising that the initial conditions chosen here work well for the 30Ma 2× PIC case as they did for 38Ma. The upper ocean is well equilibrated after about 1500 years of spin-up, as shown in Figure 7.2a. The simulation is then continued for another 1500 years to further relax deep ocean temperatures, along with Southern Ocean gateway transports and the meridional overturning circulation strength (Figure 7.3).

The associated trends and patterns of ideal age tracers (a measure for oceanic ventilation timescales; England 1995; Thiele & Sarmiento 1990) are shown further down in Figure 7.4.

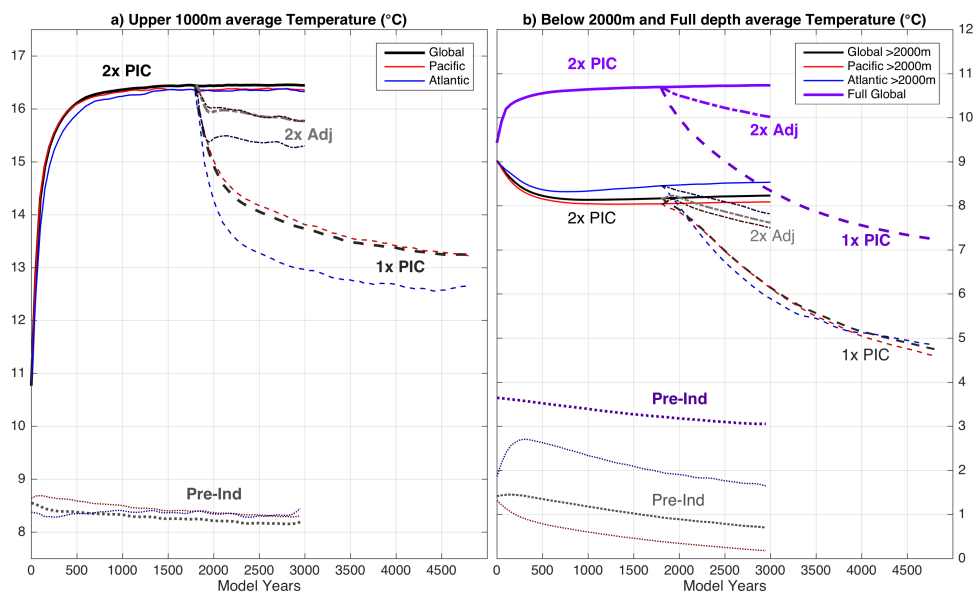


**Figure 7.2:** Time series of **a)** upper 1000m and **b)** below 2000m volume-weighted average oceanic temperatures for the 30Ma 2× PIC (solid), 2× PIC Adjusted (dash-dotted), 1× PIC (dashed) late Eocene and pre-industrial (dotted) spin-up simulations. Averages are shown globally (black) and for both the Pacific (red) and Atlantic (blue) ocean basins separately. Full depth global average temperature is also shown for each run using thick purple lines.

The 30Ma 2× PIC Adjusted case with a surface fresh water flux perturbation (lasting 200 years) shows only minor trends after some initial (local) adjustments. The simulation is then continued with the original (30Ma 2× PIC) external boundary conditions and stopped after another 1000 model years. As expected, the 1× PIC simulation responds rapidly to the reduced radiative forcing and cools down about 3°C in the upper ocean over the first 1000 years. However, the deep ocean response is slower than anticipated and still seems to be dictated by a diffusive timescale of several 1000 years. The 1× PIC case is thus only stopped after an additional 3000 model years when trends in the full depth averaged oceanic temperature are similar to those seen at the end of the 38Ma 4× PIC simulation (after 4000 model years; see Table 5.2 and Figure 5.1). Trends in global mean, volume weighted oceanic temperature are in the order of  $10^{-4}$  K/year while those of salinity are generally  $\sim 10^{-6}$  psu/year at the end (last 200 years) of all 30Ma simulations. Both temperature and salinity trends are an order of magnitude smaller at the end of the spin-up for the 2× PIC case (Table 7.1).

In both the 38Ma (Figure 5.1) and 30Ma (Figure 7.2) CESM simulations, the 2× PIC case equilibrates much faster than the others. Long spin-up procedures are tedious and pose a limit to the possibilities (e.g. model complexity, resolution, number of

experiments) of palaeoclimate modelling. Several techniques exist to accelerate the adjustment of deep ocean temperatures, such as enhanced mixing implemented by Huber & Sloan (2001). These are not without issues and still require a longer continuation of the model simulation at the end, using the standard configuration. By closely matching the full depth global mean oceanic temperature in the  $2\times$  PIC cases presented here, the required heat exchange and thus changes in total oceanic heat content during the spin-up simulation are minimised. This suggests that it can be a good alternative strategy to estimate the (full depth) average oceanic equilibrium temperature for each simulation in advance and adjust the initial state accordingly. Considering the vast differences in temperature between pre-industrial and Eocene simulations, this is not always an easy task and probably only feasible when preceding similar cases already exist.

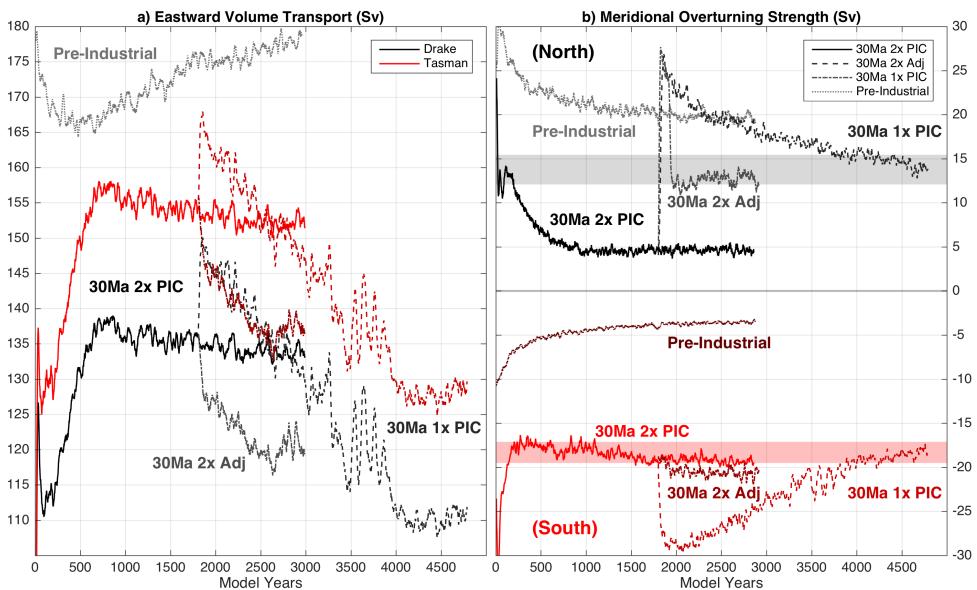


**Figure 7.3:** Time series of a) Southern Ocean gateway volume transports and b) maximum global meridional overturning for the 30Ma  $2\times$  PIC (solid),  $2\times$  PIC Adjusted (dash-dotted),  $1\times$  PIC (dashed) late Eocene and pre-industrial (dotted) spin-up simulations. Transports through two north-south transects in the Southern Ocean are considered: Drake Passage (black,  $65^\circ\text{W}$ ) and Tasmanian Gateway (red,  $150^\circ\text{E}$ ), with positive values indicating eastward flow.

The main aspects of all three 30Ma spin-up simulations are reflected in the evolution and pattern of ideal age tracers, shown in Figure 7.4. Like global mean temperature, the average ideal age of the water mass generally increases and settles down for the 30Ma  $2\times$  PIC case as the oceanic circulation equilibrates. Both the 30Ma  $2\times$  PIC Adjusted and  $1\times$  PIC simulations start with a sharp increase in upper ocean ideal age while the opposite is seen for the deep ocean. Those changes are related to the activation of one or more deep water formation sites (Figure 7.3b), acting to mix the different water masses (as shallow waters are usually younger than deeper ones).

Indeed, ideal age tracer fields at 2500m depth show the presence of young waters in the Northwest Pacific Ocean in both the  $2\times$  PIC Adjusted (contours in Figure 7.4c-d) and  $1\times$  PIC case. The enhanced mixing at  $1\times$  PIC leads to younger deep waters overall, with the exception of the Arctic Ocean which is completely isolated at this depth.

In agreement with temperature trends, the upper ocean equilibrates quite well in average ideal age while the deep ocean takes much longer to adjust. Similar to what was seen from the 38Ma simulations (Figure 5.2a-b), trends in the average ideal age remain but the overall patterns settle over the last  $\sim 1000$  years of each run (except for the shorter  $2\times$  PIC Adjusted case). However, there is a notable difference between 38Ma and 30Ma cases (even at  $2\times$  PIC; see Figure 5.2c) as the latter shows overall younger deep water masses. This is related to both reduced stratification under lower radiative forcing (for  $1\times$  PIC) and the presence of multiple deep water formation sites, but also to enhanced ventilation in the Southern Ocean after the opening of the Tasmanian Gateway and Drake Passage (deep transects in Figure 7.1 and enhanced volume transports in Figure 7.3).

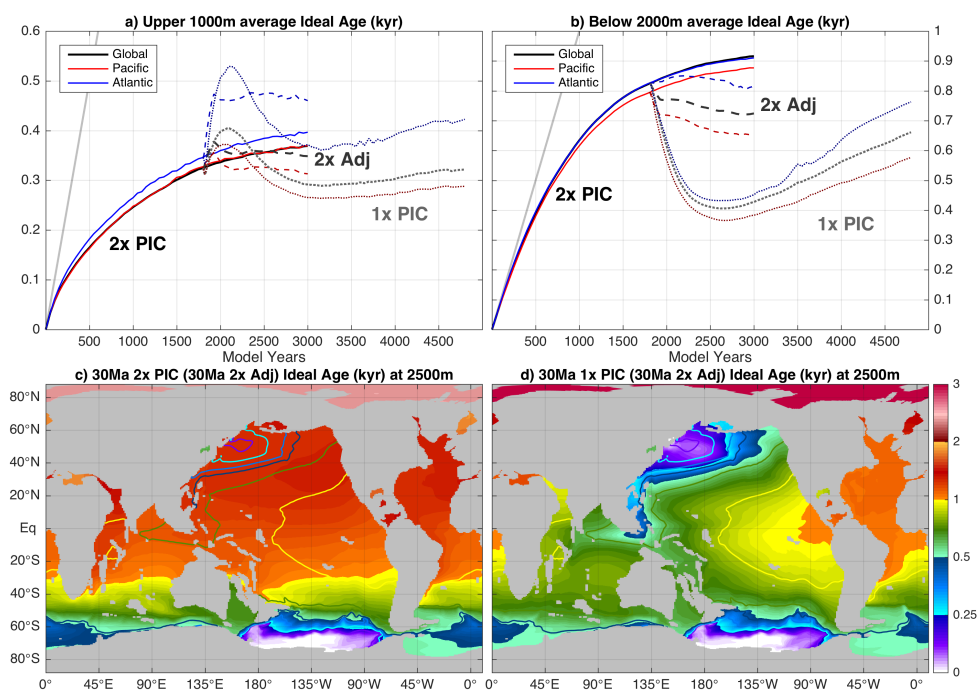


**Figure 7.4:** Time series of a) upper 1000m and b) below 2000m volume-weighted average ideal age tracers for 30Ma  $2\times$  (solid),  $2\times$  Adjusted (dashed) and  $1\times$  (dotted) PIC spin-up simulations. Averages are shown globally (black) and for both the Pacific (red) and Atlantic (blue) ocean basins separately. c) 30Ma  $2\times$  PIC and d) 30Ma  $1\times$  PIC horizontal distributions of ideal age tracers at 2500m depth at the end of each model simulation. Contours in both c) and d) indicate ideal age tracers for the 30Ma  $2\times$  PIC Adjusted case, using the same colour.



## 7.3 Equilibrium Climate for 30Ma 2× PIC

### 7.3.1 Ocean Circulation

An overview of annual mean fields, illustrating the main components of the ocean circulation for the 30Ma 2× PIC case are presented in Figure 7.5. The annual mean distribution of sea surface temperature and salinity are reminiscent of those seen in the 38Ma configuration (see Figure 5.4 for 4× PIC and Appendix Figure B.1 for 2× PIC). The zonal heterogeneity between the western South Pacific and South Atlantic Ocean has all but vanished at 30Ma, owing mainly to the absence of warm waters east of Australia. There is still an impressive warm pool in the western part of the tropical Indo-Pacific, holding sea surface temperatures of 32–34 °C. Most of the high latitude waters remain mild:  $>8^{\circ}\text{C}$  annually with the exception of the extreme southern Weddell Gyre and the Arctic Ocean. The latter is cold and relatively fresh owing to its isolation from other ocean basins which is enhanced by the closure of the Turgai Strait since 38Ma. Low salinity surface waters from the Arctic Ocean are flowing into the North Atlantic, reducing upper level density and creating a strongly stratified, mostly stagnant water mass there.

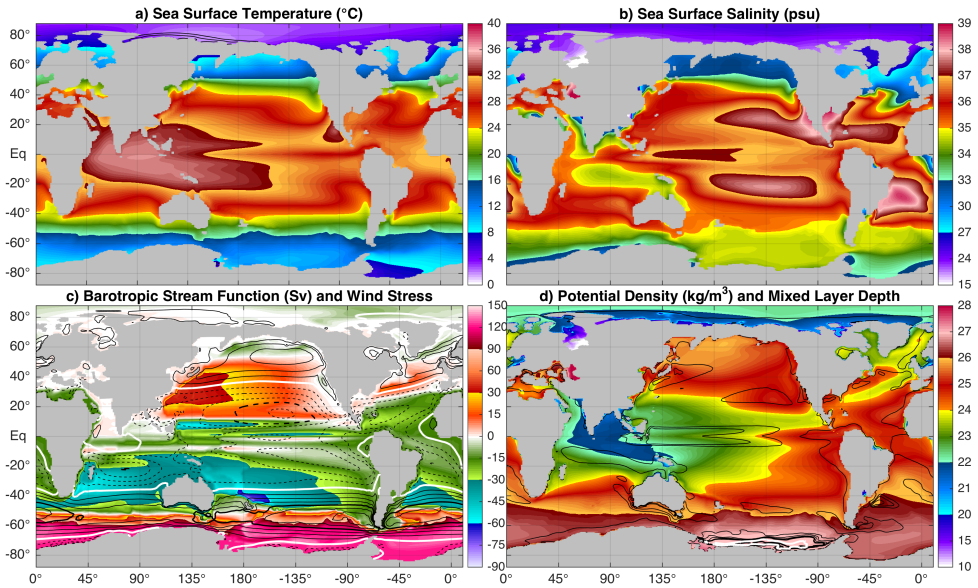


**Figure 7.5:** Annual mean **a)** sea surface temperature and **b)** salinity, **c)** barotropic stream function (positive for clockwise flow) and zonal wind stress (contours every  $2.5 \cdot 10^{-2} \text{Pa}$ , thick lines every  $1 \cdot 10^{-1} \text{Pa}$ ; solid positive and dashed negative, thick white line at  $0 \text{Pa}$ ), and **d)** upper 200m average potential density and mixed layer depth (contours every 50m down to 250m, thick lines every 250m, thick white line at 500m) for the 30Ma 2× PIC simulation. Contours in **a)** show annual mean sea ice fraction at 10% intervals.

The opening of both the Tasmanian Gateway and Drake Passage (Figure 7.1) permits the formation of a strong and deep Antarctic Circumpolar Current (ACC). Southern Ocean gateway volume transports are seen to increase to 130–150 Sv at 30Ma (Figure 7.3a), from 25–50 Sv seen at 38Ma (Figure 5.6a). Drake Passage and Tasmanian Gateway transports suggest that the ACC is at 75–85 % of its pre-industrial equivalent. Regardless of the presence of an ACC and the associated Ekman pumping (upwelling), high salinities in the South Pacific Ocean still make the water mass dense enough for deep water formation. Similar, yet slightly lower upper ocean densities are seen in the South Atlantic but these are insufficient to support deep water formation there. At Northern Hemisphere high latitudes, the densest waters are again found in the Northwest Pacific Ocean. The presence of a sharp salinity gradient between sub-tropical and sub-polar gyres in the North Pacific suggests that a deep northern overturning cell could be sustained with the help of a salt advection feedback. In combination with previous findings from ocean-only simulations (Chapter 4), this motivates the choice to perform the additional experiment with adjusted surface fresh water fluxes in the North Pacific Ocean.

In addition to the formation of a deep ACC, the opening of Southern Ocean gateways at 30Ma impacts the seasonality of both temperature and circulation patterns as shown in Figure 7.6. The strength of the ACC is linked to the meridional density gradient of the water and the zonal wind stress, both of which are weaker in summer (Southern Hemisphere: DJF). Seasonal variations in Southern Ocean gateway transports are 15–20 Sv for 30Ma, while they were just 0–5 Sv for 38Ma cases. The Southern Ocean is thus able to warm up significantly in summer, which in turn reduces the meridional density gradient. Regardless of the southern meridional overturning circulation, the entire Southern Ocean is cool in winter but not cold enough to allow the formation of sea ice. Due to its isolation, the Arctic Ocean does cool down enough for seasonal sea ice but its coverage is still limited (>50% only near the Siberian coast).

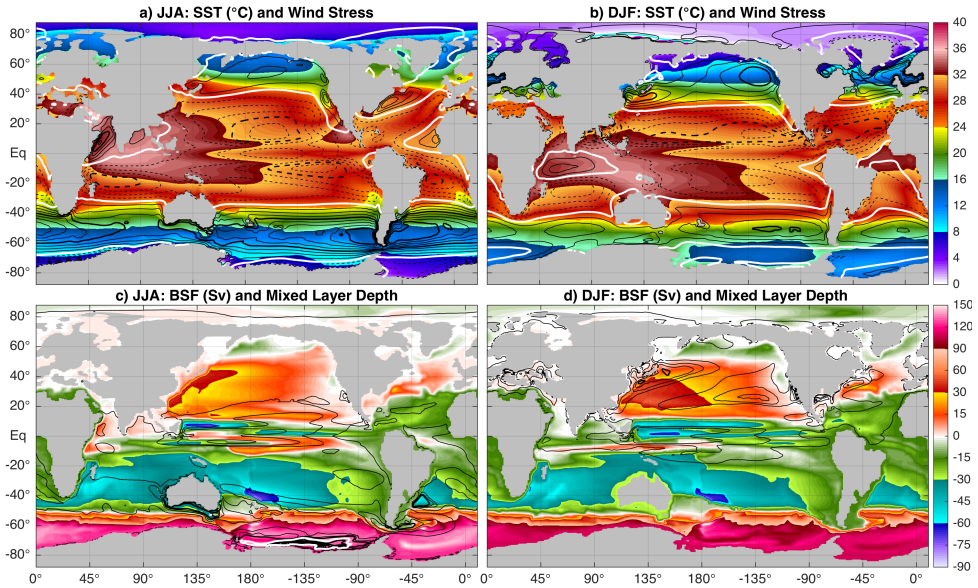


**Figure 7.6:** 30Ma 2× PIC **a)** June-July-August and **b)** December-January-February average sea surface temperature and zonal wind stress (contours every  $2.5 \cdot 10^{-2}$  Pa and thick lines every  $1 \cdot 10^{-1}$  Pa; solid positive and dashed negative values, thick white line indicating 0 Pa). **c)** and **d)** similar to **a)** and **b)**, but for the barotropic stream function and maximum mixed layer depth (contours every 50 m down to 250 m, thick lines every 250 m, thick white line at 500 m). Coloured contours in **a)** and **b)** show sea ice fraction at 50% (cyan) and 90% (magenta) in August and February, respectively.

Seasonality in wind stress is also seen in the Northern Hemisphere middle latitudes and is reflected by the strength of sub-tropical gyres. Especially the North Pacific Ocean is dominated by an expansive sub-tropical gyre, marking the extent of warm and saline waters in the basin. In contrast, Southern Hemisphere seasonality is reflected by the strength of the ACC while leaving that of the sub-tropical gyres mostly unchanged. Similar to the 38Ma cases (Figures 5.4 and 5.8) there is an eastward current at southern high latitudes, splitting and moving around Australia to meet up again on the east side. However, the contribution of the southern component at 30Ma far exceeds that of the northern one and there is little seasonal variation in where those currents meet. The northern component no longer reaches all the way south to Tasmania in summer (which it does at 38Ma; Figure B.2d), but heads eastward north of New Zealand like it does today (Figure A.2d). This shows that the changes in geography between 38Ma and 30Ma could have led to substantial regional changes in oceanic temperatures and currents over the entire Southern Ocean and especially the Southwest Pacific Ocean.

### 7.3.2 Atmosphere

Regardless of the differences in geography between 38Ma and 30Ma and their associated changes in the ocean circulation, annual mean atmospheric fields look remarkably similar (Figure 7.7; see Appendix B for the 38Ma  $2\times$  PIC case, Figure B.3). Very high temperatures are seen in low latitude continental interiors, mostly linked with monsoonal climates. A double inter-tropical convergence zone appears, just like it did in both 38Ma cases and the pre-industrial reference simulation. Middle latitudes are governed by storm tracks and westerlies, with orographically enhanced precipitation on westward facing coastlines and mountain ranges. A persistent upper level trough is evident in both hemispheres around  $90^\circ\text{E}$ , of which the upward branch further east seems to enhance moisture transport and storm tracks over the Western Pacific Ocean. A much more meridionally symmetric pattern in both temperatures and geopotential heights still exists with respect to that of today (Figure A.3). However, the presence of an ACC and a persistently strong meridional gradient keeps southern high latitudes slightly cooler at 30Ma compared to the 38Ma configuration (yet much less cold than in the pre-industrial reference). The absence of an Antarctic Ice Sheet thus seems to have a much larger impact on the Antarctic climate than the existence of a strong ACC.

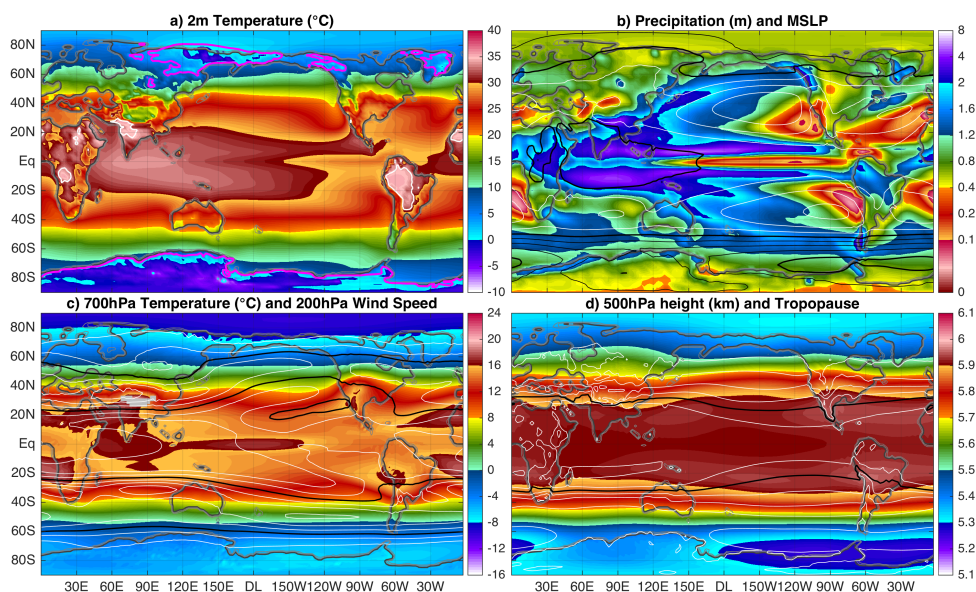


**Figure 7.7:** Annual mean for the 30Ma  $2\times$  PIC simulation with **a)** near surface (2m) air temperature (coloured) and average min/max temperature (contours; magenta  $T_{min} < 0^\circ\text{C}$  and white  $T_{max} > 40^\circ\text{C}$ ), **b)** precipitation (coloured) and mean sea level pressure (contours drawn every 5hPa, thick black lines every 20hPa,  $\leq 1000\text{hPa}$  in black and  $> 1000\text{hPa}$  in white), **c)** 700hPa temperature (coloured) and 200hPa wind speed (white contours every 5m/s starting at 10m/s, thick black lines every 20m/s), and **d)** 500hPa geopotential height (coloured) and dynamic tropopause height (contours every 1km starting at 12km, thick black line at 16km).

## 7.4 Climatic Changes between 38Ma and 30Ma 2× PIC

### 7.4.1 Ocean

Since the simulated climate of the 30Ma 2× PIC case is mostly compared to that of the 38Ma 2× PIC one from Chapter 5, specific changes between both cases are highlighted here. The associated differences in mean annual oceanic fields between the 38Ma and 30Ma 2× PIC equilibrium climate are shown in Figure 7.8. As the only difference in boundary conditions between these cases is the geography reconstruction, they serve well to illustrate the impact of general late Eocene to early Oligocene tectonically driven geography changes.

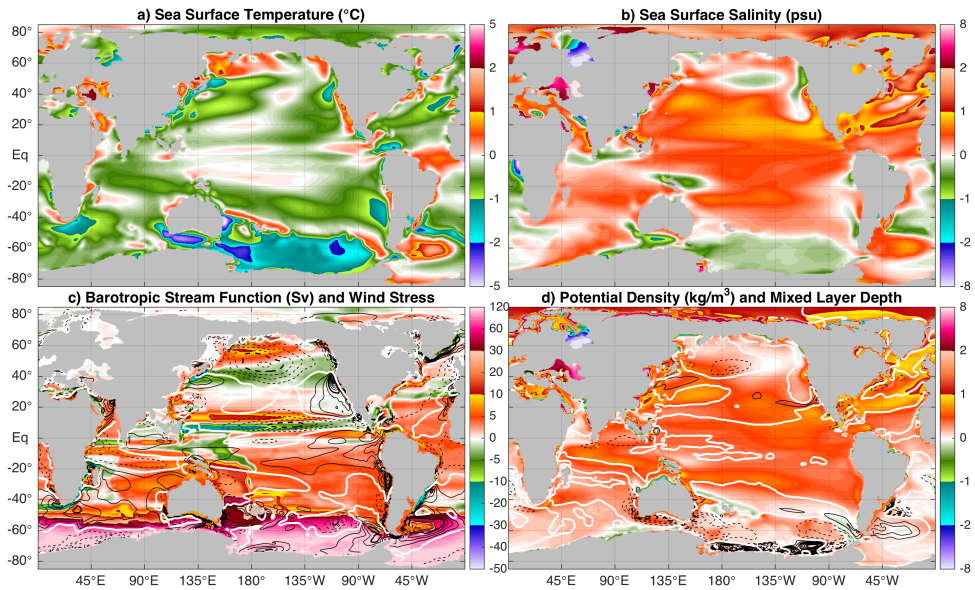


**Figure 7.8:** 30Ma - 38Ma 2× PIC difference in annual mean sea surface **a)** temperature and **b)** salinity, **c)** barotropic stream function (positive clockwise) and wind stress (contours every  $5 \cdot 10^{-3}$  Pa and thick lines every  $2 \cdot 10^{-2}$  Pa; solid positive and dashed negative, thick white line at 0 Pa), and **d)** 200m mean potential density and mixed layer depth (contours every 25m, thick lines every 100m; solid positive and dashed negative, thick white line at 0 and 500m).

Overall, surface waters in the 30Ma case are slightly cooler and more saline, thus more dense than they were at 38Ma. Within the difference plots of Figure 7.8, two types of changes can be distinguished:

- (i) direct effects from the changing land-sea mask (both from continental drift and changing coastlines), and;
- (ii) indirect effects of geography through changes in the general circulation.

Changes in temperature and salinity due to effect (i) can be seen all over the world near coastlines. These responses are most prominent around North and South America, Australia and Southeast Asia as a result of their continental drift between 38Ma and 30Ma.



Especially the closure of the Turgai Strait has a great impact on regional salinity fields, keeping (shallow) high salinity waters restricted towards the south and those with low salinity to the north (effect ii). The Arctic Ocean is slightly colder in the 30Ma case, but surprisingly also considerably saltier despite losing its connection with the Paratethys. The salinisation of the Arctic thus has to be a result of local changes in surface fresh water fluxes (precipitation - evaporation) and run-off. As a result, North Atlantic salinities are also higher than they were in the 38Ma case, yet still low (Figure 7.5b).

The main change in ocean circulation is the formation of a deep and strong ACC at 30Ma, with differences in barotropic stream function of up to 120 Sv compared to the one seen at 38Ma. The formation of this zonal current decreases southward fluxes of heat and salt and therefore causes a decrease in temperature and salinity at southern high latitudes. Especially in the South Pacific Ocean the advection of heat and salt is reduced, but the associated cooling is strong enough to compensate for the reduced density from freshening. The southerly position of the Drake Passage still forces the ACC to acquire a large meridional component in the South-East Pacific, enhancing associated fluxes of heat and salt regionally. In combination with the limited extent of this gateway, there is still a considerable advection of salt into the sub-polar gyre keeping salinities high. Further east, in the South Atlantic, the opposite effect is seen as a warming and salinisation. Both the meridional component and strength of the ACC near the Drake Passage transports warm and saline waters from the sub-tropical Pacific into the South Atlantic Ocean.

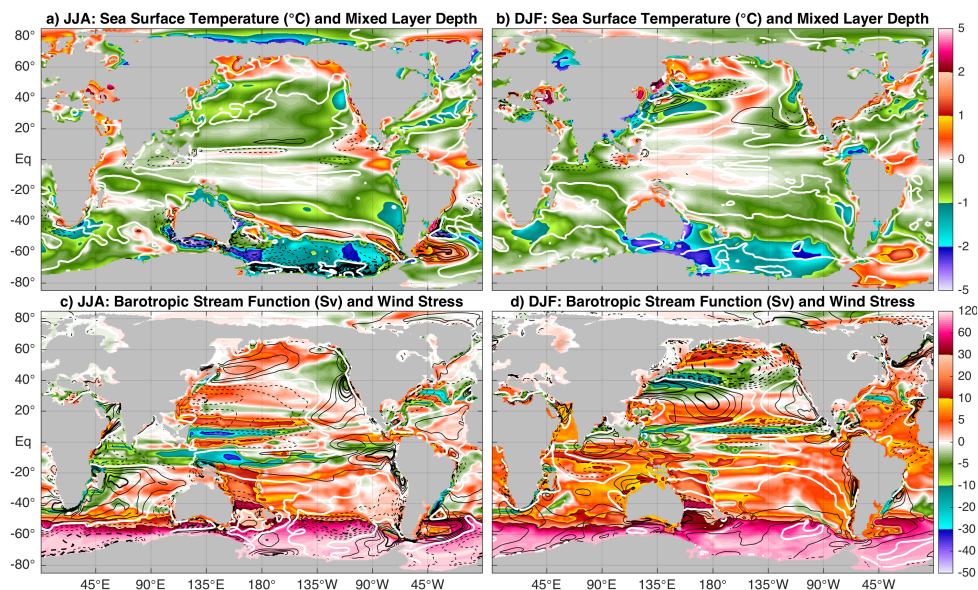


**Figure 7.9:** 30Ma - 38Ma  $2 \times$  PIC difference in the a) June-July-August and b) December-January-February averaged sea surface temperature and mixed layer depth (contours every 25m, thick lines every 100m; solid positive and dashed negative, thick white line at 0 and 500m). c) and d) similar to a) and b), but for the barotropic stream function and wind stress (contours every  $6.25 \cdot 10^{-3}$ Pa and thick lines every  $2.5 \cdot 10^{-2}$ Pa; solid positive and dashed negative, thick white line at 0Pa).

While the ACC dominates the pattern changes in ocean circulation, there are also more subtle shifts in the extent and strength of the gyre systems. The gyres are strongly related to the wind stress for which seasonal changes are more pronounced than annual ones, as illustrated in Figure 7.9. Middle latitude westerlies are strongest in winter when thermal gradients are steepest, so it is therefore no surprise that the largest differences in both wind stress and gyre structure are also seen in this season. Over the North Pacific region, there is a large weakening of westerlies reducing the strength of sub-tropical and sub-polar gyres. As a result, the temperature and salinity fronts in the North Pacific middle latitudes become less pronounced.

In the Southern Hemisphere, there is an overall reduction in the strength of sub-tropical gyres, especially across the South Indian Ocean. As a result of both the changes in gyre strength and a slight shift in the position of Africa, there is a strong regional response in temperature to a weakened Agulhas Current. More regional patterns in changes of the wind stress are seen over the Southern Ocean, but there is no large-scale increase in westerlies. It is thus not an increase in wind speed, but rather a response of the ocean in being able to absorb more of the atmospheric momentum to drive the ACC. In contrast to the gyre responses, a reduction in the southward extent of the East Australia Current prevents additional heating and leads to a significant reduction of summertime temperatures further southeast. Otherwise, changes in summer temperatures are most pronounced in low latitude shallow seas such as the Paratethys.

## 7.4.2 Atmosphere

As was seen above the ocean, changes in the atmosphere can also be divided into (i) those related to direct geography shifts and (ii) more indirect circulation shifts, as seen in Figure 7.10. Additionally, changes in topography also have a direct influence (i) on temperature and precipitation over land. By far the most pronounced example of this is a cooling and wettening over the higher Himalayas and Tibetan Plateau in the 30Ma case. Meanwhile, a warming and drying is seen over the Middle East as a result of the retreat of the Paratethys and India becoming connected to the Asian continent. A tightening and southward shift of the ITCZ takes place over the Pacific Ocean, while the tropical Indian Ocean mostly experiences a drying. As a result of reduced thermal gradients and gyre strength, North Pacific storm tracks become considerably weaker at 30Ma.

At mid-upper levels of the atmosphere, larger patterns of the response to geography changes become more distinguished as local topography effects are less pronounced. 700hPa temperature and 500hPa height changes are closely related to the positioning of the jet streams and associated stationary troughs and ridges. The pronounced trough in both hemispheres, seen at 38Ma (Figure 5.10), is amplified and shifted/expanded towards the east. Changes in the Northern Hemisphere are dominated by a wavenumber 2 (4 pairs of anomalies) pattern, related to a mode of stationary waves in the polar jet stream. In the Southern Hemisphere a far more homogeneous cooling and subsequent lower geopotential heights are present in middle and high latitudes.

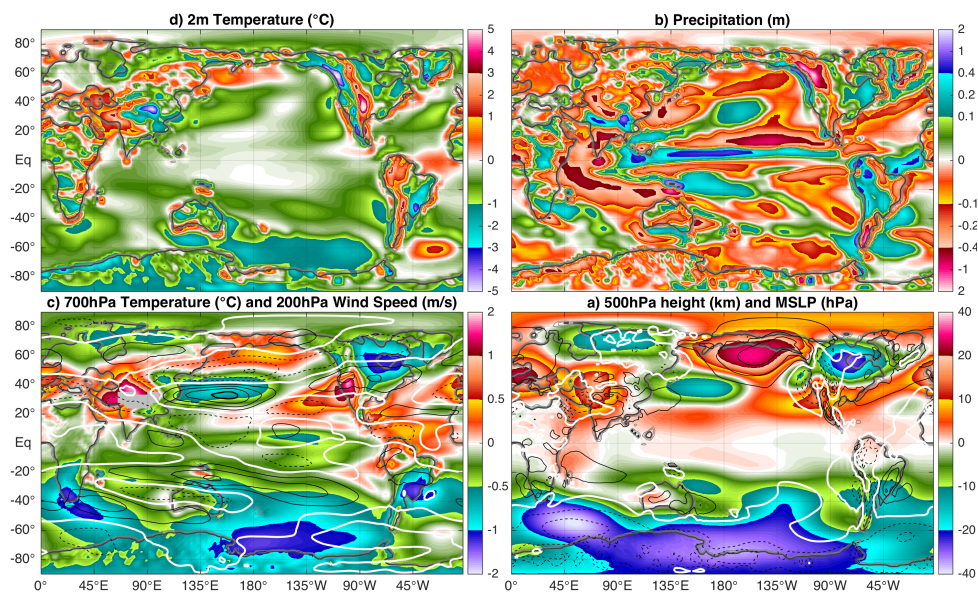


**Figure 7.10:** 30Ma - 38Ma 2× PIC difference in annual mean **a)** near surface temperature and **b)** precipitation, **c)** 700hPa temperature and 200hPa wind speed (contours every 1.25m/s and thick lines every 5m/s; solid positive and dashed negative, thick white line at 0m/s), and **d)** 500hPa geopotential height and mean sea level pressure (contours every 1hPa, thick lines every 4hPa; solid positive and dashed negative, thick white line at 0hPa).

Surprisingly, the annual mean changes seen at mid and upper atmospheric levels are far less distinct when looking at the surface. Especially over land, regional responses in temperature and precipitation are more complex (mostly related to topography) and strongly driven by seasonality as shown in Figure 7.11. To start with, there is a clear intensification of seasonality over most of the Asian continent in response to the 38–30 Ma geography changes. Summers are warmer while winters are colder, with the exception of the Himalayas which are colder in both seasons at 30Ma due to their increased elevation. Western North America also sees an increase in seasonality, with especially much colder and drier winters. The changes in winter are closely tied to the pattern shift and stationary waves seen over the Northern Hemisphere (Figure 7.12). Especially over the North Pacific region, an increase in surface pressure is associated with a powerful ridge over the Aleutians. The anticyclone thus blocks most of the moisture flow into North America, but also reduces the middle latitude westerlies and explains the weaker North Pacific oceanic gyres (Figure 7.9d).



Further west, 200hPa winds decrease over both low and high northern latitudes while strongly increasing in between. This suggests that the geographic changes over East Asia, including the uplift and expansion of the Tibetan Plateau, act to merge the polar and sub-tropical jet streams over the West Pacific Ocean similar to today (Appendix A, Figure A.3c). The excitation of a pronounced stationary trough in turn leads to the downstream development of a North Pacific Ridge and eventually through resonance a wavenumber 2 pattern seen in Figure 7.11f (and Figure 7.10d). Unlike the annual mean, a weaker but similar response can be seen in the Southern Hemisphere related to the amplification of the Australian trough. On top of the wave-like pattern in winter, there is a general equator-ward shift of the jet which is most pronounced in summer.

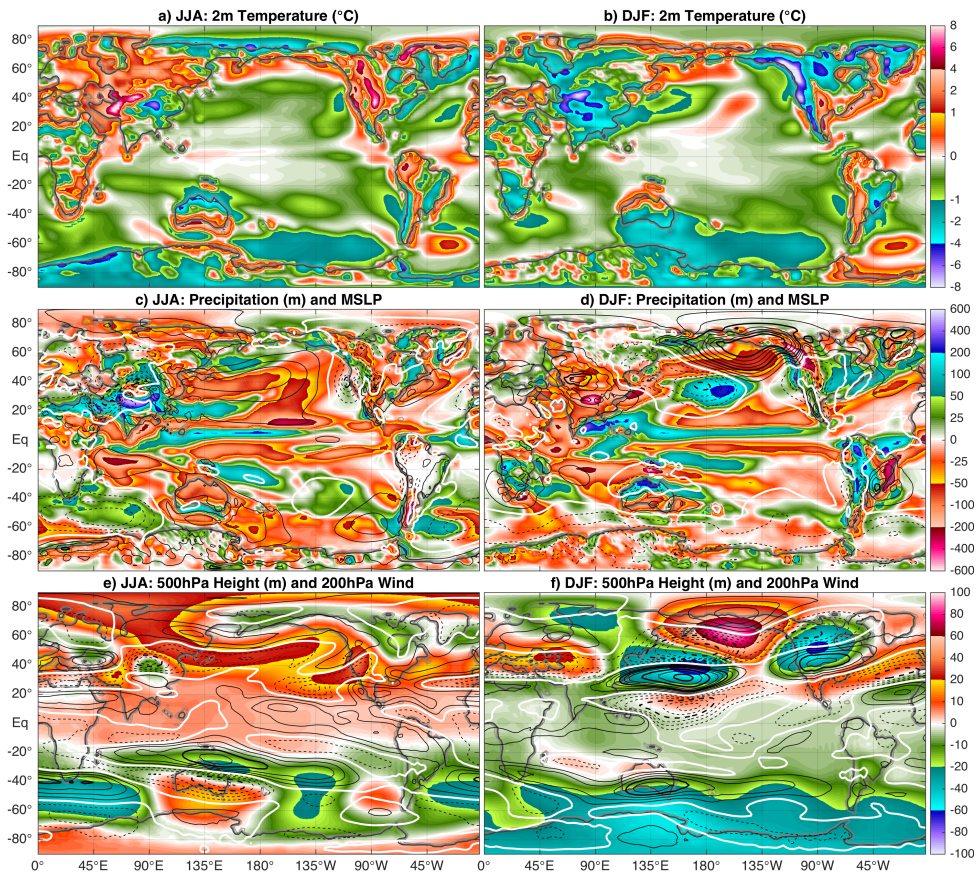


**Figure 7.11:** 30Ma - 38Ma 2× PIC difference in **a)** June-July-August and **b)** December-January-February averaged near surface temperature. **c)** and **d)** similar to **a)** and **b)**, but for precipitation and mean sea level pressure (contours every 1hPa, thick lines every 4hPa; solid positive and dashed negative, thick white line at 0hPa). **e)** and **f)** similar to **a)** and **b)**, but for 500hPa geopotential height and 200hPa wind speed (contours every 1.25m/s and thick lines every 5m/s; solid positive and dashed negative, thick white line at 0m/s).

Even in seasonal average fields, changes at the surface over Antarctica remain limited. In Southern Hemisphere winter most of the continent is cooler, but apart from the Pacific sector summer temperatures are mostly unaffected. Changes in precipitation are even smaller and insignificant other than a minor drying of East Antarctica in summer.

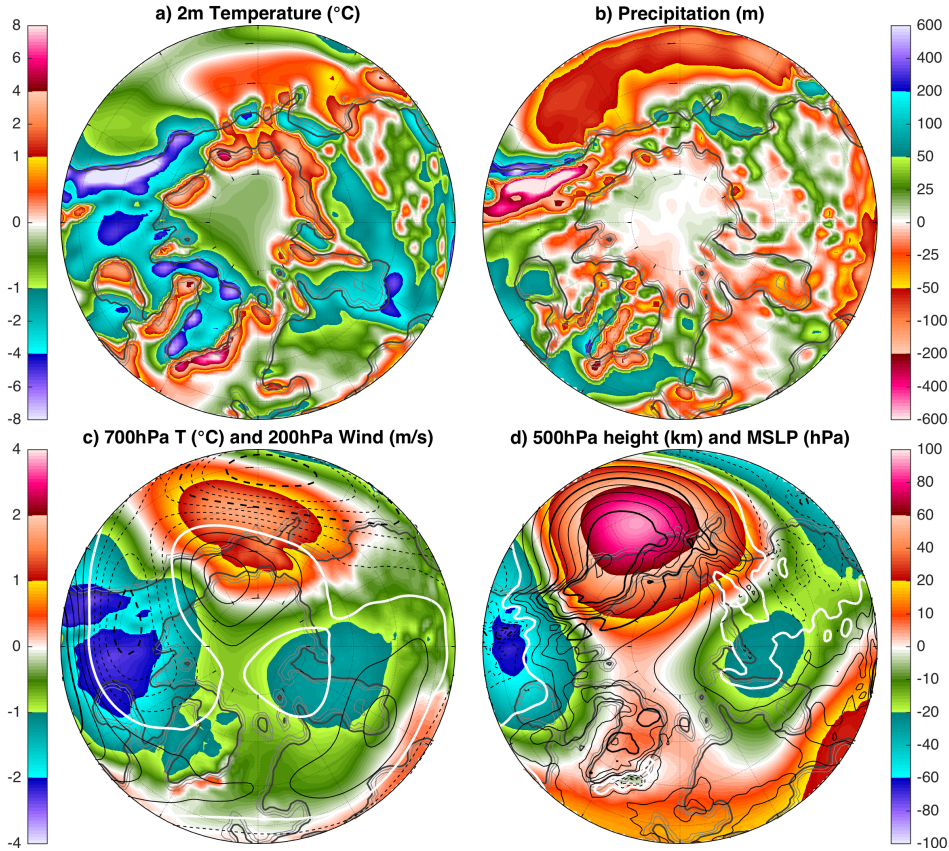


**Figure 7.12:** North polar stereographic projection of the 30Ma - 38Ma  $2\times$  PIC difference in December-January-February averaged **a)** near surface air temperature, **b)** precipitation, **c)** 700hPa temperature (shading) and 200hPa wind (contours every 1.25m/s and thick lines every 5m/s; solid positive and dashed negative, thick white line at 0m/s), and **d)** 500hPa geopotential height and mean sea level pressure (contours every 1hPa, thick lines every 4hPa; solid positive and dashed negative, thick white line at 0hPa).

## 7.5 Multiple Equilibria in the 30Ma Ocean Circulation

Using ocean-only simulations with a fixed atmospheric forcing and 38Ma boundary conditions in Chapter 4, multiple equilibria were found with either a northern or southern sinking regime. The different states of the meridional overturning circulation were featured by North or South Pacific deep water formation, respectively. The experiment is repeated here, by comparing the results of the 30Ma  $2\times$  PIC Adjusted case to those of the 30Ma  $2\times$  PIC one discussed above.

Somewhat surprising, the preferred southern overturning state in 38Ma coupled simulations persists with a 30Ma geography despite the formation of a deep ACC (Figure 7.3b). To investigate whether a similar northern overturning state also exists within a coupled model set-up, a fresh water perturbation was applied to the state of the 30Ma  $2\times$  PIC case at model year 1800. Making the high latitude North Pacific Ocean saltier, the perturbation increases the surface density enough to start deep water formation at northern high latitudes. In contrast to the forcing flux adjustments used in Chapter 4 (boxes in Figure 3.3a), the compensating fluxes are distributed globally now. This, in combination with a smaller integrated value (0.5 rather than 1 Sv), leads to overall strongly reduced fresh water flux perturbations in the 30Ma  $2\times$  PIC Adjusted case.

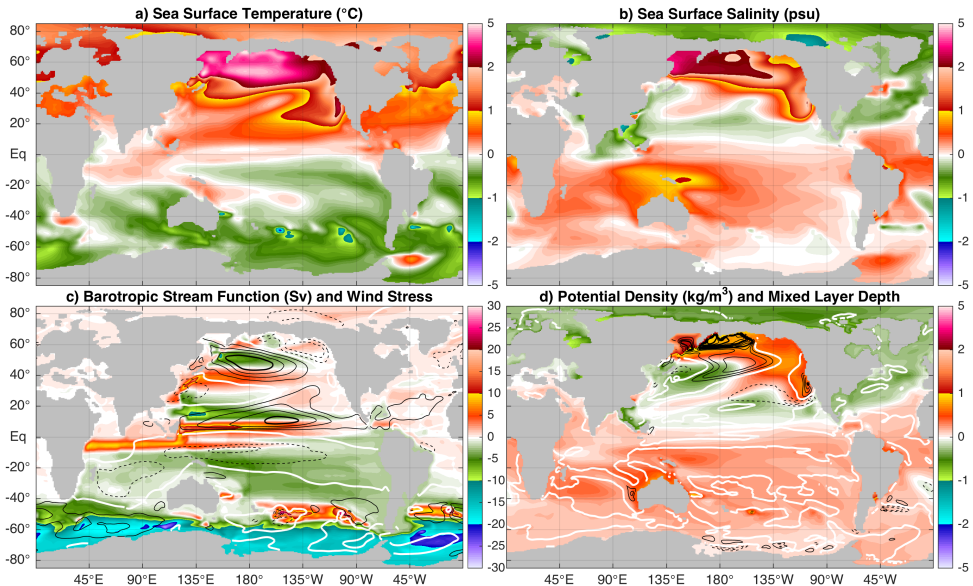


**Figure 7.13:** Similar to Figure 7.8, but for the 30Ma  $2\times$  PIC Adjusted - 30Ma  $2\times$  PIC annual mean (colour axes have changed, but contour intervals are the same).

After 200 years, a northern overturning cell has established and the simulation is continued without the perturbation for another 1000 years. Following an initial weakening related to temporally decreased surface densities, the northern overturning cell restrengthens and settles onto a new stable state (see also Figure 7.3). The existence of such multiple equilibria in the coupled model simulations is encouraging and adds confidence to the previous results from 38Ma cases in an ocean-only set-up. The major difference here is that the southern overturning cell does not disappear at the cost of the northern one. This may be related to a more limited salinity anomaly applied to the South Pacific Ocean, the use of a 30Ma geography reconstruction or simply the tendency to maintain higher salinities more easily across this region in the coupled cases.

Profound changes in sea surface salinity and temperature are seen in response to the initiation of a deep northern overturning cell (Figure 7.14a-b), which are shown in Figure 7.13. Unsurprisingly, temperature and salinity responses are strongest over the North Pacific high latitudes and collocated with the sub-polar gyre where deep water formation is taking place. A large-scale temperature increase of 2–5 °C is seen as well as mostly 2–3 psu higher salinities. Despite a strong temperature effect, the salt advection feedback is sufficient to maintain higher densities and sustain deep water formation. Moreover, an enhanced meridional density gradient in the North Pacific Ocean increases the strength of the gyres as well as causing a northward migration of the associated fronts.

The meridional stream function and respective heat fluxes are shown for all three 30Ma cases in Figure 7.14. Similar to the 38Ma equilibrium states (Figure 5.5a), a deep southern overturning cell is always present in the 30Ma results. As indicated by the time series in Figure 7.3b, the 30Ma 2× PIC Adjusted case exhibits a northern overturning cell in coexistence with the southern one. Much like the 38Ma ocean-only results in Chapter 4 (Figure 4.6a-b), the northern cell is similar in strength and structure to the one seen in the pre-industrial reference (Figure 5.5b) but is located in the North Pacific rather than the North Atlantic Ocean.

In terms of total (i.e. TOM required) heat fluxes, a meridionally symmetric pattern is seen in the 30Ma 2× PIC case (Figure 7.14c-d). Switching on the northern overturning cell induces a significant increase in oceanic heat flux into the Northern Hemisphere. In contrast to the ocean-only results, little change is seen in the Southern Hemisphere as the southern sinking cell remains active in the coupled simulations. As the ocean circulation induces a warming of Northern Hemisphere middle and high latitudes, the according top of model required meridional heat flux decreases. This results in a reduction of the atmospheric component, which is larger than the increase seen for the oceanic one to balance the total flux. Note that this does not mean that the temperature changes driven by a shift in overturning regime are cancelled out by the atmospheric response. In contrast, the atmospheric heat fluxes simply adjust to the new climatic state to keep the system thermally balanced.



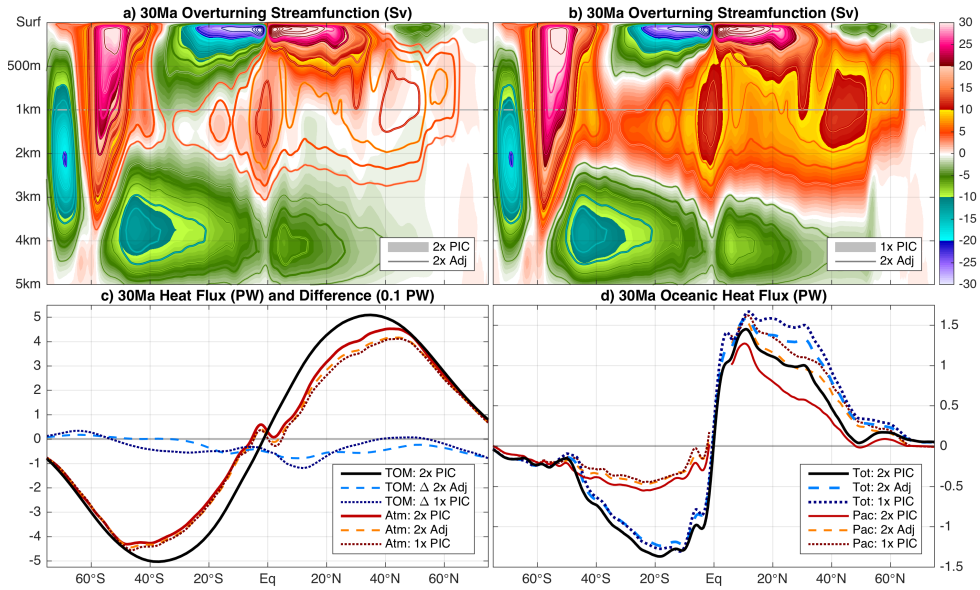


**Figure 7.14:** Global oceanic meridional overturning stream function, averaged for the last 50 model years of the **a)** 30Ma 2× and **b)** 1× PIC case. Contours show the 30Ma 2× PIC Adjusted case and are drawn in both panels every 2.5 Sv (every 5 Sv beyond 30 Sv) using the same colour scale. Total meridional heat flux is shown in **c)**, as required by top of model net fluxes (TOM) along with deduced atmospheric fluxes (Atm) for all three 30Ma cases. Differences in TOM required heat fluxes are calculated with respect to the 30Ma 2× PIC case and magnified tenfold (dashed: 2× PIC Adjusted, dotted: 1× PIC). **d)** Total integrated meridional heat fluxes in the ocean, globally (Tot) and Pacific-only (Pac). Note that all horizontal (latitude) scales cover the range [75°S, 75°N] with latitude increasing from left to right, for better comparison with the oceanic fields shown in a-b).

Similar to the changes between 38Ma and 30Ma 2× PIC cases, atmospheric responses to the onset of a deep northern overturning cell are mostly seasonally dependent and shown in Figure 7.15. In general, there is a slight cooling and drying of the Southern Hemisphere while the opposite happens on the other side of the equator. Differences in temperature are largest at high latitudes, as the tropical response is mediated by an intensification of the northern ITCZ at the expense of the southern one. Temperature changes over land are strongest in winter over both hemispheres (driven by oceanic heat fluxes), while the overall strongest response is found over the North Pacific high latitudes in summer.

Mostly in the North Pacific Ocean, increased SSTs associated with the northern overturning state affect the atmospheric circulation by the release of additional latent heat. The rising motion decreases surface pressure and weakens the large ridge seen in Figures 7.10d and 7.11d. As the temperature contrasts between the ocean and atmosphere are generally largest in winter, the related changes in circulation also are. The altered pressure pattern shifts the North Pacific storm track towards the north, while also increasing precipitation over the surrounding land masses.

The onset of northern deep water formation does not simply cool down the Antarctic continent but mainly acts to increase seasonality. The wintertime cooling over the Antarctic continent is more pronounced than the summertime warming, though. Changing the overturning circulation does not only affect the ocean and surface, but also the upper level atmospheric circulation substantially. Again, atmospheric signals are strongest in winter but there is a general northward shift of the jet streams in both hemispheres when the northern overturning cell is active. Over the Antarctic region, this means an equator-ward shift of the polar front and decreased geopotential heights in winter. Outside of the weakened North Pacific ridge, a poleward shift is seen in the Northern Hemisphere with increased heights over the Arctic. Additionally, upper level winds are generally weaker in response to a lower meridional temperature gradient. This shows that not only oceanic heat fluxes change in response to a shift in the overturning regime. Also the atmospheric heat and moisture fluxes are affected, as well as circulation patterns.

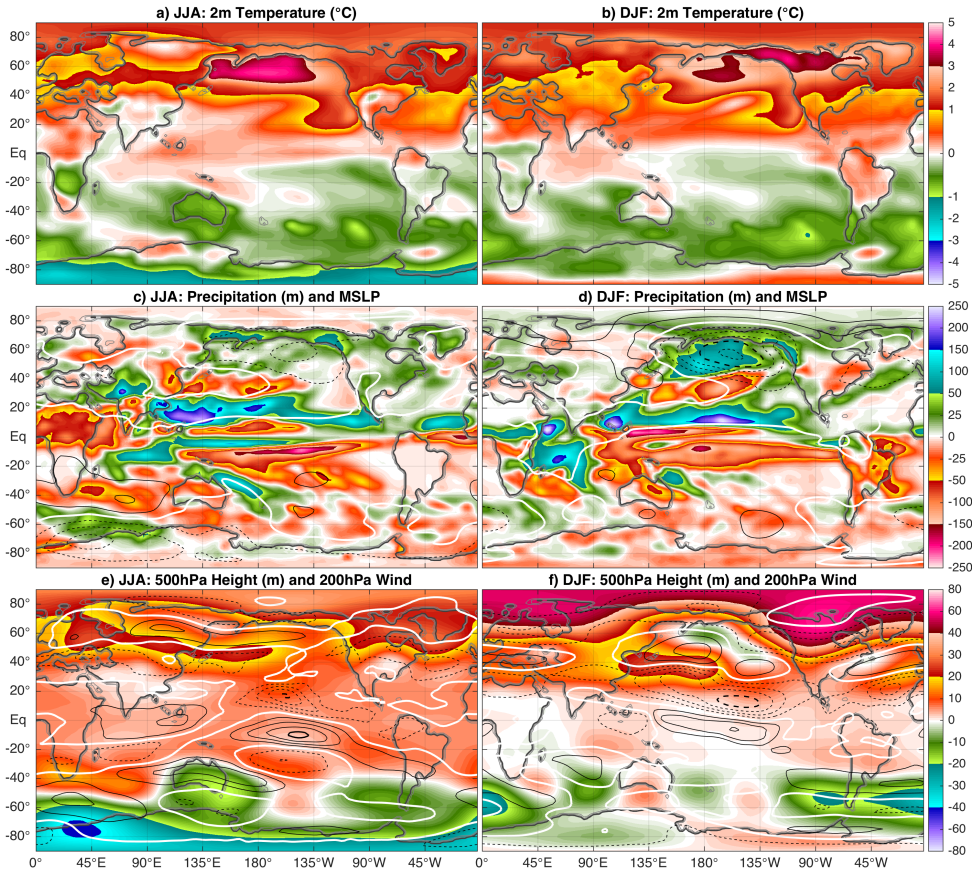


**Figure 7.15:** Similar to Figure 7.11, but for the 30Ma  $2\times$  PIC Adjusted - 30Ma  $2\times$  PIC seasonal averages (colour axes have changed, but contour intervals are the same).

## 7.6 30Ma 1× PIC Simulation and Climate Sensitivity

### 7.6.1 Transports and Meridional Overturning Strength

In addition to the case with a perturbed fresh water flux, a simulation with 1× PIC is also branched off from the state of the 30Ma 2× PIC case after 1800 model years. An overview of the evolution of Southern Ocean gateway transports and meridional overturning strength for all three 30Ma cases and the pre-industrial reference, was given above in Figure 7.3.

Immediately after changing the radiative forcing in the 1× PIC case, there are significant responses of the oceanic circulation. Southern Ocean volume transports increase while the southern meridional overturning circulation intensifies, but also a strong northern cell initiates that is similar to the one seen for the 30Ma 2× PIC Adjusted case. Most of the changes start to relax as the deep ocean adjusts to the new radiative equilibrium. However, transports keep dropping towards a ~20% weaker ACC compared to 30Ma 2× PIC and the northern cell stays active. In fact, the final strengths of the northern overturning cells seem to equilibrate at similar values for the 1× PIC and 2× PIC Adjusted cases (shading in Figure 7.3b).

Meanwhile, the enhanced southern meridional overturning circulation is driven by an additional deep water formation site in the Weddell Gyre. Cooler temperatures at 1×PIC allow the density of South Atlantic surface waters to become high enough for them to sink, but this is only a transient effect. As deep ocean temperatures adjust towards a cooler state, the southern overturning cell returns to its original configuration and South Atlantic sinking ceases to exist. Intermittent episodes of South Atlantic deep water formation are causing the oscillations in ACC strength, seen around model year 3500 for the 30Ma 1× PIC case.

### 7.6.2 Climate Sensitivity

The equilibrium climate sensitivity of the 30Ma cases is determined by the difference between the average temperature under 1× PIC and 2× PIC forcing. Similarly to the comparison of 38Ma 2× PIC and 4× PIC cases in Figure 5.15, the response to a PIC doubling at 30Ma is shown in Figure 7.16. Sensitivity values are normalised by the estimated radiative forcing from Etminan et al. (2016), which is  $4.2\text{W/m}^2$  for a first doubling of both  $\text{CO}_2$  and  $\text{CH}_4$ . The concepts of ECS, ESS and the contribution of palaeogeography from Chapter 5 can now be reconsidered using the 30Ma 1× PIC case, this will be part of the general overview in Chapter 8.

In both hemispheres, there is significant polar amplification of the warming signal that is strongest in winter. Tropical responses are mostly mediated by precipitation and cloud feedbacks, while at high latitudes surface albedo becomes more important. The general warming signal from a PIC doubling at 30Ma is reduced over the North Pacific Ocean and even reversed regionally. This peculiar response to increased radiative forcing is caused by the existence of a northern overturning cell in the 30Ma 1× PIC case. Loosing part of the overturning circulation at 2× PIC thus greatly reduces Northern Hemispheric warming, that is only partly compensated by additional heating from greenhouse gases compared to 1× PIC.

The overturning response thus effectively reduces the equilibrium climate sensitivity of the 30Ma  $1 \times \text{PIC}$  case to  $0.6^\circ\text{C}/\text{Wm}^{-2}$ . This value is lower than both the  $0.69^\circ\text{C}/\text{Wm}^{-2}$  that was found for 38Ma  $2 \times \text{PIC}$  in Chapter 5 (Figure 5.15b) and the  $0.8^\circ\text{C}/\text{Wm}^{-2}$  reported by Bitz et al. (2012).

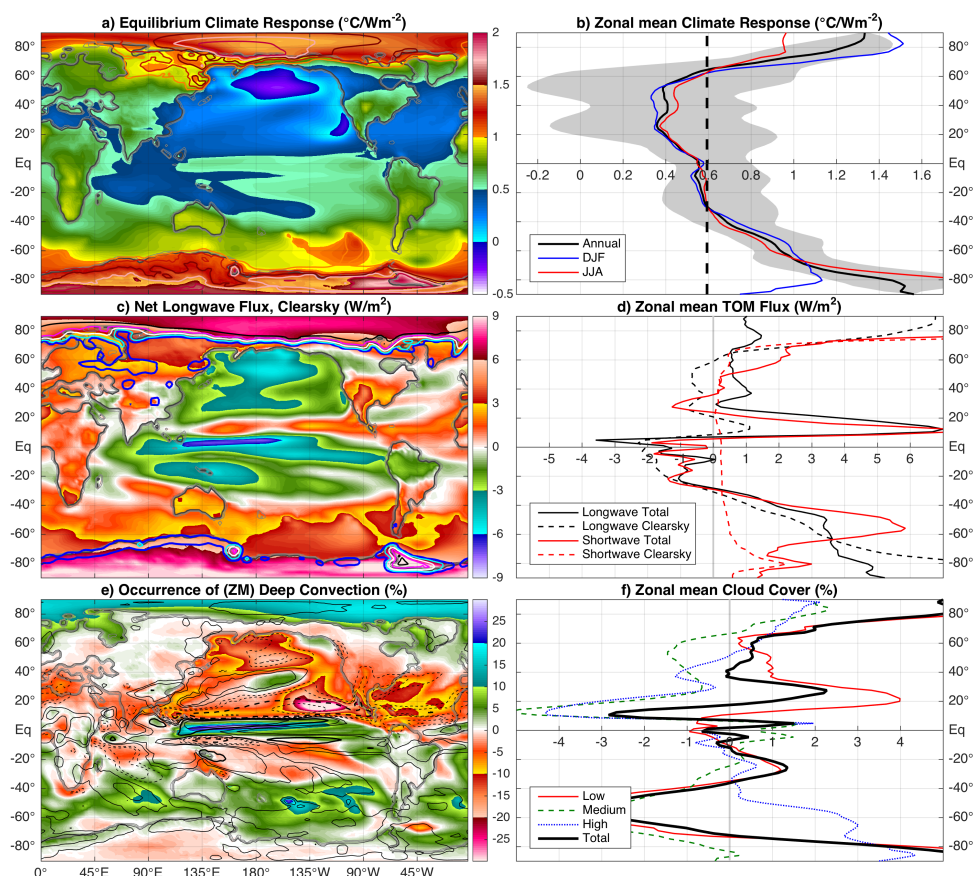


**Figure 7.16:** a) Annual mean temperature response, normalised per  $\text{W}/\text{m}^2$ , of the 30Ma  $2 \times \text{PIC} - 1 \times \text{PIC}$  equilibrium climate with contours showing the winter season (same colour scale). b) Zonal mean normalised temperature response; annual (black), December-January-February (blue) and June-July-August (red). Grey shading indicates minimum and maximum (annual mean) values for each latitude. The (area weighted) global average (i.e. ECS) is  $0.60^\circ\text{C}/\text{Wm}^{-2}$  and indicated by the black dashed line. c) Clear-sky component of the net longwave flux change ( $2 \times \text{PIC} - 1 \times \text{PIC}$ ) at the top of model (TOM), shortwave flux change in contours (blue:  $1 \text{ W}/\text{m}^2$ , cyan:  $2 \text{ W}/\text{m}^2$  and white:  $5 \text{ W}/\text{m}^2$ ). d) Zonal mean TOM change in longwave (black) and shortwave (red) flux, corresponding clear-sky components are shown using dashed lines. Longwave fluxes are defined positive upward, shortwave fluxes positive downward. e) Change in the occurrence of ZM parameterised deep moist convection and precipitation (contours at 100, 200, 500 and 1000 mm, dashed for negative changes and thick line indicating 500mm). f) Zonal mean changes in cover (%) of low (red), medium (green) and high (blue) clouds, the thick black line indicates changes in total coverage.



Indeed, there is a  $\sim 0.5^\circ\text{C}$  difference in global mean surface air temperature between the 30Ma  $2\times$  PIC and  $2\times$  PIC Adjusted cases. Therefore, the climate sensitivity increases to  $0.67^\circ\text{C}/\text{Wm}^{-2}$  when considering the  $2\times$  PIC Adjusted results (Figure 7.17), which is again similar to what was found for 38Ma. Despite being similar globally, the meridional dependency of the climate sensitivity is different between 30Ma and 38Ma responses. In the cooler ( $1\times/2\times$  PIC) 30Ma cases, temperature responses are enhanced at high latitudes but reduced near the equator. In addition to the role of ice and snow around the poles, the tropical thermostat (mostly through cloud-convective feedbacks; Figure 7.16e-f) is thus also dependent on the climatic background state.

Although at first sight the polar amplification looks similar in both hemispheres for the 30Ma response, its mechanism is different. In the Arctic region, a large difference in shortwave clear-sky radiation (Figure 7.16c) points at the importance of sea ice and snow cover, and their associated albedo feedback (in contrast to 38Ma  $2\times$  and  $4\times$  PIC). Over the Antarctic region, longwave radiation is dominant and thus most of the amplification in warming is related to cloud cover changes.

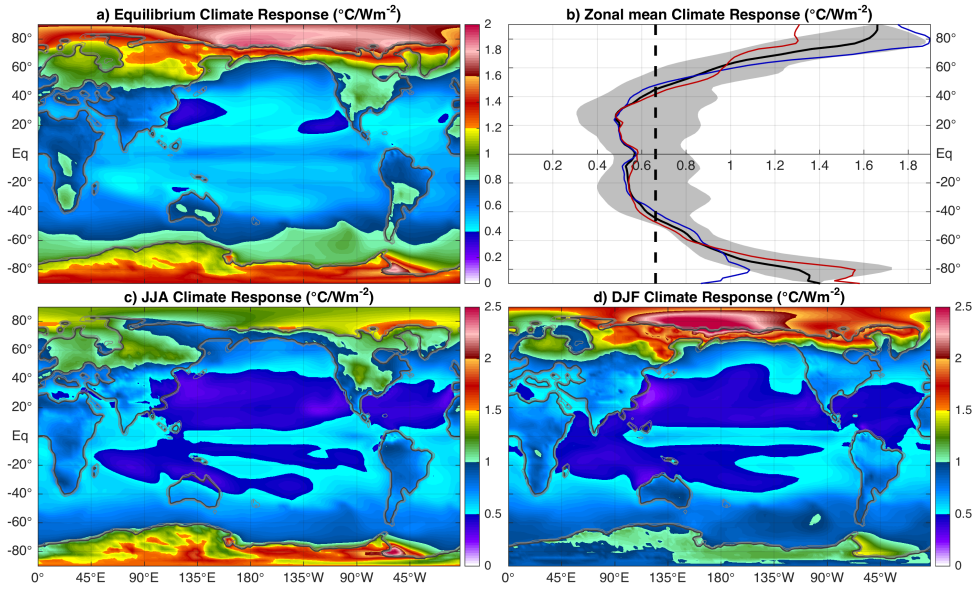


**Figure 7.17:** **a)** Annual mean temperature response, normalised per  $\text{W}/\text{m}^2$  radiative forcing of the 30Ma  $2\times$  PIC compared to the  $1\times$  PIC equilibrium climate. **b)** Zonal mean normalised temperature response; annual (black), December–January–February (blue) and June–July–August (red) average. The grey shading indicates minimum and maximum values for each latitude for the annual mean. The (area weighted) global average (i.e. climate sensitivity) is  $0.67^\circ\text{C}/\text{Wm}^{-2}$  and is indicated by the black dashed line. Seasonal mean, normalised temperature responses similar to **a)** are shown in **c)** for June–August and in **d)** for December–February (mind the different colour axes).

Looking more closely at the Antarctic climate (Figure 7.18) for 30Ma 1× and 2× PIC, reveals that it is still similar to the one seen in 38Ma simulations (Figure 6.4). Even at 1× PIC, there is strong seasonality with warm summers and a monsoonal signal. Apart from a general cooling and drying, the Antarctic climate is qualitatively similar in all simulations. Despite using just 1× PIC, the other boundary conditions (no AIS, Eocene vegetation, warm deep ocean initialisation) keep the climate in a greenhouse state. It of course remains questionable whether all of these conditions can be maintained at 1× PIC, but these results suggest that there is a strong hysteresis in the climate system that tends to remain in it's warmer state even at low radiative forcing.

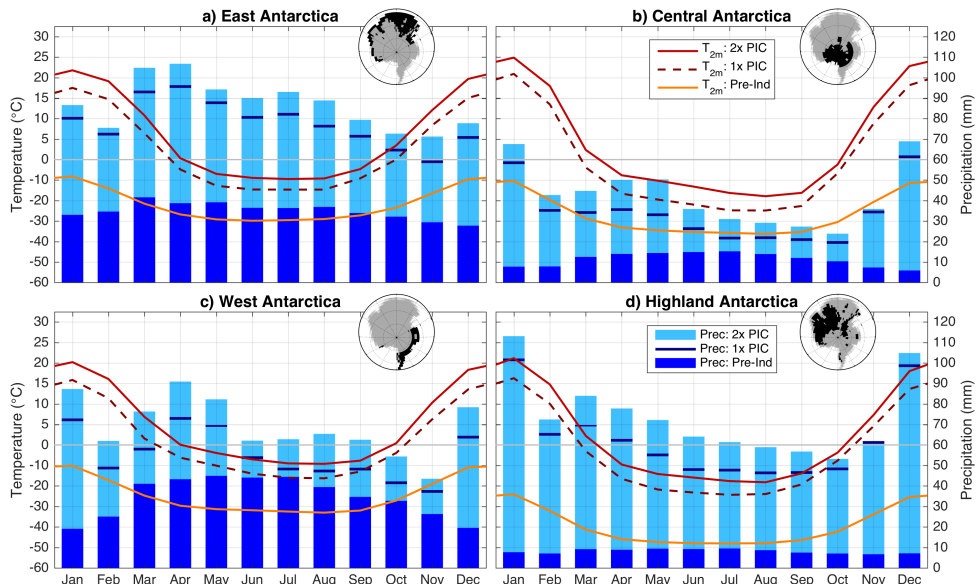


**Figure 7.18:** Monthly climatology for a) East, b) Central, c) West and d) Highland (>1km) Antarctica, showing 2m temperature (lines) and precipitation (blue bars) for 30Ma 2× and 1× PIC cases and the pre-industrial reference. The extent of each region for the 30Ma geography is highlighted by the black shaded region in the upper right corner of each panel.

## 7.7 Summary and Conclusions

Results of several CESM simulations using a 30Ma rather than a 38Ma geography reconstruction were considered to assess the impacts of late Eocene global geography changes on the climatic state. These changes mainly include the opening of Southern Ocean gateways, closure of the Turgai strait and Himalayan/Tibetan uplift during the India-Eurasia Collision as shown in Chapter 2.

In general, the simulated climate in 30Ma cases looks comparable to the one seen at 38Ma under  $2\times$  PIC in Chapter 5. The annual mean oceanic and atmospheric fields still show a mild, rather equable climate that is meridionally symmetric. A notable observation was the relatively quick relaxation during spin-up under  $2\times$  PIC compared to the other cases, for which the initialised total oceanic heat content closely matches that of the equilibrium state. Both warmer and colder cases took much longer to equilibrate, being governed by deep oceanic diffusive timescales.

The most pronounced difference in the general circulation between 38Ma and 30Ma cases is the development of a strong and deep ACC in response to Southern Ocean gateways opening, reaching 75–85 % of its pre-industrial equivalent in volume transport. The zonal heterogeneity over the South Pacific seen at 38Ma vanishes at 30Ma, showing how regionally strong effects can be felt due to circulation changes in response to global geography variations. Still, the impact on large-scale temperature and salinity fields is limited under persistent South Pacific deep water formation within a deep southern meridional overturning circulation. Meanwhile, the Arctic Ocean remains brackish and its low salinity waters flow into the Atlantic Ocean keeping it stably stratified.

As to be expected, climatic changes between 38Ma and 30Ma cases mainly concentrate around the Southern Ocean and the Asian continent in response to tectonic activity. Temperature and salinity differences are mostly related to the formation of a deep ACC, while the excitation of a stationary wave train in the Northern Hemispheric jet streams induces strong seasonal changes over the surrounding continents. The effect of geography variations on the climate is both direct and indirect; through a changing land/ocean mask or topography, and the induced circulation changes, respectively. While oceanic responses are strongest at the surface, those in the atmosphere are most pronounced at mid-upper levels. A widespread cooling of the air mass is seen over southern high latitudes at 30Ma, but the surface climate is hardly affected over land.

The existence of multiple equilibria in the ocean circulation, related to the meridional overturning regime was explored here within a coupled model framework. Using a temporary surface fresh water flux perturbation, the existence of a stable northern overturning state was shown with a 30Ma geography reconstruction featuring North Pacific deep water formation. In contrast to the ocean-only results from Chapter 4, the southern meridional overturning cell does not collapse in response to the initiation of a northern one.

Changing towards a circulation state featuring northern deep water formation also induces profound changes in both the ocean and atmosphere. While the oceanic response is mostly tied to the overturning regime, its effect on the atmospheric circulation patterns is non-trivial. The northern overturning state exhibits enhanced northward meridional heat fluxes to sustain warmer high latitude waters. Consequently, the top of model required flux decreases and thus the change in atmospheric fluxes is stronger and opposite. It is important to realise that the atmospheric heat flux does not cancel the oceanic one, but is merely a required response to sustain the new climatic state.

Finally, a 30Ma  $1\times$  PIC case was also considered to determine climate sensitivity and explore a possible late Eocene greenhouse climate under low radiative forcing. The overturning regime at  $1\times$  PIC is similar to that of the  $2\times$  PIC Adjusted case, featuring both North and South Pacific deep water formation. South Atlantic sinking is also observed during the transient cooling phase, but ceases to exist after further equilibration.

As was seen for 38Ma, there is significant polar amplification in the response to increased radiative forcing but its mechanisms are not similar. While still being strongly affected by clouds, high latitude warming is further increased through ice/snow cover changes and the tropical thermostat seems more efficient in cooler climates. Additionally, a significantly lower ECS ( $\sim 0.6$  rather than  $\sim 0.7^\circ\text{C}/\text{Wm}^{-2}$  at 38Ma) is found as a result of the different overturning regimes between the 30Ma  $1\times$  PIC and  $2\times$  PIC cases. A similar ECS of  $0.67^\circ\text{C}/\text{Wm}^{-2}$  is again obtained when comparing the 30Ma  $1\times$  PIC case to the  $2\times$  PIC Adjusted one. This effectively shows that both the climate sensitivity and polar amplification signal are dependent on the background climatic state. Furthermore, the existence of multiple stable states regarding the meridional overturning circulation can not only induce unexpected responses to geography variations, but also to changes in radiative forcing.

To conclude, the 30Ma cases showed that even under low radiative forcing the Eocene climate remains in a greenhouse state featuring reduced meridional gradients, mild high latitudes and limited snow/ice cover. The Antarctic continent still exhibits a monsoonal climate with warm and wet summers under  $1\times$  PIC and is not qualitatively different to the one seen at 38Ma  $4\times$  PIC. This indicates that in these CESM simulations, the late Eocene greenhouse climate is resilient and features a strong hysteresis, making it less likely to transition into an icehouse state.

# Overview of CESM Simulations and Implications for Antarctic Glaciation at the EOT

---

**Abstract** Several different cases considering the middle-to-late Eocene climate have been presented in Chapters 4-7. The respective simulations included both 38Ma and 30Ma geography reconstructions next to a pre-industrial reference. An array of model boundary conditions make the Eocene climate vastly different to the one of today, regardless of the radiative forcing. These boundary conditions include a different continental geometry, the absence of continental ice sheets and changes in land cover, orbital cycles and atmospheric composition.

South Pacific deep water formation occurs in all middle-to-late Eocene cases, while some other sites occasionally exhibit sinking as well. As expected, a change of the reconstructed model geography from a 38Ma to a 30Ma reference affects the general circulation albeit mostly in the ocean or only regionally. Climate sensitivity to a radiative forcing from increased greenhouse gases is fairly robust and similar at around  $0.6\text{--}0.7\text{ }^{\circ}\text{C}/\text{Wm}^{-2}$ . Polar amplification, reducing the meridional temperature gradient in warmer climates, is universal but governed by different mechanisms (albedo, clouds, water vapour) dependent on the climatic background state.

The strongly seasonal and wet climate seen over Antarctica is also recurrent in all of the late Eocene simulations and has great implications for potential ice growth. Especially warm summers and a monsoonal-like climate keeps Antarctica mostly ice free, even at very low greenhouse gas concentrations.

**Acknowledgement** The author would like to thank dr. Heiko Gölzer for carrying out the offline ice sheet model simulations to help explore and evaluate the possibilities of Antarctic glaciation.

“I have passed through fire and deep water, since we parted.  
I have forgotten much that I thought I knew,  
and learned again much that I had forgotten.”

J.R.R. Tolkien

## 8.1 Temperature and Circulation

### 8.1.1 Ocean

To compare the results of the six different CESM cases listed in Chapter 3 (Section 3.3), an overview of zonal mean sea surface temperatures (SSTs) including all of the respective climatologies is given in Figure 8.1. The corresponding global and tropical SST averages along with deep ocean temperatures are also provided in Table 8.1. The 38Ma 4× PIC case on average has very warm tropical SSTs of around 34°C and is only representative for warm episodes of the late middle Eocene such as the MECO (Bohaty & Zachos, 2003; Sluijs et al., 2013). High latitude surface waters have warmed to the point where they are mostly 10°C or higher and sea ice is as good as inexistent in this warm greenhouse climate. The mild high latitude temperatures are reflected by ~11°C average deep waters under 4× PIC forcing. A comparison to estimates from benthic  $\delta^{18}\text{O}$  and Mg/Ca values (Cramer et al., 2011; Cramwinckel et al., 2018; Zachos et al., 2008) also suggests that the 38Ma 4× PIC results are comparable to peak MECO conditions, with deep ocean temperatures of 10–11 °C (see also Figure 9.1b in Chapter 9).

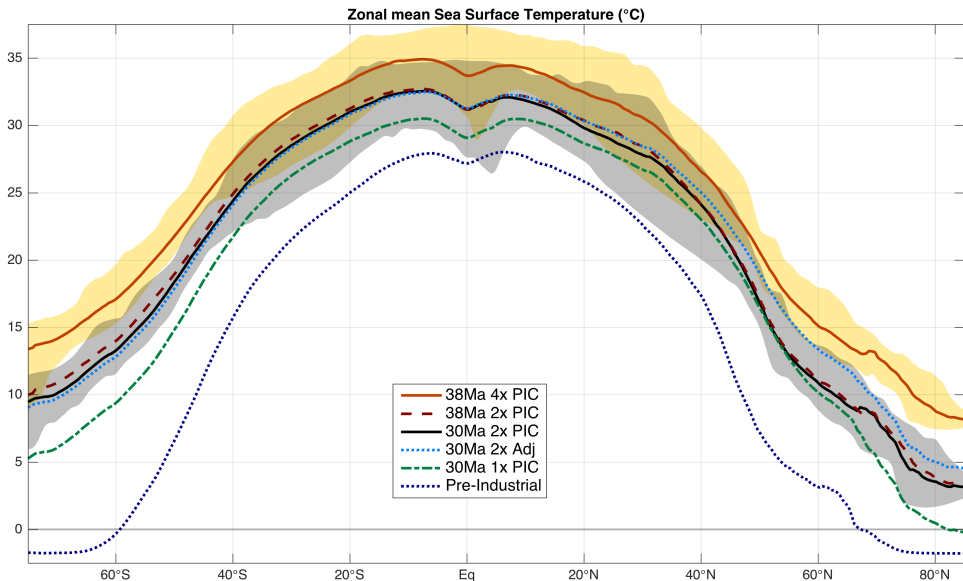


**Figure 8.1:** Zonal mean, annual mean sea surface temperatures of all the CESM simulations: 38Ma 4× PIC (orange; including zonal variation in yellow), 38Ma 2× PIC (dark red dashed), 30Ma 2× PIC (black; including zonal variation in grey), 30Ma 2× PIC Adjusted (cyan dotted), 30Ma 1× PIC (green dash-dotted) and the pre-industrial reference (dark blue dotted).

Being mostly representative for general middle-to-late Eocene conditions (tropical SST: 31–32 °C, deep ocean: ~8°C; Table 8.1), three different cases using 2× PIC have been considered as part of this study. The first using a 38Ma geography reconstruction, the second case a 30Ma one and the last also a 30Ma one but with a temporarily perturbed surface fresh water flux. Zonal mean SST changes related to different geographies are minor; the tropics and Northern Hemisphere are similar while the Southern Hemisphere is slightly (about 1°C) cooler at 30Ma. The presence of a northern overturning cell in the 30Ma 2× PIC Adjusted case significantly increases Northern Hemisphere SSTs, especially at higher latitudes.

A polar amplification signal is seen between the 38Ma 2× PIC and 4× PIC cases, with SST differences being about twice as large at the poles as those seen in the tropics. Comparing 30Ma 1× PIC and 2× PIC shows a similar effect, but the SST responses are not meridionally symmetric. The entire Southern Hemisphere cools down under lower radiative forcing at 30Ma just like the 38Ma cases, while northern middle latitudes are on average the same temperature. This asymmetry is also seen when comparing the 30Ma 2× PIC case with the 2× PIC Adjusted one. Similarly, the 30Ma 1× PIC climate has a northern meridional overturning cell in addition to the already active southern one. Even under 1× PIC forcing, the 30Ma simulated climate has average tropical SSTs of nearly 30°C and deep waters of ~4°C (late Eocene: ~5°C from benthic  $\delta^{18}\text{O}$ ). This shows that the late Eocene climate can be simulated using appropriate model boundary conditions, even under low radiative forcing.

The 30Ma 2× PIC Adjusted simulation nicely illustrates the effect of different meridional overturning patterns, which is regionally as strong as a doubling of CO<sub>2</sub> and CH<sub>4</sub>. Comparing the 30Ma 1× PIC climate to the 2× PIC Adjusted one indeed shows a similar warming pattern as the one seen between both 38Ma cases (just like the warming responses in Figures 5.15, 7.16 and 7.17).

Case \ Measure	SST <sub>glob</sub> (°C)	SST <sub>trop</sub> (°C)	T <sub>4km</sub> (°C)
38Ma 4× PIC	28.37	33.91	11.1
38Ma 2× PIC	25.83	31.71	8.38
Pre-industrial 1× PIC	18.35	26.88	0.26
30Ma 2× PIC	25.42	31.50	7.70
30Ma 2× PIC adjusted	25.65	31.58	7.47
30Ma 1× PIC	23.33	29.66	4.29

**Table 8.1:** Average equilibrium temperatures at the end of each CESM simulation, showing SST<sub>glob</sub>: global mean sea surface temperature, SST<sub>trop</sub>: tropical (<23.5°N/S) average SST, and T<sub>4km</sub>: global mean ocean bottom (4km) temperature. These values are calculated using the last 200 years of each simulation.



Pre-industrial SST's are profoundly different to those seen in any of the middle-to-late Eocene cases. In addition to being considerably colder globally compared to even the 30Ma 1× PIC case, the pre-industrial temperatures also exhibit a steeper meridional gradient. The zonal mean SST differences between 30Ma and pre-industrial 1× PIC cases suggest that the response to changes in model boundary conditions can be divided between:

- 1) the equivalent of a first PIC doubling (i.e. 2–3 °C) due to general geography changes, vegetation cover and a warmer deep ocean, and;
- 2) an additional polar amplification (another 2–3 °C regionally) from the influence of polar ice sheets and related snow/ice albedo feedbacks.

Note that SST's in polar regions are cut off at a minimum value of -1.8°C due to the implementation of sea ice in the model.

As suggested by the SST comparison above, oceanic temperatures and circulation patterns are mainly determined by geography, radiative forcing and the meridional overturning circulation. The respective overturning regime and associated meridional heat fluxes for all six different CESM cases are illustrated in Figure 8.2.

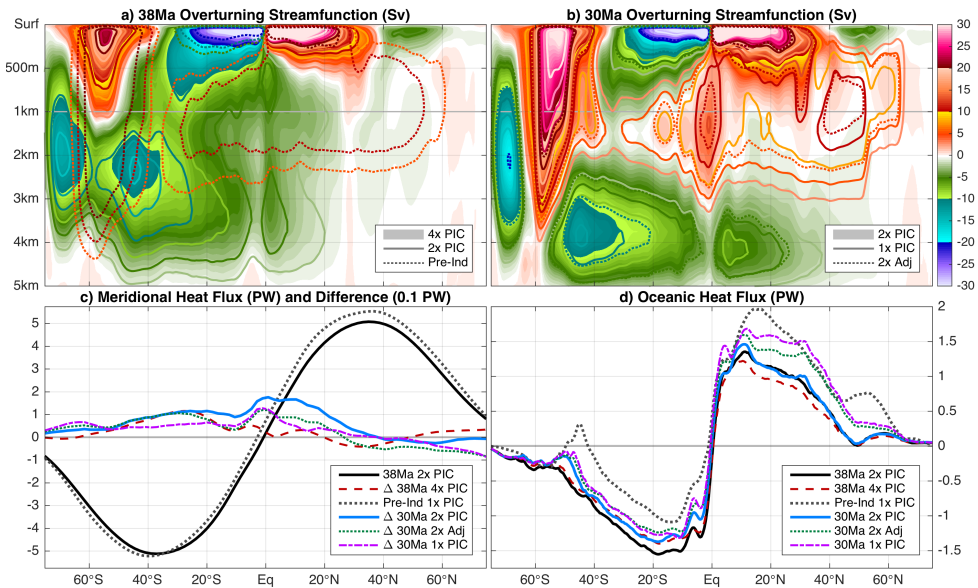


**Figure 8.2:** Comparison of the a-b) meridional overturning stream function, c) top of model required total meridional heat flux, and d) oceanic meridional heat flux in the different CESM simulations. Shading in a) shows the stream function for the 38Ma 4× PIC and contours for the 2× PIC case, dotted contours are used for the pre-industrial reference. The same convention is used in b), but for the 30Ma 2× PIC, 1× PIC and 2× PIC Adjusted cases, respectively. Contours and shading all use the same colour axis shown to the right. Total fluxes in c) are only shown for the 38Ma 2× PIC case and pre-industrial reference, while the for other cases the difference with respect to 38Ma 2× PIC is considered. Differences are indicated in the legend using a Δ and multiplied tenfold.

Regardless of any differences in structure and intensity, a deep southern overturning cell is present in all of the Eocene cases presented here. The pre-industrial ocean still exhibits deep water formation in the Southern Hemisphere, but the outflow of those Antarctic Bottom Waters towards the north is much more restricted compared to the Eocene configuration. The structure of the southern overturning cell is influenced by the presence and strength of an Antarctic Circumpolar Current (ACC). Mainly Ekman upwelling as a result of strong zonal flow in the ACC forms a narrow but intense deep northern overturning cell at southern middle latitudes. The associated northward flow reduces the generally southward meridional flux of heat in that region and even locally reverses it for the pre-industrial case. Since the ACC is much stronger and deeper in the 30Ma cases than it is for 38Ma ones, the associated Ekman upwelling also generates a deeper and more intense northern overturning cell. Still, this does not prevent the larger southern overturning cell from extending well into the Northern Hemisphere while having only a limited influence on meridional heat fluxes.

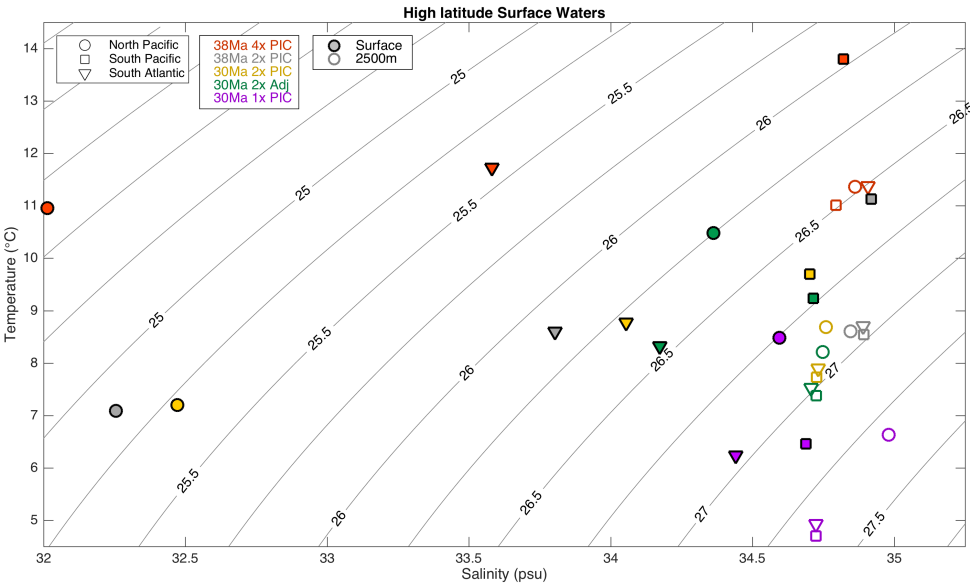


**Figure 8.3:** Mean high latitude water properties at potential deep water formation sites in all 38 and 30Ma CESM cases; temperature and salinity, the inferred potential density (reference: surface, in  $\text{kg/m}^3$ ) is indicated with contours. Ocean basins considered here are the North Pacific (circles), South Pacific (squares) and South Atlantic ones. Filled markers show surface properties (i.e. actual density) while open markers indicate those at 2500m depth (i.e. potential density).

Another difference between 38Ma and 30Ma circulations is the depth of the outflow of southern component waters. The presence of a large northern overturning cell in some of the 30Ma cases may suggest that this influences the extent of the deep southern cell. However, there is no difference in the structure of the southern cell between 30Ma  $2\times$  PIC and  $2\times$  PIC Adjusted cases. The change in depth of the southern overturning cell is thus a result of the density difference between that of the respective deep water source regions and the rest of the ocean. For the 30Ma  $2\times$  PIC Adjusted case, the North Pacific source region is on average about  $0.5\text{kg/m}^3$  lower in density than the South Pacific one (Figure 8.3).

While occurring in the Pacific rather than the Atlantic Ocean, the 30Ma northern overturning shows large similarities in both strength and structure to that of the Pre-industrial one. Again this is not necessarily related to the presence of a southern overturning cell, but rather to the density difference between deep water formation sites (about  $0.3\text{kg/m}^3$  for 30Ma  $1\times$  PIC).

Both the North Pacific and North Atlantic Ocean are limited in their northern extent within the considered 38Ma and 30Ma geography reconstructions (Figure 7.1), limiting the minimum temperature and thus the density at which deep water can form. This also limits density differences between most high latitude ocean regions and generally increases the importance of the salinity distribution. In line with the ocean-only results in Chapter 4, the Eocene geography may thus be conducive for having multiple potential deep water formation sites and possible shifts between overturning regimes.

Zonally integrated fluxes of meridional heat transport in both the ocean and atmosphere (Figure 8.2c-d) can help explain the differences in meridional symmetry of temperatures between 38Ma, 30Ma and pre-industrial configurations. The latter shows an asymmetry in both components of about  $0.5\text{PW}$ , accounting for a  $\sim 1\text{PW}$  additional heat being transported into the Northern compared to the Southern Hemisphere. The asymmetry is completely cancelled out in both components when 38Ma cases are considered, or even shifted slightly towards the Southern Hemisphere. This symmetry nicely corresponds with the patterns in zonal mean SST, where northern and southern middle/high latitudes are comparably warm at similar latitudes for 38Ma ( $15\text{--}20^\circ\text{C}$  at  $50\text{--}60^\circ\text{N/S}$ ). Additionally, the effect of Ekman upwelling at southern middle latitudes is minimal and shifted towards the south by  $10\text{--}15$  degrees in latitude (from  $45^\circ\text{S}$  to  $50\text{--}55^\circ\text{S}$ ).

Heat fluxes into the Southern Hemisphere at 30Ma are slightly smaller than they are at 38Ma, but still considerably larger than those of the pre-industrial reference. The impact of the ACC is, however, larger and shifted northward to  $\sim 50^\circ\text{S}$  at 30Ma (compared to  $\sim 55^\circ\text{S}$  38Ma). This indicates that at least in the ocean, the deep zonal current is in fact blocking part of the southward heat flux. The top of model required flux also shows a  $0.1\text{--}0.2\text{PW}$  reduction of heat going into the Southern Hemisphere, comparing 30Ma to 38Ma  $2\times$  PIC. The atmosphere thus not necessarily compensates changes in oceanic heat flux (as seen in Figure 7.14), but the atmospheric circulation can actually contribute to the effect. It is noteworthy that the total flux difference is largest near the equator, in conjunction with the steepest gradient and indicative of a shift in flux from one hemisphere to the other.

Not much change is seen in Northern Hemisphere total heat fluxes, but the opposite is true for the oceanic component. As to be expected, a large part of the northward heat transport seen at pre-industrial conditions is restored when a northern overturning cell is active in the 30Ma  $2\times$  PIC adjusted and  $1\times$  PIC cases. As shown above (Figure 7.14), most of the changes in oceanic heat fluxes due to a shift between overturning regimes (but not geography changes) are compensated by the atmospheric component to balance the total flux. Meanwhile, overall little change in meridional heat fluxes is seen between 30Ma cases in the Southern Hemisphere as they all exhibit a similar deep southern overturning cell. Although most of the total integrated flux differences are small between the 38Ma and 30Ma equilibrium states, the atmospheric responses to a change in geography or overturning regime are often non-trivial. They can lead to amplified regional changes related to shifts in the general circulation pattern, such as those shown in Chapter 7 (Figures 7.10, 7.11 and 7.15).

Generally, apart from changes due to geography and deep water formation regimes, both the meridional overturning circulation and heat fluxes are more pronounced in cooler climates especially when meridional temperature gradients are steep. This disagrees with the suggestion that a more equable climate is sustained by enhanced meridional heat fluxes, keeping high latitudes warm and the tropics relatively cool. Meanwhile, it makes more physical sense that heat fluxes are directly related to the strength of the associated temperature gradient. One way to solve this paradox is by additional mechanisms of mixing in both the atmosphere and ocean, but the simulations presented here suggest otherwise.

The more equable climate seen at 38Ma is sustained by altered radiative fluxes rather than enhanced meridional heat transport. Changes in albedo, radiative forcing, land cover and especially clouds all add to a reduced net heat loss at high latitudes that can sustain a warmer polar climate. Mainly the 30Ma  $1\times$  PIC simulation suggests that these mechanisms have a strong hysteresis, as a warm and wet (mostly ice free) polar climate tends to stay relatively warm even under low radiative forcing.

## 8.1.2 Atmosphere

Like the SST pattern (Figure 8.1), there is a large difference between the pre-industrial reference and any of the Eocene cases in terms of zonal mean near surface air temperature (Figure 8.4; corresponding global and regional averages in Table 8.2). Annual mean temperatures in the Arctic drop down to  $-25^{\circ}\text{C}$  and further down to  $-45^{\circ}\text{C}$  over Antarctica under pre-industrial conditions. Even at 30Ma  $1\times$  PIC zonal mean, annual mean temperatures are above  $-10^{\circ}\text{C}$  everywhere which is mostly related to the absence of polar ice sheets. In any other ( $2\times/4\times$  PIC) Eocene case, there is very little surface area where annual mean (zonally averaged) temperatures are below freezing. Those mild conditions are sustained not only by the radiative forcing from greenhouse gases, but also by the general changes in boundary conditions between pre-industrial and Eocene cases.

An increase in radiative forcing causes a similar warming response for 38Ma and 30Ma cases, with a polar amplification factor close to 2 ( $\sim 2.5^{\circ}\text{C}$  at tropical versus  $\sim 5^{\circ}\text{C}$  in polar regions). Not surprisingly, air temperatures cool down slightly in the Southern Hemisphere between 38Ma and 30Ma geographies under  $2\times$  PIC. A further subtle cooling is seen for the  $2\times$  PIC Adjusted case, but this is accompanied by a more substantial warming of the Northern Hemisphere compared to 30Ma  $2\times$  PIC. The effect of both geography changes and meridional overturning regimes between Eocene cases on air temperatures is less pronounced than it is on SSTs. Zonal mean, annual mean air temperatures are thus governed by the radiative balance rather than circulation and associated flux changes. Note that there are still significant changes in atmospheric temperature between Eocene cases, but they are more regionally and seasonally dependant than the SST responses seen in Figure 8.1. This agrees with the findings in Section 7.4, where changes in the atmosphere were most pronounced in seasonal rather than annual mean fields.

While still being rather meridionally symmetric, the zonal mean air temperature pattern is skewed in a way opposite to the SST pattern. The explanation for this difference lies in the contrasting continental geometries of the polar regions, which become even more important under the absence of ice sheets. Antarctic surface air temperatures are dominated by large seasonal swings, with a  $40^{\circ}\text{C}$  amplitude between summer and winter temperatures. In contrast, the Arctic region is an open ocean for most (or all) of the time during the Eocene and thus has a dampening effect on seasonality. Without substantial sea ice cover, wintertime cooling is limited and annual mean temperatures are relatively high. Stronger seasonality is again seen across northern middle latitudes where land masses are more abundant.

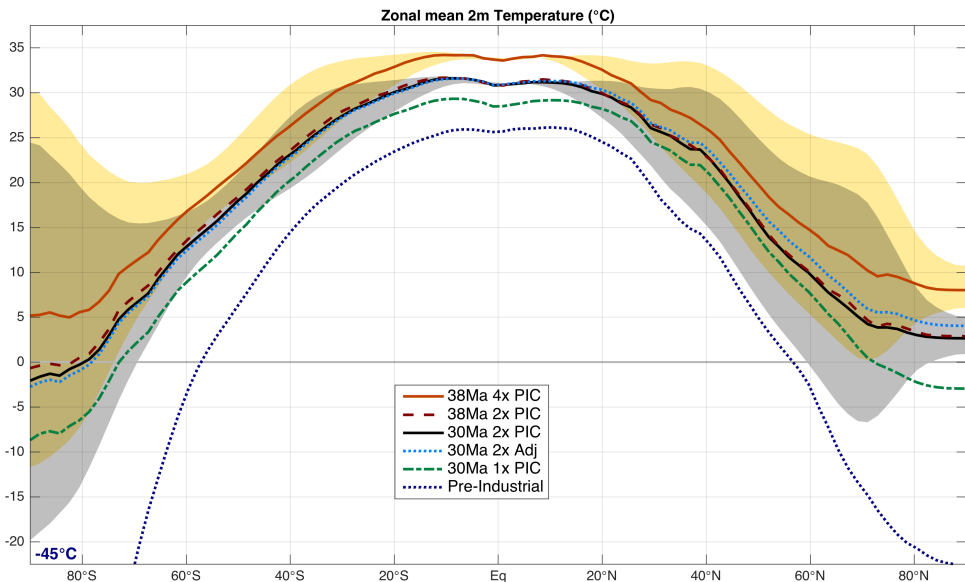


**Figure 8.4:** Zonal mean, annual mean near surface air temperature for all CESM simulations using the same colour coding as used in Figure 8.1, but with shaded areas indicating seasonal rather than zonal variation.

Considering the overview of different averages in both SST (Table 8.1) and surface air temperature (Table 8.2), there is a consistent response to radiative forcing for all Eocene cases. Overall, there is a  $\sim 3^\circ\text{C}$  warming per PIC doubling corresponding to an equilibrium climate sensitivity of just under  $0.7^\circ\text{C}/\text{Wm}^{-2}$ . As to be expected, the warming response of SSTs is slightly lower being  $\sim 2.5^\circ\text{C}$  while the deep ocean response lies in between ( $\sim 2.75^\circ\text{C}$ ). Tropical temperatures near the atmosphere-ocean interface are closely tied and see the lowest response:  $\sim 2^\circ\text{C}$  warming per PIC doubling. This justifies the proposal in Chapter 5 (Section 5.2.3; Royer et al. 2012), to estimate a global warming under increased radiative forcing by multiplying the tropical SST response by 3/2. The global mean temperature increases more in the warmer climate under a PIC doubling, mainly as a result of low latitude warming (water vapour and clouds). In contrast, cooler climates have a stronger response at high latitudes, primarily linked to snow/ice albedo feedbacks.

The equilibrium climate with a 30Ma geography is generally cooler than with a 38Ma one, most prominently at higher latitudes. The 30Ma geography thus induces a slight polar amplification of the temperature gradient, explaining  $\sim 1^\circ\text{C}$  cooler deep ocean waters. As shown in Section 7.5 the onset of a northern overturning component warms the Northern Hemisphere, partly at the expense of the southern one and especially at high latitudes. The transport of relatively warm waters towards high latitudes releases heat, warming the surface climate while creating cooler deep waters.

Looking at the pre-industrial reference as well, earlier (Section 5.2.3) estimates of the temperature difference induced by applying an Eocene configuration can be re-considered. At the tropics as well as the deep ocean, the difference is similar to or slightly higher than that of an additional PIC doubling. The added effect of continental ice sheets is a further cooling of mainly polar regions. This finally results in a total difference between the pre-industrial and Eocene  $1\times$  PIC climate of  $\sim 5^\circ\text{C}$  in SST's and  $\sim 7^\circ\text{C}$  for surface air temperature. These values both agree well with the estimates found in Chapter 5 using only the 38Ma and pre-industrial cases, justifying the assumption of a dominant linear response to geography and radiative forcing.

Case \ Measure	$T_{glob}$ ( $^\circ\text{C}$ )	$T_{trop}$ ( $^\circ\text{C}$ )	$T_{np}$ ( $^\circ\text{C}$ )	$T_{sp}$ ( $^\circ\text{C}$ )
38Ma $4\times$ PIC	26.75	33.65	9.94	8.86
38Ma $2\times$ PIC	23.66	31.01	4.57	4.53
Pre-industrial $1\times$ PIC	13.72	25.29	-16.8	-29.1
30Ma $2\times$ PIC	23.36	30.85	4.14	3.68
30Ma $2\times$ PIC Adjusted	23.65	30.93	5.81	3.23
30Ma $1\times$ PIC	20.85	28.69	-0.12	-1.44

**Table 8.2:** Average equilibrium temperatures at the end of each CESM simulation, showing  $T_{glob}$ : global mean near surface air temperature,  $T_{trop}$ : tropical ( $< 23.5^\circ\text{N/S}$ ),  $T_{np}$ : Arctic ( $> 66.5^\circ\text{N}$ , and  $T_{sp}$ : Antarctic ( $> 66.5^\circ\text{S}$ ) mean temperature. These values are calculated using the last 200 years of each simulation.



## 8.2 Southeast Asian Monsoons in the Eocene

There is quite some debate on since when the Southeast-Asian Monsoons have existed and to what extent they were similar in the middle-to-late Eocene to those seen today climate (Bosboom et al., 2014b; Bougeois et al., 2018; Huber & Goldner, 2011; Licht et al., 2014; Quan et al., 2012). The results from a set of CESM simulations presented here, using middle-to-late Eocene boundary conditions and different geographies without an Antarctic Ice Sheet, provide a unique opportunity to look at this, considering the following two questions:

- 1) what did the Southeast-Asian Monsoons look like in the middle Eocene, and;
- 2) how did they change as a result of late Eocene geography changes?

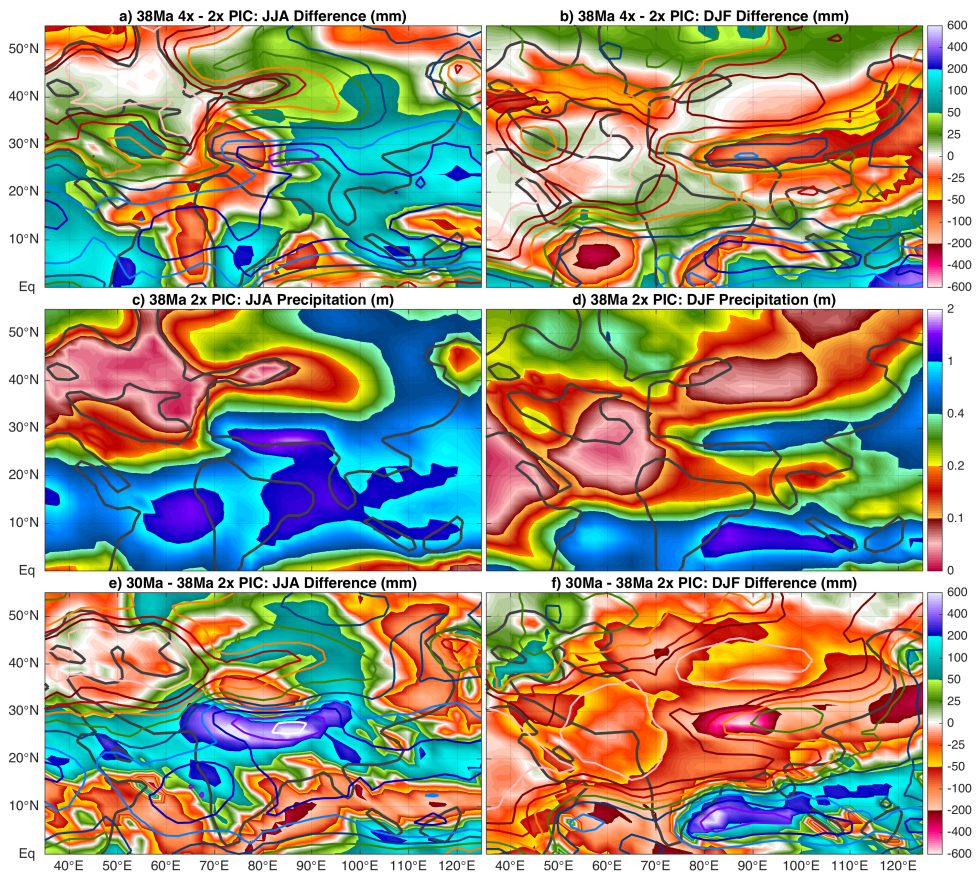


**Figure 8.5:** Seasonal precipitation over Southeast Asia in different Eocene CESM simulations. The averaged fields from the 38Ma 2× PIC case are shown in **c**) for June-July-August, and in **d**) for December-January-February. The same is done in **a**) and **b**) but instead for the 38Ma 4× PIC - 2× PIC difference, and similarly in **e**) and **f**) for the 30Ma - 38Ma 2× PIC difference. Contours in the difference plots show the corresponding mean precipitation, using the same colour scale as in **c**) and **d**).

An overview of seasonal precipitation over Southeast Asia for the 38Ma  $2\times$  PIC case is shown in Figure 8.5 along with comparisons to that of 38Ma  $4\times$  PIC and 30Ma  $2\times$  PIC. The central panels thus show a 38Ma reference state of the monsoons, the upper ones its response to increased radiative forcing and the lower ones the effect of 38–30 Ma geography changes.

The seasonal precipitation patterns depict an already well-established monsoonal climate in Southeast Asia as well as Northeast Africa. Most inland regions are much wetter in summer than they are in winter, with a distinct precipitation maximum over both western and eastern India similar to today (Appendix A, Figure A.6a). Seasonality generally increases going further inland, except over the Himalayas due to orographic lift in winter. Other exceptions to the monsoonal climate are seen further south, related to the ITCZ and along the Pacific coast where winter storm tracks provide additional winter precipitation.

Upon warming the climate, the hydrological cycle generally intensifies and along with it the East-Asian Monsoons. In summer, those regions that already receive high amounts of precipitation get wetter especially over land. Winter patterns are less clear and also influenced by other changes, such as a southward shift of the ITCZ. Mostly eastern Asia including the Himalayas sees a drying in winter, thus further increasing the seasonality in precipitation.

It would be expected that the response to 38–30 Ma geography changes is more complex and tied to regional topography (as seen in Figure 7.11), but the overall pattern is remarkably simple. There is mainly a response to the closure of several seaways (e.g. Tarim Basin and Turgai Strait) and uplift of the Himalayas and Tibet. Other than that, there is a large-scale wettening across most of eastern Asia in summer, while the same regions become significantly dryer in winter.

Looking at a similar comparison of surface air temperatures and 850hPa wind fields in Figure 8.6, the monsoonal patterns and related changes shown above (Figure 8.5) can be further explained. Both the Tibetan Plateau and the low-lying hinterland of Southeast Asia warm up significantly in summer, creating a low pressure system (cyclonic flow) that draws in moisture from the surrounding oceans. The opposite is seen in winter, with cold air on the continent building an anticyclone from which winds are mostly blowing towards the ocean (Figure 8.6c-d). An important moisture source to the summer monsoon is the development of a Somali Jet (i.e. low-level southwesterly winds over the Arabian Sea; Figure A.6c). The low pressure system over Southeast Asia is sufficiently strong to draw the ITCZ northward, regionally reversing the easterly trade winds and greatly increasing rainfall over Western India and the Himalayas.

In response to an increased radiative forcing, the Southeast Asian Monsoons were seen to intensify in terms of precipitation (Figure 8.5a-b). There is a rather homogeneous warming response of 1–2 °C over the ocean and 2–4 °C over land to a PIC doubling at 38Ma. The enhanced continental warming adds to the existing pressure gradient and thus amplifies the low pressure in summer. Otherwise, there is no significant change in the monsoonal circulation pattern in a warmer climate.

Changing the geography results in a more interesting temperature response regarding the Southeast-Asian Monsoons. The reduced presence of water on the Asian



continent leads to a stronger seasonality, with warmer summers and colder winters. In addition, a slightly higher and larger Tibetan Plateau creates locally cooler conditions but enhances the elevated heat island effect. In contrast to the 38Ma  $4\times$  PIC case, both the summer cyclone and winter Anticyclone are significantly stronger in the 30Ma  $2\times$  PIC climate compared to the 38Ma one. The temperature response is thus partly a direct consequence of the changes in topography, but also due to the enhanced monsoonal circulation. In general, the manifestation of the East Asian monsoon (seasonality in temperature, precipitation) amplifies in a warmer climate but it is the monsoon circulation itself that strengthens upon changing the geography reconstruction from 38Ma to a 30Ma one.

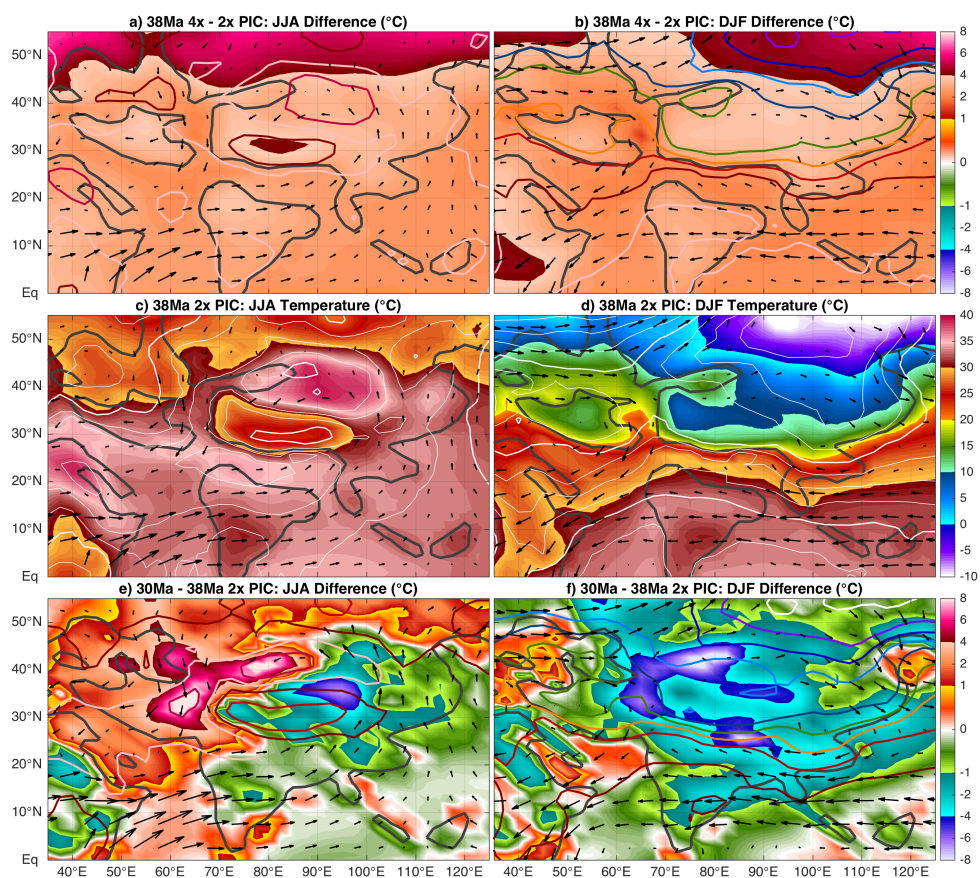


**Figure 8.6:** Seasonal near surface air temperature (shading), mean sea level pressure (white contours every 2.5hPa, thick lines every 10hPa) and 850hPa flow (arrows) over Southeast Asia. The mean fields from the 38Ma  $2\times$  PIC case are shown in **c)** for June-July-August, and in **d)** for December-January-February. The same is done in **a)** and **b)** but instead for the 38Ma  $4\times$  PIC -  $2\times$  PIC difference, and similarly in **e)** and **f)** for the 38Ma - 30Ma  $2\times$  PIC difference. Contours in the difference plots show the corresponding mean temperature, using the same colour scale as in **c)** and **d)**. Arrows always show the mean 850hPa wind and are scaled similarly (maximum arrow length 15m/s).

## 8.3 Antarctic Glaciation at the EOT

### 8.3.1 Pre-industrial versus Eocene Antarctica

As discussed in Chapter 6, Antarctica has a perennially cold and dry climate in the pre-industrial configuration (Figure 6.4). The temperature and circulation patterns stay winter-like, featuring a steep meridional temperature gradient. A nearly zonally uniform band of tight pressure gradients and associated zonal winds surrounds the Antarctic continent year-round (Figures 6.2, 6.7 and A.5). The presence of an Antarctic Ice Sheet further intensifies cold conditions on the continent and promotes the build-up of a surface anticyclone. Downslope (Katabatic) winds and subsidence over the continent suppress poleward moisture transport and precipitation.

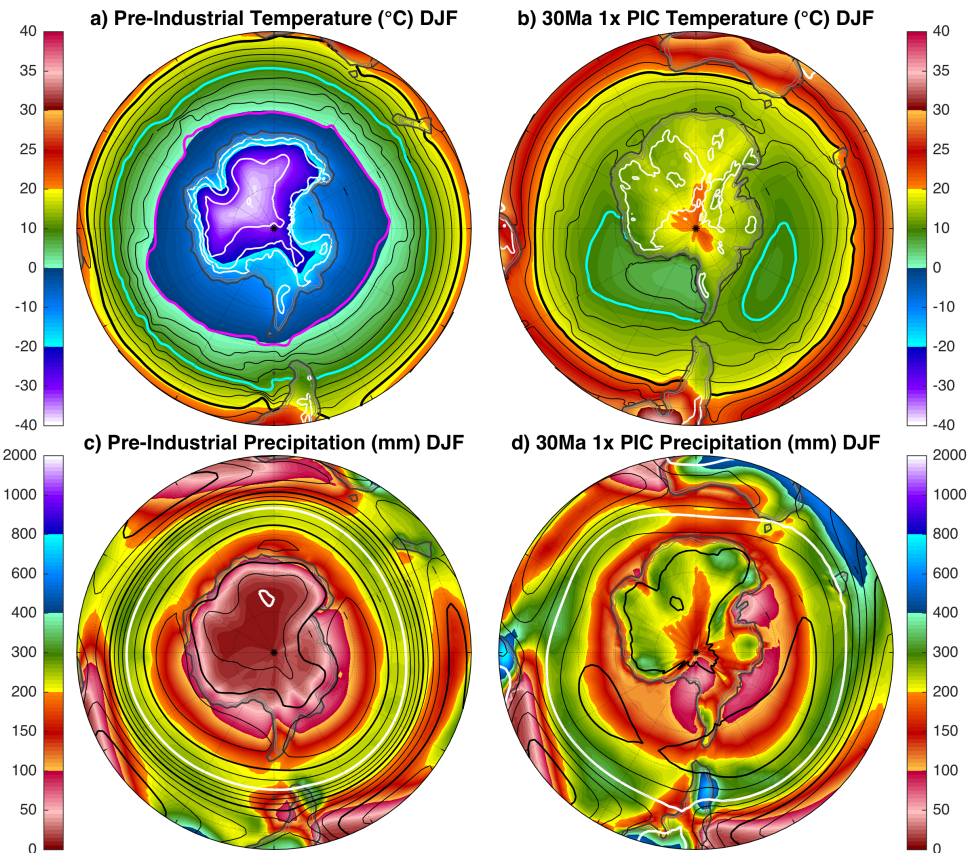


**Figure 8.7:** Southern polar, mean summertime (December-January-February) near surface air temperature (shading) and sea surface temperature (contours every  $2.5^{\circ}\text{C}$ , thick lines at every  $10^{\circ}\text{C}$ ; magenta:  $0^{\circ}\text{C}$ , cyan:  $10^{\circ}\text{C}$ , black:  $20^{\circ}\text{C}$  and white:  $30^{\circ}\text{C}$ ) for a) the pre-industrial reference and b) the 30Ma  $1\times$  PIC case. Thin white contours show model topography at 1000m intervals. c) and d) similar to a) and b) but for precipitation (shading) and mean sea level pressure (black contours every 5hPa, 2.5hPa intervals above 1000hPa, thick lines every 10hPa and thick white line at 1000hPa).

With a 30Ma geography reconstruction and under the same ( $1 \times \text{PIC}$ ) radiative forcing, there are major differences between the pre-industrial and late Eocene Antarctic summer climate (Figure 8.7). Regardless of the presence of a relatively strong ACC, overall temperature gradients are still strongly reduced by using the 30Ma geography. As it did for the 38Ma  $4 \times \text{PIC}$  case, the cyclonic vortex over Antarctica breaks in summer at 30Ma  $1 \times \text{PIC}$ , greatly enhancing the transport of heat and moisture onto the continent. The absence of an ice sheet allows the central lowlands to warm up to above  $20^\circ\text{C}$ , making it  $40\text{--}60^\circ\text{C}$  warmer than under pre-industrial conditions and partly reversing the meridional temperature gradient.

The differences between the pre-industrial and late Eocene Antarctic climate indicate that the presence of an ice sheet regionally is the most important influence. Furthermore, without substantial continental ice the effect of 38–30 Ma geography changes is limited, especially on land (as seen in Figure 7.10). While having strong zonal transports in the ocean associated with a deep ACC at 30Ma, the current still differs much from its pre-industrial equivalent. Within the 30Ma geography, Southern Ocean gateways are open but there is no unobstructed latitude for oceanic flow around the South Pole. There is thus not a single vertical column of water moving around the continent to effectively block meridional transports. Indeed, the effect of the ACC at 30Ma on both the overturning stream function and oceanic heat transports (Figures 7.14d and 8.2d) is smaller than what would be expected by only looking at its strength ( $\sim 80\%$  of pre-industrial).

A further comparison of the Antarctic climate for all Eocene and pre-industrial cases is made in Figure 8.8. As suggested by the comparison made above (Figure 8.7), temperature and precipitation on Antarctica are vastly different compared to pre-industrial values for any of the Eocene configurations. Upon decreasing the radiative forcing, temperatures generally decrease by  $\sim 5^\circ\text{C}$  and monthly precipitation by 5–10 mm per PIC halving. As shown in Chapter 6, precipitation over Antarctica is governed by three main mechanisms:

- 1) the cyclonic vortex and zonal flow in winter (May–September);
- 2) a summer monsoon (December–February), and;
- 3) autumn storms when the vortex reverses (March–May).

Despite very cold winters in the pre-industrial reference, temperature seasonality ( $20\text{--}25^\circ\text{C}$ ) is smaller than it is in the Eocene cases ( $35\text{--}40^\circ\text{C}$ ). While being low for any month, pre-industrial precipitation is highest in winter due to the influence of cyclones under enhanced baroclinicity.

One of the main goals of the CESM simulations presented here is to look at the conditions under which Antarctic glaciation took place. Therefore, the Antarctic climate is studied for the different cases to assess how it responds to changes in model boundary conditions representative for the middle-to-late Eocene; **(i)** radiative forcing, **(ii)** geography and **(iii)** meridional overturning circulation. The results discussed in Chapter 6 showed that the simulated 38Ma late middle Eocene conditions were highly unfavourable for Antarctic Ice Sheet growth. Under both  $4 \times \text{PIC}$  and  $2 \times \text{PIC}$  forcing, Antarctic summers are simply too warm to allow any accumulation of ice over the continental interior.

(i) Surprisingly, mainly the winter precipitation decreases over Antarctica under lower radiative forcing while the meridional temperature gradient increases. Meanwhile, the summer monsoon strength shows little change between the 38Ma 4× PIC and 2× PIC cases, but a larger decrease at 1× PIC due to limited moisture availability. As lowering the radiative forcing affects the winter climate more than the summer one, the already strong seasonality is further enhanced in a cooler state under Eocene conditions.

(ii) The effect of changing the geography at 2× PIC has remarkably little effect on the Antarctic climate. There is an overall slight cooling upon changing from a 38Ma to a 30Ma geography, but the climate is qualitatively the same. While the temperature response is largest in summer, monsoonal rains are mostly unaffected.

(iii) The same conclusion holds for the onset of a northern overturning circulation in the 30Ma 2× PIC Adjusted case. The effect on Antarctic temperatures is even smaller than for a 38–30 Ma geography change and most pronounced in winter. Despite having a smaller impact on temperature, the presence of a northern overturning cell decreases Antarctic precipitation more than a geography change.

Any of the temperature and precipitation responses to a change in (i) radiative forcing, (ii) geography and (iii) overturning regime thus do not affect the overall picture of a simulated perennially wet, strongly seasonal climate over Antarctica during the middle-to-late Eocene.

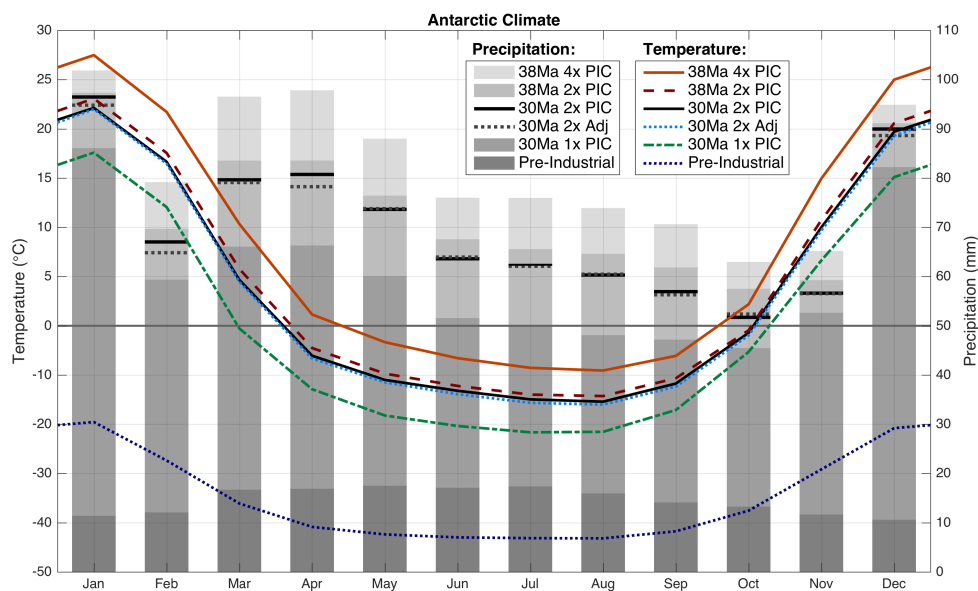


**Figure 8.8:** Overview of the mean continental Antarctic climate in all CESM simulations, showing monthly climatologies of temperature (lines) and precipitation (bars). Colour coding for temperature is the same as the one used in Figures 8.1 and 8.4. Precipitation bars of increasingly dark shading represent 38Ma 4× PIC, 38Ma 2× PIC, 30Ma 1× PIC and pre-industrial cases. For comparison to the 38Ma 2× PIC case, the 30Ma 2× PIC and 30Ma 2× PIC Adjusted precipitation climatology is indicated by solid and dashed horizontal black lines, respectively.

### 8.3.2 Antarctic Ice Growth and Equilibrium Level

Using the annual mean precipitation and monthly temperatures over Antarctica, one can estimate whether an ice sheet would be able to sustain itself under such climatic conditions. Monthly climatologies of temperature can be used to estimate the number of positive degree days (PDD), by summing the daily average temperature whenever it is above zero. Simply taking that the annual precipitation ( $P$ ) falls as snow (under the presence of an ice sheet), the annual surface mass balance (SMB) can be estimated (similar to the approach in Chapter 6, exploring the possibility of Eocene ice in Figure 6.6). With 4mm melt assumed per PDD, the surface mass balance at every model grid point ( $i, j$ ) then becomes:

$$SMB_{i,j} = P_{i,j} - 4 \cdot PDD_{i,j}. \quad (8.1)$$

To further estimate the total annual surface mass balance over the Antarctic continent, the sum is taken over all of the corresponding grid points and multiplied by their surface area.

In all of the Eocene cases considered here, the climate is much too warm to get a positive total surface mass balance, but a hypothetical ice sheet would also have a certain height. To find out what height such an ice sheet would have to be in order to sustain itself, the equilibrium level has to be determined. For a series of heights (with 250m increments), the temperature at the surface can be adjusted to that level using a vertical atmospheric lapse rate of -8K/km. Doing the same exercise as before, a new integrated mass balance can be obtained at each height level. The equilibrium level is then estimated by simply finding the intersection of the integrated mass balance with the zero line as a function of height.

Looking at the respective surface mass balance curves in Figure 8.9, it is clear that an Antarctic Ice Sheet would have a hard time sustaining itself in any of the Eocene cases without additional changes. Of course, the presence of such an ice sheet would significantly alter the surrounding climate, but little ice will grow if the equilibrium level is significantly higher than the topography (mostly at 1–2 km) to start with. At  $4 \times \text{PIC}$ , the equilibrium line would be at 3.75km which is higher than most of the Antarctic Ice Sheet today. For every PIC halving, the equilibrium line drops by about 0.5km meaning that it is still positioned at 2.75km for the 30Ma  $1 \times \text{PIC}$  climate. As expected, changing from a 38Ma to a 30Ma geography does lower the estimated average equilibrium line over Antarctica, but not substantially. The slight cooling seen in Figure 8.8 between 38Ma and 30Ma cases is partly being offset by reduced precipitation in the SMB.

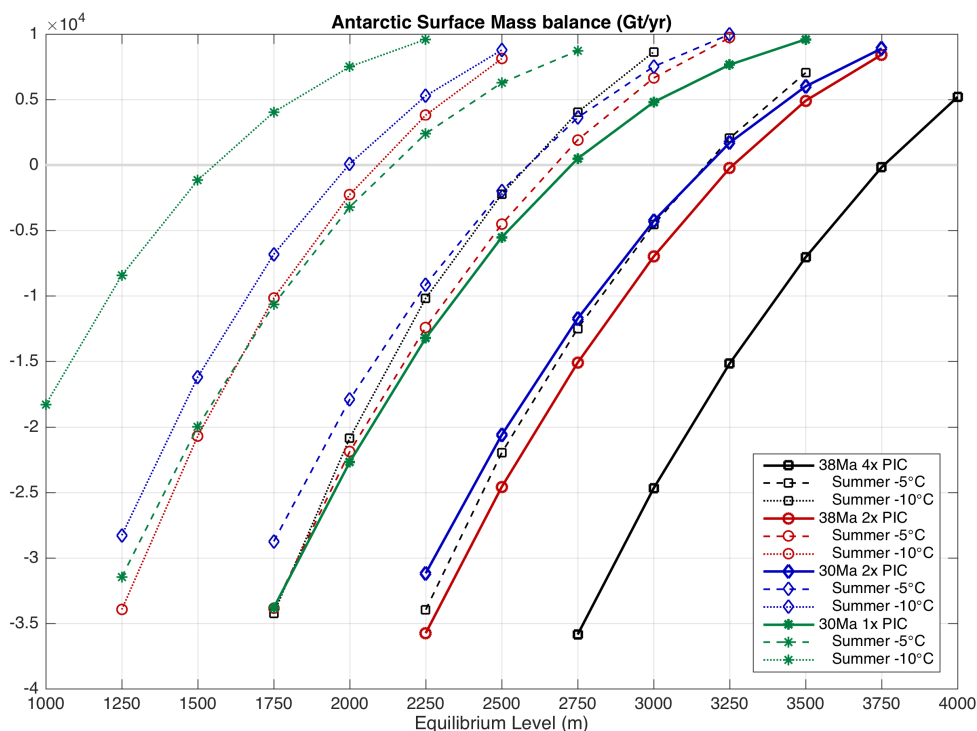


**Figure 8.9:** Integrated Antarctic surface mass balance as a function of hypothetical equilibrium level for the different Eocene CESM simulations; 38Ma 4× PIC (black squares), 38Ma 2× PIC (red circles), 30Ma 2× PIC (blue diamonds) and 30Ma 1× PIC (green stars). Results are shown for the unaltered climate (solid lines), with 5°C cooler summers (dashed lines) and 10°C cooler summers (dotted lines).

There are several mechanisms (e.g. orbital cycles, volcanism, biological activity) that can induce long term cooler periods within the mean climate. To explore the impact of such a cold period, the equilibrium level is also calculated using a 5°C and 10°C cooler climate which are both shown for the 38Ma 2× PIC case in Figure 8.10. As the Antarctic climate in the Eocene features a strong seasonality in temperature, a similar exercise is also done using only a change in summer temperatures. The same reductions of 5°C and 10°C are used, but with a fraction of 1 for December/January, 0.75 for November/February and 0.25 for October/March, effectively dampening the summer peak with a sinusoidal-like function.

A 5°C cooling over Antarctica would result in a reduction of the equilibrium level of about 600m, which is slightly larger than for a PIC halving seen above (Figure 8.9). While resulting in a similar temperature response (Table 8.2), a PIC halving has a slightly smaller effect on the equilibrium level as it generally also decreases precipitation. The surface mass balance hardly changes between an adjustment of either annual or only summer temperatures, especially at higher values (i.e. near zero). This shows that indeed the main inhibitor for Antarctic glaciation in the late Eocene is warmth-induced summertime melt.



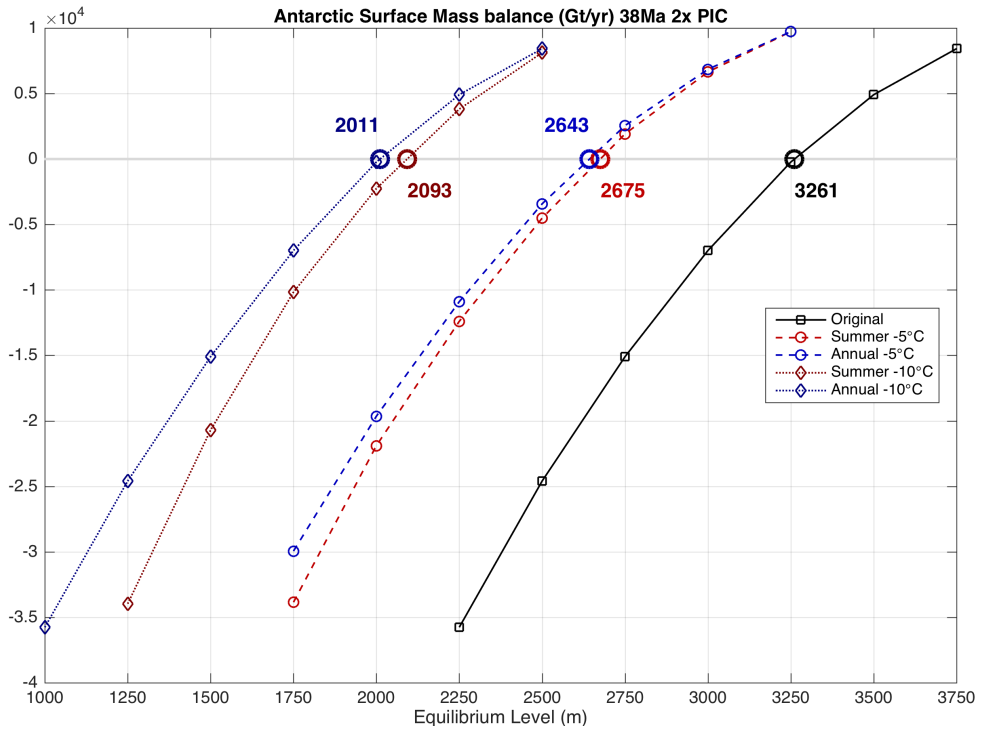


**Figure 8.10:** Similar to Figure 8.9, but only for the 38Ma 2× PIC case and distinguishing between adjusting only summer (red) or annual (blue) temperatures by 5 (dashed) and 10 (dotted) °C. Interpolated estimates for the Antarctic continental-wide equilibrium level are given near the intersection of each curve with 0Gt/yr.

While looking at the average equilibrium level over the Antarctic continent is indicative of whether glaciation is possible, it does not show any spatial variation. In reality, the surface mass balance is different at each location and therefore also the corresponding equilibrium level. Similar to what was done above, an estimate of the equilibrium level at each grid point can be found by again adjusting the temperature as a function of height and finding the intersection of the mass balance with zero. Now the spatial structure of temperature and precipitation, in combination with the surface topography indicates where any ice would grow under (either 38Ma or 30Ma) 2× PIC middle-to-late Eocene conditions (Figure 8.11).

Without any adjustment to the Antarctic climate, there is only little surface area where ice could grow in both the 38Ma and 30Ma  $2\times$  PIC climate. The overlap of relatively low equilibrium levels and high topography favours some near coastal regions in Dronning Maud Land and on the Antarctic Peninsula. (similar to the isolated regions suggested in Chapter 6, Figure 6.6) The mainland of Antarctica does not allow any ice growth due to the presence of both overall drier conditions and warmer summers. Even under  $2\times$  PIC forcing, the equilibrium level exceeds 3km over most of the continent and even 4km over the Antarctic interior.

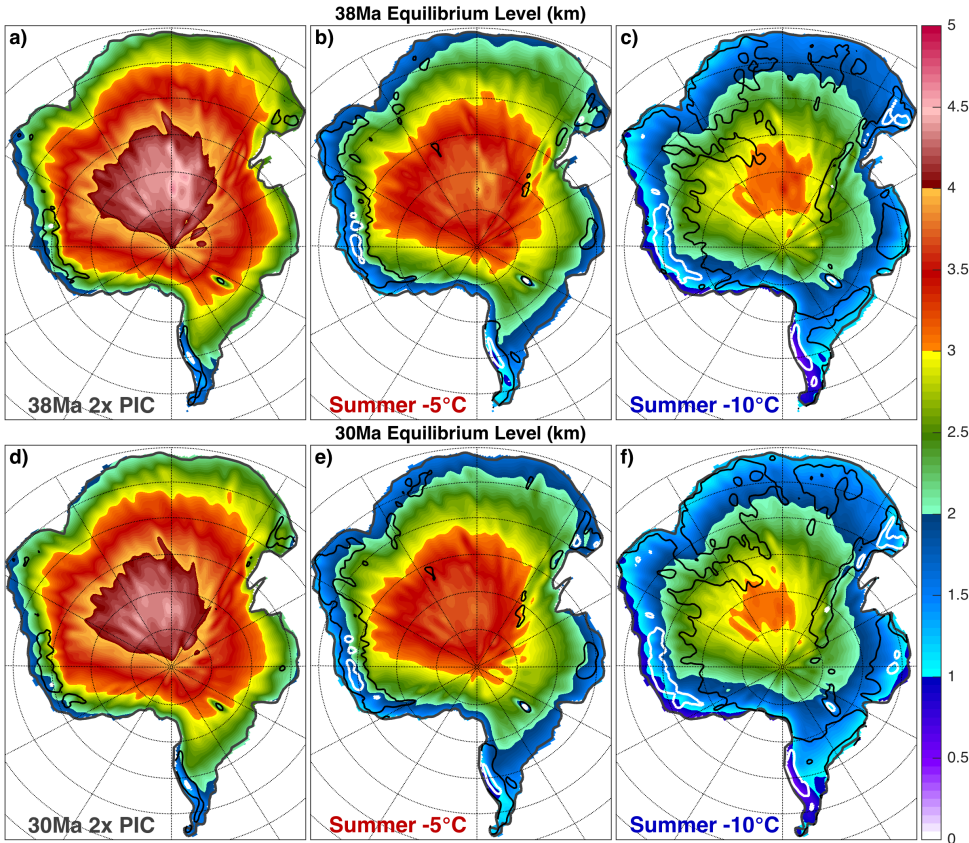


**Figure 8.11:** Spatial distribution of the estimated equilibrium level (through interpolation of the curves shown in Figures 8.9 and 8.10 for each grid point individually) in the simulated 38Ma  $2\times$  PIC Antarctic climate; a) unadjusted, b) 5°C, and c) 10°C cooler summer. White contours show the intersection of the equilibrium level with local topography, black ones mark a difference of 1km. d), e) and f) similar to a), b) and c), but for the 30Ma  $2\times$  PIC case.



Decreasing summer temperatures by 5°C shows a picture similar to that of the 30Ma 1× PIC climate, with still highly limited potential for ice growth. Again, most of the Antarctic mainland is inhospitable to land ice and only in some near coastal regions the surface topography approaches the equilibrium level. In this case also the Transantarctic Mountains start to become a focus for potential glaciation together with a larger portion of Drønning Maud Land and the Antarctic Peninsula. Even more cooling is needed in order to get a substantial surface area above the equilibrium level, surrounded by areas that can be covered by an expanding ice sheet (equilibrium level <1km above the surface). Even at this stage, most inland regions are still not susceptible to substantial ice growth. It is clear that under such conditions, regions like the Gamburtsev Range cannot be one of the main inception points for Antarctic glaciation as suggested by previous modelling studies (DeConto & Pollard, 2003; DeConto et al., 2008; Gasson et al., 2014).

In order to check whether using such a simple estimate for the equilibrium is a decent (qualitative) measure to explore the possibility of Antarctic Glaciation, additional model simulations are considered using an offline ice-sheet model. For this study, the model IMAUICE (Boer et al., 2014) is applied using the shallow ice approximation at a horizontal grid resolution of 40km. The surface mass balance is calculated from the CESM 38Ma 2× PIC climate with an insolation-temperature method described in Berg et al. (2008) and Boer et al. (2014). The ice-sheet model uses an altered version of the Wilson et al. (2012) late Eocene Antarctic topography. The latter is shifted in order to be compatible with the 38Ma PaleoMag geography from Chapter 2, and projected onto a south polar-referenced equidistant grid (see Figure 8.12 below).

A large number of 30 000-year simulations have been carried out using different parameter combinations for melt, stresses, orbital cycles and lapse rates but none of them produces significant ice sheets over Antarctica (<10% of the present-day AIS volume). Only when summer temperatures are cooled by 10°C in the 2× PIC climate (or 5°C under 1× PIC) there is substantial ice growth, shown at different time intervals in Figure 8.12. Several ice caps form in regions which closely overlap with those suggested by the equilibrium level estimates in Figure 8.11c. Most of those ice caps stop growing after several 1000 years and remain small, but the one over Drønning Maud land keeps expanding and eventually forms a partial ice sheet over East Antarctica. Despite the higher surface elevation, no ice is seen over the Gamburtsev Range as suggested above (Figure 8.11).

At the end of the ice-sheet model simulation (30 000 model years), the ice sheet over East Antarctica is still growing. At this point, it is no longer physically realistic to consider its evolution without feedback from the CESM. Probably already after  $\sim 10\,000$  years (Figure 8.12c), there is enough ice to start altering the Antarctic climate significantly and feedbacks between the ice and the atmosphere-ocean circulation start playing a role. Even without knowing its further course, it can be concluded that the situation discussed here is a minimum requirement for large-scale ice growth on Antarctica. This means that, using the results from CESM simulations performed in this study, Antarctic glaciation is only possible at low greenhouse gas concentrations ( $1\text{--}2\times \text{PIC}$ ), during dramatic climatic events that significantly lower summer temperatures over the continent.

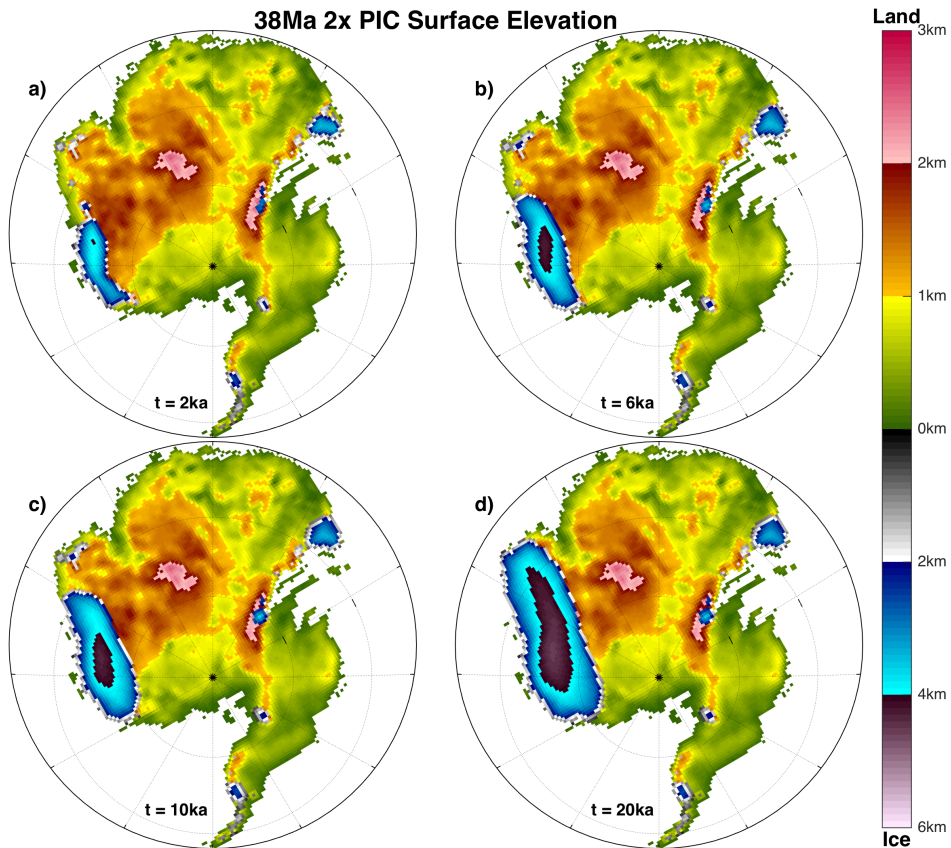


**Figure 8.12:** Results of ice-sheet model simulations using IMAUCE with climatology forcing from the 38Ma  $2\times \text{PIC}$  CESM simulation, at a) 2000, b) 6000, c) 10 000 and d) 20 000 year intervals. The upper part of the scale indicates land surface topography at the ice-sheet model resolution, the lower half shows the ice surface elevation.

## 8.4 Summary and Conclusions

A comparison of zonal mean SSTs and near surface air temperatures from the different CESM simulations showed that either of the  $2\times$  PIC cases provides a good baseline climate that is representative of middle-to-late Eocene conditions. In addition, the 38Ma  $4\times$  PIC results best match late middle Eocene peak (MECO) warmth while cooler late Eocene intervals are best reproduced by those of the 30Ma  $1\times$  PIC case. This shows that the model can reproduce middle-to-late Eocene conditions well in its configuration used here, under limited and thus realistic radiative forcing from atmospheric greenhouse gases.

The impacts of late Eocene (38–30 Ma) geography changes on the simulated climate are limited and mainly act to slightly cool the Southern Hemisphere. The activation of a northern meridional overturning circulation leads to a warming of the Northern Hemisphere in 30Ma cases, but its effects over land are reduced and strongly regional/seasonal. The 30Ma  $1\times$  PIC simulation pointed out the large influence of different model boundary conditions compared to the pre-industrial reference, especially due to integrated geography changes (including vegetation and ice sheets). In terms of a zonal mean temperature response, the difference between pre-industrial and late Eocene conditions is equivalent to that of a first PIC doubling globally and a second one regionally from significant polar amplification.

A general response of  $\sim 3^\circ\text{C}$  to a PIC doubling was seen for any of the Eocene cases, being slightly larger for warmer climates but featuring an enhanced polar amplification in colder ones. In agreement with the estimates from Chapter 5, a  $5\text{--}7^\circ\text{C}$  difference in global mean temperatures was found between the pre-industrial reference and 30Ma  $1\times$  PIC case. In summary, the simulations showed that not only radiative forcing but also the geography and meridional overturning regime determine the circulation and temperature patterns and eventually the climatic state.

The different climatic states in the CESM simulations could be explained by considering their meridional overturning circulation and according heat fluxes. All of the Eocene cases feature a deep southern overturning cell, of which the extent is limited by the presence of Ekman upwelling associated with a deep ACC at 30Ma (and almost completely blocked in the pre-industrial configuration). The resulting outflow of bottom waters can be directly linked to the density profile of the according source regions. As the Eocene geography limits the impact of temperature on the density of surface waters, the importance of salinity feedbacks is elevated. This may explain why the middle-to-late Eocene climate seems more susceptible than the pre-industrial one to the occurrence of multiple equilibria regarding the meridional overturning circulation.

Integrated meridional heat fluxes pointed out why the Eocene climate is on average more meridionally symmetric than the pre-industrial one. Even though a deep ACC forms with the 30Ma geography reconstruction, it does not consist of a single column of water flowing around the pole and thus has a limited effect on the total southward heat flux.

Considering the different model experiments that were conducted here, three different responses of the meridional heat flux can be described:

1) Radiative forcing: overall increased fluxes were seen under a lower radiative forcing, in response to a steeper meridional temperature gradient. The effect is largest in the oceanic component, sometimes leading to a small reversed atmospheric heat flux change. This may also be related to continued transient responses in both the 38Ma  $4\times$  PIC and 30Ma  $1\times$  PIC cases, which were shown to retain the largest temperature drifts at the end of the simulations.

2) Geography: the total heat flux change from variations in global geography is usually divided between the atmospheric and oceanic component to redirect heat from one place to another. In addition to the global signal, there are non-trivial regional responses due to geography-related circulation (e.g. ACC or jet stream) changes.

3) Meridional overturning circulation: a shift in overturning regime induces a significant response of oceanic heat fluxes while smaller opposing changes are seen in the atmosphere. As was shown in Chapter 7, the atmospheric heat flux does not cancel out changes seen in the ocean, but acts to balance the altered top of model required fluxes within a new climatic state.

Consistently with Chapter 5, these findings indicated that an equable climate in the Eocene is not sustained by enhanced fluxes but by an altered radiative balance.

The occurrence and strength of Southeast-Asian Monsoons were studied in the simulated middle-to-late Eocene climate, and found to be already well-established in the 38Ma  $2\times$  PIC case. The effects of Southeast-Asian Monsoons are amplified in a warmer climate, through an enhanced hydrological cycle and thermal contrasts in summer. Meanwhile, it is the monsoonal circulation itself that strengthens at 30Ma versus 38Ma showing the influence of tectonic changes across the Asian continent.

The Antarctic climate of the middle-to-late Eocene was shown to be generally warm and wet, exhibiting strong seasonality and a summer monsoon. Although there is a decrease in temperature and precipitation under lower radiative forcing, the Antarctic climate is qualitatively similar in any of the simulated Eocene cases.

Estimates of the surface mass balance and equilibrium level of a hypothetical ice sheet indicated that it would be very hard to grow or even sustain an Antarctic Ice Sheet in the climate simulated here. These measures were validated by performing offline ice-sheet model simulations, which mainly showed that ice sheet inception in the continental interior is indeed unlikely to occur.

The main inhibitor to ice growth over Antarctica is summertime melt related to the strong seasonality, so a dramatic reduction of summer temperatures is needed before significant ice sheets are able to form. Only after a further  $5\text{--}10^\circ\text{C}$  cooling under  $2\text{--}1\times$  PIC, respectively, an East Antarctic Ice Sheet could grow to the point where it starts to have a considerable impact on the Antarctic climate and positive feedback mechanisms may lead to glacial inception.

The great difficulty forming an Antarctic Ice Sheet agrees with the concept of a strong hysteresis in the middle-to-late Eocene climate in the CESM simulations presented here. This challenges the idea of a simple threshold in radiative forcing, that was crossed at the EOT eventually leading to widespread glaciation of Antarctica.

# Summary and Outlook

---

This study has focussed on the middle-to-late Eocene climate, considering the results of both ocean-only (Chapter 4) and coupled (Chapters 5 through 8) model simulations together with temperature proxy record compilations. Although relatively poorly sampled, the period treated here spans a crucial interval between extreme early Eocene warmth and the transition towards an icehouse world at the Eocene-Oligocene transition.

There has been special attention for the respective influence of greenhouse gases (Chapters 5, 7 and 8), global geography (Chapters 2, 4, 6 and 7) and the existence of multiple stable states in the ocean circulation (Chapters 4 and 7) on both the global and regional climate, either gradually or more abruptly. In Chapter 1 of this thesis the research goals were stated in the form of three central questions, which will be readdressed and evaluated here;

1. Can we simulate the middle-to-late Eocene climate using new geographical boundary conditions within a higher resolution climate model to improve the agreement with the proxy record?
2. Do changes in global geography affect the simulated late Eocene climate, which different equilibrium states exist and what are their consequences for the EOT?
3. Can we reproduce the warm and wet Eocene conditions on Antarctica suggested by proxies and how do they affect continental glaciation?

As the answers to these questions lead to new insights but also new challenges, they motivate additional future research topics treated in the outlook below.



“Don’t adventures ever have an end? I suppose not.  
Someone else always has to carry on the story.”

J.R.R. Tolkien

## 9.1 Summary

### **Q1: Can we simulate the middle-to-late Eocene climate using new geographical boundary conditions within a higher resolution climate model to improve the agreement with the proxy record?**

In Chapter 2, a new method was presented to create global geography reconstructions to be used in palaeoclimate modelling studies. This method was successfully adopted to the 38Ma and 30Ma time frames, considering both a PaleoMag and Hot Spot based plate-tectonic reconstruction. The corresponding model boundary conditions were presented in Chapter 3, where it was clear that changes in global geography between the different reconstructions would be significant even at the model grid resolution used here.

Using an ocean-only model (POP) simulation under a middle Eocene atmospheric forcing, the middle-to-late Eocene ocean circulation was studied in Chapter 4. The main features standing out in these results were a relatively weak and shallow Antarctic Circumpolar Current (ACC), a predominantly gyre-driven circulation and a fresh Arctic Ocean of which the outflow stratifies North Atlantic surface waters. The oceanic temperature and circulation patterns found here were representative of late middle Eocene conditions and provided an adequate basis for sensitivity tests.

Another set of model simulations was performed with the fully coupled version of the CESM (Chapter 5). The results were generally similar but displayed an overall warmer ocean than the one seen using the standalone POP with a 38Ma geography reconstruction. Under the highest radiative forcing ( $4\times$  PIC), tropical sea surface temperatures (SSTs) reached over  $36^{\circ}\text{C}$  but a comparison with recent proxy estimates showed that this is not unrealistic.

Mostly a good match was obtained between modelled and proxy derived SSTs, with the exception of some high latitude locations where the proxies may be biased towards summertime conditions. The model resolution resolves regional patterns well, such as a distinct zonal heterogeneity in the Southern Ocean and relatively cool SSTs in equatorial upwelling zones. Another important feature of the simulated 38Ma circulation is the location of the Southern Hemisphere polar front, being much further poleward than its pre-industrial equivalent and allowing a greater extent of sub-tropical warmth.

Due to their limited coverage, terrestrial temperature proxies were more difficult to compare to the model results. Across middle and high latitudes, there is again good agreement but the available low latitude proxies are much cooler than the modelled temperatures. Proxy temperatures are probably limited towards higher than present-day temperatures, so it is difficult to tell how realistic the regionally very warm continental interiors are in the model.

The difference between 38Ma 2× PIC and 4× PIC average temperatures yielded an equilibrium climate sensitivity of  $0.69^{\circ}\text{C}/\text{Wm}^{-2}$ , which is slightly lower than estimates for the pre-industrial reference. Significant polar amplification was found, with high latitudes warming twice as fast compared to low latitude regions. Between greenhouse states there is little effect of snow/ice albedo feedbacks, so the amplification is caused by other mechanisms such as changes in cloud cover. Compared to the pre-industrial reference both oceanic and total meridional heat fluxes are redirected towards the Southern Hemisphere in the 38Ma climate, sustaining a more symmetric global temperature pattern. Otherwise, changes in total heat fluxes are generally small indicating that the equable climate of the Eocene is sustained by an altered radiation balance rather than enhanced heat fluxes.

As shown in Figure 9.1, the different Eocene cases of CESM simulations nicely capture the range of oceanic temperatures indicated by various middle-to-late Eocene (42–34 Ma) proxies (Cramwinckel et al., 2018). Both the 38Ma and 30Ma 2× PIC cases provide a good baseline climatology, that captures most of the spread seen in tropical SSTs. The 30Ma 1× PIC climate matches well with tropical SST proxies for the late Eocene (38–34 Ma), while 38Ma 4× PIC values are indicative of MECO (~40Ma) conditions. Note that the estimates from ODP site 959 are near the lower bounds of both the model and proxy inferred tropical SST spread throughout the considered period. This is not surprising, as the drill site is located in the eastern tropical Atlantic Ocean and influenced considerably by cooler waters from equatorial upwelling.

Deep ocean temperatures can be compared to (ice-free) benthic  $\delta^{18}\text{O}$  and Mg/Ca values rather unambiguously and provide a good indication of high latitude conditions. Again, 2× PIC cases are generally representative of the middle-to-late Eocene climate, with bottom waters maybe on the warm side. In agreement with the tropical SST comparison, modelled bottom water temperatures capture late Eocene conditions at 1× PIC and peak MECO warmth under 4× PIC forcing.

This shows that the CESM simulations presented here reconstruct the middle-to-late Eocene climate quite well. Average temperatures over the considered ~8Ma period are reproduced under 2× PIC forcing, while most of the variability is covered under 1× PIC and 4× PIC for both cool and warm extremes, respectively.

Comparing the results of the CESM simulations presented here to those from other recent studies (Herold et al., 2014; Hutchinson et al., 2018), shows that the use of newer model versions and higher resolution results in better model-data comparisons for the middle-to-late Eocene under limited radiative forcing. This is on one hand thanks to improved model complexity (cloud parameterisation, aerosol treatment, vegetation etc.), but on the other hand also a result of the combination of new adequate geography reconstructions and sufficiently high model resolution. The model-data comparisons in Chapter 5 (and Appendix C) show an overall good agreement. In addition, the results in Chapter 6 indicate that the model simulations also prove useful to study regional climatic conditions within deep time climatic reconstructions.



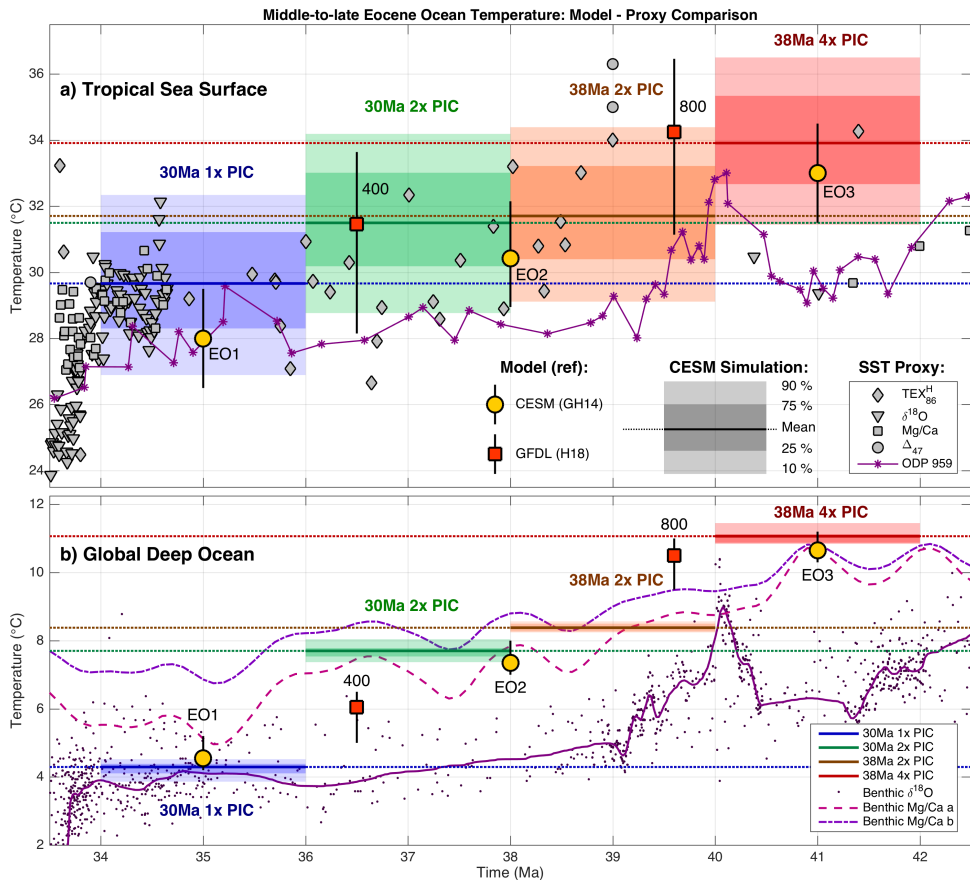


**Figure 9.1:** Comparison of new CESM results, previous model studies and proxy based annual mean **a)** tropical sea surface and **b)** global deep ocean temperatures. Coloured boxes show the respective distributions (i.e. 10, 25, 75 and 90 percentiles) from four of the middle-to-late Eocene model cases: 30Ma 1× PIC (blue), 30Ma 2× PIC (green), 38Ma 2× PIC (orange) and 38Ma 4× PIC (red). Horizontal lines indicate the corresponding mean values, note that the horizontal extent of each box is not necessarily chosen to match a specific time frame but rather to visualise the distribution of possible temperatures. Tropical average SST and spread (10/90 percentiles) are also shown from the results of Goldner et al. (2014) (GH14; yellow circles – see also Figure 5.9 in Chapter 5), where EO1, 2 and 3 denote the number of CO<sub>2</sub> doublings (i.e. 560, 1120 and 2240 ppm), respectively. The same is done for the simulations of Hutchinson et al. (2018) (H18; red squares – 400 and 800 ppm CO<sub>2</sub> cases shown), who also use the 38Ma PaleoMag geography reconstruction from Chapter 2. A compilation of tropical sea surface temperature proxies and benthic δ<sup>18</sup>O inferred bottom water temperatures is adopted from Cramwinckel et al. (2018). Deep water temperature estimates from benthic Mg/Ca are also considered, using two possible calibrations (a and b; Cramer et al. 2011).

## **Q2: Do changes in global geography affect the simulated late Eocene climate, which different equilibrium states exist and what are their consequences for the EOT?**

Two different comparisons were made to test the sensitivity of the late Eocene climate to reconstructed geography variations:

- 1) 38Ma Hot Spot or PaleoMag based reconstruction using ocean-only simulations;
- 2) 30Ma versus 38Ma PaleoMag geography with the coupled version of the CESM.

1) An interesting sensitivity to the different 38Ma reconstructions was found in Chapter 4, where the solutions had a different meridional overturning circulation. Both of these regimes were found to exist within the same (PaleoMag) geography, indicating a change of preferred state rather than a dramatic shift between geographies. Nevertheless, the presence of multiple equilibria in the late Eocene ocean circulation may have caused rapid transitions between states as a result of long term geography changes. An analysis of the estimated  $\delta^{18}\text{O}$  response to a shift from southern to northern sourced deep waters could not reproduce the signal seen at the first step of the EOT at ODP site 1218 (Coxall et al., 2005). More interesting is the occurrence of a dissolution event right before this first step. The transition towards a considerably older water mass can explain such an event, suggesting a possible shift in the oceanic circulation state that preconditioned the climate for the EOT.

A similar existence of different overturning regimes was found in Chapter 7 using the CESM with a 30Ma geography. In contrast to the 38Ma results, the southern sinking cell does not cease to exist when the northern one is initiated. Furthermore, the northern overturning cell also exists in the 30Ma  $1 \times \text{PIC}$  case showing a dependency to the radiative forcing as well. Intermittent South Atlantic sinking is seen in the transient cooling regime at  $1 \times \text{PIC}$ , but North Atlantic sinking never occurs in any but the pre-industrial reference simulation. Changes in geography and greenhouse gas concentrations may thus both have resulted in sudden shifts between oceanic circulation states in the late Eocene.

2) The difference in climatic conditions between simulations using a 38Ma and 30Ma geography reconstruction is relatively small. A much stronger and deeper ACC is present in the 30Ma case, but it does not prevent mild conditions at southern high latitudes. More pronounced regional and especially seasonal responses to the geography changes are found. The East Asian Monsoon is amplified in the 30Ma case and a response to Asian topography excites high amplitude waves in the polar jet stream. At the surface these changes result in significantly colder and dryer winters regionally, especially over North America.

In general, the difference in geographical boundary conditions (including tectonics, vegetation and ice cover) are key to explaining the differences between the pre-industrial and middle-to-late Eocene climate. On the other hand, geography changes during the late Eocene seem relatively unimportant despite considerable impacts on the circulation state. As expected, meridional heat fluxes are overall stronger in cooler climates in correspondence to an enhanced meridional temperature gradient. Changes in the circulation state can regionally shift heat within the climate system, but do not cause major differences in global temperature.

### **Q3: Can we reproduce the warm and wet Eocene conditions on Antarctica suggested by proxies and how do they affect continental glaciation?**

The Antarctic climate in 38Ma CESM simulations was studied in more detail in Chapter 6 and found to be strongly seasonal and wet. These results suggest that in the middle-to-late Eocene, Antarctica warmed up significantly in summer resulting in a reversal of the temperature gradient and associated polar jet. The absence of a band with strong zonal winds and ocean currents in combination with the atmospheric temperature structure allowed a virtually unrestricted meridional flow of heat and moisture onto the Antarctic continent. While coastal regions were perennially mild and wet the continental interior saw dry, cold winters alternated by warm, wet summers in what resembles a sub-tropical monsoon climate.

The fascinating regional climate over Antarctica presented here can for the first time reconcile proxy indications of simultaneous frost weary, sub-tropical vegetation and the possibility of Eocene ice. In contrast to previous studies, especially near-coastal elevated regions are found to exhibit conditions that are conducive for ice growth. Localised ice caps can have produced ice rafted debris at nearby marine terminating glaciers, while on the other side of the continent temperate conditions persisted.

The modelled warm, wet and strongly seasonal Antarctic climate seems robust to changes in geography as well as radiative forcing. Even in the 30Ma  $1\times$  PIC case, a monsoonal climate with high summer temperatures exist. The resulting summer melt prevents the growth of an Antarctic Ice Sheet at conditions far beyond the previously assumed threshold of  $2.5\text{--}3\times$  PIC. This suggests that the transition between a greenhouse and icehouse climatic state has a strong hysteresis and cannot be explained by the crossing of a simple threshold value (e.g. of  $\text{CO}_2$ ).

## 9.2 Outlook

The CESM results presented here provide a step forward towards understanding the middle-to-late Eocene climate. Both the new geography reconstructions and improved model resolution were important for a more adequate interpretation of proxy records and to study regional climatic features. A next step would be to further increase the resolution in order to resolve oceanic eddies and tropical cyclones. Within such a warm climate, tropical cyclones could play a crucial role by transporting heat between low and middle latitudes. High resolution simulations would only be possible starting from an already obtained (lower resolution) equilibrium state to reduce the required spin-up time. A similar procedure was applied by Viebahn et al. (2016), where the influence of closing the Drake Passage was assessed within a global eddy resolving ocean model. As they pointed out, the role of high resolution features can be of great importance to further increase our understanding of greenhouse climates and their response to an external forcing.

One of the main limitations in validating the model results was the lacking availability of terrestrial climate proxies. Extreme continental conditions in the models cannot be excluded thus far, as there are no present-day analogues for comparisons. Additionally, coverage of the available proxies is poor while they provide little information on past circulation and precipitation patterns. A substantial increase in the number, type and quality of terrestrial proxies is thus needed before an adequate comparison can be made with model results.

It seems that this study is the first to suggest the existence of multiple equilibria in the ocean circulation of the middle-to-late Eocene climate based on GCM results. The associated states are related to different meridional overturning regimes, found in both POP and CESM simulations. The 38Ma simulations using differently referenced geography reconstructions were only carried out using an ocean-only model. Multiple oceanic circulation states were also found in the coupled model framework, but using the 30Ma geography and a limited integration time. Ideally both the 38Ma and 30Ma experiments would need to be repeated using a fully coupled model and a longer simulation, respectively.

The findings considering the Antarctic climate are encouraging, as they provide a plausible explanation for the different available proxy records of the middle-to-late Eocene. Ice melt due to high summer temperatures is inherently related to this climate, and is never reduced to the point where it allows Antarctic glaciation in the considered model simulations. The key is in finding at which point the regional Antarctic greenhouse climate breaks down and ice sheets can grow. The relatively small effects of both geography changes and reduced radiative forcing suggest that neither can cause such a response. Lacking here are the potential feedbacks from ice, which may become significant after a prolonged period of reduced summer warmth. Using a dynamically coupled ice-sheet model could provide the answer to whether a partially glaciated Antarctica responds drastically different to the same external forcing, eventually leading to inception of the Antarctic Ice Sheet.

# Pre-industrial Reference Climatology

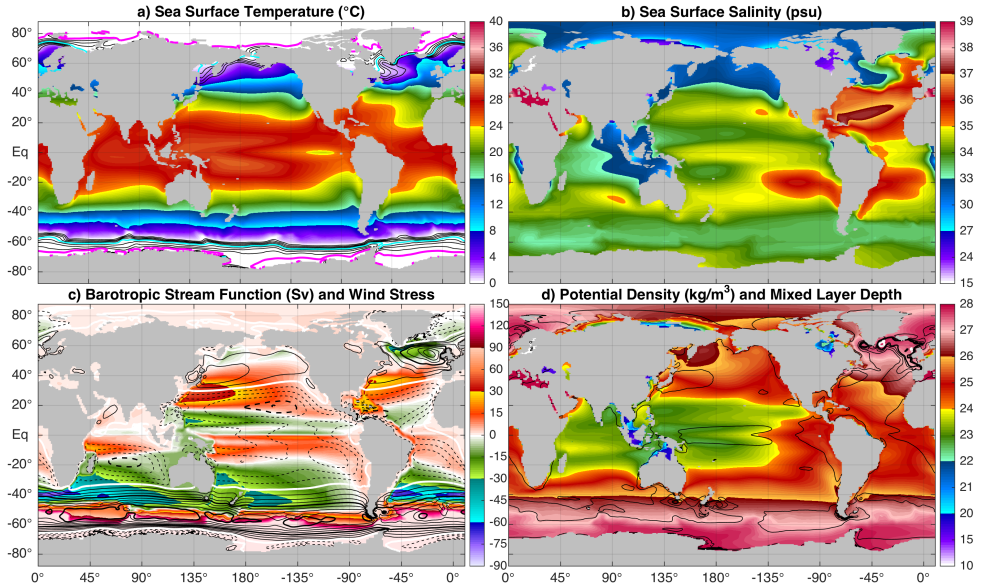


**Figure A.1:** Annual mean sea surface **a)** temperature and **b)** salinity, **c)** barotropic stream function (positive for clockwise flow) and zonal wind stress (contours every  $2.5 \cdot 10^{-2}$  Pa, thick lines every  $1 \cdot 10^{-1}$  Pa; solid positive and dashed negative, thick white line at 0 Pa), and **d)** upper 200m average potential density and mixed layer depth (contours every 50m down to 250m, thick lines every 250m, thick white line at 500m) for the pre-industrial reference simulation. Contours in **a)** show annual mean sea ice fraction at 10% intervals, thick cyan line at 50% and magenta at 90%.

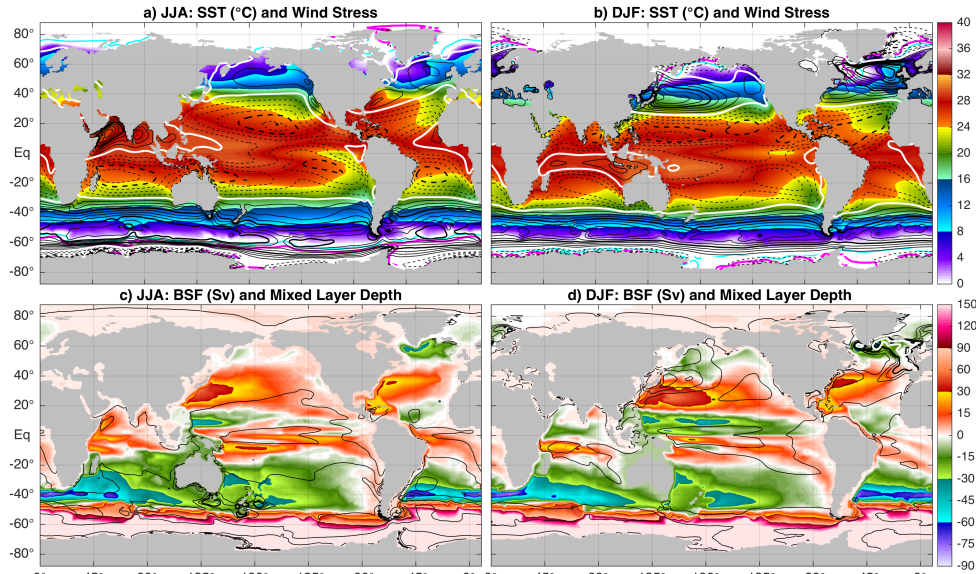


**Figure A.2:** Pre-industrial reference **a)** June-July-August and **b)** December-January-February averaged sea surface temperature and zonal wind stress (contours every  $2.5 \cdot 10^{-2}$  Pa and thick lines every  $1 \cdot 10^{-1}$  Pa; solid positive and dashed negative, thick white line at 0 Pa). **c)** and **d)** similar to **a)** and **b)**, but for the barotropic stream function and maximum mixed layer depth (contours every 50m down to 250m, thick lines every 250m, thick white line at 500m). Coloured contours in **a)** and **b)** show sea ice fraction at 50% (cyan) and 90% (magenta) in August and February, respectively.

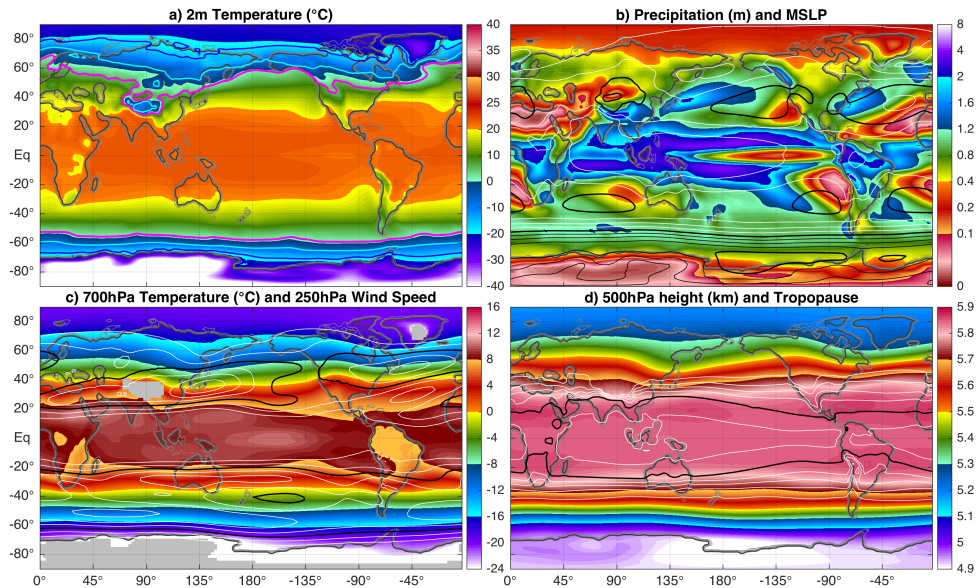


**Figure A.3:** Annual mean for the pre-industrial reference simulation with **a)** near surface (2m) air temperature (coloured) and average min/max temperature (contours; magenta:  $T_{min} < 0^\circ\text{C}$ , cyan:  $T_{min} < -10^\circ\text{C}$ , blue:  $T_{min} < -20^\circ\text{C}$  and white:  $T_{max} > 40^\circ\text{C}$ ), **b)** precipitation (coloured) and mean sea level pressure (contours every 5hPa, thick black lines every 20hPa,  $\leq 1000\text{hPa}$  in black and  $> 1000\text{hPa}$  in white), **c)** 700hPa temperature (coloured) and 200hPa wind speed (white contours every 5m/s starting at 10m/s, thick black lines every 20m/s), and **d)** 500hPa geopotential height (coloured) and dynamic tropopause height (contours every 1km starting at 12km, thick black line at 16km).



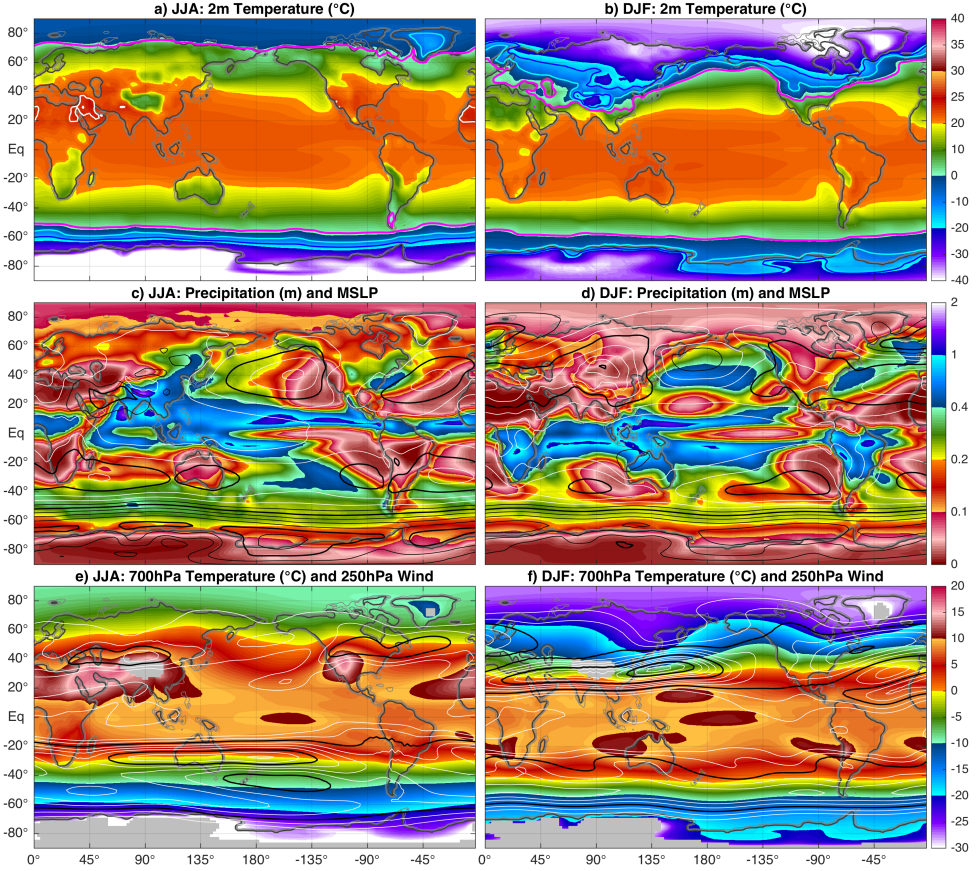


**Figure A.4:** Pre-industrial reference **a)** June-July-August and **b)** December-January-February mean 2m air temperature with contours indicating minimum and maximum values (magenta:  $T_{min} < 0^{\circ}\text{C}$ , cyan:  $T_{min} < -10^{\circ}\text{C}$ , blue:  $T_{min} < -20^{\circ}\text{C}$ , white:  $T_{max} > 40^{\circ}\text{C}$  and yellow:  $T_{max} > 50^{\circ}\text{C}$ ), **c)** and **d)** similar for total precipitation and mean sea level pressure, and **e)** and **f)** for 700hPa temperature and 200hPa wind speed. Colour scales and contour values are all similar to those used in Figure A.3.

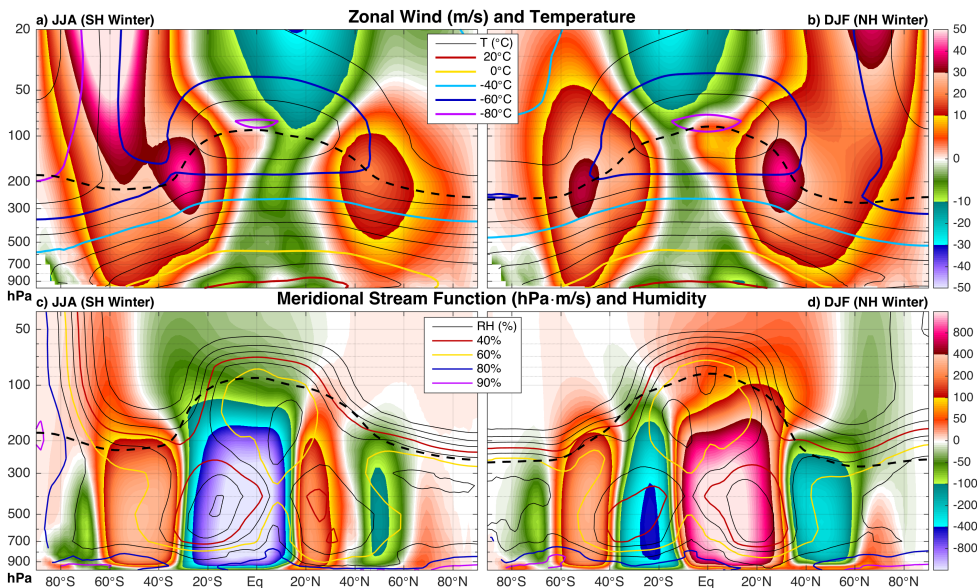


**Figure A.5:** Pre-industrial reference **a)** zonal average zonal wind (shading) and temperature (contours every 10°C) for the months June-July-August, **b)** similar to a) for December-January-February. **c)** Zonally integrated meridional stream function (shading) and relative humidity (contours every 10%) for the months June-July-August, **d)** similar to b) for December-January-February. Tropopause height (zonal mean) is indicated by the dashed black line and pressure is used as the vertical coordinate.

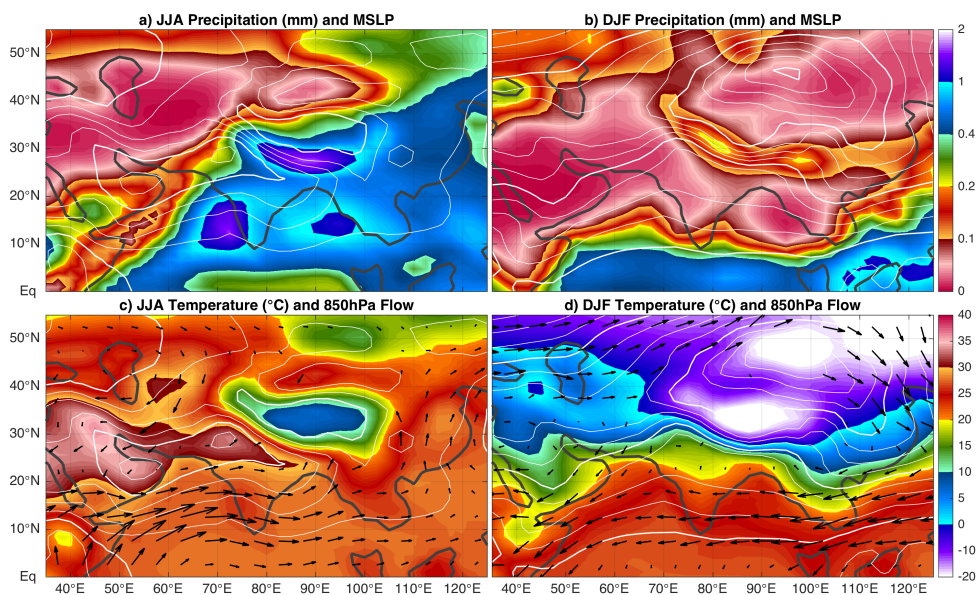


**Figure A.6:** Pre-industrial reference precipitation (shading) and mean sea level pressure (white contours every 2.5hPa, thick lines every 10hPa) over Southeast Asia for **a)** June-July-August and **b)** December-January-February. **c)** and **d)** Similar to a) and b) but for near surface air temperature (shading), mean sea level pressure (contours) and 850hPa flow (vectors; maximum arrow length is 15m/s).



# 38Ma 2× PIC Climatology

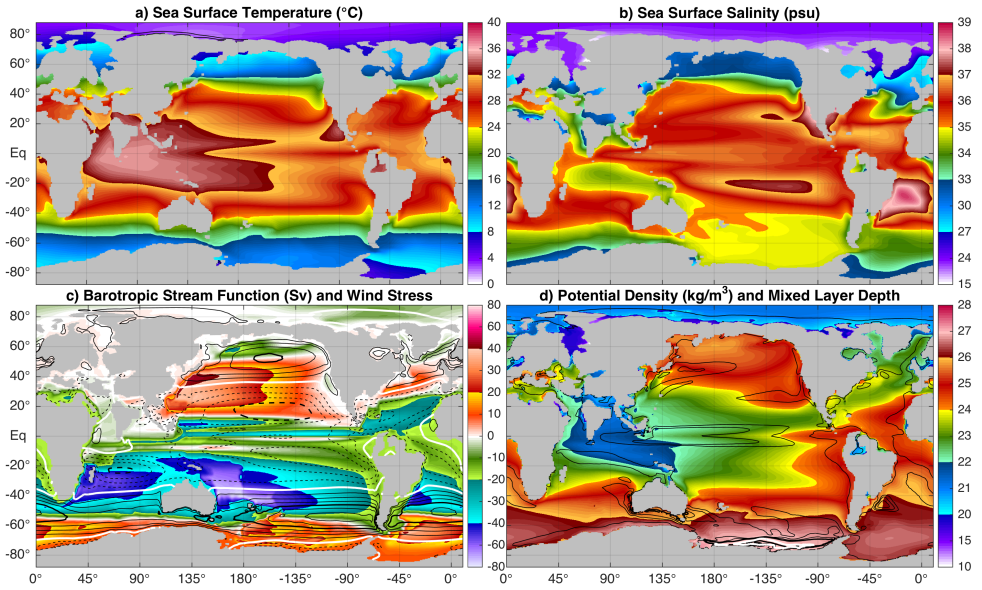


**Figure B.1:** Annual mean sea surface **a)** temperature and **b)** salinity, **c)** barotropic stream function (positive for clockwise flow) and zonal wind stress (contours every  $2.5 \cdot 10^{-2} \text{ Pa}$ , thick lines every  $1 \cdot 10^{-1} \text{ Pa}$ ; solid positive and dashed negative, thick white line at  $0 \text{ Pa}$ ), and **d)** upper 200m average potential density and mixed layer depth (contours every 50m down to 250m, thick lines every 250m, thick white line at 500m) for the 38Ma 2× PIC simulation. Contours in **a)** show annual mean sea ice fraction at 10% intervals, thick blue line at 50% and magenta at 90%.

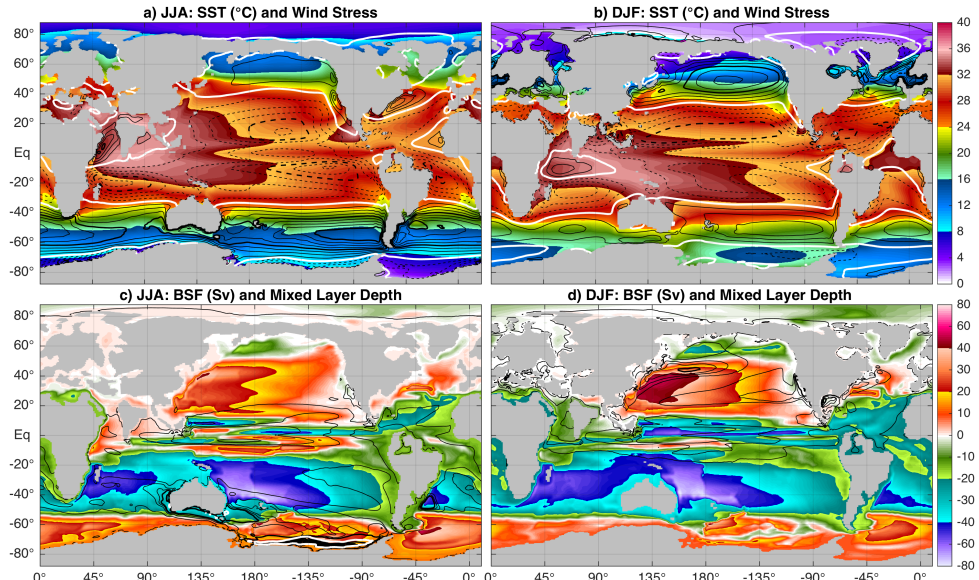


**Figure B.2:** 38Ma 2× PIC a) June-July-August and b) December-January-February averaged sea surface temperature and zonal wind stress (contours every  $2.5 \cdot 10^{-2}$  Pa and thick lines every  $1.10 \cdot 10^{-1}$  Pa; solid positive and dashed negative, thick white line at 0 Pa). c) and d) Similar to a) and b), but for the barotropic stream function and maximum mixed layer depth (contours every 50m down to 250m, thick lines every 250m, thick white line at 500m). Coloured contours in a) and b) show sea ice fraction at 50% (cyan) and 90% (magenta) in August and February, respectively.

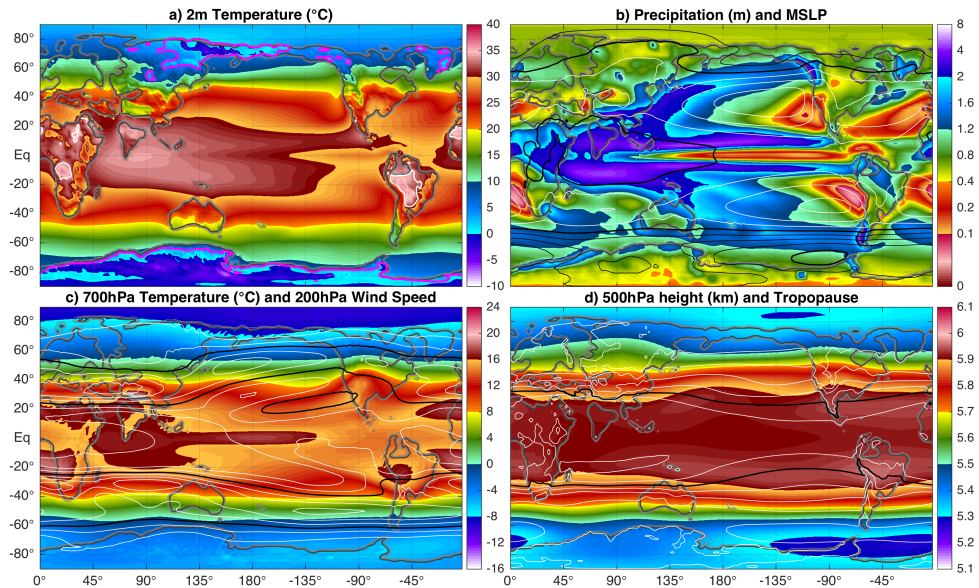


**Figure B.3:** Annual mean for the 38Ma 2× PIC simulation with a) 2m above ground level air temperature (coloured) and average min/max temperature (contours; magenta:  $T_{min} < 0^\circ\text{C}$  and white:  $T_{max} > 40^\circ\text{C}$ ), b) precipitation (coloured) and mean sea level pressure (contours every 5hPa, thick black lines every 20hPa,  $\leq 1000$ hPa in black and  $> 1000$ hPa in white), c) 700hPa temperature (coloured) and 200hPa wind speed (white contours every 5m/s starting at 10m/s, thick black lines every 20m/s), and d) 500hPa geopotential height (coloured) and dynamic tropopause height (contours every 1km starting at 12km, thick black line at 16km).

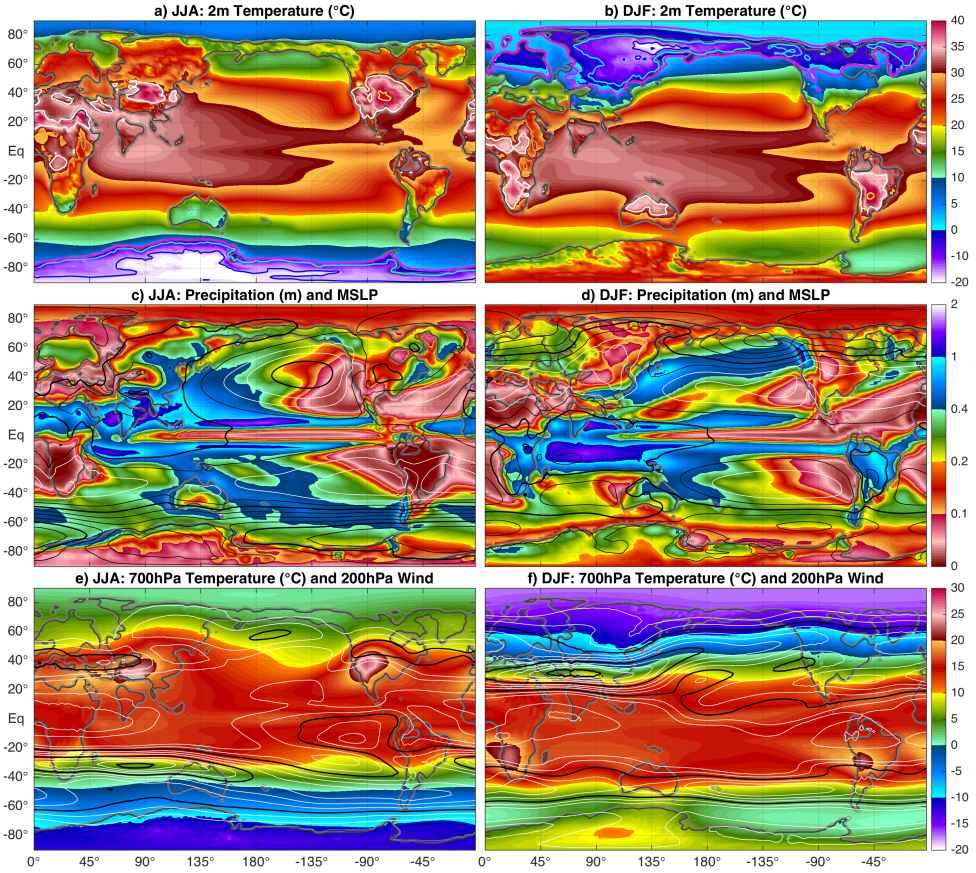


**Figure B.4:** 38Ma 2× PIC **a)** June-July-August and **b)** December-January-February mean 2m air temperature with contours indicating minimum and maximum values (magenta:  $T_{min} < 0^{\circ}\text{C}$ , cyan:  $T_{min} < -10^{\circ}\text{C}$ , blue:  $T_{min} < -20^{\circ}\text{C}$ , white:  $T_{max} > 40^{\circ}\text{C}$  and yellow:  $T_{max} > 50^{\circ}\text{C}$ ), **c)** and **d)** similar for total precipitation and mean sea level pressure, and **e)** and **f)** for 700hPa temperature and 200hPa wind speed. Color scales and contour values are all similar to those used in Figure A.3.



# Additional Model-Proxy Comparisons

## C.1 Sea Surface Temperature Proxies

### 42–38 Ma SST Proxies:

Site	p-lat	p-lon	SST (°C)	$\sigma$ (°C)	Reference	Method
DSDP 277	-55.5	178.1	28	4.7	Hines et al. (2017)	Mg/Ca
ODP 865	11.8	-147.0	31	4.7	Tripathi et al. (2003)	Mg/Ca
ODP 925	3.5	-30.9	32	2.5	Liu et al. (2009)	TEX <sub>86</sub> <sup>H</sup>
ODP 929	-1.8	-31.2	30	2.5	Liu et al. (2009)	TEX <sub>86</sub> <sup>H</sup>
ODP 959	-5.23	-2.59	31.5	2.5	Cramwinckel et al. (2018)	TEX <sub>86</sub> <sup>H</sup>
ODP 1052	24.2	-61.6	32	1.2	Okafor et al. (2009)	Mg/Ca
ODP 1172	-57.8	157.9	24	2.5	Bijl et al. (2009)	TEX <sub>86</sub> <sup>H</sup>
ACEX	82.5	-5.7	10	2.7	Evans et al. (2018)	UK <sub>37</sub>
Gulf Coast, US	28.3	-74.1	26	1.4	Kobashi et al. (2004)	$\delta^{18}\text{O}$
Istra More 5	34.1	13.1	24	0.7	Pearson et al. (2001)	$\delta^{18}\text{O}$
Java KW01	0.1	114.5	35	2.0	Evans et al. (2018)	$\Delta_{47}$
			36.3	1.9	Evans et al. (2018)	$\Delta_{47}$

Table C.1: Overview of 42–38 Ma SST proxies; site location, 38Ma reconstructed coordinates (p-lat,p-lon), SST estimate, calibration error, reference and method used.

Site	p-lat	p-lon	SST (°C)	$\sigma$ (°C)	Reference	Method
New Zealand	-49.3	-169.7	26	4.7	Hines et al. (2017)	Mg/Ca
Seymour Is.	-68.5	-62.5	12.7	2.4	Douglas et al. (2014)	$\Delta_{47}$
			13.1	2.4	Douglas et al. (2014)	$\Delta_{47}$
			20.3	2.5	Douglas et al. (2014)	TEX <sub>86</sub> <sup>H</sup>
Tanzania	-16.6	40.6	34	2.5	Pearson et al. (2007)	TEX <sub>86</sub> <sup>H</sup>
Tanz. Lindi	-17.6	40.6	32	0.7	Pearson et al. (2001)	$\delta^{18}\text{O}$
Hamp. Bas., UK	43.6	-2.9	23.2	2.6	Evans et al. (2018)	$\Delta_{47}$

Table C.1: Continued.

### 38–34 Ma SST Proxies:

Site	p-lat	p-lon	SST (°C)	$\sigma$ (°C)	Reference	Method
DSDP 277	-55.5	178.1	26.6	2.5	Liu et al. (2009)	TEX <sub>86</sub> <sup>H</sup>
			25.6	4.7	Liu et al. (2009)	UK <sub>37</sub>
DSDP 336	55.7	-11.0	20	1.5	Liu et al. (2009)	UK <sub>37</sub>
DSDP 511	-58.8	-30.4	19.5	2.5	Liu et al. (2009)	TEX <sub>86</sub> <sup>H</sup>
			19.6	1.5	Liu et al. (2009)	UK <sub>37</sub>
ODP 689	-68.3	14.0	12.3	4.6	Petersen et al. (2015)	$\Delta_{47}$
			22.0	1.5	Petersen et al. (2015)	$\Delta_{47}$
ODP 803	-0.8	-169.1	27.4	2.5	Liu et al. (2009)	TEX <sub>86</sub> <sup>H</sup>
ODP 913	66.2	-2.4	18.3	1.5	Liu et al. (2009)	UK <sub>37</sub>
ODP 925	3.5	-30.9	30	2.5	Liu et al. (2009)	TEX <sub>86</sub> <sup>H</sup>
ODP 929	-1.8	-31.2	29	2.5	Liu et al. (2009)	TEX <sub>86</sub> <sup>H</sup>
ODP 959	-5.23	-2.59	28.5	2.5	Cramwinckel et al. (2018)	TEX <sub>86</sub> <sup>H</sup>
ODP 998	14.6	-69.4	22.1	2.5	Liu et al. (2009)	TEX <sub>86</sub> <sup>H</sup>
ODP 1052	24.2	-61.6	30	1.2	Okafor et al. (2009)	Mg/Ca
ODP 1090	-51.9	157.9	22	2.5	Bijl et al. (2009)	UK <sub>37</sub>
ODP 1172	-57.8	157.9	22	2.5	Bijl et al. (2009)	TEX <sub>86</sub> <sup>H</sup>
Alabama, US	27.6	-72.4	27	0.7	Pearson et al. (2001)	$\delta^{18}\text{O}$
Browns C., Aus	-53.8	147.2	18.9	0.7	Kamp et al. (1990)	$\delta^{18}\text{O}$
Gulf Coast, US	28.3	-74.1	22	1.4	Kobashi et al. (2004)	$\delta^{18}\text{O}$
New Zealand	-49.3	-169.7	30.9	4.7	Hines et al. (2017)	Mg/Ca
Panama	0.9	-72.9	32	1.4	Tripathi et al. (2002)	$\delta^{18}\text{O}$
Seymour Is.	-68.5	-62.5	12.2	2.4	Douglas et al. (2014)	$\Delta_{47}$
			13.0	3.0	Douglas et al. (2014)	$\Delta_{47}$
			16.0	2.5	Douglas et al. (2014)	TEX <sub>86</sub> <sup>H</sup>
St Stephens Q.	27.2	-72.2	32.5	2.2	Wade et al. (2012)	Mg/Ca
			34.9	4.7	Wade et al. (2012)	Mg/Ca
			30.5	2.5	Wade et al. (2012)	TEX <sub>86</sub> <sup>H</sup>
Tanzania	-16.6	40.6	29.5	0.7	Pearson et al. (2007)	$\delta^{18}\text{O}$
			33.0	2.5	Pearson et al. (2007)	TEX <sub>86</sub> <sup>H</sup>
			29.7	3.2	Evans et al. (2018)	$\Delta_{47}$
Tanz. Lindi	-17.6	40.6	30.0	0.7	Pearson et al. (2001)	$\delta^{18}\text{O}$

Table C.2: Overview of 38–34 Ma SST proxies; site location, 38Ma reconstructed coordinates (p-lat,p-lon), SST estimate, calibration error, reference and method used.

## C.2 Terrestrial Temperature Proxies

### Late Middle Eocene Land Temperature Proxies:

Site	T <sub>a</sub> (°C)	T <sub>x</sub> (°C)	T <sub>n</sub> (°C)	p-lat	p-lon	Reference
<b>North Atlantic:</b>						
ODP 913 MBT	14.5	16.0	12.5	66.2	-2.4	Schouten et al. (2008)
ODP 913 Pollen	13.3	16.2	11.8	66.2	-2.4	Eldrett et al. (2009)
<b>North America:</b>						
Florissant CO	14.6	17.5	10.7	37.0	-86.9	Boyle et al. (2008)
Comstock (OR)	21	22.4	19.6	44.7	-102.9	Retallack et al. (2004)
Copper B. (NV)	9.5	10.5	8.5	41.5	-96.0	Wolfe et al. (1998)
Badger's N. (CA)	14.5	17.1	12.5	42.1	-100.6	Prothero (2008)
Sevier (UT)	13.2	13.2	13.2	38.7	-94.7	Gregory-Wodzicki (1997)
Gray B. (OR)	14.0	19.3	8.8	45.0	-100.6	Smith et al. (1998)
<b>South America:</b>						
Nirihuau (Chile)	18.4	18.4	18.4	-49.4	-59.5	Hinojosa et al. (2005)
<b>Europe:</b>						
Stare Sedlo	23.9	29	21.3	43.7	9.3	Uhl et al. (2007)
Weiße Elster	22.6	24	18.7	44.9	8.3	Uhl et al. (2007)
<b>China:</b>						
Dalianhe	16.5	16.5	16.5	54.2	129.1	Quan et al. (2012)
Huanghua	18.1	18.3	17.9	52.7	129.4	Quan et al. (2012)
Jushu	15.9	16.1	15.6	52.4	126.5	Quan et al. (2012)
Hunchun	17.5	18.4	16.5	50.8	130.9	Quan et al. (2012)
Huadian	17.0	18.4	15.6	50.8	126.4	Quan et al. (2012)
Jijuntun	16.8	17	16.5	49.6	123.3	Quan et al. (2012)
Xilutan	17.0	18.4	15.6	49.6	123.3	Quan et al. (2012)
Kongdian	17.5	18.4	16.5	47.4	118.7	Quan et al. (2012)
Shahejie	17.1	18.4	15.7	45.6	116.3	Quan et al. (2012)
Sanduo	17.1	18.4	15.7	40.7	118.4	Quan et al. (2012)
Dingyuan	15.5	16.1	14.8	39.6	116.1	Quan et al. (2012)
Shuangta	16.1	16.4	15.7	38.8	117.9	Quan et al. (2012)
Qingjiang	16.5	16.5	16.5	35.5	115.5	Quan et al. (2012)
Wenzhou	17.6	18.4	16.8	34.6	121.8	Quan et al. (2012)
Tantou	17.1	18.4	15.7	40.7	110.7	Quan et al. (2012)

Table C.3: Overview of late middle Eocene terrestrial temperature proxies; site location, mean annual temperature, highest annual temperature, lowest annual temperature and 38Ma reconstructed coordinates.

Site	T <sub>a</sub> (°C)	T <sub>x</sub> (°C)	T <sub>n</sub> (°C)	p-lat	p-lon	Reference
Unnamed Unit 1	15.9	18.4	13.3	45.6	105.8	Quan et al. (2012)
Unnamed Unit 2	13.7	16.1	11.3	42.5	101.8	Quan et al. (2012)
Honggou	17.2	21.1	13.3	42.6	99.9	Quan et al. (2012)
Relu	14.1	16.4	11.7	36.3	95.1	Quan et al. (2012)
Huoshagou	16.4	21.7	11.0	45.4	93.7	Quan et al. (2012)
Lulehe	17.1	18.4	15.7	41.2	86.0	Quan et al. (2012)
Lulehe	17.1	18.4	15.7	37.0	88.1	Quan et al. (2012)
Totohe	14.9	16.5	13.3	34.6	87.3	Quan et al. (2012)
Wulagen	18.2	20.8	15.6	39.3	74.4	Quan et al. (2012)
Shenhu	16.6	21.7	11.5	30.0	113.3	Quan et al. (2012)
Liushagang	17.6	23.9	11.3	28.1	109.7	Quan et al. (2012)
Changchang	18.9	20.8	17	26.8	110.6	Quan et al. (2012)
<b>Australia:</b>						
Anglesea	16.2	19.3	13.9	-53.4	148.2	Greenwood et al. (2004)
Hasties	16.2	16.2	16.2	-55.3	153.8	Greenwood et al. (1995)
West Dale	16.1	17.9	14.2	-49.1	111.4	Greenwood et al. (2004)
<b>Antarctica:</b>						
McMurdo	13.0	13.0	13.0	-72.1	158.2	Passchier et al. (2013)
SA Islands AP	12.0	15.0	10.5	-67.5	-63.5	Passchier et al. (2013)

Table C.3: Continued.

### Late Eocene Land Temperature Proxies:

Site	T <sub>a</sub> (°C)	T <sub>x</sub> (°C)	T <sub>n</sub> (°C)	p-lat	p-lon	Reference
<b>North Atlantic:</b>						
ODP 913 MBT	14.0	15.9	7.9	66.2	-2.4	Schouten et al. (2008)
ODP 913 Pollen	13.4	16.2	11.8	66.2	-2.4	Eldrett et al. (2009)
<b>North America:</b>						
Florissant CO	14.6	17.5	10.7	37.0	-86.9	Boyle et al. (2008)
Comstock (OR)	21	22.4	19.6	44.7	-102.9	Retallack et al. (2004)
Copper B. (NV)	9.5	10.5	8.5	41.5	-96.0	Wolfe et al. (1998)
Badger's N. (CA)	14.5	17.1	12.5	42.1	-100.6	Prothero (2008)
Sevier (UT)	13.2	13.2	13.2	38.7	-94.7	Gregory-Wodzicki (1997)
Gray B. (OR)	14.0	19.3	8.8	45.0	-100.6	Smith et al. (1998)

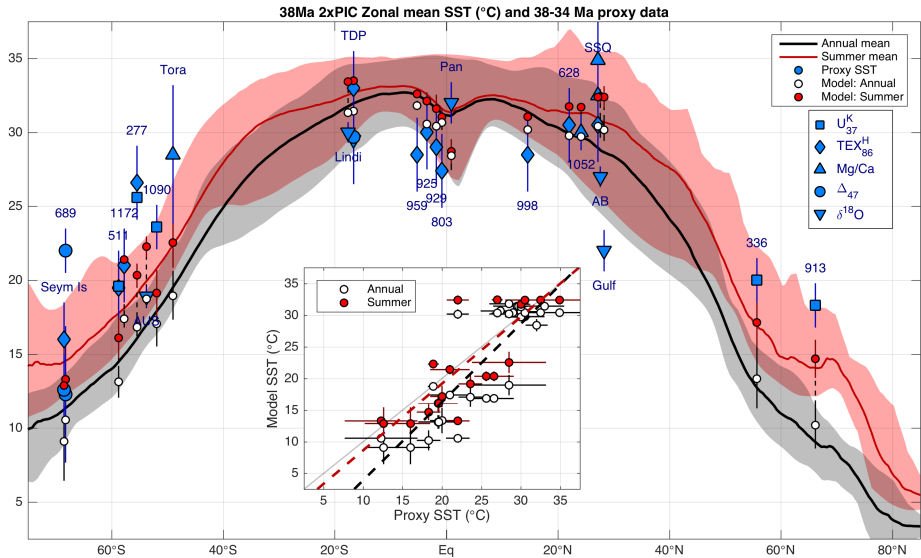
Table C.4: Overview of late Eocene terrestrial temperature proxies; site location, mean annual temperature, highest annual temperature, lowest annual temperature and 38Ma reconstructed coordinates.



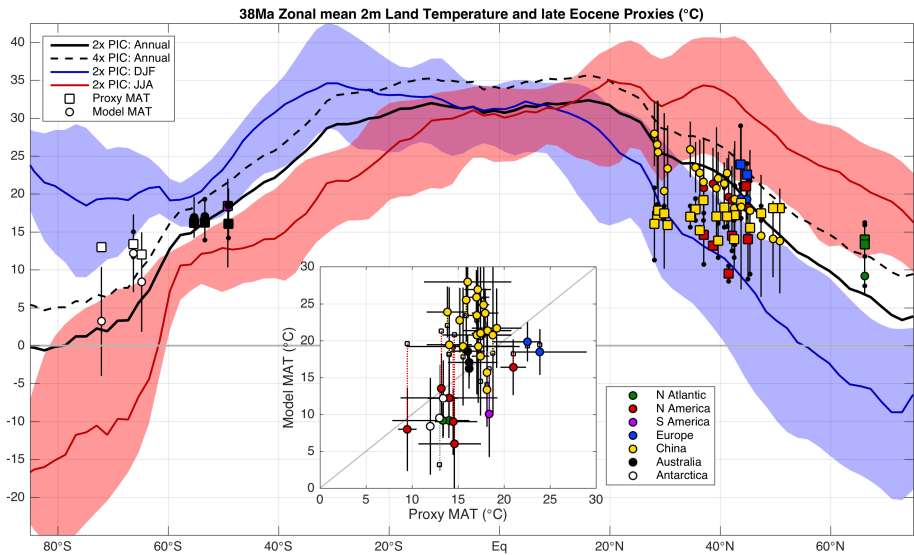
Site	T <sub>a</sub> (°C)	T <sub>x</sub> (°C)	T <sub>n</sub> (°C)	p-lat	p-lon	Reference
<b>South America:</b>						
Ñirihuau (Chile)	18.4	18.4	18.4	-49.4	-59.5	Hinojosa et al. (2005)
<b>Europe:</b>						
Stare Sedlo	23.9	29	21.3	43.7	9.3	Uhl et al. (2007)
Weiße Elster	22.6	24	18.7	44.9	8.3	Uhl et al. (2007)
<b>China:</b>						
Hunchun	18.2	18.4	17.9	50.8	130.9	Quan et al. (2012)
Gengjiajie	18.2	18.4	17.9	49.6	123.3	Quan et al. (2012)
Shahejie	17.5	18.4	16.5	47.4	118.7	Quan et al. (2012)
Sanduo	18.2	20.8	15.6	40.7	118.4	Quan et al. (2012)
Dingyuan	13.9	16.1	11.6	39.6	116.1	Quan et al. (2012)
Linjiang	18.0	19.4	16.5	35.5	115.5	Quan et al. (2012)
Pinghu	17.0	18.4	15.6	34.6	121.8	Quan et al. (2012)
Unnamed Unit 2	14.1	16.5	11.6	42.5	101.8	Quan et al. (2012)
Honggou	17.2	21.1	13.3	42.6	99.9	Quan et al. (2012)
Relu	15.2	15.6	14.8	36.3	95.1	Quan et al. (2012)
Huoshagou	15.6	21.7	9.4	45.4	93.7	Quan et al. (2012)
Xiaganchaigou	17.1	18.4	15.7	41.2	86.0	Quan et al. (2012)
Wanbaogou	19.2	21.9	16.5	37.0	88.1	Quan et al. (2012)
Bashibulake	17.1	20.8	13.3	39.3	74.4	Quan et al. (2012)
Xiaokuzibai	18.8	20.8	16.8	43.8	78.7	Quan et al. (2012)
Youganwo	17.2	18.6	15.7	28.6	110.8	Quan et al. (2012)
Liushagang	16.1	20.8	11.3	28.1	109.7	Quan et al. (2012)
Yongning Gr.	17.8	18.4	17.2	28.8	106.8	Quan et al. (2012)
Nadu	15.9	16.1	15.7	30.5	106.0	Quan et al. (2012)
Dagzhuka	17.5	18.4	16.5	29.9	87.6	Quan et al. (2012)
<b>Antarctica:</b>						
McMurdo	13.0	13.0	13.0	-72.1	158.2	Passchier et al. (2013)
King George	13.4	15.0	11.7	-66.3	-64.5	Passchier et al. (2013)
ODP 1166	12.0	12.0	12.0	-64.8	87.3	Passchier et al. (2013)

Table C.4: Continued.

### C.3 2× PIC Model-Proxy Temperature Comparison



**Figure C.1:** Zonally averaged annual mean (black) and summer mean (red) SST, shaded regions showing zonal spread for the 38Ma 2× PIC case. Blue markers indicate SST proxy estimates, whereas white (annual) and red (summer) circles depict model values at the corresponding 38Ma locations. Error bars represent proxy calibration errors and the model spatial variation within a 4°×4° box. The inset shows a scatter plot of model versus proxy SST, with a linear fit using annual mean (black) or summer mean (red; only outside of the tropics) model values.



**Figure C.2:** Zonally averaged annual mean (black), December–February (blue) and June–August (red) near surface air temperature (land-only) for the 38Ma 2× PIC case (solid line; dashed: 4× PIC). Red and blue shading indicates zonal variability of the according seasonal averages. Markers show late Eocene proxy estimates (squares) and corresponding model annual mean (circles), colour coded for their respective region. Error bars (black dots) are indicative of the spread at each site (proxies) or spatial variation in a 5°×4° box (model). The inset shows a scatter plot of model versus proxy air temperatures, the former being corrected for differences in model and reconstructed topography (uncorrected: small squares).

## C.4 4× PIC Model-Model Comparison

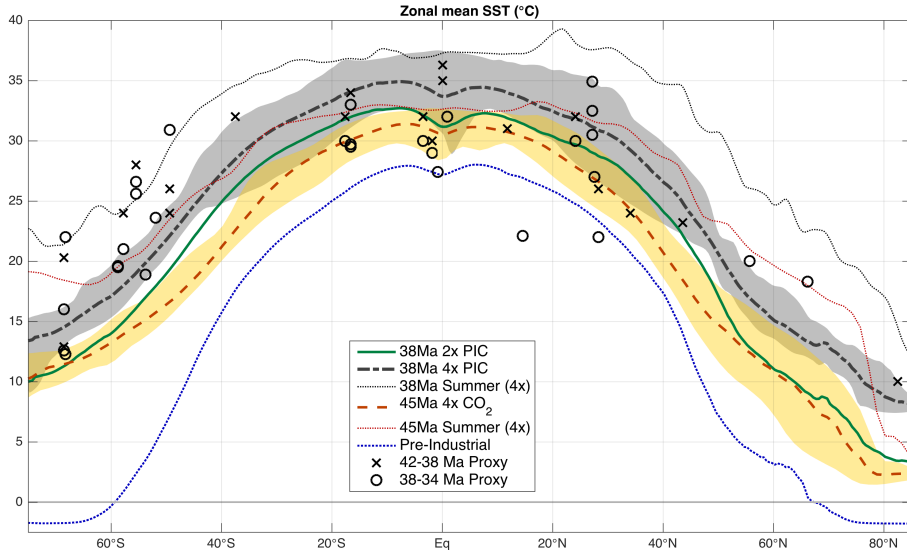


**Figure C.3:** Annual mean, zonal mean sea surface temperature for the 38Ma 4× PIC (thick black) and 2× PIC (thick green), 45Ma 4× CO<sub>2</sub> (thick dashed red; GH14 Goldner et al. 2014) and pre-industrial reference (thick dotted blue) simulations. Estimates from proxy data are represented by crosses for 42–38 Ma and circles for the 38–34 Ma period in accordance with other figures. Shading indicates the zonal range in temperatures for both the 38Ma 4× PIC (grey) and 45Ma 4× CO<sub>2</sub> (yellow) case, while thin dashed lines show the highest summer temperatures at each latitude.

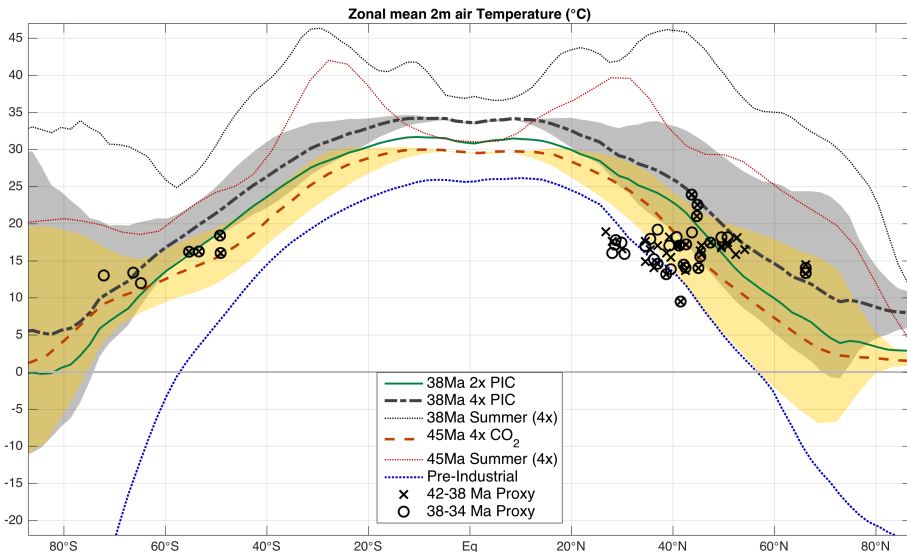


**Figure C.4:** Annual mean, zonal mean near-surface (2m) air temperature for the 38Ma 4× PIC (thick black) and 2× PIC (thick green), 45Ma 4× CO<sub>2</sub> (thick dashed red; GH14) and pre-industrial reference (thick dotted blue) simulations. Estimates from proxy data are represented by crosses for 42–38 Ma and circles for the 38–34 Ma period in accordance with other figures. Shading indicates the seasonal (DJF, JJA) range in temperatures for both the 38Ma 4× PIC (grey) and 45Ma 4× CO<sub>2</sub> (yellow) case, while thin dashed lines show the highest summer temperatures at each latitude.



---

# Bibliography

---

- Abbot, D. S., M. Huber, G. Bousquet & C. C. Walker (2009)**, “High-CO<sub>2</sub> cloud radiative forcing feedback over both land and ocean in a global climate model”, *Geophysical Research Letters*, vol. 36, no. 5, 2-5.
- Anagnostou, E. et al. (2016)**, “Changing atmospheric CO<sub>2</sub> concentration was the primary driver of early Cenozoic climate”, *Nature*, vol. 533, no. 7603, 380-384.
- Baatsen, M. L. J. et al. (2016)**, “Reconstructing geographical boundary conditions for palaeoclimate modelling during the Cenozoic”, *Climate of the Past*, vol. 12, no. 8, 1635-1644.
- Baatsen, M. L. J., A. S. von der Heydt, M. A. Kliphuis, J. Viebahn & H. A. Dijkstra (2018a)**, “Multiple states in the late Eocene ocean circulation”, *Global and Planetary Change*, vol. 163, no. January, 18-28.
- Baatsen, M. L. J. et al. (2018b)**, “Equilibrium state and sensitivity of the simulated middle-to-late Eocene climate”, *Climate of the Past Discussions*, no. April, 1-49.
- Baatsen, M. L. J., P. K. Bijl, A. S. von der Heydt, A. Sluijs & H. A. Dijkstra (2018c)**, “Antarctic Summer Monsoons in the Middle-to-late Eocene (in prep.)”, *Nature Geoscience*.
- Barron, E. J. & W. M. Washington (1984)**, “The role of geographic variables in explaining paleoclimates: Results from Cretaceous climate model sensitivity studies”, *Journal of Geophysical Research*, vol. 89, no. D1, 1267-1279.
- Basak, C. & E. E. Martin (2013)**, “Antarctic weathering and carbonate compensation at the Eocene-Oligocene transition”, *Nature Geoscience*, vol. 6, no. 2, 121-124.
- Beerling, D., R. A. Berner, F. T. Mackenzie, M. B. Harfoot & J. A. Pyle (2009)**, “Methane and the CH<sub>4</sub>-related greenhouse effect over the past 400 million years”, *American Journal of Science*, vol. 309, no. 2, 97-113.
- Beerling, D. J. & D. L. Royer (2011)**, “Convergent Cenozoic CO<sub>2</sub> history”, *Nature Geoscience*, vol. 4, no. 7, 418-420.
- Beerling, D. J., A. Fox, D. S. Stevenson & P. J. Valdes (2011)**, “Enhanced chemistry-climate feedbacks in past greenhouse worlds”, *Proceedings of the National Academy of Sciences*, vol. 108, no. 24, 9770-9775.
- Bellucci, A., S. Gualdi & A. Navarra (2010)**, “The double-ITCZ syndrome in coupled general circulation models: The role of large-scale vertical circulation regimes”, *Journal of Climate*, vol. 23, no. 5, 1127-1145.

- Berg, J. van den, R. van de Wal & H. Oerlemans (2008)**, “A mass balance model for the Eurasian Ice Sheet for the last 120,000 years”, *Global and Planetary Change*, vol. 61, no. 3-4, 194-208.
- Bijl, P. K., S. Schouten, A. Sluijs, G.-J. Reichert, J. C. Zachos & H. Brinkhuis (2009)**, “Early Palaeogene temperature evolution of the southwest Pacific Ocean.”, *Nature*, vol. 461, no. 7265, 776-779.
- Bijl, P. K. et al. (2010)**, “Transient Middle Eocene atmospheric CO<sub>2</sub> and temperature variations.”, *Science*, vol. 330, no. 6005, 819-821.
- Bijl, P. K. et al. (2013)**, “Eocene cooling linked to early flow across the Tasmanian Gateway.”, *Proceedings of the National Academy of Sciences of the United States of America*, vol. 110, no. 24, 9645-9650.
- Bitz, C. M. et al. (2012)**, “Climate sensitivity of the community climate system model, version 4”, *Journal of Climate*, vol. 25, no. 9, 3053-3070.
- Blackmon, M. et al. (2001)**, “The Community Climate System Model”, *Bulletin of the American Meteorological Society*, vol. 82, 2357-2376.
- Boer, B. de, P. Stocchi & R. S. Van De Wal (2014)**, “A fully coupled 3-D ice-sheet-sea-level model: Algorithm and applications”, *Geoscientific Model Development*, vol. 7, no. 5, 2141-2156, arXiv: [1011.1669v3](#).
- Bohaty, S. M. & J. C. Zachos (2003)**, “Significant Southern Ocean warming event in the late middle Eocene”, *Geology*, vol. 31, no. 11, 1017-1020.
- Bosboom, R. E., H. A. Abels, C. Hoorn, B. C. J. van den Berg, Z. Guo & G. Dupont-Nivet (2014a)**, “Aridification in continental Asia after the Middle Eocene Climatic Optimum (MECO)”, *Earth and Planetary Science Letters*, vol. 389, 34-42.
- Bosboom, R. E. et al. (2014b)**, “Linking Tarim Basin sea retreat (west China) and Asian aridification in the late Eocene”, *Basin Research*, vol. 26, 621-640.
- Bosboom, R. E. et al. (2014c)**, “Timing, cause and impact of the late Eocene step-wise sea retreat from the Tarim Basin (west China)”, *Palaeogeography, Palaeoclimatology, Palaeoecology*, vol. 403, 101-118.
- Boschman, L., D. van Hinsbergen, T. Torsvik, W. Spakman & J. Pindell (2014)**, “Kinematic reconstruction of the Caribbean region since the Early Jurassic”, *Earth Science Reviews*, vol. 138, 102-136.
- Bougeois, L. et al. (2018)**, “Asian monsoons and aridification response to Paleogene sea retreat and Neogene westerly shielding indicated by seasonality in Paratethys oysters”, *Earth and Planetary Science Letters*, vol. 485, 99-110.
- Boyden, J. A. et al. (2011)**, “Next-generation plate-tectonic reconstructions using GPlates”, in Keller, R. and Barz, C. eds., *Geoinformatics*, Cambridge, UK, 95-114.
- Boyle, B., H. Meyer, B. Enquist & S. Salas (2008)**, “Higher taxa as paleoecological and paleoclimatic indicators: A search for the modern analog of the Florissant fossil flora”, in: *Paleontology of the Upper Eocene Florissant Formation, Colorado*, ed. by Meyer, H. W. & Smith, D. M., The Geological Society of America, chap. 3, 33-51.
- Brinkhuis, H. et al. (2006)**, “Episodic fresh surface waters in the Eocene Arctic Ocean.”, *Nature*, vol. 441, no. 7093, 606-609.
- Broecker, W. S. (1989)**, “The salinity contrast between the Atlantic and Pacific oceans during glacial time”, *Paleoceanography*, vol. 4, no. 2, 207-212, arXiv: [1011.1669v3](#).

- Caballero, R. & M. Huber (2010)**, “Spontaneous transition to superrotation in warm climates simulated by CAM3”, *Geophysical Research Letters*, vol. 37, no. 11, 1-5.
- Caballero, R. & M. Huber (2013)**, “State-dependent climate sensitivity in past warm climates and its implications for future climate projections”, *Proceedings of the National Academy of Sciences*, vol. 110, no. 35, 14162-14167.
- Carter, A., T. R. Riley, C. D. Hillenbrand & M. Rittner (2017)**, “Widespread Antarctic glaciation during the Late Eocene”, *Earth and Planetary Science Letters*, vol. 458, 49-57.
- Caves, J. K., D. J. Sjostrom, H. T. Mix, M. J. Winnick & C. P. Chamberlain (2014)**, “Aridification of Central Asia and uplift of the Altai and Hangay Mountains, Mongolia: Stable isotope evidence”, *American Journal of Science*, vol. 314, no. 8, 1171-1201.
- Close, D. I., a. B. Watts & H. M. J. Stagg (2009)**, “A marine geophysical study of the Wilkes Land rifted continental margin, Antarctica”, *Geophysical Journal International*, vol. 177, no. 2, 430-450.
- Conte, M. H. et al. (2006)**, “Global temperature calibration of the alkenone unsaturation index ( $U_{37}^K$ ) in surface waters and comparison with surface sediments”, *Geochemistry, Geophysics, Geosystems*, vol. 7, no. 2.
- Contreras, L. et al. (2013)**, “Early to Middle Eocene vegetation dynamics at the Wilkes Land Margin (Antarctica)”, *Review of Palaeobotany and Palynology*, vol. 197, 119-142.
- Contreras, L. et al. (2014)**, “Southern high-latitude terrestrial climate change during the Palaeocene-Eocene derived from a marine pollen record (ODP Site 1172, East Tasman Plateau)”, *Climate of the Past*, vol. 10, no. 4, 1401-1420.
- Coxall, H. K., P. a. Wilson, H. Pälike, C. H. Lear & J. Backman (2005)**, “Rapid step-wise onset of Antarctic glaciation and deeper calcite compensation in the Pacific Ocean.”, *Nature*, vol. 433, no. 7021, 53-57.
- Coxall, H. K. & P. a. Wilson (2011)**, “Early Oligocene glaciation and productivity in the eastern equatorial Pacific: Insights into global carbon cycling”, *Paleoceanography*, vol. 26, no. 2, 1-18.
- Coxall, H. K. et al. (2018)**, “Export of nutrient rich Northern Component Water preceded early Oligocene Antarctic glaciation”, *Nature Geoscience*, vol. 11, no. 3, 190-196.
- Cramer, B. S., J. R. Toggweiler, J. D. Wright, M. E. Katz & K. G. Miller (2009)**, “Ocean overturning since the late cretaceous: Inferences from a new benthic foraminiferal isotope compilation”, *Paleoceanography*, vol. 24, no. 4, 1-14.
- Cramer, B. S., K. G. Miller, P. J. Barrett & J. D. Wright (2011)**, “Late Cretaceous-Neogene trends in deep ocean temperature and continental ice volume: Reconciling records of benthic foraminiferal geochemistry ( $\delta^{18}O$  and Mg/Ca) with sea level history”, *Journal of Geophysical Research: Oceans*, vol. 116, no. 12, 1-23.
- Cramwinckel, M. J. et al. (2018)**, “Synchronous tropical and polar temperature evolution in the Eocene letter”, *Nature*, vol. 559, no. 7714, 382-386.
- Crosby, A. G., D. McKenzie & J. G. Sclater (2006)**, “The relationship between depth, age and gravity in the oceans”, *Geophysical Journal International*, vol. 166, no. 2, 553-573.

- Danabasoglu, G., R. Ferrari & J. C. McWilliams (2008)**, “Sensitivity of an ocean general circulation model to a parameterization of near-surface eddy fluxes”, *Journal of Climate*, vol. 21, no. 6, 1192-1208.
- Danabasoglu, G. et al. (2012)**, “The CCSM4 ocean component”, *Journal of Climate*, vol. 25, no. 5, 1361-1389.
- DeConto, R. M. & D. Pollard (2003)**, “Rapid Cenozoic glaciation of Antarctica induced by declining atmospheric CO<sub>2</sub>”, *Nature*, vol. 421, no. 6920, 245-249.
- DeConto, R. M., D. Pollard, P. a. Wilson, H. Pälike, C. H. Lear & M. Pagani (2008)**, “Thresholds for Cenozoic bipolar glaciation.”, *Nature*, vol. 455, no. 7213, 652-656.
- Dekker, M. M., A. S. von der Heydt & H. A. Dijkstra (2018)**, “Cascading transitions in the climate system”, *Earth System Dynamics Discussions*, no. May, 1-29.
- Dingle, R. V., S. A. Marenssi & M. Lavelle (1998)**, “High latitude Eocene climate deterioration: Evidence from the northern Antarctic Peninsula”, *Journal of South American Earth Sciences*, vol. 11, no. 6, 571-579.
- Douglas, P. M. J. et al. (2014)**, “Pronounced zonal heterogeneity in Eocene southern high-latitude sea surface temperatures”, *Proceedings of the National Academy of Sciences*, vol. 111, no. 18, 6582-6587, arXiv: [1408.1149](#).
- Dupont-Nivet, G., W. Krijgsman, C. G. Langereis, H. a. Abels, S. Dai & X. Fang (2007)**, “Tibetan plateau aridification linked to global cooling at the Eocene-Oligocene transition.”, *Nature*, vol. 445, no. 7128, 635-638.
- Dupont-Nivet, G., C. Hoom & M. Konert (2008)**, “Tibetan uplift prior to the Eocene-Oligocene climate transition: Evidence from pollen analysis of the Xining Basin”, *Geology*, vol. 36, no. 12, 987-990.
- Dutton, A. L., K. C. Lohmann & W. J. Zinsmeister (2002)**, “Stable isotope and minor element proxies for Eocene climate of Seymour Island, Antarctica”, *Paleoceanography*, vol. 17, no. 2, 6-1-6-13.
- Eldrett, J. S., I. C. Harding, P. a. Wilson, E. Butler & A. P. Roberts (2007)**, “Continental ice in Greenland during the Eocene and Oligocene.”, *Nature*, vol. 446, no. 7132, 176-179.
- Eldrett, J. S., D. R. Greenwood, I. C. Harding & M. Huber (2009)**, “Increased seasonality through the Eocene to Oligocene transition in northern high latitudes”, *Nature*, vol. 459, no. 7249, 969-973, arXiv: [1011.1669v3](#).
- England, M. H. (1995)**, *the Age of Water and Ventilation Timescales in a Global Ocean Model*.
- England, M. H., D. K. Hutchinson, A. Santoso & W. P. Sijp (2017)**, “Ice-atmosphere feedbacks dominate the response of the climate system to drake passage closure”, *Journal of Climate*, vol. 30, no. 15, 5775-5790.
- Etminan, M., G. Myhre, E. J. Highwood & K. P. Shine (2016)**, “Radiative forcing of carbon dioxide, methane, and nitrous oxide: A significant revision of the methane radiative forcing”, *Geophysical Research Letters*, vol. 43, no. 24, 12,614-12,623.
- Evans, D. et al. (2018)**, “Eocene greenhouse climate revealed by coupled clumped isotope-Mg/Ca thermometry.”, *Proceedings of the National Academy of Sciences of the United States of America*, p. 201714744.



- Fretwell, P. et al. (2013)**, “Bedmap2: Improved ice bed, surface and thickness datasets for Antarctica”, *Cryosphere*, vol. 7, no. 1, 375-393, arXiv: [arXiv:1011.1669v3](https://arxiv.org/abs/1011.1669v3).
- Gaina, C., D. J. J. van Hinsbergen & W. Spakman (2015)**, “Tectonic interactions between India and Arabia since the Jurassic reconstructed from marine geophysics, ophiolite geology, and seismic tomography”, *Tectonics*, vol. 34, 875-906.
- Garcia, D. (2010)**, “Robust smoothing of gridded data in one and higher dimensions with missing values”, *Computational Statistics and Data Analysis*, vol. 54, no. 4, 1167-1178.
- Gasson, E. et al. (2014)**, “Uncertainties in the modelled CO<sub>2</sub> threshold for Antarctic glaciation”, *Climate of the Past*, vol. 10, no. 2, 451-466.
- Gent, P. R. & J. C. McWilliams (1990)**, *Isopycnal Mixing in Ocean Circulation Models*.
- Gent, P. R. et al. (2011)**, “The community climate system model version 4”, *Journal of Climate*, vol. 24, no. 19, 4973-4991.
- Goldner, A., M. Huber & R. Caballero (2013)**, “Does Antarctic glaciation cool the world?”, *Climate of the Past*, vol. 9, no. 1, 173-189.
- Goldner, A., N Herold & M Huber (2014)**, “Antarctic glaciation caused ocean circulation changes at the Eocene-Oligocene transition”, *Nature*, vol. 511, no. 7511, 574-577.
- Greenwood, D. R. & S. L. Wing (1995)**, “Eocene continental climates and latitudinal temperature gradients”, *Geology*, vol. 23, no. 11, 1044-1048.
- Greenwood, D. R., P. Wilf, S. L. Wing & D. C. Christophel (2004)**, “Paleotemperature Estimation Using Leaf-Margin Analysis: Is Australia Different?”, *PALAIOS*, vol. 19, no. 2, 129-142.
- Gregory, J. M. et al. (2004)**, “A new method for diagnosing radiative forcing and climate sensitivity”, *Geophysical Research Letters*, vol. 31, no. 3, 2-5.
- Gregory-Wodzicki, K. M. (1997)**, “The Late Eocene House Range Flora, Sevier Desert, Utah: Paleoclimate and Paleoelevation”, *PALAIOS*, vol. 12, no. 6, 552-567.
- Hague, A. M., D. J. Thomas, M. Huber, R. Korty, S. C. Woodard & L. B. Jones (2012)**, “Convection of North Pacific deep water during the early Cenozoic”, *Geology*, vol. 40, no. 6, 527-530.
- Hall, R. (2002)**, “Cenozoic geological and plate tectonic evolution of SE Asia and the SW Pacific”, *Journal of Asian Earth Sciences*, vol. 20, 353-431.
- Harzhauser, M. et al. (2007)**, “Biogeographic responses to geodynamics: A key study all around the Oligo-Miocene Tethyan Seaway”, *Zoologischer Anzeiger*, vol. 246, no. 4, 241-256.
- Haug, G. H. & R. Tiedemann (1998)**, “Effect of the formation of the Isthmus of Panama on Atlantic Ocean thermohaline circulation”, *Nature*, vol. 393, no. 6686, 673-676.
- Hawkins, E. et al. (2011)**, “Bistability of the Atlantic overturning circulation in a global climate model and links to ocean freshwater transport”, *Geophysical Research Letters*, vol. 38, no. 10, 1-6.
- Haywood, A. M. et al. (2011)**, “Pliocene model intercomparison project (PlioMIP): Experimental design and boundary conditions (Experiment 2)”, *Geoscientific Model Development*, vol. 3, no. 1, 227-242.

- Heavens, N. G., C. A. Shields & N. M. Mahowald (2012)**, “A paleogeographic approach to aerosol prescription in simulations of deep time climate”, *Journal of Advances in Modeling Earth Systems*, vol. 4, no. 11, 1-13.
- Heinemann, M., J. H. Jungclaus & J. Marotzke (2009)**, “Warm Paleocene/Eocene climate as simulated in ECHAM5/MPI-OM”, *Clim. Past*, vol. 5, no. 1987, 785-802.
- Herold, N., M. Seton, R. D. Mueller, Y. You & M. Huber (2008)**, “Middle Miocene tectonic boundary conditions for use in climate models”, *Geochemistry, Geophysics, Geosystems*, vol. 9, no. 10.
- Herold, N. et al. (2014)**, “A suite of Early Eocene (~55 Ma) climate model boundary conditions”, *Geoscientific Model Development*, vol. 7, no. 1, 2077-2090.
- Heydt, A. S. von der & H. A. Dijkstra (2006)**, “Effect of ocean gateways on the global ocean circulation in the late Oligocene and early Miocene”, *Paleoceanography*, vol. 21, no. 1, 1-18.
- Heydt, A. S. von der, H. A. Dijkstra, P. Köhler & R. S. W. van de Wal (2014)**, “On the background state dependency of (palaeo) climate sensitivity”, *Geophysical Research Letters*, vol. 41, no. 2, 6484-6492.
- Hill, D. J. et al. (2013)**, “Paleogeographic controls on the onset of the Antarctic circumpolar current”, *Geophysical Research Letters*, vol. 40, no. 19, 5199-5204.
- Hines, B. R., C. J. Hollis, C. B. Atkins, J. A. Baker, H. E. Morgans & P. C. Strong (2017)**, “Reduction of oceanic temperature gradients in the early Eocene Southwest Pacific Ocean”, *Palaeogeography, Palaeoclimatology, Palaeoecology*, vol. 475, 41-54.
- Hinojosa, L. F. & C. Villagrán (2005)**, “Did South American Mixed Paleofloras evolve under thermal equability or in the absence of an effective Andean barrier during the Cenozoic?”, *Palaeogeography, Palaeoclimatology, Palaeoecology*, vol. 217, no. 1-2, 1-23.
- Hinsbergen, D. J. J. van, P. Kapp, G. Dupont-Nivet, P. C. Lippert, P. G. Decelles & T. H. Torsvik (2011)**, “Restoration of Cenozoic deformation in Asia and the size of Greater India”, *Tectonics*, vol. 30, no. 5, 1-31.
- Hinsbergen, D. J. J. van et al. (2012)**, “Greater India Basin hypothesis and a two-stage Cenozoic collision between India and Asia”, *Proceedings of the National Academy of Sciences*, vol. 109, no. 20, 7659-7664.
- Hinsbergen, D. J. J. van, R. L. M. Vissers & W. Spakman (2014)**, “Origin and consequences of western Mediterranean subduction, rollback, and slab segmentation”, *Tectonics*, vol. 33, no. 4, 393-419.
- Hinsbergen, D. J. J. van et al. (2015)**, “A Paleolatitude Calculator for Paleoclimate Studies”, *PLoS One*, vol. 10, no. 863.
- Hollis, C. J. et al. (2012)**, “Early Paleogene temperature history of the Southwest Pacific Ocean: Reconciling proxies and models”, *Earth and Planetary Science Letters*, vol. 349-350, 53-66.
- Hoorn, C. et al. (2010)**, “Amazonia through time: Andean uplift, climate change, landscape evolution, and biodiversity.”, *Science*, vol. 330, no. 6006, 927-931.
- Hoskins, B. J. & D. J. Karoly (1981)**, “The Steady Linear Response of a Spherical Atmosphere to Thermal and Orographic Forcing”, *Journal of the Atmospheric Sciences*, vol. 38, no. 6, 1179-1196.

- Huber, M. & L. C. Sloan (2001)**, “Heat transport, deep waters, and thermal gradients: Coupled simulation of an Eocene greenhouse climate”, *Geophysical Research Letters*, vol. 28, no. 18, 3481-3484.
- Huber, M. et al. (2004)**, “Eocene circulation of the Southern Ocean: Was Antarctica kept warm by subtropical waters?”, *Paleoceanography*, vol. 19, no. 4, 1-12.
- Huber, M. & D. Nof (2006)**, “The ocean circulation in the southern hemisphere and its climatic impacts in the Eocene”, *Palaeogeography, Palaeoclimatology, Palaeoecology*, vol. 231, no. 1-2, 9-28.
- Huber, M. & R. Caballero (2011)**, “The early Eocene equable climate problem revisited”, *Climate of the Past*, vol. 7, no. 2, 603-633.
- Huber, M. & A. Goldner (2011)**, “Eocene monsoons”, *Journal of Asian Earth Sciences*, vol. 44, 3-23.
- Huber, M. (2012)**, “Progress in greenhouse climate modeling”, in: *Reconstructing Earth's Deep-Time Climate—The State of the Art in 2012*, Paleontological Society Short Course. Ed. by **Ivany, L. C. & Huber, B. T.**, vol. 18, The Paleontological Society, 213-262.
- Huisman, S. E., M. den Toom, H. A. Dijkstra & S. Drijfhout (2010)**, “An Indicator of the Multiple Equilibria Regime of the Atlantic Meridional Overturning Circulation”, *Journal of Physical Oceanography*, vol. 40, no. 3, 551-567.
- Hunke, E. C. & W. H. Lipscomb (2008)**, “The Los Alamos sea ice model, documentation and software.”, *Tech. Rep. LA-CC-06-012*, vol. version 4.
- Hurrell, J. W. et al. (2013)**, “The community earth system model: A framework for collaborative research”, *Bulletin of the American Meteorological Society*, vol. 94, 1339-1360.
- Hutchinson, D. K., A. M. de Boer, H. K. Coxall, R. Caballero, J. Nilsson & M. Baatsen (2018)**, “Climate sensitivity and meridional overturning circulation in the late Eocene using GFDL CM2.1”, *Climate of the Past*, vol. 14, 789-810.
- Inglis, G. N. et al. (2015)**, “Cooling inferred from GDGT distributions”, *Paleoceanography*, vol. 30, no. 7, 1000-1020.
- Jacques, F. M., G. Shi, H. Li & W. Wang (2014)**, “An early-middle Eocene Antarctic summer monsoon: Evidence of 'fossil climates'”, *Gondwana Research*, vol. 25, no. 4, 1422-1428.
- Kamp, P. J., D. B. Waghorn & C. S. Nelson (1990)**, “Late eocene-early oligocene integrated isotope stratigraphy and biostratigraphy for paleoshelf sequences in southern Australia: paleoceanographic implications”, *Palaeogeography, Palaeoclimatology, Palaeoecology*, vol. 80, no. 3-4, 311-323.
- Kennedy, A. T., A. Farnsworth, D. J. Lunt, C. H. Lear & P. J. Markwick (2015)**, “Atmospheric and oceanic impacts of Antarctic glaciation across the Eocene-Oligocene transition”, *Philosophical Transactions of the Royal Society A: Mathematical, Physical and Engineering Sciences*, vol. 373, no. 2054.
- Kennett, J. P. (1977)**, “Cenozoic evolution of Antarctic glaciation, the circum-Antarctic Ocean, and their impact on global paleoceanography”, *Journal of Geophysical Research*, vol. 82, no. 27, 3843-3860.

- Kiehl, J. T., C. A. Shields, J. J. Hack & W. D. Collins (2006)**, “The climate sensitivity of the Community Climate System Model version 3 (CCSM3)”, *Journal of Climate*, vol. 19, no. 11, 2584-2596.
- Kiehl, J. T. & C. A. Shields (2013)**, “Sensitivity of the Palaeocene-Eocene Thermal Maximum climate to cloud properties”, *Phil Trans R Soc A*, vol. 371, no. September, 1-22.
- Kobashi, T., E. L. Grossman, D. T. Dockery & L. C. Ivany (2004)**, “Water mass stability reconstructions from greenhouse (Eocene) to icehouse (Oligocene) for the northern Gulf Coast continental shelf (USA)”, *Paleoceanography*, vol. 19, no. 1.
- Kowalski, E. A. & D. L. Dilcher (2003)**, “Warmer paleotemperatures for terrestrial ecosystems”, *Proceedings of the National Academy of Sciences*, vol. 100, no. 1, 167-170.
- Ladant, J.-B., Y. Donnadieu, V. Lefebvre & C. Dumas (2014)**, “The respective role of atmospheric carbon dioxide and orbital parameters on ice sheet evolution at the Eocene-Oligocene transition”, *Paleoceanography*, vol. 29, no. 8, 810-823.
- Lagabriele, Y., Y. Godd  ris, Y. Donnadieu, J. Malavieille & M. Suarez (2009)**, “The tectonic history of Drake Passage and its possible impacts on global climate”, *Earth and Planetary Science Letters*, vol. 279, no. 3-4, 197-211.
- Large, W. G., J. C. McWilliams & S. C. Doney (1994)**, “Oceanic Vertical Mixing - a Review and a Model with a Nonlocal Boundary-Layer Parameterization”, *Reviews of Geophysics*, vol. 32, no. 94, 363-403.
- Lawrence, D. M. et al. (2011)**, “Parameterization improvements and functional and structural advances in Version 4 of the Community Land Model”, *Journal of Advances in Modeling Earth Systems*, vol. 3, no. 1.
- Lear, C. H., T. R. Bailey, P. N. Pearson, H. K. Coxall & Y. Rosenthal (2008)**, “Cooling and ice growth across the Eocene-Oligocene transition”, *Geology*, vol. 36, no. 3, 251-254.
- Lefebvre, V., Y. Donnadieu, P. Sepulchre, D. Swingedouw & Z. S. Zhang (2012)**, “Deciphering the role of southern gateways and carbon dioxide on the onset of the Antarctic Circumpolar Current”, *Paleoceanography*, vol. 27, no. 4, 1-9.
- Licht, a et al. (2014)**, “Asian monsoons in a late Eocene greenhouse world.”, *Nature*, vol. 513, 501-506.
- Liu, W., S.-p. Xie, Z. Liu & J. Zhu (2017)**, “Overlooked possibility of a collapsed Atlantic Meridional Overturning Circulation in warming climate”, *Science Advances*, vol. 3, no. 1, e1601666.
- Liu, Z. et al. (2009)**, “Global Cooling During the Eocene-Oligocene Climate Transition”, *Science*, vol. 323, no. February, 1187-1190.
- Livermore, R., A. Nankivell, G. Eagles & P. Morris (2005)**, “Paleogene opening of Drake Passage”, *Earth and Planetary Science Letters*, vol. 236, no. 1-2, 459-470.
- Loptson, C. A., D. J. Lunt & J. E. Francis (2014)**, “Investigating vegetation-climate feedbacks during the early Eocene”, *Climate of the Past*, vol. 10, no. 2, 419-436.
- Lunt, D. J. et al. (2010a)**, “CO<sub>2</sub>-driven ocean circulation changes as an amplifier of Paleocene-Eocene thermal maximum hydrate destabilization”, *Geology*, vol. 38, no. 10, 875-878.

- Lunt, D. J., A. M. Haywood, G. A. Schmidt, U. Salzmann, P. J. Valdes & H. J. Dowsett (2010b)**, "Earth system sensitivity inferred from Pliocene modelling and data", *Nature Geoscience*, vol. 3, no. 1, 60-64.
- Lunt, D. J. et al. (2012)**, "A model-data comparison for a multi-model ensemble of early Eocene atmosphere-ocean simulations: EoMIP", *Climate of the Past*, vol. 8, no. 5, 1717-1736.
- Lunt, D. J. et al. (2016)**, "Palaeogeographic controls on climate and proxy interpretation", *Climate of the Past*, vol. 12, no. 5, 1181-1198.
- Lunt, D. J. et al. (2017)**, "The DeepMIP contribution to PMIP4: Experimental design for model simulations of the EECO, PETM, and pre-PETM (version 1.0)", *Geoscientific Model Development*, vol. 10, no. 2.
- Markwick, P. J. (1998)**, "Fossil crocodilians as indicators of Late Cretaceous and Cenozoic climates: Implications for using palaeontological data in reconstructing palaeoclimate", *Palaeogeography, Palaeoclimatology, Palaeoecology*, vol. 137, no. 3-4, 205-271.
- Markwick, P. J. & P. J. Valdes (2004)**, "Palaeo-digital elevation models for use as boundary conditions in coupled ocean - Atmosphere GCM experiments: A Maastriichtian (late Cretaceous) example", *Palaeogeography, Palaeoclimatology, Palaeoecology*, vol. 213, no. 1-2, 37-63.
- Markwick, P. J. (2007)**, "The palaeogeographic and palaeoclimatic significance of climate proxies for data-model comparisons", *Deep-Time Perspectives on Climate Change: Marrying the Signal from Computer Models and Biological Proxies*, 251-312.
- McQuarrie, N. & D. J. J. van Hinsbergen (2013)**, "Retrodeforming the Arabia-Eurasia collision zone: Age of collision versus magnitude of continental subduction", *Geology*, vol. 41, no. 3, 315-318.
- Meulenkamp, J. E. & W. Sissingh (2003)**, "Tertiary palaeogeography and tectonostratigraphic evolution of the Northern and Southern Peri-Tethys platforms and the intermediate domains of the African-Eurasian convergent plate boundary zone", *Palaeogeography, Palaeoclimatology, Palaeoecology*, vol. 196, no. 1-2, 209-228.
- Moreau, M. G., J. Besse, F. Fluteau & M. Greff-Lefftz (2007)**, "A new global Paleocene-Eocene apparent polar wandering path loop by "stacking" magnetostratigraphies: Correlations with high latitude climatic data", *Earth and Planetary Science Letters*, vol. 260, 152-165.
- Mulder, T. E., M. L. J. Baatsen, F. W. Wubs & H. A. Dijkstra (2017)**, "Efficient computation of past global ocean circulation patterns using continuation in paleobathymetry", *Ocean Modelling*, vol. 115.
- Müller, R. D., M. Sdrolias, C. Gaina & W. R. Roest (2008a)**, "Age, spreading rates, and spreading asymmetry of the world's ocean crust", *Geochemistry, Geophysics, Geosystems*, vol. 9, no. 4, 1-19.
- Müller, R. D., M. Sdrolias, C. Gaina, B. Steinberger & C. Heine (2008b)**, "Long-term sea-level fluctuations driven by ocean basin dynamics.", *Science*, vol. 319, no. 5868, 1357-1362.

- Neale, R. B. et al. (2013)**, “The Mean Climate of the Community Atmosphere Model (CAM4) in Forced SST and Fully Coupled Experiments”, *Journal of Climate*, vol. 26, no. 14, 5150-5168.
- Okafor, C. U., D. J. Thomas, B. S. Wade & J. Firth (2009)**, “Environmental change in the subtropics during the late middle Eocene greenhouse and global implications”, *Geochemistry, Geophysics, Geosystems*, vol. 10, no. 7, 1-13.
- Oleson, K. W. et al. (2010)**, “Technical Description of version 4.0 of the Community Land Model ( CLM )”, *NCAR Tech. Note*, vol. NCAR/TN-47, no. 257.
- Passchier, S. et al. (2013)**, “Early eocene to middle miocene cooling and aridification of east antarctica”, *Geochemistry, Geophysics, Geosystems*, vol. 14, no. 5, 1399-1410.
- Passchier, S., D. J. Ciarletta, T. E. Miriagos, P. K. Bijl & S. M. Bohaty (2017)**, “An antarctic stratigraphic record of stepwise ice growth through the eocene-oligocene transition”, *Bulletin of the Geological Society of America*, vol. 129, no. 3-4, 318-330.
- Pearson, P. N. et al. (2001)**, “Warm tropical sea surface temperatures in the Late Cretaceous and Eocene epochs”, *Nature*, vol. 413, no. 6855, 481-487.
- Pearson, P. N. et al. (2007)**, “Stable warm tropical climate through the Eocene Epoch”, *Geology*, vol. 35, no. 3, 211-214.
- Peterse, F. et al. (2012)**, “Revised calibration of the MBT-CBT paleotemperature proxy based on branched tetraether membrane lipids in surface soils”, *Geochimica et Cosmochimica Acta*, vol. 96, 215-229.
- Petersen, S. V. & D. P. Schrag (2015)**, “Antarctic ice growth before and after the Eocene-Oligocene transition: New estimates from clumped isotope paleothermometry”, *Paleoceanography*, vol. 30, no. 10, 1305-1317.
- Pross, J. et al. (2012)**, “Persistent near-tropical warmth on the Antarctic continent during the early Eocene epoch”, 3-7.
- Prothero, D. R. (2008)**, “No Title”, in: *Paleontology of the Upper Eocene Florissant Formation, Colorado*, ed. by **Meyer, H. W. & Smith, D. M.**, Boulder, CO: The Geological Society of America, chap. 5, 71-87.
- Quan, C., Y. S. C. Liu & T. Utescher (2012)**, “Eocene monsoon prevalence over China: A paleobotanical perspective”, *Palaeogeography, Palaeoclimatology, Palaeoecology*, vol. 365-366, 302-311.
- Rahmstorf, S. & J. Willebrand (1995)**, *The Role of Temperature Feedback in Stabilizing the Thermohaline Circulation*.
- Ramstein, G., F. Fluteau, J. Besse & S. Joussaume (1997)**, “Effect of orogeny, plate motion and land-sea distribution on Eurasian climate change over the past 30 million years”, *Nature*, vol. 386, no. 6627, 788-795.
- Retallack, G. J., W. N. Orr, D. R. Prothero, R. A. Duncan, P. R. Kester & C. P. Ambers (2004)**, “Eocene-Oligocene extinction and paleoclimatic change near Eugene, Oregon”, *Bulletin of the Geological Society of America*, vol. 116, no. 7-8, 817-839.

- Robert, C. & J. P. Kennett (1997)**, “Antarctic continental weathering changes during Eocene-Oligocene cryosphere expansion: Clay mineral and oxygen isotope evidence”, *Geology*, vol. 25, no. 7, 587-590.
- Royer, D. L., M. Pagani & D. J. Beerling (2012)**, “Geobiological constraints on Earth system sensitivity to CO<sub>2</sub> during the Cretaceous and Cenozoic”, *Geobiology*, vol. 10, no. 4, 298-310.
- Sagoo, N., P. J. Valdes, R. Flecker & L. J. Gregoire (2013)**, “The Early Eocene equable climate problem: can perturbations of climate model parameters identify possible solutions?”, *Philosophical transactions. Series A, Mathematical, physical, and engineering sciences*, vol. 371, no. 2001, p. 20130123.
- Scher, H. D., S. M. Bohaty, J. C. Zachos & M. L. Delaney (2011)**, “Two-stepping into the icehouse: East Antarctic weathering during progressive ice-sheet expansion at the Eocene-Oligocene transition”, *Geology*, vol. 39, no. 4, 383-386.
- Scher, H. D., S. M. Bohaty, B. W. Smith & G. H. Munn (2014)**, “Eocene glaciation”, *Paleoceanography*, vol. 29, 628-644.
- Schouten, S., J. Eldrett, D. R. Greenwood, I. Harding, M. Baas & J. S. Damsté (2008)**, “Onset of long-term cooling of Greenland near the Eocene-Oligocene boundary as revealed by branched tetraether lipids”, *Geology*, vol. 36, no. 2, 147-150.
- Schouten, S., E. C. Hopmans & J. S. Sinninghe Damsté (2013)**, “The organic geochemistry of glycerol dialkyl glycerol tetraether lipids: A review”, *Organic Geochemistry*, vol. 54, 19-61.
- Seton, M. et al. (2012)**, “Global continental and ocean basin reconstructions since 200Ma”, *Earth-Science Reviews*, vol. 113, no. 3-4, 212-270.
- Sewall, J., L. Sloan, M. Huber & S. Wing (2000)**, “Climate sensitivity to changes in land surface characteristics”, *Global and Planetary Change*, vol. 26, 445-465.
- Sijp, W. P. & M. H. England (2004)**, “Effect of the Drake Passage Throughflow on Global Climate”, *Journal of Physical Oceanography*, vol. 34, no. 5, 1254-1266.
- Sijp, W. P., M. H. England & J. R. Toggweiler (2009)**, “Effect of Ocean gateway changes under greenhouse warmth”, *Journal of Climate*, vol. 22, no. 24, 6639-6652.
- Sijp, W. P., M. H. England & M. Huber (2011)**, “Effect of the deepening of the Tasman Gateway on the global ocean”, *Paleoceanography*, vol. 26, no. 4, 1-18.
- Sijp, W. P., A. S. von der Heydt, H. a. Dijkstra, S. Flögel, P. M. J. Douglas & P. K. Bijl (2014)**, “The role of ocean gateways on cooling climate on long time scales”, *Global and Planetary Change*, vol. 119, 1-22.
- Sijp, W. P., A. S. Von Der Heydt & P. K. Bijl (2016)**, “Model simulations of early westward flow across the Tasman Gateway during the early Eocene”, *Climate of the Past*, vol. 12, no. 4, 807-817.
- Sinha, B. et al. (2012)**, “Mountain ranges favour vigorous Atlantic meridional overturning”, *Geophysical Research Letters*, vol. 39, no. 2, 1-7.
- Slotnick, B. S., V. Lauretano, J. Backman, G. R. Dickens, A. Sluijs & L. Lourens (2015)**, “Early Paleogene variations in the calcite compensation depth: new constraints using old boreholes across Ninetyeast Ridge in the Indian Ocean”, *Climate of the Past*, vol. 11, no. 4, 473-493.

- Sluijs, A. et al. (2006)**, “Subtropical Arctic Ocean temperatures during the Palaeocene/Eocene thermal maximum”, *Nature*, vol. 441, no. 7093, 610-613.
- Sluijs, A. et al. (2008)**, “Article late Paleocene - Early Eocene paleoenvironments with special emphasis on the Paleocene-Eocene thermal maximum (Lomonosov Ridge, Integrated Ocean Drilling Program Expedition 302)”, *Paleoceanography*, vol. 23, no. 1, 1-17.
- Sluijs, A., R. E. Zeebe, P. K. Bijl & S. M. Bohaty (2013)**, “A middle Eocene carbon cycle conundrum”, *Nature Geoscience*, vol. 6, no. 6, 429-434.
- Smith, G. A., S. R. Manchester, M. Ashwill, W. C. McIntosh & R. M. Conrey (1998)**, “Late Eocene-early Oligocene tectonism, volcanism, and floristic change near Gray Butte, central Oregon”, *Bulletin of the Geological Society of America*, vol. 110, no. 6, 759-778.
- Smith, R. D. & J. C. McWilliams (2003)**, “Anisotropic horizontal viscosity for ocean models”, *Ocean Modelling*, vol. 5, no. 2, 129-156.
- Smith, R. D. et al. (2010)**, “The Parallel Ocean Program (POP) reference manual: Ocean component of the Community Climate System Model (CCSM)”, *Los Alamos National Laboratory Tech. Rep. LAUR-10-01853*, vol. 141, 1-141.
- Sobel, E. R. et al. (2013)**, “Oceanic-style subduction controls late Cenozoic deformation of the Northern Pamir orogen”, *Earth and Planetary Science Letters*, vol. 363, 204-218.
- Sømme, T. O., W. Helland-Hansen & D. Granjeon (2009)**, “Impact of eustatic amplitude variations on shelf morphology, sediment dispersal, and sequence stratigraphic interpretation: Icehouse versus greenhouse systems”, *Geology*, vol. 37, no. 7, 587-590.
- Song, X. & G. J. Zhang (2009)**, “Convection parameterization, tropical pacific double ITCZ, and upper-ocean biases in the NCAR CCSM3. Part II: Coupled feedback and the role of ocean heat transport”, *Journal of Climate*, vol. 23, no. 3, 800-812.
- Srokosz, M. A. & H. L. Bryden (2015)**, “Observing the Atlantic Meridional Overturning Circulation yields a decade of inevitable surprises”, *Science*, vol. 348, no. 6241.
- Stampfli, G. M. & G. D. Borel (2002)**, “A plate tectonic model for the Paleozoic and Mesozoic constrained by dynamic plate boundaries and restored syntetic ocean isochrons”, *Earth and Planetary Science Letters*, vol. 196, 17-33.
- Steele, M., R. Morley & W. Ermold (2001)**, “PHC: A global ocean hydrography with a high-quality Arctic Ocean”, *Journal of Climate*, vol. 14, no. 9, 2079-2087.
- Stein, C. A. & S. Stein (1992)**, “A model for the global variation in oceanic depth and heat flow with lithospheric age.”, *Nature*, vol. 359, 123-129.
- Stickley, C. E. et al. (2004)**, “Timing and nature of the deepening of the Tasmanian Gateway”, *Paleoceanography*, vol. 19, no. 4, 1-18.
- Stouffer, R. J. et al. (2006)**, “Investigating the causes of the response of the thermohaline circulation to past and future climate changes.”, *Journal of Climate*, vol. 19, no. 8, 1365-1387.
- Thiele, G. & J. Sarmiento (1990)**, “Tracer Dating and Ocean Ventilation”, *Journal of Geophysical Research*, vol. 95, no. C6, 9377-9391.
- Thomas, D. J., R. Korty, M. Huber, J. A. Schubert & B. Haines (2014)**, “Nd isotopic structure of the Pacific Ocean 70-30 Ma and numerical evidence for vigorous



- ocean circulation and ocean heat transport in a greenhouse world”, *Paleoceanography*, vol. 29, 454-469.
- Tigchelaar, M., A. S. Von Der Heydt & H. A. Dijkstra (2011)**, “A new mechanism for the two-step  $\delta^{18}\text{O}$  signal at the Eocene-Oligocene boundary”, *Climate of the Past*, vol. 7, no. 1, 235-247.
- Toggweiler, J. R. & H. Bjornsson (2000)**, “Drake Passage and palaeoclimate”, *Journal of Quaternary Science*, vol. 15, 319-328.
- Toom, M. den, H. A. Dijkstra & F. W. Wubs (2011)**, “Spurious multiple equilibria introduced by convective adjustment”, *Ocean Modelling*, vol. 38, no. 1-2, 126-137.
- Torsvik, T. H., R. D. Mu, R. V. D. Voo, B. Steinberger, C. Gaina & R. D. Mu (2008)**, “Global Plate Motion Frames: Toward a Unified Model”, *Reviews of Geophysics*, vol. 46, no. 2007, 1-44.
- Torsvik, T. H. et al. (2012)**, “Phanerozoic polar wander, palaeogeography and dynamics”, *Earth-Science Reviews*, vol. 114, no. 3-4, 325-368.
- Traiser, C., S. Klotz, D. Uhl & V. Mosbrugger (2005)**, “Environmental signals from leaves-a physiognomic analysis of European vegetation.”, *The New phytologist*, vol. 166, no. 2, 465-484.
- Trenberth, K. E. & J. M. Caron (2001)**, “Estimates of Meridional Atmosphere and Ocean Heat Transports”, *Journal of Climate*, vol. 14, no. 16, 3433-3443.
- Tripati, A. K. & J. Zachos (2002)**, “Late Eocene tropical sea surface temperatures : A perspective from Panama”, vol. 17, no. 3.
- Tripati, A. K., M. L. Delaney, J. C. Zachos, L. D. Anderson, D. C. Kelly & H. Elderfield (2003)**, “Tropical sea-surface temperature reconstruction for the early Paleogene using Mg/Ca ratios of planktonic foraminifera”, *Paleoceanography*, vol. 18, no. 4.
- Uhl, D. et al. (2007)**, “Cenozoic paleotemperatures and leaf physiognomy - A European perspective”, *Palaeogeography, Palaeoclimatology, Palaeoecology*, vol. 248, no. 1-2, 24-31.
- Viebahn, J. P., A. S. von der Heydt, D. Le Bars & H. A. Dijkstra (2016)**, “Effects of Drake Passage on a strongly eddying global ocean”, *Paleoceanography*, vol. 31, no. 5, 564-581, arXiv: [1510.04141](https://arxiv.org/abs/1510.04141).
- Wade, B. S. et al. (2012)**, “Multiproxy record of abrupt sea-surface cooling across the Eocene-Oligocene transition in the Gulf of Mexico”, *Geology*, vol. 40, no. 2, 159-162.
- Walker, J. D., J. W. Geissman, S. A. Bowring & L. E. Babcock (2013)**, “The Geological Society of America Geologic Time Scale”, *Geological Society of America Bulletin*, vol. 125, no. 3-4, 259-272.
- Wang, G., D. Garcia, Y. Liu, R. de Jeu & a. Johannes Dolman (2012)**, “A three-dimensional gap filling method for large geophysical datasets: Application to global satellite soil moisture observations”, *Environmental Modelling and Software*, vol. 30, 139-142.

- Wilson, D. S., S. S. R. Jamieson, P. J. Barrett, G. Leitchenkov, K. Gohl & R. D. Larter (2012)**, "Antarctic topography at the Eocene-Oligocene boundary", *Palaeogeography, Palaeoclimatology, Palaeoecology*, vol. 335-336, 24-34.
- Wing, S & D Greenwood (1993)**, "Fossils and fossil climate: The case for equable continental interiors in the Eocene", *Philosophical Transactions of the Royal Society of London B Biological Sciences*, vol. 341, no. 1297, 243-252.
- Winguth, A., C. Shellito, C. Shields & C. Winguth (2010)**, "Climate response at the paleocene-eocene thermal maximum to greenhouse gas forcing-a model study with CCSM3", *Journal of Climate*, vol. 23, no. 10, 2562-2584.
- Wolfe, J. A., C. E. Forest & P. Molnar (1998)**, "Paleobotanical evidence of Eocene and Oligocene paleoaltitudes in midlatitude western North America", *Bulletin of the Geological Society of America*, vol. 110, no. 5, 664-678.
- Yang, J., R. A. Spicer, T. E. Spicer & C. S. Li (2011)**, "CLAMP Online': A new web-based palaeoclimate tool and its application to the terrestrial Paleogene and Neogene of North America", *Palaeobiodiversity and Palaeoenvironments*, vol. 91, no. 3, 163-183.
- Ye, D.-Z. & G.-X. Wu (1998)**, "The role of the heat source of the Tibetan Plateau in the general circulation", *Meteorology and Atmospheric Physics*, vol. 67, no. 1-4, 181-198.
- Zachos, J. C., D Stott & K. C. Lohmann (1994)**, "Evolution of early Cenozoic marine temperatures at Equator", *Paleoceanography*, vol. 9, no. 2, 353-387.
- Zachos, J. C., M Pagani, L Sloan, E Thomas & K Billups (2001)**, "Trends, rhythms, and aberrations in global climate 65 Ma to present.", *Science*, vol. 292, no. 5517, 686-693.
- Zachos, J. C., G. R. Dickens & R. E. Zeebe (2008)**, "An early Cenozoic perspective on greenhouse warming and carbon-cycle dynamics.", *Nature*, vol. 451, no. 7176, 279-283.
- Zhang, C. (2005)**, "Madden-Julian Oscillation", *Reviews of Geophysics*, vol. 43.
- Zhang, G. J. & N. A. McFarlane (1995)**, "Sensitivity of climate simulations to the parameterization of cumulus convection in the canadian climate centre general circulation model", *Atmosphere - Ocean*, vol. 33, no. 3, 407-446.

---

# List of Publications

---

## Lead Author

### Published

(1) Baatsen, M. L. J., D. J. J. van Hinsbergen, A. S. von der Heydt, H. A. Dijkstra, A. Sluijs, H. A. Abels, et al. (2016), “Reconstructing geographical boundary conditions for palaeoclimate modelling during the Cenozoic”, *Climate of the Past*, vol. 12, no. 8, 1635-1644.

(2) Baatsen, M. L. J., A. S. von der Heydt, M. A. Kliphuis, J. Viebahn & H. A. Dijkstra (2018a), “Multiple states in the late Eocene ocean circulation”, *Global and Planetary Change*, vol. 163, no. January, 18-28.

(3) Baatsen, M. L. J., A. S. von der Heydt, M. Huber, M. A. Kliphuis, P. K. Bijl, A. Sluijs, et al. (2018b), “Equilibrium state and sensitivity of the simulated middle-to-late Eocene climate”, *Climate of the Past Discussions*, no. April, 1-49.

### In Preparation

(4) Baatsen, M. L. J., P. K. Bijl, A. S. von der Heydt, A. Sluijs & H. A. Dijkstra (2018c), “Antarctic Summer Monsoons in the Middle-to-late Eocene (in prep.)”, *Nature Geoscience*.

## Co-Author

(1) Lunt, D. J., M. Huber, E. Anagnostou, M. L. J. Baatsen, R. Caballero, R. De-Conto, et al. (2017), “The DeepMIP contribution to PMIP4: Experimental design for model simulations of the EECO, PETM, and pre-PETM (version 1.0)”, *Geoscientific Model Development*, vol. 10, no. 2.

(2) Mulder, T. E., M. L. J. Baatsen, F. W. Wubs & H. A. Dijkstra (2017), “Efficient computation of past global ocean circulation patterns using continuation in paleobathymetry”, *Ocean Modelling*, vol. 115.

(3) Hutchinson, D. K., A. M. de Boer, H. K. Coxall, R. Caballero, J. Nilsson & M. Baatsen (2018), “Climate sensitivity and meridional overturning circulation in the late Eocene using GFDL CM2.1”, *Climate of the Past*, vol. 14, 789-810.

---

# About the Author

---

Michiel Baatsen was born on 15 July 1990 in Brasschaat, which lies near Antwerp in Belgium. After finishing his school there, he went to study physics at the University of Antwerp which is what one does who is interested to know 'how things work'. While successfully finishing the Bachelor and starting a Master in solid state physics, something was nagging and his fascination for the weather and climate system was growing. At that point, he decided to move to Utrecht and switch studies into the Meteorology, Physical Oceanography and Climate Master organised by IMAU. This choice was never regretted and things moved forward quickly from that point.

A year later he started an internship at the nearby KNMI, which was a great experience and resulted in a well-received thesis and led to his first scientific publication. Afterwards, he returned to IMAU and switched from studying the future climate to that of the distant past. Working with climate models on cyclones and the interaction between tropical and extra-tropical dynamics shifted towards looking into the intriguing and notoriously difficult to simulate greenhouse worlds of the Eocene. He decided to continue working on palaeoclimate models for another year and is lucky to be able to start a tenure track on Atmospheric Dynamics and Earth System Modelling soon after, becoming a Junior Professor at IMAU. As this is a prefect opportunity to combine personal interests with professional experience, he is very excited to start this new phase and continue to be crazy about the weather.

